Photoelectrochemical characterization of thermal oxide developed on metal and model alloys

Anusara Srisrual

UNIVERSITÉ DE GRENOBLE

THÈSE

Pour obtenir le grade de

DOCTEUR DE L'UNIVERSITÉ DE GRENOBLE

Spécialité : **Matériaux, Mécanique, Génie Civil, Electrochimie**

Arrêté ministériel : 7 août 2006

Présentée par

Anusara SRISRUAL

Thèse dirigée par **Jean-Pierre PETIT**

préparée au sein du **Laboratoire SIMaP**
dans **l'École Doctorale I-MEP2**

Caractérisation photoélectrochimique d'oxydes thermiques développés sur métaux et alliages modèles

Thèse soutenue publiquement le **5 Juillet 2013**,
devant le jury composé de :

M. Michel MERMOUX
Directeur de Recherche – CNRS de Grenoble, Président
Mme Michèle PIJOLAT
Professeur – ENSM Saint-Etienne, Rapporteur
M. Nicolas ALONSO VANTE
Professeur – Université de Poitiers, Rapporteur
M. Loïc MARCHETTI
Ingénieur de Recherche – CEA de Saclay, Examinateur
Mme Céline PASCAL
Maître de Conférences – Université Joseph Fourier, Invitée
M. Jean-Pierre PETIT
Professeur – Grenoble INP, Directeur de thèse

ACKNOWLEDGEMENTS

First and foremost, I would like to gratefully acknowledge Ministry of Sciences and Technology, Royal Thai Government for the PhD scholarship during three and half years; and also the Faculty of Applied Science, King Mongkut's University of Technology North Bangkok for the financial support in the first half year.

I would like to express the sincere thanks my thesis supervisor, Prof. Jean–Pierre Petit, for his invaluable help and constant encouragement throughout the course of this research. I wish to thank you sincerely Prof. Alain Galarie who gave me an opportunity to be the member of this marvelous group and for many useful consults, Prof. Yves Wouters who firstly guided me the photoelectrochemical world, and also Asst. Prof. Celine Pascal who promptly to give me any supports although we occasionally meet. I must thank you Assoc. Prof. Somrerk Chandra–ambhorn and Dr. Kittichai Fakpan who introduced me this research team.

An honest thanks to Prof. Michèle Pijolat and Prof. Nicolas Alonso Vante for accepting to be thesis referee, Dr. Michel Mermoux for accepting to be president in my thesis defense and also for some consults and suggestions, Dr. Loïc Marchetti for accepting to be examiner and for his helps.

This Ph.D. research would not have been completed without the help of others at University of Grenoble. The special thanks are given to Karine Guilly and Muriel Merenda for their support at the laboratory of engineering school of PHELMA for X–ray diffraction, hydraulic uniaxial pressing, and the set–up for hydrogen oxidation. I wish to thank again Dr. Alexandre Crisci for the excellent Raman results, Pierre Chollat and Guy Espagnac for technical supports, Valarie Parry and Grégory Berthomé who give me the kindly help in some occasions.

I would also like to thank Abdelhalim Loucif, Minh Thi Trans, Jacqueline Cuoq, Nour Baccar, Virginie Brizé, Piyorose Promdirek, Jérome Issartel, Luduvic Couture, Guilhem Martin, Jean–Marie Lebrun, Madi Youcef, Evangéline Ahtoy, Ismaël Guillotte, Wichitra Wongpromrat, and Milan Skocic for the occasionally helps and also for a lively atmosphere in the group. Apart from persons who I said, I still would like to say thank you to anyone who used to contact with me and gave me the helps in any opportunities (the persons in SIMaP, LEPMI, CMTC, and also my friends in TISTR).

For the life in France where are absolutely far from my family, I really thanks the Thai communities in France – especially in Grenoble, for the funny activities and a delicious food during the weekend and long holiday. I give the special thanks to Patoomporn, Pakorn, and Nattavut who spend their time to read my manuscript.

Finally, I most gratefully acknowledge my parents and my brothers for all their support throughout the period of this research and all my teachers and my students who push me on to this position.

Anusara SRISRUAL

TABLE OF CONTENTS

INTRODUCTION

Context and objectives

The aim of the PhD work reported in the present manuscript was to contribute developing novel tools in the field of photoelectrochemical characterizations as applied to the domain of High Temperature Corrosion (HTC) of metals and alloys, which has nowadays an high industrial interest (needs for increasing times to failure for services in more severe environments) but whose complexity increases.

The latter complexity arises from oxidation mechanisms which are very sensitive to service operating conditions of great diversity. It also comes from the tuning of the metallurgical parameters of the alloys, an increasing part of them being now micro−structured, which permits technical progresses but increases the difficulty of oxidation studies. The thermal scales which are formed, whose structural and physico−chemical properties do control the corrosion process, are very heterogeneous, both in their chemical compositions and the three−dimensional spatial distribution of their components.

To characterize the properties of the oxidation layers, numerous more or less usual or sophisticated techniques have been and are still used, among them as energy−dispersive X−ray spectroscopy (EDS) for elemental analysis, X−Ray Diffraction (XRD) and Raman spectroscopy.

PhotoElectroChemical (PEC) techniques, which have been particularly developed at SIMaP, are less commonly used in the HTC domain. However, these techniques were already shown to be able to provide, both at the macroscopic and microscopic levels, interesting results as concerns chemical and electronic properties of the thermal scales, and to be particularly sensitive to small differences between samples.

Nevertheless, it appeared interesting to further develop the experimental and analysis tools of the photoelectrochemical techniques, to take into account to the increasing complexity of the oxidation layers. Three directions were chosen.

The first goal was to provide a photoelectrochemical parameters database for single or mixed oxides which are present together in thermal scales grown at high temperature on steels and other alloys, i.e. hematite, chromia, and hematite/chromia solid solutions ($Fe_{2-x}Cr_xO_3$) at several ratios, to help identifying these oxides in the thermal layers formed on chromia−forming alloys.

The second goal was to develop and validate an original mesoscopic PEC set−up, allowing to use, on selected samples areas of 30−40 µm in diameter, all the tools available at

the macroscopic scale; indeed, if photelectrochemical imaging set–ups (1 µm spatial resolution) have already been built and used, due to the restricted number of available laser lines, studies were restricted to a poor set of photon energies.

The third goal was to contribute developing and validating models and/or procedures to improve the analysis tools of Photocurrent Energy Spectra (PES) used in the lab and the literature.

Structure of the manuscript

The manuscript will be outlined as follows.

Chapter 1 will first give an introduction to high temperature corrosion (thermodynamics, defects, oxidation reaction rates, and diffusion phenomena). Then, previous works in the literature on oxidation of metals and alloys (for both ferrous and non–ferrous materials) will be presented. Finally, principles and procedures of photoelectrochemical characterization will be given, and illustrated by works reported in the literature.

Chapter 2 describes the materials and experimental procedures which were used throughout the work.

Chapter 3 will focus on the photoelectrochemical characterization of chromia, hematite and some of their solid solutions. Firstly, photoelectrochemical results on pure chromium oxidized in different conditions will be presented. Then several characterizations (XRD, Raman spectroscopy, and PEC) of $Fe_{2-x}Cr_xO_3$ samples prepared by solid state reaction will be reported.

Chapter 4 will first present the novel mesoscopic photoelectrochemical tool and its interest in the HTC field will be illustrated. Then, the performances of multiscale PEC characterizations, and of the PES analysis model recently developed in our group, will be shown, for the cases of duplex stainless steel and Ni–based alloy oxidized in diverse conditions, using complementary characterizations i.e. SEM/EDS, XRD, and Raman spectroscopy.

Finally, general conclusions and perspectives will be addressed.

CHAPTER 1
PHOTOELECTROCHEMISTRY AND HIGH TEMPERATURE: AN INTRODUCTION

As stated in the preceding introduction, the aim of this work was to enlarge the set of photoelectrochemical tools available for characterizing semiconducting samples, focusing on the case of thermal oxidation layers on metals and metallic alloys. Considering that photoelectrochemists are not necessarily familiar with the field of high temperature corrosion, and, conversely, that photoelectrochemistry is not yet an usual characterization technique in the latter field, this chapter intends to give brief but reasonable introductions to both scientific domains, hopefully sufficient to follow the results of this work exposed in the next chapters.

In the first part of this chapter (1.1), an overview of basic concepts and knowledge in high temperature oxidation will be given, as regards thermodynamics, defects in solids, oxidation reaction rates and diffusion mechanisms. In paragraphs 1.2 and 1.3, results reported in the literature on the oxidation of ferrous and non ferrous metallic alloys will then be presented. The last part (1.4) will present basics of photoelectrochemistry as a characterization tool, together with the results of photoelectrochemical studies previously reported in the literature as regards stainless steels, pure chromium and Ni–based alloys.

1.1 Basics theory of high temperature corrosion

High temperature corrosion generally covers dry corrosion processes in gaseous atmospheres (oxidation). The latter processes are governed by thermodynamics and kinetics. The main phenomena taking place during reactions of metals with oxygen (oxidation mechanism) are presented in Figure 1.1. Initially, the gas adsorbs on the metal surface as atomic oxygen; then oxide nucleates and grows to form a complete thin film. Next, the layer thickens, soon acting as a scale barrier to protect the metal from the gas. Scale growth results from concomitant moving of electrons, oxide ions, metal ions and oxygen diffusion through the scale. As the scale grows up, cavities and microcracks may be created from generated stresses, leading to failure of the scale.

One of the basic knowledge which helps understanding the growth mechanisms is that of diffusion processes. Crystal structures of the considered materials are also important oxidation parameters. The following text will thus address thermodynamics, defects, oxidation reaction rates, and diffusion. The details of these subjects can be found in the standard textbooks [1–4].

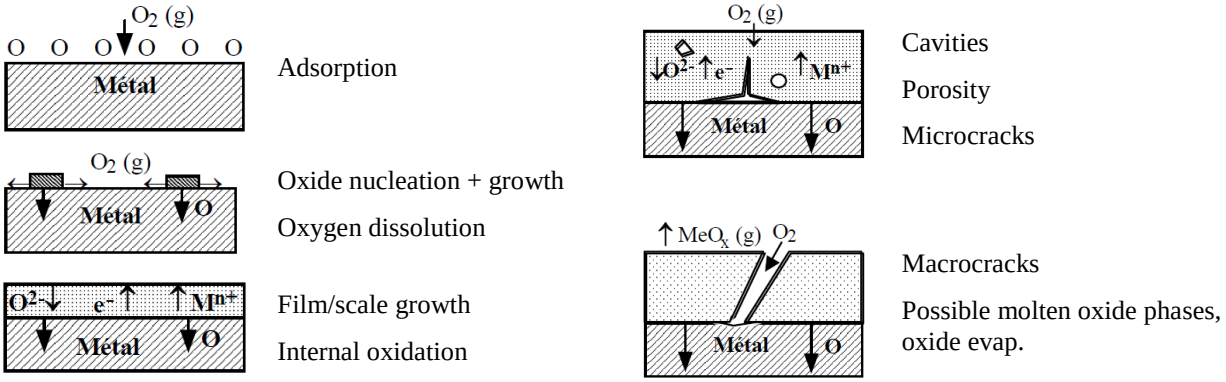

Figure 1.1 A schematic illustration of some main phenomena arising while metals react with oxygen [2]

1.1.1 Thermodynamics of high temperature corrosion

The simplest chemical reaction for the oxidation of metal, which is the reaction of a metal, M, and oxygen gas, O_2, to form the oxide M_xO_y, may by written as:

$$xM + (\frac{y}{2})O_2 \rightarrow M_xO_y \qquad (1.1)$$

The Gibbs energy change, ΔG, is the driving force for the reaction. At constant temperature and pressure, ΔG can be expressed by the second law of thermodynamics as follows:

$$\Delta G = \Delta H - T\Delta S \qquad (1.2)$$

where ΔH is the enthalpy of the reaction, T is the absolute temperature, and ΔS is the entropy change. Spontaneous processes will take place when ΔG is negative. If $\Delta G = 0$, the process is at equilibrium, and if ΔG is positive, the reaction is thermodynamically disfavored; that is, the reverse reaction will proceed spontaneously. The driving force or ΔG for reaction (1.1) can be expressed in term of the standard Gibbs energy change, ΔG^0:

$$\Delta G = \Delta G^0 + RT \ln\left[\frac{a_{M_xO_y}}{(a_M)^x \cdot (a_{O_2})^{y/2}}\right] \qquad (1.3)$$

where the chemical activity, a, of each reactant or product is raised to the power of its stoichiometric coefficient, and R is the gas constant.

In most cases, the activities of the solids (metals and oxides) are invariant, i.e. activities = 1 for pure solids, and for the relatively high temperature and moderate pressures usually encountered in oxidation reactions, the activity of oxygen gas, a_{O_2}, can be approximated by its pressure. Therefore, at equilibrium where $\Delta G = 0$:

$$\Delta G^0 = -RT \ln\left[\frac{a_{prod}}{a_{react}}\right] \cong + \frac{y}{2} RT \ln p_{O_2} \quad (1.4)$$

where p_{O_2} is the partial pressure of oxygen. So, the equilibrium partial pressure of oxygen is:

$$p_{O_2} = \exp\left(\frac{2}{y}\frac{\Delta G^0}{RT}\right) \quad (1.5)$$

In solid solution such as an alloy, the partial molar Gibbs energy of a substance is usually called chemical potential, μ. If 1 mole of pure A is dissolved in a massive of solution, the Gibbs energy change for the mole of A is:

$$\Delta \overline{G}_A = \mu_A - \mu_A^0 = RT \ln a_A \quad (1.6)$$

where μ_A^0 is the chemical potential of 1 mole of pure A (the standard chemical potential), the chemical potential μ_A is the value in the solution, and a_A is the activity of A in the solution.

Thermodynamically unstable oxides, metastable oxides, are often formed in gaseous corrosion systems. The Gibbs energy of the metastable oxide formation is less negative than for a stable oxide, but in fact an unstable oxide can often exist. For instance, rapid kinetics can favor the formation of a less stable oxide on an alloy, an alloy AB could oxidize to form oxide AO and BO, but if BO is more stable than AO, then any AO formed in contact with B should convert to BO by the reaction:

$$B + AO \rightarrow BO + A \quad (1.7)$$

Nevertheless, if AO grows rapidly compared with BO and the conversed reaction is slow, AO can be the main oxide found on the alloy.

Thermodynamically unstable crystal structures of oxides are also sometimes found. A growing oxide film tends to try to align its crystal structure with that of the substrate on which it is growing. This epitaxy can cause the formation of an unstable structure that fits the substrate best. For example, the formation of cubic Al_2O_3 replaces the stable rhombohedral Al_2O_3 on aluminium alloys.

1.1.2 Defects

Defects or imperfections in crystalline solids are divided into three groups according to geometry or dimensionality: point defects, line defects, and plane defects. In oxidation processes, these defects may promote the transport of species through the scale.

1.1.2.1 Point defects

Point defects are associated with the missing or the irregular placing of atoms in the lattice. These imperfections may be presented as vacancies, self–interstitials, substitution and interstitial impurities.

Vacancy or vacant lattice site is the simplest of the point defects which results from the missing of an atom (Figure 1.2(a)). Vacancies are always present in all crystalline solids, especially at high temperatures when atoms are frequently and randomly changing their positions leaving empty lattice sites. The existence of vacancies correlates with the principles of thermodynamics as they increase the entropy in the crystal. The number of vacancies, N_v, increases exponentially with the absolute temperature, T, as follows:

$$N_v = N \exp\left(-\frac{Q_v}{kT}\right) \tag{1.8}$$

where N is the total number of atomic sites, Q_v is the energy required for the formation of a vacancy, and k is the Boltzmann's constant (1.38×10^{-23} J/atom·K).

Self–interstitial is an atom of the same nature as the lattice atoms is squeezed into an interstitial site as shows in Figure 1.2(b). A self–interstitial atom being larger than the interstitial site, a strong distortion happens in the surrounding lattice. The presence of such a defect has a low probability, compared to the one of a vacancy.

Interstitial and substitution impurities (Figure 1.2(c) and (d)) are point defects corresponding to the presence of foreign atoms. An interstitial impurity usually consists of an atom which is smaller than a lattice atom. It introduces a less distortion to the lattice, is more common and more mobile, compared with the self–interstitial defect. For a substitution impurity, the impurity atom replaces a host atom in its site.

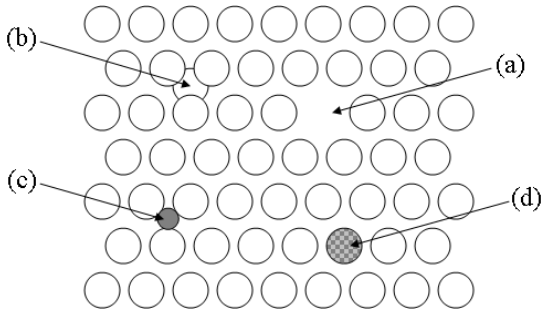

Figure 1.2 Schematic illustration of point defects in crystals: (a) vacancy (b) self–interstitial (c) interstitial impurity and (d) substitution impurity

1.1.2.2 Line defects

Line defects or dislocations occur from a misalignment of atoms, and are mainly divided into edge dislocations and screw dislocations. *Edge dislocations* (Figure 1.3(a)) are made up of an extra plane or half–plane of atoms which terminate their edge within the crystal. *Screw dislocations* (Figure 1.3(b)) correspond to distortions introduced by a shear stress. Most dislocations in materials are never being only edge or screw dislocations, but a combination of both types are always presented.

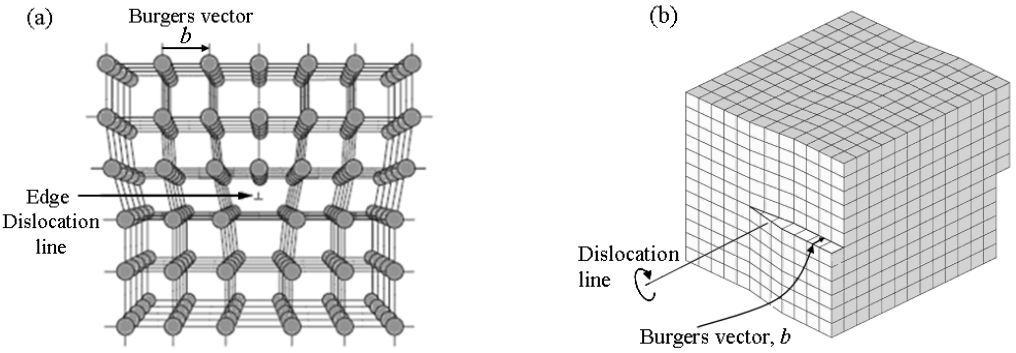

Figure 1.3 Schematic of linear defects of crystals (a) edge dislocation and (b) screw dislocation [5]

1.1.2.3 Plane defects

Plane defects are two–dimension imperfections located at the interfaces between homogeneous regions of the material. They are classified as external surfaces, grain boundaries, twin boundaries, stacking faults, and phase boundaries.

1.1.2.4 Defect structure of ionic oxides

In ionic crystals, the bonding is provided by coulomb forces between positive and negative charges which commonly provide point defects in structure. The imbalance among charges tends to balance itself to maintain charge neutrality and its stoichiometry. The main defect structures of ionic oxides which lead to an ionic conductivity are Schottky defects and/or Frenkel defects.

A Frenkel defect (Figure 1.4(a)) is a pair made of a cation vacancy and of an interstitial cation. The smaller ion, definitely cation, is displaced from its position to an interstitial site. It creates a vacancy defect at its original site and an interstitial defect at its new location. Since anions are larger than cations, it is difficult to form an interstitial anion.

A Schottky defect, Figure 1.4 (b), is a pair of anion and cation vacancies in the proper ratio necessary to maintain electric neutrality. The defect forms when oppositely charged ions leave their lattice sites, creating vacancies. The ions must diffuse into the appropriate adjacent vacancies to allow mass transfer and ionic electrical conductivity.

Both defects are implied for ion diffusion in the oxide growth process.

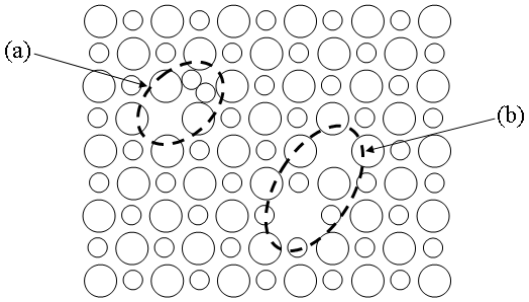

Figure 1.4 Schematic of defect structure of ionic oxides: (a) Frenkel defects and (b) Schottky defects

1.1.2.5 Defect structure of semiconductor oxides

The defect structure of semiconducting oxides can be divided into three categories that is p–type, n–type, and amphoteric. The schematics of ionic arrangement in some semiconductor oxides are illustrated in Figure 1.5.

A p–type oxide is a nonstoichiometric compound with *metal cation vacancies* or *oxygen interstitials*. According to the growth of metal–deficient oxides with predominant defects of metal cation vacancies, cations diffuse in the lattice by exchange with these vacancies. Charge neutrality in the lattice is maintained by the presence of electron holes or metal cations of higher than average positive charge. The electronic current is due to positively charged electron holes.

An n–type oxide could be a cation interstitial metal–excess or anion vacancy. An *n–type cation interstitial metal–excess* oxide contains interstitial cations, in addition to the cations in the crystal lattice. Charge neutrality is established through an excess of negative conduction electrons, which promote electrical conductivity. An *n–type anion vacancy* oxide contains oxygen anion vacancies in the crystal lattice. Current is passed by electrons, which are present in excess to establish charge neutrality.

Amphoteric oxide is a nonstoichiometric with either a deficiency of cations or a deficiency of anions, depending on the elemental composition.

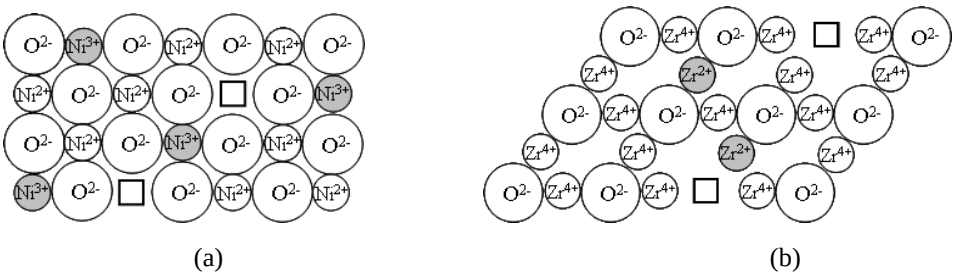

Figure 1.5 Schematic of ionic arrangements in some semiconductor oxides: (a) p–type NiO, cation vacancies are indicated as open squares. The Ni^{3+} cations are shaded, and (b) n–type ZrO_2, anion vacancies are indicated as open squares; Zr^{2+} ions are shaded [3]

1.1.3 Oxidation reaction rate

1.1.3.1 Linear oxidation reaction rates

If the metal surface is not protected by a barrier of oxide, the oxidation rate usually remains constant with time. The linear oxidation rate is presented as:

$$\frac{dx}{dt} = k_L \tag{1.9}$$

where x is the mass or thickness of oxide formed, t is the time of oxidation, and k_L is the linear rate constant. The rate constant is a function of the metal, the oxidation atmospheres composition and pressure, and of the temperature. Integration of eq. (1.9) gives the linear oxidation equation as follows:

$$x = k_L t \tag{1.10}$$

Linear oxidation is to be expected if the Pilling–Bedworth ratio, the ratio of the volume of oxide formed to the volume of metal consumed, is less than 1. Situations which can occur in this case are such as volatilization or meltage of the oxide, scale spallations or cracks due to internal stresses, or formation of non–protective oxide on the metal.

1.1.3.2 Logarithmic and inverse logarithmic reaction rates

Logarithmic and inverse logarithmic kinetics is usually observed at low temperature when only a thin oxide film is formed. Transport processes across the film are rate determining, electric fields across the film being the driving force. The oxidation equation in logarithmic and inverse logarithmic cases is given in equations (1.11) and (1.12) respectively.

$$x = k_e \log(at+1) \tag{1.11}$$

$$\frac{1}{x} = b - k_i \log t \tag{1.12}$$

where k_e, k_i, a, and b are constants. Due to the difficulties to make mass measurements in the thin film range, it is very difficult to discriminate between logarithmic and inverse logarithmic oxidation rates.

1.1.3.3 Parabolic reaction rates

Parabolic kinetics is usually observed when the diffusion of ions through a compact barrier layer of oxide is rate controlling, the chemical potential gradient being the driving force. As the oxide becomes thicker, the “diffusion distance” increases, and the oxidation rate slows down. The rate is inversely proportional to the oxide thickness as written in eq. (1.13) and the parabolic equation in eq. (1.14) is obtained after integration.

$$\frac{dx}{dt} = \frac{k_p}{x} \tag{1.13}$$

$$x^2 = \frac{k_p}{2} t \tag{1.14}$$

where k_p is the parabolic rate constant.

Hence the logarithmic (or inverse logarithmic) or the parabolic oxidation rates should be found where the protective oxide cover the materials, whereas the linear oxidation rate present where the failure of protective oxide occurs or the non–protective oxide forms.

1.1.4 Diffusion

Diffusion is a transport phenomenon in which particles move (in a random way) using their own thermal energy: no bulk motion (convection) is required. The rate of global movement of the particles depends mainly on temperature and on the sizes/masses of the particles. According to the phenomenological Fick's law, the flux of diffusing particles is proportional to the gradient of concentrations, and is direct from higher to lower concentration zones. Diffusive equilibrium is reached when the concentration of the diffusing substance in the two compartments becomes equal. Diffusion in materials provides gradual mixing; in a phase with uniform temperature, no other external forces acting on the particles, the diffusion process would ultimately lead to complete mixing.

Diffusion can be mainly classified as *interdiffusion* when a foreign atom diffuses in a host matrix and *self–diffusion* when the diffusing atom is of the same nature as the atoms of the host matrix.

1.1.4.1 Diffusion mechanisms

In solids, the diffusion of particles may occur by vacancy diffusion or interstitial diffusion. Particles motion may distort the lattice during the displacement.

Vacancy diffusion (Figure 1.6(a)) is the interchange of an atom from a normal lattice position to an adjacent vacant lattice site. Indeed, the presence of a vacancy is necessary, and the diffusion rate is a function of the number of vacancies which depends on temperature. Since diffusing atoms and vacancies exchange positions, the diffusion flux of atoms is in the opposite direction of the one of vacancies. Both self–diffusion and interdiffusion may be observed.

Interstitial diffusion (Figure 1.6(b)) involves migrations of atoms from interstitial positions to a neighboring one which is empty. So, the atoms must have a smaller

size than that of the host atoms, adequate to fit into the interstitial site. This mechanism is usually found for interdiffusion of impurities.

Apart from vacancy and interstitial mechanism, *interstitialcy mechanism* can take place. In the interstitialcy mechanism, the interstitial atom pushes one of its neighboring atoms on a regular lattice position into another interstitial position, and then occupies the site of the displaced atom.

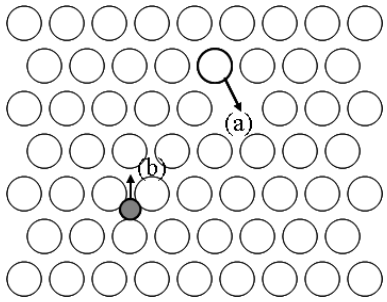

Figure 1.6 Schematic of diffusion mechanisms: (a) vacancy diffusion and (b) interstitial diffusion

1.1.4.2 Steady–state diffusion

In steady–state conditions, the rate of mass transfer, usually expressed as the diffusion flux (J) is proportional to the negative gradient of concentrations ($\frac{\partial \phi}{\partial x}$) according to Fick's first law as follows:

$$J = -D\frac{\partial \phi}{\partial x} \tag{1.15}$$

where D is diffusion coefficient, ϕ is the concentration of diffusing species which is time independent, and x is the position in the solid phase.

1.1.4.3 Nonsteady–state diffusion

The most of practical diffusions are nonsteady–state, that is the diffusion flux and the concentration gradient at some particular point in a solid vary with time (t), resulting in a net accumulation or depletion of the diffusing species. A nonsteady–state diffusion can be described by the partial differential equation of Fick's second law as below:

$$\frac{\partial \phi}{\partial t} = D\frac{\partial^2 \phi}{\partial x^2} \tag{1.16}$$

1.1.4.4 Factors affecting on diffusion

Diffusion rates and diffusion coefficients depend on many factors such as the nature of the diffusing species, the temperature, the defect concentrations, crystal orientations, and nature and concentration of impurities. The *diffusing species* evidently

influence the diffusion coefficient: for instance the diffusion coefficient associated to carbon interdiffusion is greater than the one of self–diffusion in iron. The latter comparison also illustrates that the rate of diffusion via vacancies (self–diffusion of iron) is lower than via interstitial mechanism (interdiffusion of carbon).

The diffusion coefficient exponentially increases with increasing *temperature* according to the following Arrhenius equation:

$$D = D_0 \exp\left(-\frac{Q_d}{RT}\right) \tag{1.17}$$

where D_0 is a temperature–independent pre–exponential factor, Q_d is the activation energy for diffusion, R is the gas constant, and T is the absolute temperature. The activation energies (Q) of interstitial diffusion are much lower than the ones of vacancy diffusion.

When considering two systems, S_1 and S_2, at the same temperature, if the chemical potential of S_1 is greater than the one of S_2 ($\mu_1>\mu_2$), an energy flow will occur from S_1 to S_2 because the fact that the system always prefers low energy and maximum entropy.

The diffusion coefficient in rather stoichiometric compounds can usually be assumed to be proportional to the *defect concentration*. The diffusion coefficient can also depend on *crystal orientation* in noncubic crystals while it is independent of orientation in cubic crystals.

Impurities, which perhaps come from the alloy before oxidation or from gas phase during oxidation, always exist in thermal oxides. They affect the diffusivities in the oxide, and consequently the oxidation rates. For example, in p–type oxide such as NiO, any substitutional cation with a valence greater than the Ni^{2+} ion tends to increase the concentration of cation vacancies which also tends to increase the diffusivity of Ni^{2+} cation through the oxide.

Short–circuit diffusion, the diffusion along grain boundaries and crystalline defects, provide lower activation energies for diffusion. In metals, diffusion along dislocations is more important than volume diffusion below about one–half of the absolute melting point. At high temperatures, volume diffusion predominates in both metals and oxides.

1.2 Oxidation of ferrous alloys

The use of metals and alloys at high temperature always faces with oxidation/corrosion issues. Stainless steel, a ferrous alloy containing at least 10.5% chromium, is widely used for high temperature applications because of its extraordinary corrosion resistance. Not only chromium but also nickel and molybdenum are allowed with iron to improve the corrosion resistance of steels, whereas nitrogen can increase mechanical strength and enhance pitting resistance. According to their crystalline structure and strengthening precipitates, stainless steels are divided in five categories: ferritic, austenitic, martensitic, duplex, and precipitation–hardening. A protective layer is generally formed containing always chromia (Cr_2O_3). Other oxides which are often encountered in the layer are iron oxides (wüstite FeO, magnetite Fe_3O_4, or hematite Fe_2O_3). The latter chromium and iron oxides usually are also found as solid solutions especially with the corundum structure ($Fe_{2-x}Cr_xO_3$). In this work, duplex stainless steel, consisting of ferritic and austenitic grains, will be studied. Hence the oxidation of ferritic, austenitic, and duplex stainless steels is briefly reviewed in this section.

1.2.1 Ferritic stainless steel

Ferritic is a stainless steel which mainly composes of iron and chromium and has a very low nickel content. The alloying element which stabilizes the ferritic phase is chromium. Ferritic stainless steel is a ferromagnetic material with the body–centered cubic (BCC) crystal structure. It exhibits low in ductility and work hardenability but high in yield strength and stress corrosion cracking resistance.

Oxidation of ferritic stainless steel at high temperature was broadly studied. The resulting common knowledge is that oxidation depends on many factors such as the chemical composition of alloys, and the oxidizing atmosphere, temperature, and time. The kinetics of oxidation often exhibit a parabolic law, oxides rapidly growing up at the initial stages and becoming stable as the protective oxide is formed; however the kinetic rate can turn new growing up when the protective oxide is spalling [6–8]. Thermal oxide type and structure certainly depend on various parameters however rhombohedral forms of chromia (Cr_2O_3), hematite (Fe_2O_3), hematite–chromia solid solution ($Fe_{2-x}Cr_xO_3$), and of the spinel manganese–chromium oxide ($MnCr_2O_4$) are generally observed. Some parameters of interest for the oxidation process of ferritic steels are presented below.

1.2.1.1 Effect of exposure time and temperature

Oxidation time and temperature are well–acknowledged to affect the oxidation kinetics. The oxide thickness generally increases with time and a higher oxidation rate is found when increase the oxidation temperature. For instance, in the study of P. Jian et

al. [6], temperature dependence of the parabolic rate constant is reported for oxidation in air. In addition, this paper proposed a schematic view of oxide scale formation (Figure 1.7), based on XRD/SEM/EDS characterizations, showing a duplex oxide microstructure with $MnCr_2O_4$ on top of Cr_2O_3. An anomalous temperature dependence of the rate constant for intermediate–Cr contents (~10–12%) steels for oxidation in steam was reported by J. Zurek et al. [9]. Oxidation rates did not steadily increase with increasing temperature due to the formation of a thin protective oxide layer at higher temperature, and a rapidly growing up of less–protective oxide at lower temperature, whereas increasing the temperature increased oxidation rate in steels with higher or lower Cr contents.

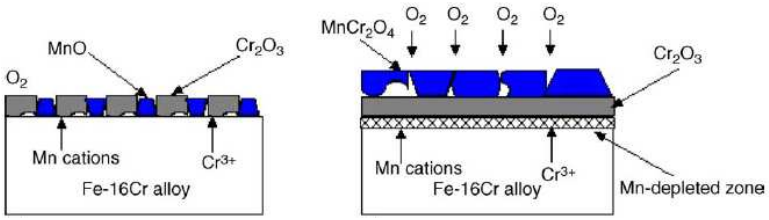

Figure 1.7 Schematics illustration of oxidation processes of the Fe–16Cr alloy in air [6]

The initial stage of oxidation of ferritic stainless steel AISI 430 under $O_2/H_2O/N_2$ at 1273 K was studied by I. Saeki et al. [10–11]. The oxidation was rapid at the initial stages, and then decreased, but not following the parabolic equation. Time dependence of the scale morphology was demonstrated, and it was shown that the thermal oxide was composed of corundum oxides of $(Fe,Cr)_2O_3$. An oxidation model was proposed as in Figure 1.8 [11]. Fe–rich oxide was lunched at the very initial stage and it turned to a Cr–rich oxide when time increased. Spinel oxides appeared after the formation of corundum oxide. The outer oxide composed of spinel oxide with a small amount of corundum oxide [10]. A. Srisrual et al. [12] reported the initial stages of oxidation of AISI 441. The Fe–rich corundum oxide was formed at the very early stage, and then turned to a Cr–rich oxide, a spinel oxide of $MnCr_2O_4$ being present on the top of the layer. Cr content in corundum oxide increased with time and temperature.

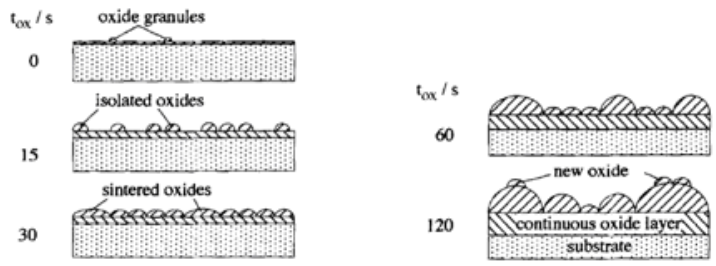

Figure 1.8 Schematic illustration of the initial oxidation process of stainless steel 430 in O_2–H_2O–N_2 at 1273 K [11]

1.2.1.2 Effect of alloying elements

Alloying elements are parameters influencing directly the characteristics of the alloys and of their thermal oxides. The study of I. Saeki et al. [13] is an example of the researches which were performed on the effect of the manganese content, in the case of the initial oxidation of stainless steel 430 at 1273 K in O_2/N_2 atmosphere. The influence of different amounts of Mn (0.09, 0.38, and 0.9 mass%) on the oxidation mechanism was investigated. For the lower Mn content, only corundum oxide was formed. The structure and the composition of the oxide changed during the first 30 seconds (Fe–rich corundum oxide was lunched at the start and then Fe was replaced by Cr in the oxide after the formation of a thicker and more compact oxide), and then became constant (oxide grew up at the surface by sintering and recrystallization of the original nuclei without the formation of new nuclei). For higher Mn contents, the first transient stage was similar, except for differences in morphology and for the presence of an outer spinel oxide which nucleated from pre–existing corundum oxide. Moreover Mn increased the oxidation rate at steady state because of the rapid diffusivity of metal ions through the spinel oxide.

1.2.1.3 Effect of gas compositions

The *effect of hydrogen* gas in the oxidizing atmosphere was reported by E. Park et al. [14]. Hydrogen containing atmosphere promoted a Cr–rich oxide layer on the surface. The oxidation process was proposed as to be the one illustrated in Figure 1.9 showing an Fe–rich oxide at the beginning, and then the formation of a duplex oxide layer, with an Fe–rich outer layer and an Cr–rich inner layer. The duplex oxide turned to a Cr–rich mono–layer with increasing time.

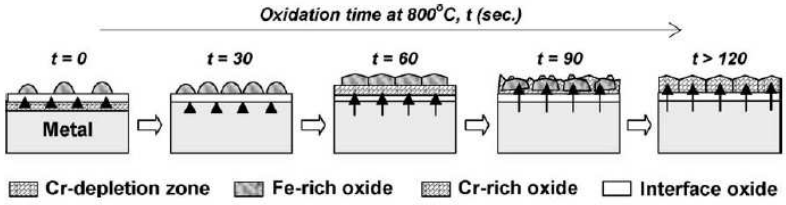

Figure 1.9 Schematic of the oxidation process of a polished Fe–15 at.% alloy surface [14]

The *effect of the oxygen partial pressure* was also studied, and for instance, reported by Anette N. Hansson and M.A.J. Somers [15]. The study presented the influence of the oxidation environment on the scale morphology and on the oxidation rate for Fe–22Cr alloys. Thermal oxide layers consisted of $MnCr_2O_4$ on top of Cr_2O_3. The wrinkle of the oxide morphology was the result from the growth stress which was formed higher at higher oxygen partial pressures.

A whisker oxide, which was suggested to grow by surface diffusion of cations along a tunnel surface inside the whiskers, was observed in H_2/H_2O while being absent in air/H_2O. Lower oxygen partial pressures provided a slower oxide growth because of the lower oxygen anion diffusion. Other researches [10–11] reported that increasing the oxygen partial pressure promoted Cr–rich oxide, while Fe–rich and spinel oxide was resisted.

The influence of water vapor was widely studied. A. Galerie et al. [8] studied the oxidation of ferritic stainless steel and found that the parabolic oxidation rate was higher in water vapor than in oxygen, affecting accelerated failure of the protective chromia scale. The report of Z. Yang et al. [16] also focused on the effect of water vapor and found that adding water vapor in the atmosphere resulted in nucleation and growth of hematite in the scale, in accordance with a previous work of our group [12] which showed that the presence of water vapor in atmosphere yielded Fe_2O_3 in the thermal oxide layer.

1.2.2 Austenitic stainless steel

Austenitic stainless steels are obtained by adding austenite stabilizers, commonly nickel, but also manganese and nitrogen. The crystal structure is face–centered cubic (FCC). Austenitic stainless steels are a non–ferromagnetic material. Interesting mechanical properties such as high ductility and excellent toughness are obtained. Due to the limitations to the increase of Cr content, Mo is also added to improve corrosion resistance. Oxidation of austenitic stainless steel indeed depends on diverse parameters as in the case of the ferritic ones. Some studies on the influence of the latter factors are presented now.

1.2.2.1 Effect of exposure time and temperature

L. Dong–sheng et al. [17] reported on the temperature dependence of the oxidation of an austenitic stainless steel (Cr18Ni11Cu3Al3MnNb). Oxidation was done in air at 700°C, 800°C, and 900°C. It was again shown that the higher oxidation rate was obtained at the higher temperatures. At 700°C and 800°C, oxidation followed the parabolic law and a dense oxide film was obtained, mainly composed of hexagonal Al_2O_3, Fe_2O_3, and of a small amount of Cr oxide at 700°C. At 900°C, the oxide film started to delaminate, and was composed of $(Cr,Fe)_2O_3$ and of the spinels $CuCrMnO_4$ and $Fe(Cr,Al)_2O_4$. J. A. Poston Jr. et al. [18] also reported an oxidation temperature and time dependences, using X–ray photoelectron spectroscopic (XPS) to trace the oxygen penetration depth in oxides grown on Fe–16Cr–16Ni–2Mn–1Mo–2Si austenitic stainless steel. Oxidation was conducted at 973 and 1073 K with exposure times of 25, 100, 193, 436 and 700 h. Surface and near surface rearrangements following oxidation resulted in a region of high Cr concentration on all oxidized samples. The presence of Cr, Mn, Fe and Mo at the initial oxidized surface indicated

that the oxide film formed is not exclusively Cr_2O_3. Temperature and time dependence to O_2 penetration depth was observed. The penetration depth is significantly greater for the samples oxidized at 1073 K and was generally found to increase with increased exposure times up to 436 h, no increase in depth being then observed between 436 and 700 h exposure times.

The initial stage of oxidation of austenitic stainless steel AISI 304 at 1273 K for up to 1 h was studied by I. Saeki et al. [19], together with the one of ferritic stainless steel AISI 430 in the same conditions. The initially formed oxide on AISI 304 is only an iron–rich corundum–type oxide. In the later stage, the oxide was composed of an inner layer of chromium–rich corundum oxide with an outer mixed layer of corundum and spinel oxides. A similar reaction is also postulated to take place in the oxidation of AISI 430.

1.2.2.2 Effect of alloying elements

Chemical compositions are key factors in oxidation of metals. G. Cao et al. [20] compared the corrosion resistance of different austenitic stainless steels, i.e. stainless steel types 316 and type 310, and Alloy 800H, in supercritical CO_2 at 650 °C and 20 MPa for 3000 h. Alloy 800H (32 wt.% of Ni and 21 wt.% of Cr) exhibited the best corrosion resistance followed by type 310 (21.5 wt.% of Ni and 25 wt.% of Cr) and type 316 (12 wt.% of Ni, 17 wt.% of Cr, and 2.5 wt.% of Mo). The difference in corrosion performances was related to the compositions and morphologies of the oxides. For 316 stainless steel, the outer layer consisted of large equiaxed grained Fe_3O_4 (magnetite) and an inner spinel $FeCr_2O_4$ layer. For the 310 stainless steel, Cr–rich oxide layers Cr_2O_3 and $Cr_{1.4}Fe_{0.7}O_3$ improved corrosion resistance. For Alloy 800H the superior corrosion resistance stems from the formation of oxide layers of multiple stoichiometries including, Cr_2O_3, $Cr_{1.4}Fe_{0.7}O_3$, $FeCr_2O_4$, and $Ni_{1.4}$ $Fe_{1.7}O_4$, $FeMn_2O_4$, and Al_2O_3. A very thin SiO_2 layer was also observed for type 310 stainless steel and Alloy 800H (known for its protective qualities). The oxidation of Alloy 800H and stainless steel type 310 followed a diffusion controlled growth parabolic law. Stainless steel type 316 exhibited a higher oxide growth rate with more oxide spallations. Discontinuous islands of carburized regions were observed underneath the oxide layers which appeared to promote delamination of oxide layer from the alloy substrate. Hence the difference in chemical compositions led to the different oxidation mechanisms, providing diverse kinetic rates and oxide types, that absolutely affected to corrosion resistance of materials.

Apart from the different grades of stainless steel, the influence of other alloying elements was also reported. For instance, increasing of the *nitrogen* content in austenitic stainless steel contributed to improve the corrosion, erosion and corrosion–erosion

resistance [21]; moreover, it promoted a homogeneous microstructure and decreased the charge carriers which affected the protecting and electronic properties of the oxide layer [22]. Increasing either the chromium or nickel contents delayed the accelerated corrosion and spallation in austenitic stainless steel [23].

1.2.2.3 Effect of gas compositions

The presence of water vapor was shown to accelerate the oxidation of austenitic stainless steel, leading to a faster breakaway oxidation [24]. Adding oxygen gas in atmosphere also accelerated scale growth, when iron based oxides were formed [25]. The increasing of partial pressure of nitrogen in the gas mixture could produce thermal layers with higher hardness and adequate corrosion resistance [26]. In the oxy–fuel–combustion atmosphere (fuel gases and pure oxygen) [27], the partial pressure of SO_2 provided the higher depth of corrosive attack on samples; besides, increasing the partial pressures of carbon dioxide led apparently to rapid and massive internal carbon enrichment in the oxide scale.

1.2.3 Duplex stainless steel

Duplex stainless steels (DSS), consisting of two phases of ferrite and austenite, are mainly composed of iron and chromium with lower amounts of Ni, Cu, and Mo. A higher corrosion resistance and mechanical properties superior to those of ferritic and austenitic stainless steels, are obtained by the balance of the ferritic and austenitic phases. As ferritic materials, DSS are ferromagnetic materials. Concerning the thermal properties, DSS have a higher thermal conductivity and a lower thermal expansion coefficient than the austenitic stainless steels.

Oxidation of DSS was shown to depend on the alloying elements and on the oxidation environment. Different metallurgical variables of both ferritic and austenitic phases also strongly affect the oxidation of individual grains. Generally, Cr, Mo, and Si preferably, presented in ferritic phase while Fe, Ni, and Mn preferably presented in austenitic phase (these elements play a role as ferritic and austenitic stabilizers [28–29]). Oxidation of DSS is commonly observed to be parabolic [30–31].

1.2.3.1 Effect of exposure time and temperature

Iron oxide and chromium oxides are the main thermal oxides which can be observed on the oxidized duplex stainless steel (ODSS). The temperature dependence of the oxidation of duplex stainless steel 2205 was reported by C. Donik et al. [32–33]. Below 300°C, small increases in temperature above room temperature resulted in increasing the amounts of iron oxides and reduced the ratios of chromium oxides on the surface, with the formation of almost pure Fe oxides. Above 400°C the composition of the oxide layers

changed, the ratio of chromium oxide on the surface increased. Iron enriched oxide on the surface together with increased ratios of oxide of chromium in depth and at the interface between oxide and bulk material were observed at all temperatures.

1.2.3.2 Effect of alloying elements

The oxidation at 1220°C of three kinds of duplex stainless steel, one standard alloy and two super alloys, was investigated by L.–F. Li et al. [31]. Superalloys presented a lower oxidation rate both in the parabolic and linear regimes, whereas the standard alloy showed a dramatic growth up to breakaway oxidation by forming nodules. Moreover the thickness of γ–oxide layer is slightly higher on the standard alloy than in super alloys.

As concern *the effect of the microstructure*, the difference in metallurgic compositions and crystal structures, result in the growth of different thermal oxide on individual grains. Consequently, the oxidation resistances of ferritic and austenitic phases in DSS are different. A. Bautista et al. [34] studied austenitic and ferritic steels, together with their duplex stainless steel produced by powder metallurgy. Ferritic stainless steel showed higher temperature corrosion resistance than the austenitic one, due to the Ni content which promotes the formation of a poorly protective $NiFe_2O_4$ phase and hinders the formation of a continuous protective Cr_2O_3 layer. For the duplex stainless steel sample, the resistance to oxidation was greater when the alloy had a higher percentage of ferrite. The higher oxidation resistance in ferritic phase was confirmed by the work of M.A.E. Jepson et al. [35] where UNS S32101 was oxidized in simulating propane combustion at 1000°C. For an hour oxidation time, a thicker oxide formed on the ferritic phase while the oxide thickness turned to be higher on the austenitic phase for longer oxidation times (2 hours). EDS maps showed that oxide on ferritic always consisted of an inner layer of a chromium manganese oxide and of an outer layer of manganese oxide, whereas the oxide on the austenitic grains exhibited craters in which an outer iron rich oxide and an inner chromium rich oxide together with mixed internal oxide and voids (Figure 1.10). Another study reported on a thin and dense protective chromium enriched oxide film preferentially formed on ferrite while a thicker and less protective oxide formed on austenite [31].

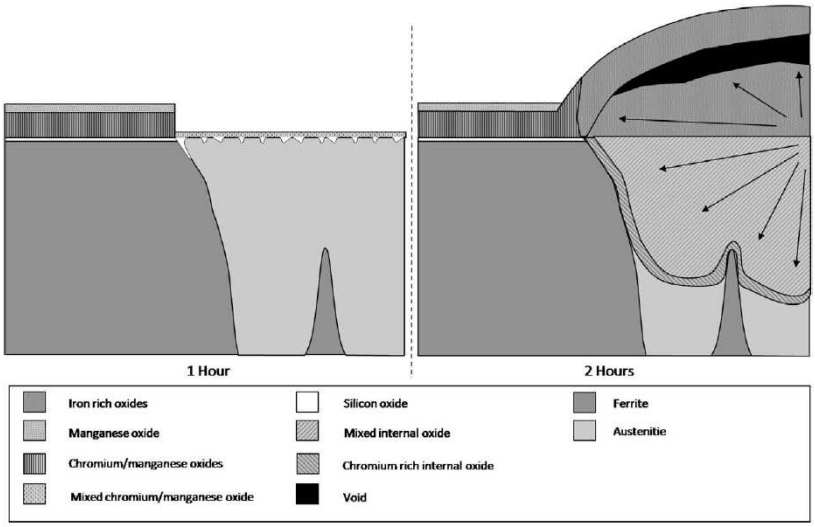

Figure 1.10 Schematics showing the oxidation of polished S32101 after oxidation at 1000°C in simulated propane combustion products [35]

1.2.3.3 Effect of gas compositions

The influence of the oxygen partial pressure in the oxidizing environment was reported by D. Kempf et al. [36]. The thin oxide film developed on duplex stainless steel UNS S31803 (DSS 2205) oxidized at 500°C under secondary vacuum for 1 h was investigated. The oxide was thicker on the austenitic than on the ferritic phase. On both phases, the oxide film was composed of chromium–containing species. Increasing oxygen partial pressure, chromium oxide was found on both phases whereas iron oxide was only detected on the austenitic.

1.3 Oxidation of non–ferrous metal and alloy

This part focuses on the oxidation of non–ferrous materials i.e. pure chromium metal and nickel–based alloys. Since Cr_2O_3 and Al_2O_3 are the main protective oxides at high temperature, the study of oxidation of pure chromium can give us more understanding in oxidation of chromia–forming alloys. Nickel and its alloys are practically important to modern industry because they are highly resistant to corrosion in many environments, especially in basic (alkaline). They are widely used in high temperature corrosion applications such as in petrochemical industries and nuclear reactors.

1.3.1 Pure chromium

Oxidation of pure chromium was broadly studied in diverse environments to understanding how chromia grows depending on several factors. Chromia, Cr_2O_3, is the stable oxide of chromium which is generally found at high temperature, whereas chromium hydroxide and nitride can be observed in some conditions. The oxidation kinetics was also

investigated. More or less parabolic and/or logarithmic oxidations laws were generally found when a protective oxide was formed, depending on temperature [37, 38], surface finish [39], and/or gas composition [40, 41]. For instance, the study of K.P. Lillerud and P. Kofstad [38] on pure chromium oxidized from 800°C to 1100°C reported a logarithmic law at 800°C while the parabolic law was shown above 900°C.

1.3.1.1 Effect of exposure temperature

As expected, temperature directly affects the oxidation rate of pure chromium. I. V. Oryshich et al. [37] oxidized 97.5% purity chromium (obtain from powder metallurgy methods) in a temperature domain ranging from 900°C to 1400°C. The parabolic oxidation law constant was found up to 1100°C, whereas the oxidation rate increased at higher temperatures.

1.3.1.2 Effect of gas compositions

The presence of nitrogen in oxidizing gas was shown to promote nitride components in the thermal scale [40, 42]. E.I. Alessandrini and V. Brusic [40] oxidized Cr thin films in oxygen gas and nitrogen gas from 400°C to 600°C. All oxidized samples always revealed the stable oxide of Cr_2O_3 but nitride was observed above 450°C. The amounts of both compounds increased with oxidation time at all temperatures.

The effect of the presence of water vapor is always an interesting issue. Y. P. Jacob et al. [42] presented the effect of small amounts of water vapor on the isothermal high–temperature oxidation of powder–metallurgical (PM) chromium in argon/oxygen and nitrogen/oxygen which contained 20 % of oxygen. In argon/oxygen, water vapor slightly increased the oxidation rate and was the main oxygen source for the oxidation process. The presence of water did not influence the type of kinetics and growth mechanism of oxide formation on pure chromium. In nitrogen/oxygen, the addition of water vapor reduced the oxide growth rate by about 50%. The mass transport mechanisms responsible for the formation of an oxide layer did not change.

S. Henry et al. [43] also presented the effect of water vapor on oxidation of pure chromium. Oxidation was performed at 900°C in oxygen and in water vapor. The duplex structure of Cr_2O_3 formed with an equiaxed internal subscale and a columnar external subscale, more easily observable in water vapor, growing by the opposite transport of chromium and of oxide/hydroxide ions. In addition, another study [44] reported that the presence of water vapor in atmosphere could improve a scale adherence because water vapor promoted oxide formation at the scale/metal interface thereby suppressing excessive growth of existing voids.

The effect of oxygen partial pressure was studied by M. Michalik et al. [45]. Growth rates of oxide scales were higher in low–pO_2 gases than in high–pO_2 gases. The scales formed in the low–pO_2 gases showed substantially better adherence during cooling, than scales formed in the high–pO_2 gases. These differences in growth rate and adherence could be correlated with differences in size and location of the in–scale voids formed during the isothermal exposure.

1.3.1.3 Transport mechanism of oxygen

To understand the diffusion mechanism taking place in oxidation of pure chromium, oxygen was traced investigated by SIMS in a study of C. Brunner et al. [46]. Oxidation was performed in two stages: the first stage used ^{16}O isotope while the second stage used ^{18}O, at 900°C. Results showed that the formation of the second oxide layer (^{18}O layer) occurred by diffusion of chromium from the bulk through the already grown oxide layer (^{16}O layer) and reaction of these chromium atoms with oxygen from the gaseous phase. Hence, it was concluded that thermal oxides developed by the diffusion of chromium (or cation).

1.3.2 Nickel–based alloys

Nickel–based alloys are important materials for industry because of their ability to resist to a wide variety of severe operating conditions involving corrosive environments, high temperatures, high stresses, and combinations of these factors. Nickel and its alloys are ductile and tough, and have a good corrosion resistance. Due to the nearly complete 3d electron shell of nickel, large additions of alloying element can be used before encountering phase instabilities. Because of this, nickel allows to design a wide variety of alloys, running them as needed.

This part briefly reviews the oxidation of nickel–based alloys, emphasizing on the case of Inconel–690 which not only has a good corrosion resistance but also appears to be less vulnerable to the stress corrosion cracking. Alloy 690 is now widely used as structural material for steam generator tubes in pressurized water reactors (PWRs) due to its superior corrosion resistance compared to the one of Alloy 600.

Chromia is always detected on the oxidized alloy surface with other oxides or hydroxides depending on oxidation environments and metallurgy conditions. In the literature [47, 48], it is generally proposed that in the oxidation mechanism, Cr rich oxides form initially through solid–state reactions, and then Ni and Fe diffuse outwards and combine with the originally formed Cr rich oxides to produce spinel oxides in the outer layer.

1.3.2.1 Effect of exposure temperature

The temperature was shown to have effects on the oxide nature and structure. For instance, oxidation of Inconel–690 in air was reported by G.C. Allen et al. [49] who showed that a layer formed essentially of α–Cr_2O_3 at room temperature, while at 600 K, the formation of a duplex oxide film with a thin outer layer of iron (III) oxide and an inner mixed chromium, iron, nickel oxide was observed.

1.3.2.2 Effect of alloying elements

Chromium is the main alloying element which is generally added to Ni–based alloys to enhance the corrosion and stress corrosion cracking behavior. A study of F. Delabrouille et al. [50] on the effect of the chromium content was launched for alloys containing chromium concentrations ranging from 5 %wt to 30 %wt. This range covered the composition of the industrial alloys 600 (15%Cr) and 690 (30%Cr). The oxide scales were grown in simulated PWR primary water conditions and the characterizations of the oxide scales were performed by SEM, TEM and SIMS. A schematic of the observed oxide structure for nickel–based alloys with chromium content above 10% was proposed (Figure 1.11). In case of lower chromium content, numerous filaments were presented on top and the chromium rich oxide layer was not continuous. In all cases, increasing chromium content in alloys resulted in an increase of chromium content in the protective oxide scale and a decrease of the oxide thickness.

Another sample of the study of the influence of alloying elements was reported by T. M. Angeliu et al. [51]. The influences of chromium, carbon, and yttrium on the nature of the surface film formed on nickel–based alloys was investigated after 100 h of exposure to high purity, deaerated, hydrogenated water at 360°C. The chemical composition of an ultrahigh purity (UHP) alloy of Ni–17Cr–9Fe–0.0030C was altered by varying the Cr content, doping with C, or ion implanting Y. XPS and STEM provided information on the chemical composition, structure, morphology, and thickness of the surface film. Increasing the chromium content from 5 to 17 %wt dramatically changed the surface film from predominantly $Ni(OH)_2$ to Cr_2O_3, whereas increasing the Cr content from 17 to 30 %wt did not significantly modify the type, distribution, or thickness of the oxide phases formed. This suggested that a critical chromium concentration controlled the formation of Cr_2O_3. The addition of carbon increased the film thickness and promoted the formation of $Ni(OH)_2$, possibly by an increase in the diffusion of Ni or by an enhancement of the surface activity of the Ni atoms. Yttrium implantation (up to 2.4 %at) produced similar film thickness and

composition profiles. Yttrium was reported likely to promote the formation of Cr_2O_3 by acting as nucleation sites for the similarly structured chromia.

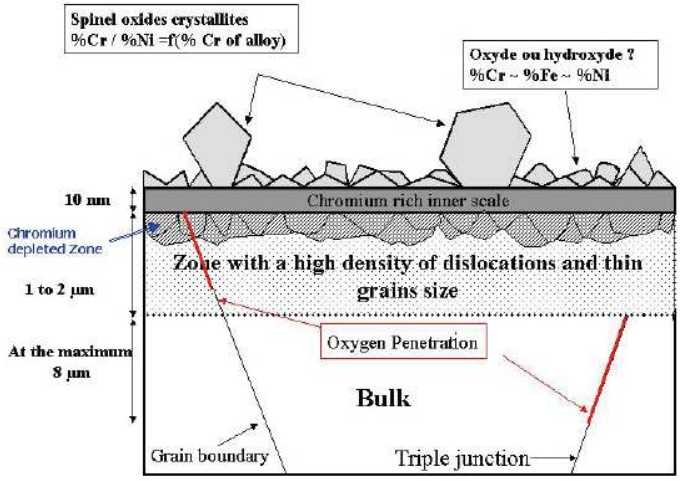

Figure 1.11 Schematic illustration of the oxide structure observed for nickel based alloys with chromium contents above 10% oxidized in simulated primary water conditions [50]

1.3.2.3 Effect of gas compositions

For example, dissolved oxygen in simulated primary water reactor increased the intergranular attack (IGA) sensitivity of Alloy 690TT (thermally treated) [52].

1.3.2.4 Effect of crystallographic orientation

Orientation dependence of the oxidation rate was only evident for short oxidation times as reported by L. P. Bonfrisco and M. Frary [53]. Oxidation of nickel was done at 700°C in air, EBSD and optical profiler analysis being used to investigate the thermal oxidation layer. The oxidation rate was strongly related with surface orientation; the slowest oxidation rate was found on (111), followed by (011) and (001). Furthermore the oxidation rate was shown to increase as the surface normal direction deviated away from <111>. The relative influence of the crystallographic orientation on the oxidation rate decreased with increasing oxidation times. The surface oxide thickness differences among grains again decreased with increasing oxidation time. For oxidation times greater than 30 minutes, no effect of orientation on oxidation rate could be detected.

Grain boundaries affect the oxidation resistance. P. Xu et al. [54] used grain boundary engineering (GBE) to modify the grain boundary characteristics of alloy 690, and then oxidized these samples in supercritical water at 500 °C and 24 MPa. GBE samples showed better oxide layer compared to the as–received sample. XRD results indicated that nickel oxide, chromium oxide, and spinel oxide were the three main types of oxides that form on as–received and GBE alloy 690. As illustrated in Figure 1.12, three distinct regions were identified on the oxidized surface. Only at random grain boundaries, chromium oxidation was

found as a flake, leading to formation of thick Cr_2O_3 layer on the surface and chromium depletion underneath. The chromium oxidation was attributed to fast chromium diffusion through random boundaries and mechanically deformed regions. In addition, orientation–dependence could also be observed from the different oxide shapes in flat and rough regions.

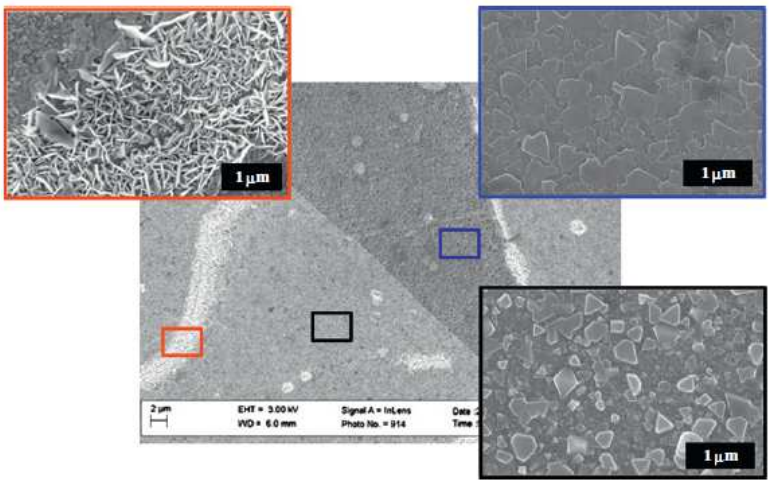

Figure 1.12 Typical morphology of oxides that form on alloy 690 after exposure to SCW. This figure shows the images for the TMP35 sample after 4 weeks SCW exposure. The region highlighted in blue box is relatively flat and marked as ‘‘flat region’’, the region highlighted in black box is relatively rough and marked as ‘‘rough region’’, and the region highlighted in red consists of agglomerated flakes most of which formed at grain boundaries [54]

1.3.2.5 Effect of surface finish

Z. Zhang et al. [52] reported that surface finishing only affected the oxide morphology but did not affect the corrosion rate. As illustrated in Figure 1.13, a triple–layer oxide film formed. The intermediated layer with a loose sheet–like oxide was found on the ground surface while a needle–like oxide was observed on the electropolished surface.

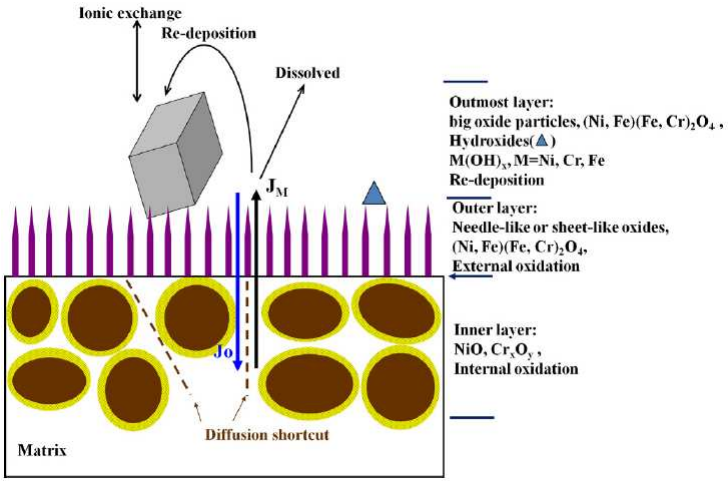

Figure 1.13 Schematic drawing for the growth of oxide films on Alloy 690TT with different surface conditions in 1500 mg/L B + 2.3 mg/L Li solution with 1.40 cm^3 (STP) O_2/kg H_2O at 325°C and 15.6 MPa [52]

H. Leflaix et al. [55] presented the influence of subsurface defects on oxidation of Alloy 690 in PWR primary water. Microstructural observations and NRA measurements underlined the role played by defects on the crystallinity of the continuous oxide spinel layer, on the nucleation of Cr_2O_3 nodules and on the oxidation rate. The higher defects concentration seemed to modify the oxygen diffusion in the oxide scale.

M. Sennour et al. [56, 57] reported the influence of surface defects on the formation of passive film of Alloy 690. TEM and SEM revealed on oxide layer with the structure illustrated in Figure 1.14. The influence of alloy surface defects was underlined in two main consequences. Firstly, the growth kinetics of the internal spinel rich in chromium increased with the surface defect density. Besides that, when the defects density increased, the oxide scale became more finely crystallized. Secondly, the quantity of Cr_2O_3 nodules increased with the number of surface defects, revealing that the nodules nucleated preferentially at defect locations.

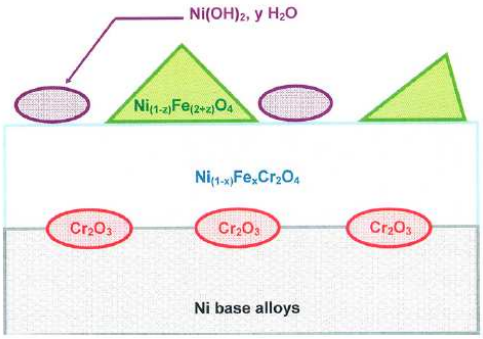

Figure 1.14 Schematic view of the oxide scale that forms during the exposition of Ni–based alloys in PWR primary water [57]

1.3.2.6 Transport mechanism of oxygen

For understanding the transport mechanisms of oxygen through the corrosion product scales formed in the primary fluid on Alloy 690 [55], corrosion tests were also conducted in a sequential exposure under $H_2(^{16}O)$ and $H_2(^{18}O)$. SIMS depth profile evidently indicated ^{16}O and ^{18}O at inner and outer layer. The presence of ^{18}O at near surface revealed outward diffusion of cationic species.

1.4 Photoelectrochemical characterization in high temperature oxidation application

Photoelectrochemistry (PEC) takes benefit of the photovoltaic effect at a semiconductor/ electrolyte interface, firstly discovered by Becquerel [58] in 1839, and thus also sometimes called “Becquerel effect”. First experiment was placing silver–chloride in an acidic solution and illuminated it while connecting it to platinum electrodes; providing a photovoltage and a

photocurrent. Whereas photoelectrochemical issues were studied since the 1940s [59], photoelectrochemical techniques were applied to characterize the properties of thermal oxides, only in the last few decades [60].

Photoelectrochemistry can be used as a characterization tool, in–situ [61, 62] or ex–situ [63–66], at either macroscopic or microscopic scales, for semiconducting materials such as the numerous metallic oxides, sulfides, and carbides. It provides the optical and electronic properties such as the bandgap and semiconducting type, but also possibly energetic parameters of the semiconductor/electrolyte interface such as the energy positions of the surface conduction and valence bandedges. A brief theoretical background of PEC will be now presented (the details can also be found in the standard textbooks [67–69]). Then applications of photoelectrochemistry to high temperature corrosion studies will be illustrated.

1.4.1 Basics of photoelectrochemistry

1.4.1.1 Band model of a semiconductor

Figure 1.15 shows energy band models of solids divided in three categories as conductor, semiconductor, and insulator. The highest occupied energy band is called the *valence band*, and the lowest empty energy band is called the *conduction band*. In a conductor, the highest energy band is not fully occupied, therefore it represents also unoccupied energy band. The valence and conduction bands are separated by a forbidden energy gap, E_G, the so–called *bandgap*. $E_G = E_C - E_V$, where E_V and E_C are respectively the energies of the top of the valence band and of the bottom of the conduction band. The distinction between semiconductors and insulators remains ambiguous; roughly, materials are said semiconductors when electronic conduction can be reached, in given condition, and insulators when not.

Electrical conduction in semiconductors can originate in movements of negative electrons in the conduction band or of positive hole of electrons (or simply: holes) in the valence band. Electrical current can be carried by either electrons in the conduction band or holes in the valence band, or by both kinds of charge carriers. Mobile charge carriers can be generated by three different mechanisms (Figure 1.16) i.e. thermal excitation, photo–excitation, and doping. *Thermal excitation* can promote an electron from the valence band to the conduction band if the bandgap energy is sufficiently small compared to kT. In case of *photo–excitation* an electron can be promoted from the valence band to the conduction band when the incident photon energy exceeds the bandgap energy. *Doping* is a process introducing new energy levels into the bandgap. Doping can be effected by either disturbing the stoichiometry of the semiconductor or by substituting a foreign element into the

semiconductor lattice. For *n–type doping* occupied donor level (E_d) are introduced at energies near the conduction band edge. Electrons from the donor level are readily promoted to the conduction band by thermal excitation. Electrons in the conduction band outnumber the few thermally–generated holes in the valence band; hence, current is carried mainly by negative charge carriers. Likewise, *p–type doping* corresponds to the formation of empty acceptor levels (E_a) near the valence band edge. The acceptor levels trap electrons from the valence band, creating positive charge carriers. Semiconductors are commonly described as n–type or p–type to indicate the pre–dominant charge carriers; undoped semiconductors are referred to as intrinsic semiconductors.

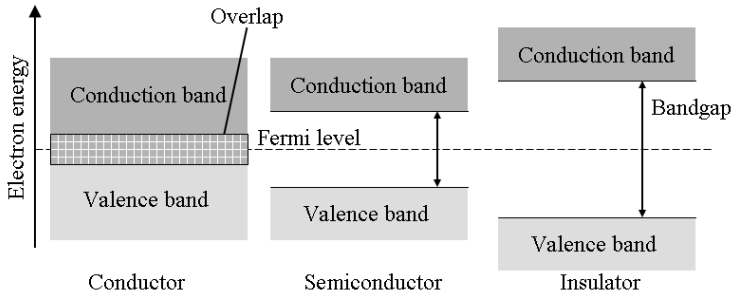

Figure 1.15 Energy bands in solids

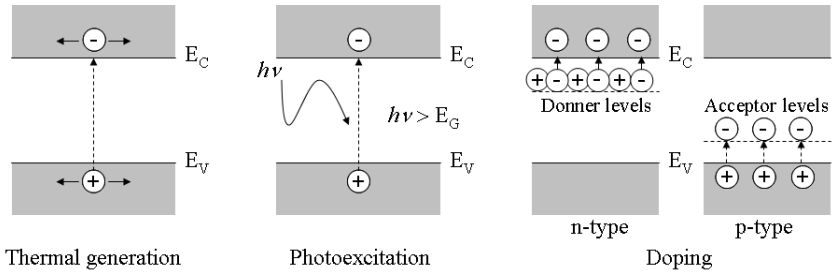

Figure 1.16 Mechanisms of charge carrier generation in semiconductors or insulators[70]

The Fermi level (E_F), which for electrochemists represent the electrochemical potential of the electron in the solid phase, lies near the middle of the bandgap for an intrinsic semiconductor. Doping shifts the Fermi level with respect to the band edges; n–type doping results in a shift of E_F towards E_C while p–type doping shifts E_F nearer to E_V.

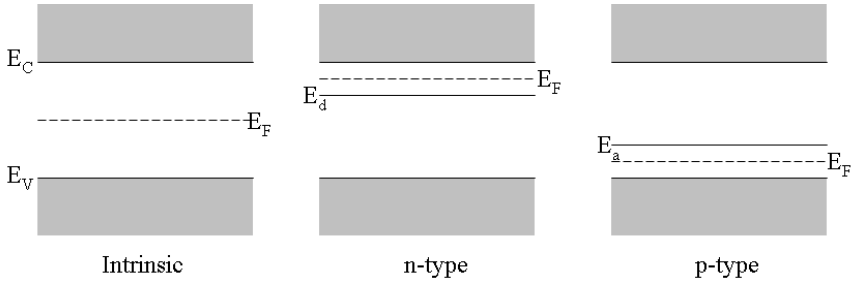

Figure 1.17 Typical Fermi level positions in intrinsic, n– and p–type semiconductors

1.4.1.2 Semiconductor/electrolyte contact at equilibrium (in dark)

When a semiconducting material is put in contact with an electrolyte (a redox solution), an electrical potential gradients established at the interface. The potential profile across the semiconductor/electrolyte interface may be illustrated as in Figure 1.18. Depending on the redox Fermi level (the electrochemical potential) of the electrolyte with respect to the conduction and valence surface bandegdes of the semiconductor, transient charge transfers may lead to mainly three situations at equilibrium. A flatband situation, where there is no potential gradient in the semiconductor, and which is obtained when the Fermi redox level equal the flatband potential of the semiconductor. Otherwise, a band bending is created in a region near the surface of the semiconductor in contact with the electrolyte. This band bending corresponds either to depleting or accumulations of majority charge carriers in the latter region, which is therefore called space charge layer. The depletion situation for both n– and p–type semiconductors is illustrated in Figure 1.19.

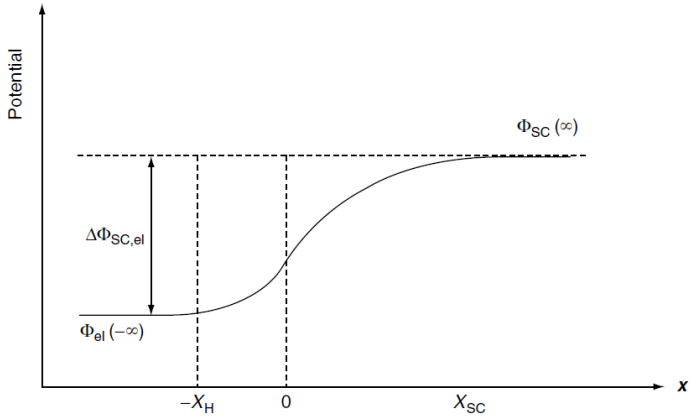

Figure 1.18 Galvanic potential profile across the semiconductor/electrolyte interface [67]. Φ_{SC} and Φ_{el} are the potentials in the semiconductor and the electrolyte, $\Delta\Phi_{SC,el}$ is the galvanic potential difference between semiconductor and electrolyte, X_{SC} and X_H are the space–charge region and double layer thickness, respectively.

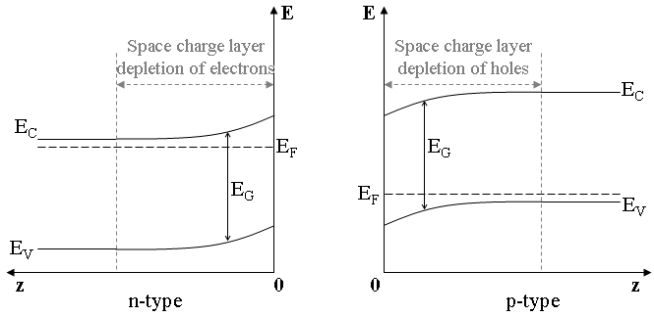

Figure 1.19 Band bending corresponding to depletion conductions for a semiconductor in contact with an electrolyte

The different space charge situations may be also obtained on the same interface, by changing U, the electrochemical potential applied to system. The polarization

situations for semiconductor–electrolyte interfaces are presented in Figure 1.20 where U_{fb} represents flatband potential.

$U = U_{fb}$: At this situation, the semiconductors (both n– and p–type) no band bending is obtained.

$U > U_{fb}$: for n–type semiconductor, the concentration of electrons at the surface is reduced, leading to a *depletion region*. For p–type semiconductor, holes accumulate at the surface, leading to *accumulation region*.

$U < U_{fb}$: for n–type semiconductor, the surface concentration of electrons in the conduction band is enhanced, providing an *accumulation region* of electrons at surface. In case of p–type semiconductor, a *depletion region* of hole is promoted. Roughly analyzed, these schemes imply that, in dark conditions, high reduction (oxidation) electrochemical currents may be expected for the accumulation of electrons (holes) situations of n–type (p–type) semiconductors, because electrons (holes) are the n–type (p–type) majority

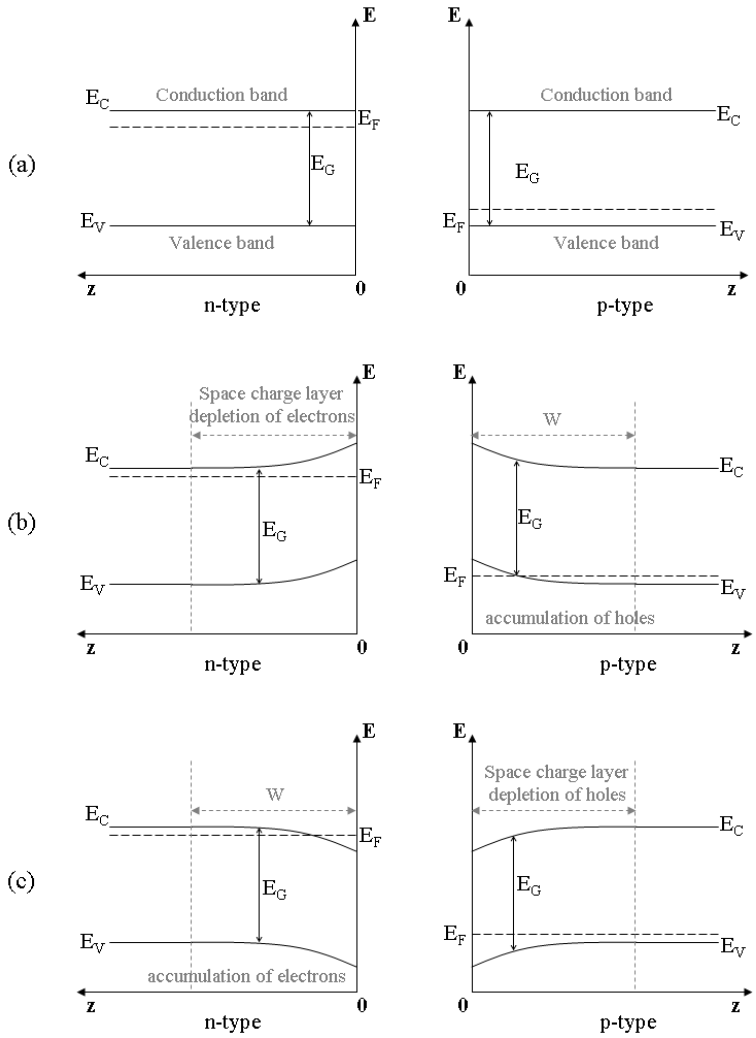

Figure 1.20 Schematic of band bendings in a SC contacting an electrolyte for both n– and p–type semiconductor: (a) at $U = U_{fb}$ (b) at $U > U_{fb}$ and (c) at $U < U_{fb}$

charge carriers. Conversely, show holes oxidation (reduction) electrochemical currents are expected from n–type (p–type) SCs in depletion conditions, for holes (electrons) are minority charge carriers in n–type (p–type) SCs. In fact, a semiconductor/electrolyte junction behaves as a Schottky diode.

1.4.1.3 Semiconductor/electrolyte contact under illumination

Illumination of semiconductor/electrolyte interfaces by photons having energies (hν) larger than the bandgap (E_G) will generate electron–hole pairs in the semiconductor. Applying an adequate potential to the semiconductor allows these electron–hole pairs to be separated by the electrical field in the space charge region. The photogenerated majority charge carriers are driven towards the bulk of the semiconductor to the external circuit whereas the minority photogenerated charge carriers are driven to the surface where they are transferred to adequate redox species in the electrolyte. This generates an additional electrochemical current, the so–called *photocurrent*.

The schematics in Figure 1.21 illustrates such generation of photocurrents. In the case of an n–type semiconductor, electrons are driven to the external circuit while photoholes are driven to the electrolyte, resulting to an anodic photocurrent. In the converse case of a p–type semiconductor, a photoelectron in conduction band transfers to redox species, leading to a cathodic photocurrent. Figure 1.22 illustrates anodic and cathodic photocurrent vs potential curves for n– and p–GaAs. For reasonably doped SCs, photocurrents are generated only when the applied potential is higher (resp. lower) than the flatband potential in case of n–type (resp. p–type) semiconductor, that means when the semiconductor/electrolyte junction is in depletion conditions.

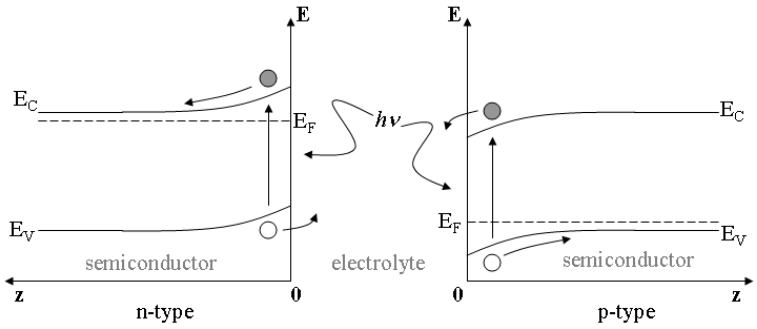

Figure 1.21 Generating mechanism of the photocurrent; gray and white circle represent electron and hole respectively.

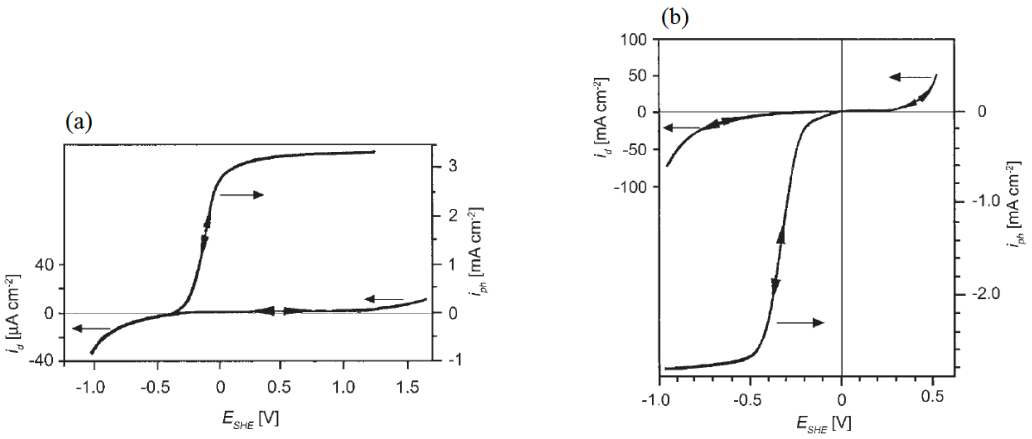

Figure 1.22 Photocurrent density i_{ph} and dark current density i_d depend on the potential in 0.2 $mol \cdot cm^{-3}$ H_2SO_4: (a) n–GaAs and (b) p–GaAs [68]

A simple but robust model of the photocurrents was proposed by *Gärtner* and *Butler* model [71, 72], assuming no recombinations of the photogenerated electron–hole pairs. The photocurrent i_{ph} is proportional to the photon flux I_0 and is affected by the relative ratio between the width of the space charge layer W_{SC}, the penetration depth of the photons in the semiconductor represented by the inverse of the absorption coefficient α_{SC}, and the mean diffusion length of the minority charges carrier l_{CC} according to the equation. Briefly speaking, all photons absorbed within a distance equals to $W_{SC} + l_{CC}$ create electron–hole pairs whose minority carriers will be transferred to the electrolyte and thus participate to the photocurrent, which thus follows equation (1.18):

$$i_{ph} = I_0 \left[1 - \frac{\exp(-\alpha_{SC} \cdot W_{SC})}{1 + \alpha_{SC} \cdot l_{CC}} \right] \tag{1.18}$$

For conditions where $\alpha_{SC} \cdot W_{SC} << 1$ and $\alpha_{SC} \cdot l_{CC} << 1$, the photocurrent may be approximated by:

$$i_{ph} = I_0 \cdot \alpha_{SC} \cdot W_{SC} \tag{1.19}$$

From the *Mott–Schottky* theory of Schottky diode, the width of the space–charge layer in depletion conditions may be written as:

$$W_{SC} = \sqrt{\frac{2\varepsilon\varepsilon_0}{e_0 N_{CC}} (U - U_{fb})} \tag{1.20}$$

where N_{CC} represents the majority charge carriers concentration (assumed to be equal to the doping level) of the semiconductor, e_0 is the electron charge (1.6022×10^{-19} C), ε and ε_0 are the relative permittivity of the semiconductor and the permittivity of the vacuum respectively.

Substituting the value of W_{SC} in eq. (1.20) in the expression of i_{ph} in eq. (1.18) allows to account for the shapes of the photovoltammograms illustrated in Figure 1.22.

Substituting the expression of W_{SC} in eq. (1.20), it comes:

$$i_{ph} = I_0 \alpha_{SC} \sqrt{\frac{2\varepsilon\varepsilon_0}{e_0 N_{CC}} \left(U - U_{fb}\right)} \tag{1.21}$$

It is usually accepted that the absorption coefficient depends on the light energy, hν, according to equation (1.22):

$$\alpha_{SC} = \text{const} \frac{\left(h\nu - E_G\right)^n}{h\nu} \tag{1.22}$$

with n = 0.5 for allowed direct band to band transitions, and n = 2 for allowed indirect band to band transitions.

Thus at constant potential,

For direct transitions: $$\left(\frac{i_{ph} \cdot h\nu}{I_0}\right)^2 = \text{const} \cdot \left(h\nu - E_G\right) \tag{1.23}$$

For indirect transitions: $$\left(\frac{i_{ph} \cdot h\nu}{I_0}\right)^{1/2} = \text{const} \cdot \left(h\nu - E_G\right) \tag{1.24}$$

The linear relations in eq. (1.23) and (1.24) are generally used to determine the band gap energy, E_G, from photocurrent vs photon energy i.e. from photocurrent energy spectra measurements when the applied potential is fixed, by the value of the intercept of $\left(\frac{i_{ph} \cdot h\nu}{I_0}\right)^{1/n} = 0$ with the energy axis. In the following chapters, the curves $\left(\frac{i_{ph} \cdot h\nu}{I_0}\right)^{1/n} = f\left(E\right)$ will be referred as linear transforms.

From eq. (1.21), at a known constant wavelength, the photon energy or square of the photocurrent would be proportional to the applied potential, as follows:

$$i_{ph}^2 = C\left(U - U_{fb}\right) \tag{1.25}$$

when C is constant. It turns out that, in the literature, the flatband potential was rarely, but sometimes indeed successfully estimated by extrapolation at $i_{ph}^2 = 0$, whereas the linear transforms were widely successfully used, at least on single component.

1.4.2 Interpretation for photoelectrochemical characterization

In high temperature oxidation studies, the photoelectrochemical technique is mostly used at the macroscopic scale to characterize electronic and chemical properties of the oxidation layers. Results obtained from PEC characterizations generally take benefit of both photocurrent vs applied potential curve (photovoltammograms), and photocurrent vs photon energy curves (photon energy spectra). Photovoltammograms tend to get informations about the semiconducting type and the flat band potential of the oxide, while, the PES intend to assess the oxide bands gaps. Typical examples of PEC curves and of their analysis will be presented in the next paragraphs.

1.4.2.1 Photocurrent vs potential curve

The shapes encountered for photovoltammograms rarely are near the ones expected from the Gärtner–Butler model presented above and illustrated in the case of single crystals in Figure 1.22. Real materials such as oxidation layers, even when consisting of a single semiconducting material, exhibit photovoltammograms with various shapes, deviating from the Gärtner–Butler model.

This feature is mainly due to the fact that photogenerated electron–hole pairs may recombine directly or via various kinds of defects in the material, in the bulk, in the space charge layer or near/at the surface. Figure 1.23 illustrates shape changes induced on photovoltammograms by field–sensitive recombinations in the space charge layer [73], i.e. when considering that the photocurrent is due to the photons which have been absorbed in the space charge (Gärtner–Butler), but have created electron–hole pairs which did not recombine, and that the electron–hole pairs recombinations depend on the electrical where they have been created, and thus of the distance to electrode surface.

Particular V–shaped photovoltammograms (when the modulus of the photocurrent is plotted on the y–axis instead of is algebric value) may be encountered [74], signing more insulating samples, who may give both anodic and cathodic photocurrents depending on if the applied potential is above or below the flatband potential. Figure 1.24 [73] illustrates how such V–shaped curves can be obtained, with different values for the bulk recombination rates: one considers that all the photons absorbed in the semiconductor of thickness d may participate to the photocurrent for the electron–hole pairs are all created in a region where a constant electrical field, but that a constant recombination rate exists.

The shapes of the photovoltammograms obtained in high temperature corrosion (HTC) studies thus can be roughly categorized in 3 typical patterns. The shape was the photocurrent increases with increasing applied potential, signs a globally n–type behavior

of the semiconducting layer. A shape was the photocurrent decreases when increasing the applied potential refers to p–type behavior. The last one where photocurrents exhibit a V–shape corresponds to an insulator. For instance, thermal oxides grown on duplex stainless steel in diverse atmospheres and exposure times presented the different in semiconducting behavior as in Figure 1.25 which (a), (b), and (c) present the n–type oxides, the p–type oxides, and a mixed behavior of insulator (V–shape) and n–type oxides respectively.

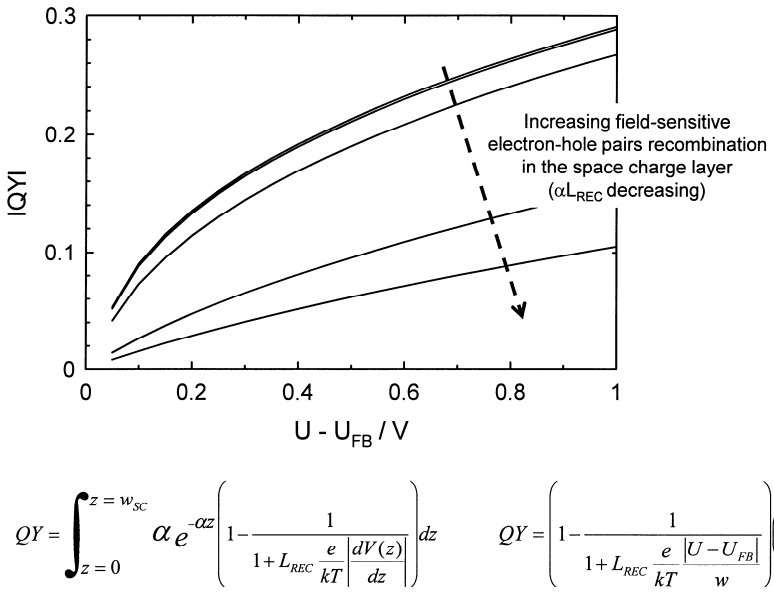

$$QY = \int_{z=0}^{z=w_{SC}} \alpha e^{-\alpha z}\left(1 - \frac{1}{1 + L_{REC}\frac{e}{kT}\left|\frac{dV(z)}{dz}\right|}\right)dz \qquad QY = \left(1 - \frac{1}{1 + L_{REC}\frac{e}{kT}\frac{|U - U_{FB}|}{w}}\right)\left(1 - e^{\alpha w_{SC}}\right)$$

Figure 1.23 Shape changes induced on photovoltammograms by field–sensitive recombinations in the space charge layer [73]. |QY| was quantum yield.

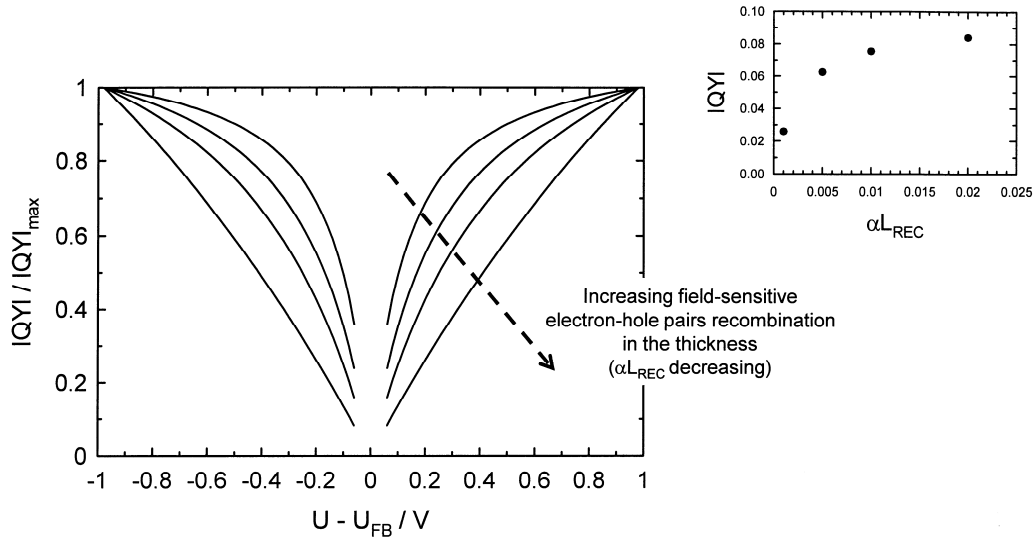

$$QY = \int_{z=0}^{z=d} \alpha e^{-\alpha z}\left(1 - \frac{1}{1 + L_{REC}\frac{e}{kT}\left|\frac{dV(z)}{dz}\right|}\right)dz \qquad QY = \left(1 - \frac{1}{1 + L_{REC}\frac{e}{kT}\frac{|U - U_{FB}|}{d}}\right)\left(1 - e^{\alpha d}\right)$$

Figure 1.24 The V–shaped curves with different values of the bulk recombination rates [73]. |QY| and $|QY|_{max}$ were the quantum yield and the maximum of quantum yield on the whole tested potential range, respectively.

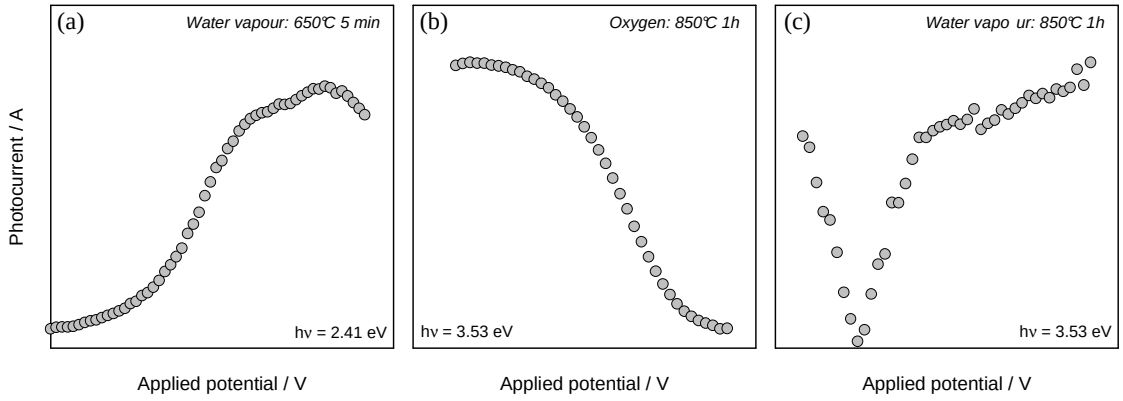

Figure 1.25 Typical examples of photovoltammograms observed in HTC studies (a) n–type semiconducting behavior (b) p–type semiconducting behavior and (c) insulating behavior. These curves were obtained in this work from duplex stainless steel 2205 sample oxidized in diverse atmospheres and oxidation times. The moduli of the photocurrent are plotted on the Y–axis.

1.4.2.2 Photocurrent vs photon energy curve

Photocurrent energy spectra (PES) are used to assess bandgaps of semiconductors, more or less directly for samples containing more than one semiconductor. The bandgap value is one of the signatures of a semiconductor. Numerous oxides, sulfides, nitride, carbides, have been studied in the literature, by photoelectrochemical or other techniques, and their bandgap values have been reported, although for some of them the reported values are rather dispersed. Furthermore, bandgap values of such components may be estimated from extensive thermodynamic data [75-77]. Assessing bandgap values "present" in thermal scales gives thus access to the chemical nature of the oxides present. Bandgap data are usually determined using the linear transforms of the PES spectra. Figure 1.26(a) and (b) show an example of a PES and its linear transform, respectively. Since these spectra obtained from a pure Cr_2O_3 pellet, it was not difficult to find the bandgap. However, if a scale formed on alloys, the complexity of the thermal scale always introduces more than one contribution to the photocurrent, resulting in more difficult bandgap assessment. Figure 1.27 illustrates linear transforms of spectra obtained from an oxidized duplex stainless steel at different applied potentials. Both plots reveal the combination of photocurrent, several of components, which is confirmed by the influence of the applied potential on the shape of the spectra. The latter trend being possibly an advantage characterization performed for not all the oxides will be photoelectrochemically active at all applied potentials. Complementary characterizations via other techniques are often performed to confirm PEC results.

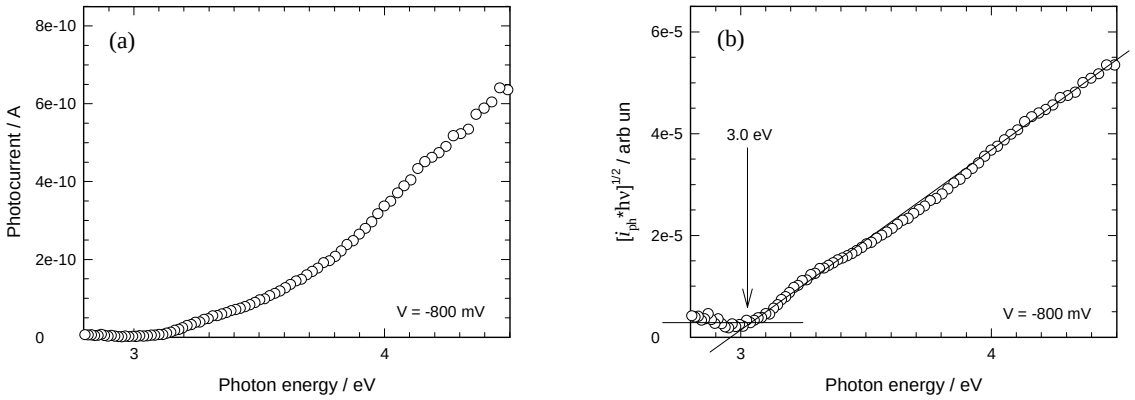

Figure 1.26 Photocurrent vs photon energy curve (a) and linear transforms plots (b) obtained from a pellet of pure Cr_2O_3. PEC was performed in 0.1 M H_2SO_4 at –800 mV vs MSE.

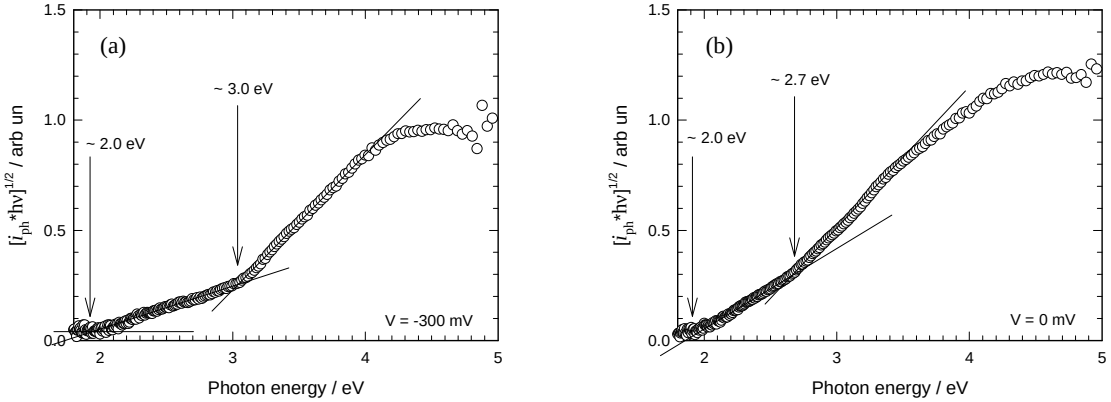

Figure 1.27 Linear transforms plots evaluated from data of duplex stainless steel 2205 oxidized in water vapor for 5 minutes. PEC was performed in 0.1 M H_2SO_4 and the potentials applied at (a) –300 mV and (b) 0 mV vs MSE.

1.4.3 Photoelectrochemical imaging

In the previous sections, the photoelectrochemical characterizations presented have been performed by illuminating the semiconductor on a large surface area, so they are called *macroscopic photoelectrochemical characterizations*. Photoelectrochemical imaging is a photoelectrochemical mapping on a selected surface area using a monochromatic light (laser) focused spot. PEC image gives information about the spatial distribution of heterogeneity on the surface. The resolution is about 1 μm. Since this technique provides local information on small surface area, it is called *microscopic photoelectrochemical*.

PEC imaging of semiconducting oxide was initially proposed by Butler [78, 79] who performed a photoelectrochemical mapping of passive films on titanium. Microscopic photoelectrochemical has been performed on various materials such as titanium [78–82], iron [83], stainless steel [84–85], and zirconium [86–87]. At constant applied potential, the intensity of photocurrent signal is a complex function of diverse variables as film thickness,

photon energy, light intensity (photon flux), and kinetics of charge transfer at the passive film–electrolyte interface. Analysis of PEC images consist in analyzing the local amplitudes of the photocurrent varying the applied potential and the photon energy when recording different images (however, lasers offer only few lines). Notice that photocurrent can be delivered from all kind of oxides which have bandgap below the photon energy of the probe hence photocurrent could be issued from more than one oxide in the case of high photon energy. For instance, Figure 1.28 shows photoelectrochemical images of an oxide scale grown on Zircaloy–4, which revealed the locations of Fe_2O_3, Cr_2O_3, and perhaps $(Fe_xCr_{1-x})_2O_3$ on the selected surface area.

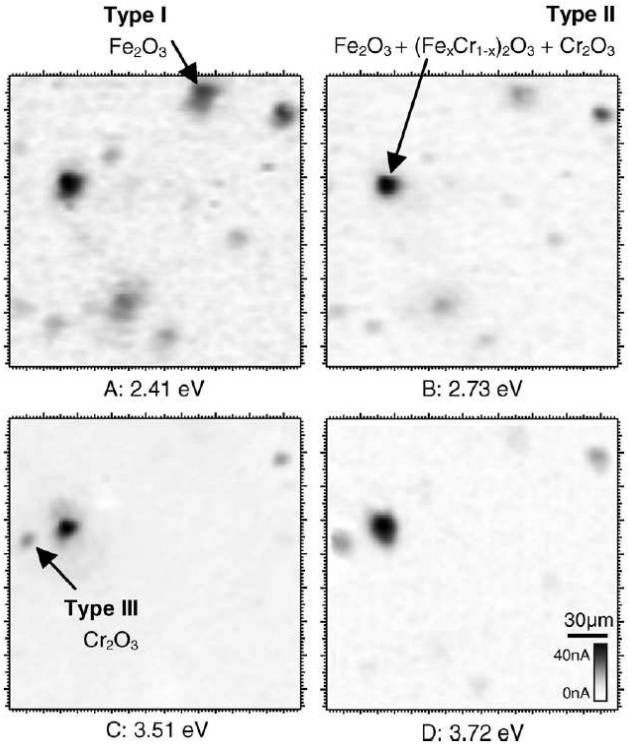

Figure 1.28 Photoelectrochemical image of the oxide scale grown at 470°C during 1 h in oxygen on Zircaloy–4 (applied potential: 0 V/MSE). Image 220 × 220 µm, point spacing 2 µm. A: laser energy 2.41 eV, B: laser energy 2.73 eV, C: laser energy 3.51 eV, D: laser energy 3.72 eV [87].

1.4.4 Applications of photoelectrochemistry in the oxidation of stainless steel

In case of the oxidation of stainless steel, thermal layers containing mainly oxides of chromium and iron were generally observed using various characterization techniques. Other compounds such as hydroxides, nitrides, and carbides were also detected, depending on metallurgy variables and oxidation conditions. From the survey of photoelectrochemical studies of the oxidation of stainless steel (ferritic, austenitic), bandgap and semiconducting type data of the compounds grown on thermal layer could be obtained, they are summarized in Table 1.1. These informations indicate that Fe_2O_3 is seen an n–type

semiconducting oxide, whereas Cr_2O_3, an amphoteric oxide, can behave as p– or n–semiconducting depending on the nature of the base materials and on the oxidation conditions.

Photoelectrochemical imaging was also applied to oxidized stainless steel, for instance by A. R. J. Kucernak et al. [88] which used the in situ scanning laser photoelectrochemical microscopy technique to image the heterogeneities of surface chemistry around sulfide inclusions in stainless steel (Figure 1.29). PEC image supported the hypothesis that the adsorbed sulfur resulted in accelerated pitting, and showed a detrimental effect of sulfide inclusions.

Table 1.1 Semiconducting type and bandgap of components detected on stainless steel oxidized in diverse conditions

Materials	Oxidation conditions	Components detected in thermal layer	Semiconducting type	Bandgap (eV)	Ref.
AISI 441	T = 650°C and 850°C Atmosphere: synthetic air or 20%H_2O in N_2	Fe_2O_3	n	1.9–2.0	[12]
		$Fe_{2-x}Cr_xO_3$	n	2.4–2.7	
		Cr_2O_3	n	3.0	
AISI 316L	In solution of NaOH and H_2SO_4 pH 8, T = 350°C and pH 10, T = 320°C	Fe oxide	n	2.4	[89]
		Cr oxide	p		
AISI 441 and AISI 430	T = 900°C (Thermobalance) P_{O2} = 150 mbar, P_{total} = 1 bar	Cr_2O_3	(close to) Insulator	3.5	[90, 44]
	P_{H2O} = 150 mbar, P_{total} = 1 bar	Cr_2O_3	n	3.0	

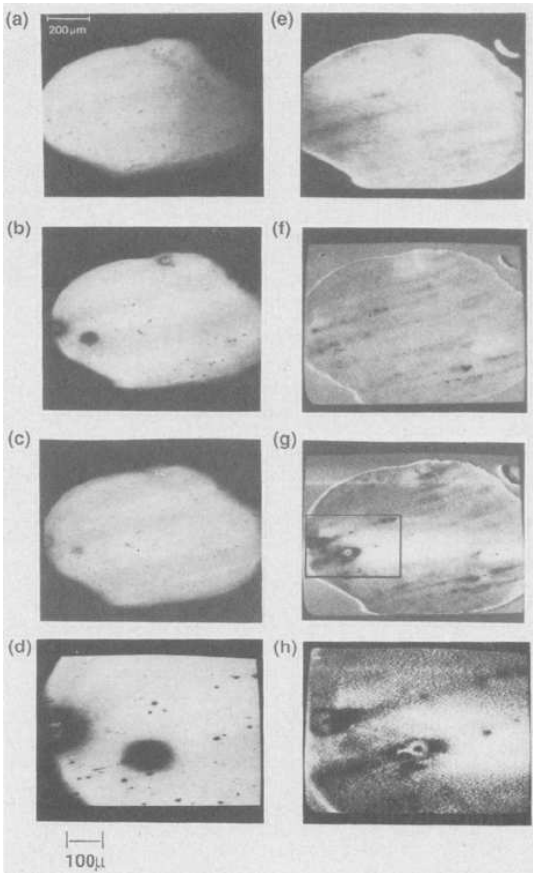

Figure 1.29 Optical and SCALPEM images of stainless steel in 0.1 mol/dm^3 $NaClO_4$ soon after polarizing at 1.1 V (NHE) (t = 0) and after 2 h at this potential (t = 2 h): (a) optical image at 442nm, t = 0; (b) optical image at 442 nm, t = 2 h; (c) as (b) but at 633 nm; (d) detail of (b); (e) "lock in" photocurrent image, t = 0, beam scan speed 200 ms/line, 140 s/frame, 442 nm, intensity modulation frequency 3 kHz, beam intensity 6 $\times 10^{15}$ photon/s, image range 0 (full black) to 20 nA (full white); (f) "direct" photocurrent image, t = 0, 30 ms/line, 21 s/frame, full black is –20 nA, full white 20 nA; (g) "direct" photocurrent image, t =2 h; (h) detail of (g) [88]

1.4.5 Applications of photoelectrochemistry in the oxidation of pure chromium

Oxidation of pure chromium at high temperature was widely studied as exposed on preceding section but photoelectrochemical techniques were quite rarely used. In a previous works [90, 91], our group reported on a duplex Cr_2O_3 structure (an equiaxed internal and a columnar external) for pure chromium oxidized at 900°C. In pure oxygen gas, the internal Cr_2O_3 revealed the bandgap of 3.0 eV and n–semiconducting behavior whereas the external Cr_2O_3 indicated the bandgap of 3.5 eV and p–semiconducting behavior. Photocurrent energy spectra obtained from oxidized pure chromium are presented in Figure 1.30. In pure water vapor, both Cr_2O_3 parts were reported to behave n–type while bandgap was pointed at 3.0 eV and 3.53 eV, repectively. Hence Cr_2O_3 is an amphoteric oxide and the presence of water vapor can modify the semiconducting behavior of oxide from p– to n–type. Photoelectrochemical images performed on the oxidized chromium were presented (Figure 1.31). PEC images evidently showed the differences between chromia scales grown in water

vapor and in oxygen. In water vapor, photocurrents were uniform due to the good metal–oxide contact. In oxygen, photocurrents presented two zones (in grey and in white), the white zones corresponding to areas of stress relaxation, still adherent to the metal, but with many dislocations acting as electron–hole recombination sites.

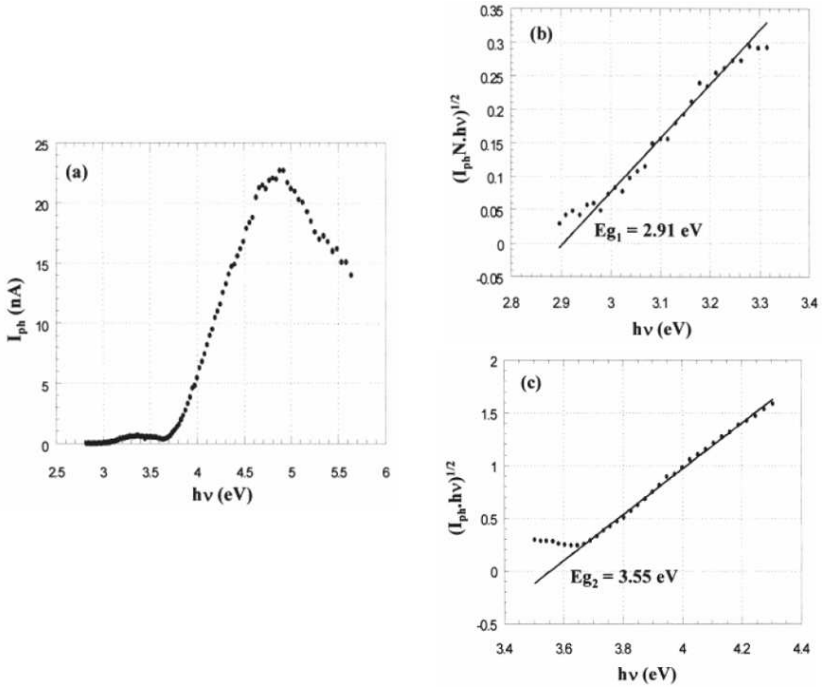

Figure 1.30 (a) Photocurrent spectrum measured in 0.1 M Na_2SO_4 for a Cr_2O_3 scale (~ 1 μm) formed by thermal oxidation in 150 mbar of water vapor at 900°C. (b) and (c) Determination of the values of the two band gaps [91]

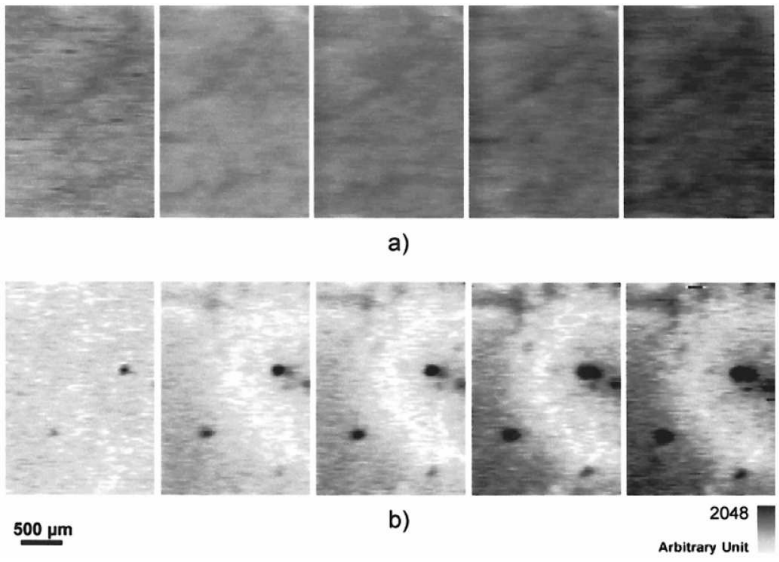

Figure 1.31 Photoelectrochemical image of the oxide scale grown on pure chromium at 900°C in 150 mbar of (a) water vapor and (b) oxygen [91]

The passive film formed on pure chromium at room temperature also presented a bandgap of anhydrous Cr_2O_3 at 3.5 eV with a p–semiconducting behavior, whereas $Cr(OH)_3$ was revealed with the bandgap at 2.5 eV [92]. Furthermore, the linear correlation between the

bandgap values of chromium oxi–hydroxides and their density was pointed out, and this suggested a bandgap of 2.95 eV for CrOOH. Finally, G. Goodlet et al. [93] reported the dependence of the substrate nature on the semiconducting behavior of Cr_2O_3 by sputtering Cr_2O_3 films on different substrates. After heat treatment at 450°C for 2 h, Cr_2O_3 film formed on chromium revealed p–type behavior while Cr_2O_3 film formed on iron substrate revealed both p– and n–type behavior due to the diffusion of iron into chromium oxide.

1.4.6 Application of photoelectrochemistry in the oxidation of Ni–based alloys

Semiconducting properties of thermal oxides formed on alloys 690 and 600 were also characterized by photoelectrochemical techniques. Table 1.2 summarizes some results. Generally, the oxide grown on Ni–based alloys was $Ni(OH)_2$ or $Cr(OH)_3$ or mixtures of both with bandgap at 2.2 eV – 2.3 eV, Cr_2O_3 with bandgap at 2.9 eV and 3.5 eV, and $Ni_{1-x}Fe_xCr_2O_4$ with bandgap at 3.9 eV – 4.4eV. These oxides could behave as n– or p–type depending on the nature of the based alloys [94] and on the oxidation environments [94–97]. In Alloy 600 and Alloy 690, the pH of the environment was reported to not change the duplex character of the film but affected the proportion of chromium oxide and of iron oxide in the film in correlation with the semiconducting behavior [94]. Similarly dissolved hydrogen in environment influenced the semiconducting type which changed from n–type at lower content of hydrogen to insulating behavior at higher content of hydrogen [97]. The effect of ZnO in the aqueous solution on the semiconducting behavior of oxide layer on Alloy 600 was reported by S. Zhang et al. [95, 96]: the addition of ZnO resulted in an untypical n–type semiconductor at anodic polarization with a negative shift of the flatband potential compared to the one of the oxide films on Alloy 600 without ZnO addition.

Photoelectrochemical imaging was also applied for local analysis, for instance on Ni–based alloys corroded in PWR primary media [98]. The distribution of nickel hydroxide and/or nickel ferrite on Alloy 690 corroded for 858 h was shown (Figure 1.32) together with the distribution of Cr_2O_3 (Figure 1.33 and Figure 1.34). Apart from the information about the oxides distributions, the images in Figure 1.31 showed possibly the influence of oxidation time, with increased quantities of Cr_2O_3, attributed to increased average photocurrent intensity. In addition, the effect of crystalline orientation of the alloy grain on the growth rate of Cr_2O_3 was also revealed by the images in Figure 1.34.

Table 1.2 Semiconducting type and bandgap of film components detected on Ni–based alloys oxidized in diverse conditions

Materials	Oxidation conditions	Components detected in thermal layer	Semiconducting type	Bandgap (eV)	Ref.
Alloy 600	T = 900°C, in air condition Time = 3 h	$Ni(OH)_2$ or $Cr(OH)_3$, or mixed of both	n–p transition (not specific)	2.2	[88]
		Cr_2O_3		2.9	
		$NiCr_2O_4$		3.9–4.1	
	T = 288°C, P = 7.2 MPa, Time = 100 h	$Ni(OH)_2$ or $Cr(OH)_3$, or mixed of both	n–p transition (not specific)	2.2	
		Cr_2O_3		2.9 and 3.5	
		$Ni_{1-x}Fe_xCr_2O_4$		4.1–4.4	
Ni–30Cr	T = 900°C, P =1 bar, in air Time = 3 h	$Ni(OH)_2$ or $Cr(OH)_3$, or mixed of both	n	2.3	[91]
		Cr_2O_3	n	2.9	
		$NiCr_2O_4$	Insulator	4.1	
Alloy 690	PWR primary conditions T = 325°C, P = 155 bar, Time = 48h up to 858 h	$NiFe_2O_4$	n	2.2	[91]
		Cr_2O_3	n	2.8 and 3.5	
		$Ni_{1-x}Fe_xCr_2O_4$	n	4.1	

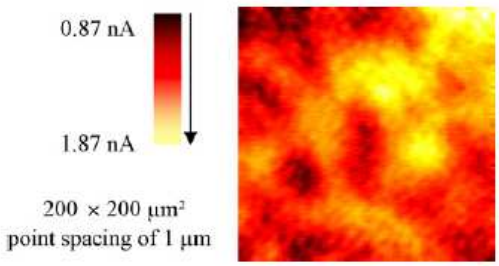

Figure 1.32 Photocurrent intensity mapping of Alloy 690 samples corroded in PWR primary medium during 858 h performed with an applied potential of 50 mV/MSE, and a wavelength of 454.5 nm (hν = 2.7 eV) [98]

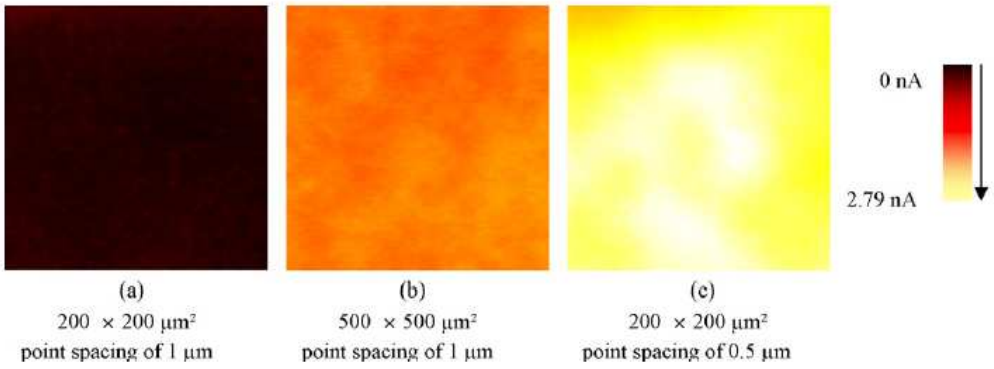

Figure 1.33 Photocurrent intensity mapping of Alloy 690 samples corroded in PWR primary medium during (a) 48 h, (b) 406 h and (c) 858 h performed at a potential of 50 mV/MSE and a wavelength of 351 nm (hν = 3.5 eV) [98]

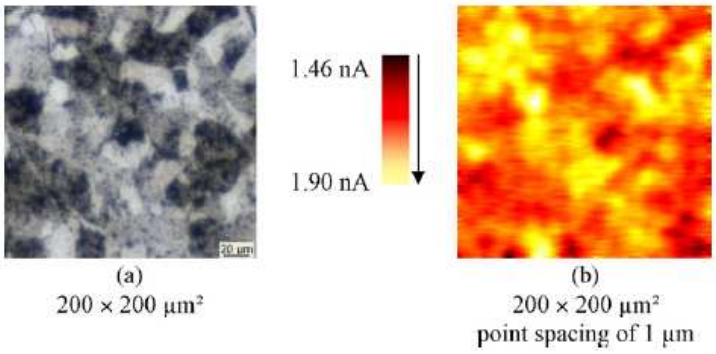

Figure 1.34 Optical image (a) and associated photocurrent intensity mapping (b) of Alloy 600 sample corroded in PWR primary medium during 858 h performed with a potential of 50 mV/MSE and a wavelength of 351 nm (hν = 3.5 eV) [98]

1.5 Concluding remarks

From the informations given in the preceding sections, it clearly appears that high temperature oxidation of metallic alloys, and particularly of microstructured ones, exhibits mechanisms depending on numerous and diverse parameters as concerns as well the nature and structure of the bulk and the surface of the alloy itself, as the oxidation operating conditions. Thermal layers formed on the alloys very often are rather complex. On the one hand, several primary, binary, ternary oxides are encountered in the scales together with solutions of these oxides. On the other hand, the thermal scales are spatially heterogeneous both in thickness (e.g. duplex structures) and laterally (e.g. presence of oxide nodules, heterogeneities due to microstructure or chemically heterogeneous underlying metallic matrix).

Investigations in the HTC domain therefore need to take benefit of a large panel of experimental elaboration, multiscale characterization and modeling tools. Photoelectrochemistry is one of these tools. PEC, although being not yet very common in the

HTC community, was already shown to be an interesting tool at both macroscopic and microscopic levels (see paragraph 1.4), and has been particularly developed in our research group at Grenoble INP – SIMaP.

In the latter group, Profs A. Galerie, J.–P. Petit and Y. Wouters decided a few years ago to focus specific efforts (and particularly my own PhD work) on the development of novel photoelectrochemical measurement and analysis tools, to better adapt these techniques to the increasing complexity of the thermal scales encountered today. The goals assigned to my PhD work were therefore the following:

- to build a bandgap and semiconducting type data based for solid solutions of iron and chromium oxides at different ratios, by elaborating these solutions from hematite and chromia powders by solid state reaction, and investigating them by PEC;
- to contribute developing, and to validate experimentally, a set–up allowing complete photoelectrochemical investigations (photovoltammograms and photocurrent energy spectra) of sample surface areas of typically 30–40 µm in diameter, which would be complementary of the macroscopic and imaging photoelectrochemical set–ups, and was never reported before;
- to contribute developing and validating tools to improve the usual analyses made up to now of PES as well in our group as in the works reported in the literature.

The next chapters will be devoted to the results obtained in this context.

REFERENCES

[1] P. Kofstad, *High temperature corrosion*, England: Elsevier Applied Science, 1988.

[2] P. Sarrazin, A. Galerie, J. Fouletier, *Mechanisms of high temperature corrosion a kinetic approach*, Zurich: Trans Tech Publications Ltd, 2008.

[3] ASM International Handbook Committee, Metals Handbook Ninth Edition Volume 13, Corrosion, Park (Ohio): ASM International, 1987.

[4] D. Young, *High temperature oxidation and corrosion of metals*, Great Britain: Elsevier, 2008.

[5] W. D. Callister, Jr., *Materials Science and engineering an introduction 7th edition*, USA: John Wiley & Sons, Inc., 2007, pp. 89–90.

[6] P. Jian, L. Jian, H. Bing, G. Xie, Oxidation kinetics and phase evolution of a Fe–16Cr alloy in simulated SOFC cathode atmosphere, *J. Power Sources* **158** (2006) 354–360.

[7] A.M. Huntz, A. Reckmann, C. Haut, C. Severac, M. Herbst, F.C.T. Resende, A.C.S. Sabioni, Oxidation of AISI 304 and AISI 439 stainless steels, *Mater. Sci. Eng. A* **447** (2007) 266–276.

[8] A. Galerie, S. Henry, Y. Wouters, M. Mermoux, J.–P. Petit, L. Antoni, Mechanisms of chromia scale failure during the course of 15–18Cr ferritic stainless steel oxidation in water vapour, *Mater. High Temp.* **22 (1/2)** (2005) 105–112.

[9] J. Zurek, E. Wessel, L. Niewolak, F. Schmitz, T.U. Kern, L. Singheiser, W.J. Quadakkers, Anomalous temperature dependence of oxidation kinetics during steam oxidation of ferritic steels in the temperature range 550–650 °C, *Corr. Sci.* **46** (2004) 2301–2317.

[10] I. Saeki, H. Konno, R. Furuichi, T. Nakamura, K. Mabuchi, M. Itoh, The effect of the oxidation atmosphere on the initial oxidation of type 430 stainless steel at 1273 K, *Corr. Sci.* **40** (1998) 191–200.

[11] I. Saeki, H. Konno, and R. Furuichi, The initial oxidation of type 430 stainless steel in O_2–H_2O–N_2 atmosphere at 1273 K, *Corr. Sci.* **38** (1996) 19–31.

[12] A. Srisrual, S. Coindeau, A. Galerie, J.–P. Petit, Y. Wouters, Identification by photoelectrochemistry of oxide phases grown during the initial stages of oxidation of AISI 441 ferritic stainless steel in air or in water vapour, *Corr. Sci.* **51** (2009) 562–568.

[13] I. Saeki, H. Konno, and R. Furuichi, The initial oxidation of type 430 stainless steel with 0.09–0.9 Mn in O_2–H_2O–N_2 atmosphere at 1273 K, *Corr. Sci.* **38 (9)** (1996) 1595–1612.

[14] E. Park, B. Hüning, M. Spiegel, Evolution of near–surface concentration profiles of Cr during annealing of Fe–15Cr polycrystalline alloy, *Appl. Surf. Sci.* **249** (2005) 127–138.

[15] A.N. Hansson, M.A.J. Somers, Influence of the oxidation environment on the scale morphology and the oxidation rate of Fe–22Cr, *Mater. High Temp.* **22 (3/4)** (2005) 223–229.

[16] Z. Yang, G. Xia, P. Singh, J.W. Stevenson, Effects of water vapor on oxidation behavior of ferritic stainless steels under solid oxide fuel cell interconnect exposure conditions, *Solid State Ionics* **176** (2005) 1495–1503.

[17] L. Dong–sheng, D. Qi–xun, C. Xiao–nong, W. Rong–rong, H. Yan, High temperature oxidation resistance of austenitic stainless steel Cr18Ni11Cu3Al3MnNb, *J. Iron and Steel Res. Int.* **19(5)** (2012) 74–78.

[18] J. A. Poston Jr., R. V. Siriwardane, J.S. Dunning, D.E. Alman, J.C. Rawers, X–ray photoelectron spectroscopic analysis of oxidized Fe–16Cr–16Ni–2Mn–1Mo–2Si austenitic stainless steel, *Appl. Surf. Sci.* **253** (2007) 4872–4885.

[19] I. Saeki, T. Saito, R. Furuichi, Growth process of protective oxides formed on type 304 and 430 stainless steels at 1273 K, *Corr. Sci.* **40(8)** (1998) 1295–1302.

[20] G. Cao, V. Firouzdor, K. Sridharan, M. Anderson, T.R. Allen, Corrosion of austenitic alloys in high temperature supercritical carbon dioxide, *Corr. Sci.* **60** (2012) 246–255.

[21] D. Lopez, N. A. Falleiros, A. P. Tschiptschin, Effect of nitrogen on the corrosion–erosion synergism in an austenitic stainless steel, *Tribol. Int.* **44** (2011) 610–616.

[22] M. Metikos–Hukovic, R. Babic, Z. Grubac, Z. Petrovic, N. Lajci, High corrosion resistance of austenitic stainless steel alloyed with nitrogen in an acid solution, *Corr. Sci.* **53** (2011) 2176–2183.

[23] R. Peraldi and B. A. Pint, Effect of Cr and Ni contents on the oxidation behavior of ferritic and austenitic model alloys in air with water vapour, *Oxid. Met.* **61 (5/6)** (2004) 463–483.

[24] S.–Y. Cheng, S.–L. Kuan, W.–T. Tsai, Effect of water vapor on annealing scale formation on 316 SS, *Corr. Sci.* **48** (2006) 634–649.

[25] D. Huenert and A. Kranzmann, Impact of oxyfuel atmospheres $H_2O/CO_2/O_2$ and H_2O/CO_2 on the oxidation of ferritic–martensitic and austenitic steels, *Corr. Sci.* **53** (2011) 2306–2317.

[26] R.R.M. de Sousa, F.O. de Araujo, L.C. Gontijo, J.A.P. da Costa, C. Alves Jr., Cathodic cage plasma nitriding (CCPN) of austenitic stainless steel (AISI 316): Influence of the different ratios of the nitrided layers properties, *Vacuum* **86** (2011) 2048–2053.

[27] G. Stein–Brzozowska, J. Maier, G. Scheffknecht, Impact of oxy–foel combustion on the corrosion behavior of advanced austenitic superheater materials, *Energy Procedia* **4** (2011) 2035–2042.

[28] R. Badji, M. Bouabdallah, B. Bacroix, C. Kahloun, K. Bettahar, and N. Kherrouba, Effect of solution treatment temperature on the precipitation kinetics of σ–phase in 2205 duplex stainless steel welds, *Materials Science and Engineering A* **496** (2008) 447–454.

[29] D. Villalobos, A. Albiter, C. Maldonado, Microstructure change in SAF 2507 superduplex stainless steel produced by thermal cycle, *Revista Matéria* **14 (3)** (2009) 1061–1069.

[30] Y. Xu, Q. Jin, J. Li, X. Xiao, X. Zhang, L. Jiang, Oxidation induced phase transformation of duplex stainless steel 25Cr–10Mn–2Ni–3Mo–0.8Cu–0.5N, *Corr. Sci.* **55** (2012) 233–237.

[31] Lian–Fu Li, Zhou–Hua Jiang , Yves Riquier, High–temperature oxidation of duplex stainless steels in air and mixed gas of air and CH4, *Corr. Sci.* **47** (2005) 57–68.

[32] C. Donik, A. Kocijan, Dj. Mandrino, I. Paulin, M. Jenko, and B. Pihlar, Initial oxidation of duplex stainless steel, *Appl. Surf. Sci.* **255** (2009) 7056–7061.

[33] C. Donik, A. Kocijan, J. T. Grant, M. Jenko, A. Drenik, and B. Pihlar, XPS study of duplex stainless steel oxidized by oxygen atoms, *Corr. Sci.* **51** (2009) 827–832.

[34] A. Bautista, F. Velasco, M. Campos, M. E. Rabanal, and J. M. Torralba, Oxidation behavior at 900°C of austenitic, ferritic, and duplex stainless steels manufactured by powder metallurgy, *Oxid. Met.* **59 (3/4)** (2003) 373–393.

[35] M.A.E. Jepson , and R.L. Higginson, The influence of microstructure on the oxidation of duplex stainless steels in simulated propane combustion products at 1000 °C, *Corr. Sci.* **51** (2009) 588–594.

[36] D. Kempf, V. Vignal, N. Martin and S. Virtanen, Relationships between strain, microstructure and oxide growth at the nano– and microscale, *Surf. Interface.* **40** (2008) 43–50.

[37] I. V. Oryshich, N. E. Poryadchenko, I. G. Slys', N. P. Brodnikovskii, and A. V. Golovash, Air oxidation of chromium–based composites, *Powder Metall. Met. C+* **46** (3–4) (2007) 189–193.

[38] K.P. Lillerud and P. Kofstad, On high temperature oxidation of Chromium I. Oxidation of annealed, thermally etched chromium at 800°–1100°C, *J. Electrochem. Soc.* **127** (11) (1980) 2397–2410.

[39] K. Shanker and P. H. Holloway, Atmospheric oxidation of chromium between 270 and 490°C, *Thin Solid Films* **105** (1983) 293–303.

[40] E.I. Alessandrini and V. Brusic, Effect of varying oxidizing and nitriding parameters on the surface of Cr thin films, J. *Vac. Sci. Technol. J. Vac. Sci. Technol.* **9** (1) (1972) 83–86.

[41] P. Kofstad and K.P. Lillerud, On high temperature oxidation of Chromium II. Properties of and the oxidation mechanism of chromium, *J. Electrochem. Soc.* **127** (11) (1980) 2410–2419.

[42] Y. P. Jacob, V. A. C. Haanappel, M. F. Stroosnijder, H. Buscail, P. Fielitz, and G. Borchardt, The effect of gas composition on the isothermal oxidation behavior of PM chromium, *Corr. Sci.* **44** (2002) 2027–2039.

[43] S. Henry, J. Mougin, Y. Wouters, J.–P. Petit, and A. Galerie, Characterization of chromia scales grown on pure chromium in different oxidizing atmospheres, *Microscopy of Oxidation* (2000) 231–234.

[44] A. Galerie, J.–P. Petit, Y. Wouters, J. Mougin, A. Srisrual, P.Y. Hou, Water vapour effects on the oxidation of chromia–forming alloys, *Mater. Sci. Forum* **696** (2011) 200–205.

[45] M. Michalik, M. Hänsel, J. Zurek, L. Singheiser, and W. J. Quadakkers, Effect of water vapour on growth and adherence of chromia scales formed on Cr in high and low pO_2–environments at 1000 and 1050°C, *Microscopy of Oxidation* (2001) 39–47.

[46] C. Brunner, H. Hutter, P. Wilhartitz, and M. Grasserbauer, Investigation of the formation and properties of protective oxide layer on high purity chromium with SIMS imaging techniques, *Mikrochem. Acta* **125** (1997) 69–72.

[47] W. Kuang, X. Wu, E.–H. Han, J. Rao, The mechanism of oxide film formation on alloy 690 in oxygenated high temperature water, *Corr. Sci.* **53** (2011) 3853–3860.

[48] F. Carrette, M. C. Lafont, G. Chatainier, L. Guinard, and B. Pieraggi, Analysis and TEM examination of corrosion scales grown on Alloy 690 exposed to pressurized water at 325°C, *Surf. Interface Anal.* **34** (2002) 35–138.

[49] G.C. Allen, J.M. Dyke, S.J. Harris, and A. Morris, The oxidation of Inconel–690 alloy at 600 K in air, *Appl. Surf. Sci.* **31** (1988) 220–238.

[50] F. Delabrouille, L. Legras, F. Vaillant, P. Scott, B. Viguier, E. Andrieu, Effect of the chromium content and strain on the corrosion of nickel based alloys in primary water of pressurized water reactors, in *Proceedings of the 12th International Conference on Environmental Degradation of Materials in Nuclear Power System – Water Reactors*, ed. T.R. Allen et al. (TMS, Utah, 2005) pp. 903–911.

[51] T. M. Angeliu, G. S. Was, The effect of chromium, carbon, and yttrium on the oxidation of nickel–base alloys in high temperature water, *J. Electrochem. Soc.* **140 (7)** (1993) 1877–1883.

[52] Z. Zhang, J. Wang, E.–H. Han, W. Ke, Influence of dissolved oxygen on oxide films of alloy 690TT with different surface status in simulated primary water, *Corr. Sci.* **53** (2011) 3623–3635.

[53] L. P. Bonfrisco, M. Frary, Effects of crystallographic orientation on the early stages of oxidation in nickel and chromium, *J. Mater. Sci.* **45** (2010) 1663–1671.

[54] P. Xu, L.Y. Zhao, K. Sridharan, T.R. Allen, Oxidation behavior of grain boundary engineered alloy 690 in supercritical water environment, *J. Nucl. Mater.* **422** (2012) 143–151.

[55] H. Leflaix–Jeuland, L. Marchetti, S. Perrin, M. Pijolat, M. Sennour, R. Molins, Oxidation kinetics and mechanisms of Ni–base alloys in pressureised water reactor primary conditions: Influence of subsurface defects, *Corr. Sci.* **53** (2011) 3914–3922.

[56] M. Sennour, L. Marchetti, S. Perrin, R. Molins, M. Pijolat, O. Raquet, Characterization of the oxide films formed at the surface of Ni–base alloys in pressurized water reactors primary coolant by transmission electron microscopy, *Mater. Sci. Forum* **595–598** (2008) 539–547.

[57] M. Sennour, L. Marchetti, F.Martin, S. Perrin, R. Molins, M. Pijolat, A detailed TEM and SEM study of Ni–base alloys oxide scales formed in primary conditions of pressurized water reactors, *J. Nucl. Mater.* **402** (2010) 147–156.

[58] E. Becquerel, Mémoire sur les effets électriques produits sous l'influence des rayons solaires, *C. R. Acad. Science.* **9** (1839) 561–567.

[59] A. W. Copeland, O. D. Black, and A. B. Garette, The photovoltaic effect, *Chem. Rev.* **31 (1)** (1942) 177–226.

[60] E. K. Oshe and I. L. Rozenfel'd, *Electrokhimiya* **4** (1968) 1200.

[61] A. Fujishima and K. Honda, Electrochemical photolysis of water at a semiconductor electrode, *Nature* **238** (1972) 37–38.

[62] M. Grätzel, Review article photoelectrochemical cell, *Nature* **414** (2001) 338–344.

[63] M. K. Carpenter and D. A. Corrigan, Photoelectrochemistry of nickel hydroxide thin films, *J. Electrochem. Soc.* **136(4)** (1989) 1022–1026.

[64] C. Sunseri, S. Piazza, and F. Di Quarto, A photoelectrochemical study of passivating layers on nickel, *Mater. Sci. Forum* **185–188** (1995) 435–446.

[65] G. Boschloo and A. Hagfeldt, Spectroelectrochemistry of nanostructure NiO, *J. Phys. Chem. B* **105** (2001) 3039–3044.

[66] T. L. S. L. Wijesinghe and D. J. Blackwood, Electrochemical and photoelectrochemical characterization of the passive film formed on AISI 254SMO super–austenitic stainless steel, *J. Electrochem. Soc.* **154 (1)** (2007) C16–C23.

[67] P. Marcus, F. Mansfeld, *Analytical methods in corrosion science and engineering*, USA: CRC Press, Taylor & Francis Group, 2006.

[68] W. Plieth, *Electrochemistry for materials science*, Hungary: Elsevier, 2008.

[69] R. Memming, *Semiconductor electrochemistry*, Germany: WILEY–VCH, 2002.

[70] H. O. Finklea, Photoelectrochemistry, *Journal of Chemical Education* **60(4)** (1983) 325–327.

[71] W. W. Gartner, Depletion layer photoeffects in semiconductors, *Phys. Rev.* **116** (1959) 84–87.

[72] M. A. Butler, Photoelectrolysis and physical properties of the semiconducting electrode WO_3, *J. Appl. Phys.* **48** (1977) 1914–1920.

[73] Jean–Pierre Petit, Grenoble Institute of Technology, SIMaP laboratory, Private communication.

[74] M. Santamaria, F. Di Quarto, and H. Habazaki, Photocurrent spectroscopy applied to the characterization of passive films on sputter-deposited Ti-Zr alloys, *Corr. Sci.* **50** (2008) 2012–2020.

[75] Y. Wouters, A. Galerie, J.–P. Petit, Photoelectrochemical study of oxides thermally grown on titanium in oxygen or water vapor atmospheres, *J. Electrochem. Soc.* **154 (10)** (2007) C587–C592.

[76] F. di Quarto, C. Sunseri, S. Piazza, and M. C. Romano, Semiempirical correlation between optical band gap values of oxides and the difference of electronegativity of the elements. Its importance for a quantitative use of photocurrent spectroscopy in corrosion studies, *J. Phys. Chem. B* **101** (1997) 2519–2525.

[77] A K Vijh, Correlation between bond energies and forbidden gaps of inorganic binary compounds, *J. Phys. Chem. Solids* **30** (1969) 1999–2005.

[78] Butler, M. A., Localized Photoelectrochemical Measurements of Passive Films on Titanium, *J. Electrochem. Soc.* **130 (12)** (1983) 2358–2362.

[79] M.A. Butler, Photoelectrochemical imaging, *J. Electrochem. Soc.* (1984) **131 (9)** 2185–2190.

[80] L. F. Garfias–Mesias and W. H. Smyrl, In Situ High–Resolution Photoelectrochemical Imaging of Precursor Sites for Pitting in Polycrystalline Titanium, *J. Electrochem. Soc.* **146 (7)** (1999) 2495–2501.

[81] S. Kudelka and J. W. Schultze, Photoelectrochemical imaging and microscopic reactivity of oxidised Ti, *Electrochim. Acta* **42 (18)** (1997) 2817–2825.

[82] Y. Wouters, L. Marchetti, A. Galerie, and J.–P. Petit, Photoelectrochemical imaging of metal–scale decohesion on titanium thermally oxidized in oxygen, *Corr. Sci.* **50** (2008) 1122–1131.

[83] A. R. J. Kucernak, R. Peat, and D. E. Williams, Photoelectrochemical imaging – part II. The passivating oxide film on iron, *Electrochim. Acta* **38 (1)** (1993) 71–87.

[84] D. E. Williams, T. F. Mohiuddin, and Y. Y. Zhu , Elucidation of a Trigger Mechanism for Pitting Corrosion of Stainless Steels Using Submicron Resolution Scanning Electrochemical and Photoelectrochemical Microscopy, *J. Electrochem. Soc.* **145 (8)** (1998) 2664–2672.

[85] P. Schmuki and H. Böhni, Large Area Photocurrent Behavior and Laser Spot Scanning of Passivated Stainless Steels, *J. Electrochem. Soc.* **141 (2)** (1994) 362–366.

[86] F. Atmani, Y. Wouters, A. Galerie, J.–P. Petit, Y. Dali, M. Tupin, P. Bossis, Imaging by photoelectrochemical techniques of Laves–phases γ–$Zr(Fe,Cr)_2$ thermally oxidized on Zircaloy–4, *Mater. Sci. Forum* 595–598 (2008) 571–579.

[87] R. Benaboud, P. Bouvier, J.–P. Petit, Y. Wouters, and A. Galerie, Comparative study and imaging by photoelectrochemical techniques of oxide films thermally grown on zirconium and zircaloy–4, *J. Nucl. Mater.* **360** (2007) 151–158.

[88] A. R. J. Kucernak, R. Peat, and D. E. Williams, Dissolution and reaction of sulfide inclusions in stainless steel imaged using scanning laser photoelectrochemical microscopy, *J. Electrochem. Soc.* **139 (8)** (1992) 2337–2340.

[89] M. F. Montemor, M. G. S. Ferreira, N. E. Hakiki, M. Da Cunha Belo, Chemical composition and electronic structure of the oxide films formed on 316L stainless steel and nickel based alloys in high temperature aqueous environments, *Corr. Sci.* **42** (2000) 1635–1650.

[90] Y. Wouters, A. Galerie, J.–P. Petit, Photoelectrochemical characterization of chromia scales thermally grown on various metal substrates, *Mat. Sci. Forum* **1595–598** (2008) 1181–1188.

[91] S. Henry, J. Mougin, Y. Wouters, J.–P. Petit, and A. Galerie, Characterization of chromia scales grown on pure chromium in different oxidizing atmospheres, *Microscopy of Oxidation* (2000) 231–234.

[92] F. Di Quarto, S. Piazza, and C. Sunseri, A photocurrent spectroscopic investigation of passive films on chromium, *Corr. Sci.* **31** (1990) 721–726. room temperature !!

[93] G. Goodlet, S. Faty, S. Cardoso, P.P. Freitas, A.M.P. Simoes, M.G.S. Ferreira, and M. Da Cunha Belo, The electronic properties of sputtered chromium and iron oxide film, *Corr. Sci.* **46** (2004) 1479–1499.

[94] M.F. Montemor, M.G.S. Ferreira, N.E. Hakki, M. Da Cunha Belo, Chemical composition and electronic structure of the oxide films formed on 316L stainless steel and nickel based alloys in high temperature aqueous environments, *Corr. Sci.* **42** (2000) 1635–1650.

[95] S. Zhang, Y. Tan, and K. Liang, Photoelectrochemical study on semiconductor properties of oxide films on Alloy 600 in high temperature water with ZnO addition, *J. Nucl. Mater.* **434** (2013) 43–48.

[96] S. Zhang, Y. Tan, and K. Liang, Zinc addition changes the semiconductor properties of oxide films of Alloy600 in high temperature water, *Mater. Lett.* **68** (2012) 36–39.

[97] A. Loucif, J.–P. Petit, Y. Wouters, P. Combrade, "Effect of Dissolved Hydrogen, Surface Condition and Composition on the Electronic Properties of the Oxide Films Formed on Nikel–base Alloys in PWR Primary Water", in *15th International Conference on Environmental Degradation*, edited by J.T. Busby et al., TMS Conference Proceeding 2011, pp. 953–963.

[98] L. Marchetti, S. Perrin, Y. Wouters, F. Martin, M. Pijolat, Photoelectrochemical study of nickel base alloys oxide films formed at high temperature and high pressure water, *Electrochim. Acta* **55** (2010) 5384–5392.

CHAPTER 2
MATERIALS AND METHODS

This chapter deals with materials and sample preparations, and with the characterization techniques used in this work. The chemical compositions are indicated in this part, together with the oxidation conditions. The characterization part focuses on the photoelectrochemical techniques which are the core of this work. The set–up developed in our research team can work at three scales: the macroscopic, the microscopic, and for a first time, the mesoscopic scales. This set–up is described, and the photoelectrochemical procedures used are reported. Moreover the novel model which was developed to fit and analyze photocurrents vs photon energy spectra is presented. As regards complementary characterizations, i.e. scanning electron microscopy, X–ray diffraction, and Raman spectroscopy, as they are well–known, they are only briefly presented.

2.1 Materials and sample preparations

The experiments are mainly divided into two parts: the study of chromia and iron–chromium oxides solid solution, and the approval of the mesoscopic photoelectrochemical, set–up and the fitting model through applications in high temperature corrosion. In the first part, chromium oxide was obtained by oxidizing pure chromium metal sheets whereas a hematite–chromia solid solution ($Fe_{2-x}Cr_xO_3$) was prepared by mixing powder of hematite (Fe_2O_3) and chromia (Cr_2O_3) at various ratios. In the second part, the performance of the mesoscopic photoelectrochemical set–up developed for this work is first demonstrated in the case of the characterization of oxidized duplex stainless steels. Then oxidation layers formed on duplex stainless steel and nickel–based alloys are photoelectrochemically studied at several scales and the obtained photocurrent–energy spectra are analyzed by the novel model stated above.

2.1.1 Pure chromium oxidation

The metal sheets of 99.7% pure chromium with 2 mm of thickness are supplied by Goodfellow. The impurities percentage in the metal are listed in Table 2.1. The sheets are cut to dimensions of 10 x 10 mm^2, grounded with SiC abrasive paper up to 1200 grit, and then cleaned in ethanol and distilled water using an ultrasonic bath. These samples were kept in desiccators for 24 hours before thermal treatment. Figure 2.1 presents an outline schematic of the experimental set–up used for oxidation in tubular furnace. Oxidation of pure chromium was conducted at 850°C under flowing gas at atmospheric pressure. The total flow rate was

controlled to ensure laminar flow over the sample at a velocity of 5 mm/s. Oxidizing gases with different oxygen partial pressure were provided using 20% O_2 or 20% H_2O in argon gas or 3% H_2O in hydrogen gas. The influence of nitrogen in the oxidation atmosphere on the semiconducting behavior of the layer was tested using 20% O_2 or H_2O in nitrogen gas. The oxidations times ranged from 30 minutes to 16 hours, conducting oxide thickness from 0.3 μm to 2.0 μm.

Table 2.1 Impurity contents in chromium (in ppm)

	Al	C	Ca	Cu	Fe	K	Mg	Mo	Na	P	Pb	S	Si	W
ppm	10	40	20	5	2000	< 5	< 5	50	10	5	5	5	80	100

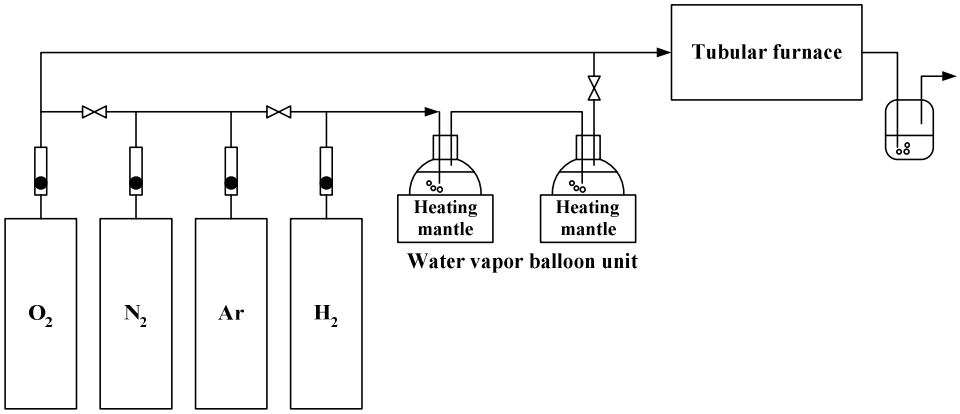

Figure 2.1 Typical experimental set–up used for oxidation in a tubular furnace

2.1.2 Hematite–chromia solid solutions

Solid solutions were prepared by solid–state reaction of mixtures of hematite and chromia powders. Powders of Fe_2O_3 are supplied by Chimie–Plus (Ref: 28312) whereas powders of Cr_2O_3 were obtained from PROLABO (No. 22.798).

The aim of these experiments was to analyze the semiconducting properties of hematite–chromia solid solutions at various iron/chromium ratios using photoelectrochemical techniques, the solid solutions were prepared as pellets to fit in the photoelectrochemical sample holder. More details on the procedures used to obtain “perfect” solid solutions and dense pellets, will be given later in Chapter 3.

2.1.3 Duplex stainless steel

Sample of the duplex stainless steel, DSS2205, were supplied by APERAM Stainless France. A heat treatment (illustrated in Figure 2.2) was applied to these samples and yielded a ratio of 50–55% in austenitic phase. An irregular shape of the austenitic phase (clear areas) with grain size around 30–40 μm was generally observed (Figure 2.3). The chemical

compositions as analyzed by electron microprobe are given in Table 2.2. DSS samples were cut in $10 \times 10 \times 2$ mm^3 and polished down to 3 μm, then ultrasonically rinsed successively in ethanol and distilled water, and stored in desiccators for 24 hours before performing oxidation experiments in a tubular furnace at 650°C and 850°C under the same flowing gas conditions for pure chromium oxidation experiments. Dry or wet atmospheres were simulated by 20% O_2 or 20% H_2O in nitrogen gas. The oxidations were performed for 5 minutes and 1 hour in each atmospheric condition, conducting thermal oxide thickness from 20 nm to 200 nm.

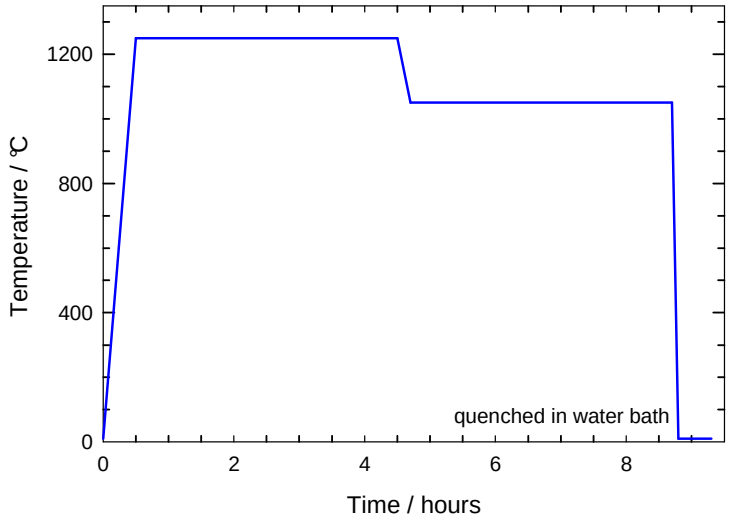

Figure 2.2 Heat treatment process applied to the 2205 duplex stainless steel

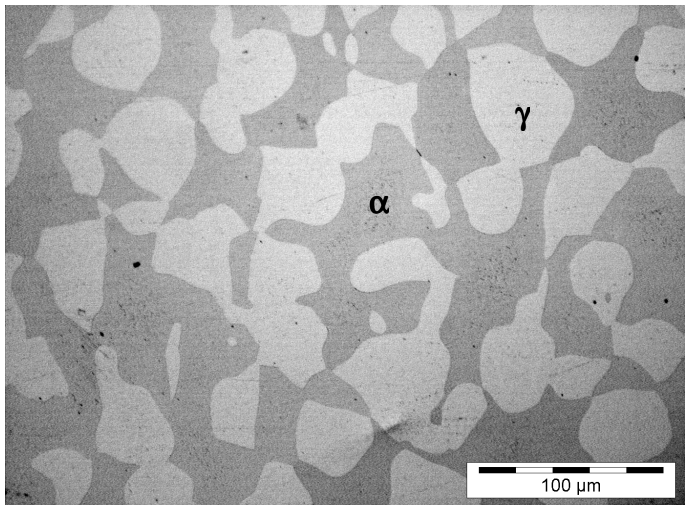

Figure 2.3 Optical micrograph of 2205 duplex stainless steel after heat treatment ; α and γ are the ferritic and austenitic phases respectively

Table 2.2 Chemical composition of the duplex stainless steel (weight%)

Element	Cr	Ni	Mo	Mn	Si	Cu	P	C	N	S	Fe
Average	22.77	5.69	3.09	1.76	0.47	0.17	0.0348	0.035	0.1810	< 0.01	Bal.
Austenitic phase	21.61	7.11	2.42	2.10	0.52	0.27		0.29	0.52		Bal.
Ferritic phase	26.00	3.80	4.15	1.74	0.64	0.12		0.08	0.05		Bal.

2.1.4 Ni–based alloys

A lab–made Ni–based alloy, Inconel 690, was supplied from CEA Saclay. The chemical composition is presented in Table 2.3. Specimens of 13 x 13 x 1 mm^3 dimensions were polished down to 1 μm and cleaned in ethanol and distilled water using an ultrasonic bath. The oxidation experiments were conducted in a SETARAM thermobalance (model B24) at 900°C under flowing gas at atmospheric pressure. The overall flow rate was 10 L/h to obtain a linear flow over the sample. Dry and wet oxidizing gases were obtained from 20% O_2 and 20% H_2O in nitrogen gas, respectively. Oxidations were done for 2 hours and 30 hours. The experimental set–up is illustrated in Figure 2.4. Moreover the oxidation experiments in natural air were also conducted in the conventional oven at 900°C without flowing gas for 21 hours. All oxide layers were thinner than 1 μm.

Table 2.3 Chemical compositions of Inconel 690 (weight%)

Element	Cr	Fe	C	S	O	N	Ni
% mass	29.79	10.14	0.0059	< 0.0005	< 0.0010	< 0.0005	Bal.

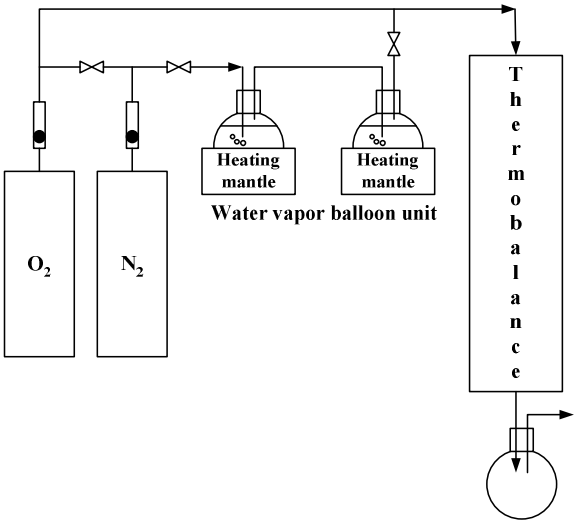

Figure 2.4 Typical experimental set–up used for oxidation in thermobalance

2.2 Photoelectrochemical characterizations

A photoelectrochemical set–up (PEC) aims at measuring additional electrochemical currents obtained when illuminating a semiconductor in contact with an electrolyte, the so–called photocurrents. This section presents the components of the set–up, the experimental conditions for the photoelectrochemical experiments and the basis of our fitting of the photocurrent energy spectra.

In the three operating modes of the photoelectrochemical set–up developed in our team, i.e. the macroscopic, microscopic, and mesoscopic modes, some components are shared such as the photoelectrochemical cell, the potentiostat, the lock–in amplifier, and the mechanical light modulator. A three electrodes electrochemical cell equipped with a flat quartz optical window (Figure 2.5) was used in all PEC experiments. The stuck sample was used as the working electrode. The electrical back contact to the sample was taken directly on one side of the oxidized metal or alloy after removing the oxidation layer. A platinum foil (area = 1 cm^2) and an Hg/Hg_2SO_4 mercury sulfate electrode (MSE) are used as the counter electrode and the reference electrode (+0.650 V/SHE) respectively. An aqueous solution of sodium sulfate (0.1 M) at pH 8.0 ± 0.1 was generally used as the electrolyte in the cell. A PAR 273 A (EG&G Instruments) potentiostat equipped with the /92 Impedance interface, was used to control the electrochemical cell. The voltage proportional to the overall electrochemical current, issued from the latter interface, was applied to the signal input of a lock–in amplifier (Stanford Research SR830), whereas the synchronization signal delivered by the light modulus (PAR 197, EG&G Instruments) was applied to the reference input of the lock–in amplifier, allowing to extract the photocurrent (modulus and phase shift) from the electrochemical current. Computer control with in–house developed software operated all interfaces in the set–up.

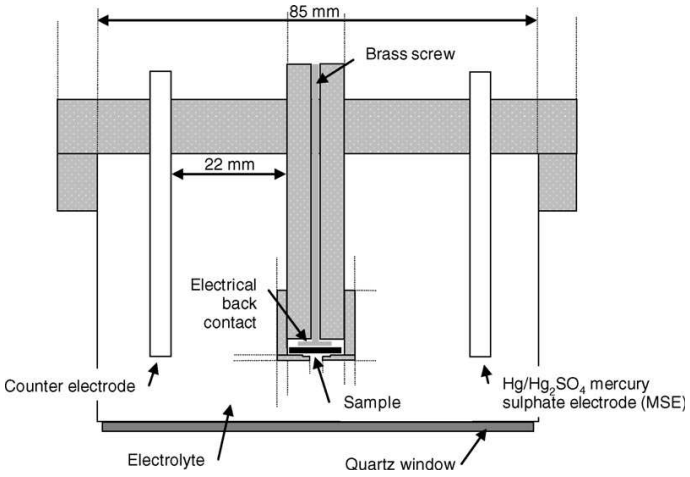

Figure 2.5 Schematic representation of the electrochemical cell [1]

2.2.1 Macroscopic photoelectrochemical characterizations

The schematic of the macroscopic PEC set–up is presented in Figure 2.6. A 150 W Xenon arc bulb (Newport, model 6255) associated to a triple grating monochromator (Newport, model 74125) was used as the light source, provided monochromatic photon at variable wavelengths with a typical spectral width of ±1 nm. In macroscopic PEC characterizations, the whole area of the sample exposed to electrolyte (typically 0.8 cm^2) was illuminated.

Photocurrent vs potential curves were recorded at a few selected photon energies, choosing the potential window to avoid electrochemical currents higher than μA in modulus, which could induce electrochemical sample modifications.

Photocurrent vs photon energy spectra were recorded under modulated light conditions, using the lock–in amplifier together with the mechanical light chopper. The spectra were measured at different applied potentials for each sample, in particular to ensure to be able to detect all the oxides present in the layer. Since the photon flux delivered by the light source is different at each wavelength, and the optical path from the source to the sample does absorb photons differently when varying the wavelength, the as–measured photocurrents, I_{PH}, converted to new values, J_{PH}, proportional to the quantum yield. To obtain J_{PH}, a calibrated silicon photodiode (Newport, model 918D–UV–OD3R) was used to measure the photon fluxes at sample position. The normalized photon flux at each wavelength, $\Phi_N(h\nu)$, was calculated by dividing the actual photon flux $\Phi(h\nu)$ by its maximum value, and J_{PH} was calculated as follows:

$$J_{PH} = \frac{I_{PH}}{\Phi_N(h\nu)} \tag{2.1}$$

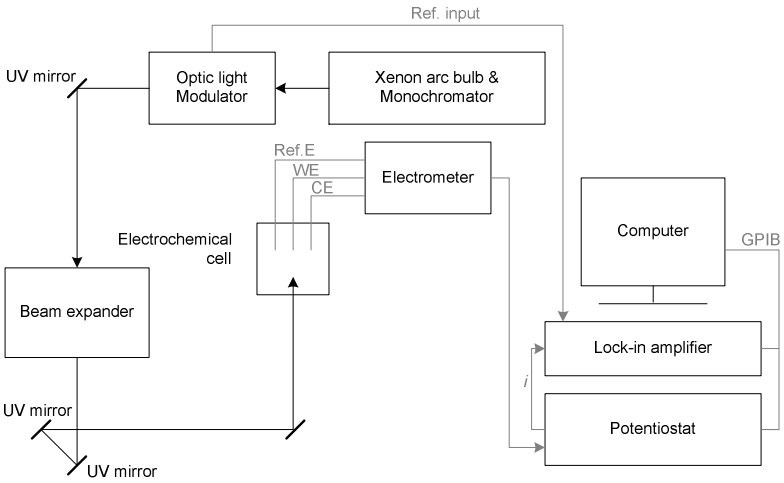

Figure 2.6 Outline schematic of the macroscopic photoelectrochemical set–up

2.2.2 Microscopic photoelectrochemical characterizations

Microscopic photoelectrochemistry aims at obtaining photoelectrochemical images to give more information about the lateral distribution of the photocurrents (and thus of the oxides). The microscopic PEC set–up is presented in Figure 2.7. A selected line of an argon laser (Innova 90 C–A6 from Coherent) is used here as the light source and focused on the sample through an inverted microscope (Olympus IX71), a built–in 50/50 beam splitter (Edmund Optics Inc) allowing to position the focused beam on the area selected on the optical image (obtained by a CCD camera) with the help of an high resolution XY motorized Marzhauser microscope stage (Scan IM120 x 100).

Procedures to construct a PEC image started with selecting an area from the optical image giving by CCD camera, setting a distance between 2 points of the image (point interval typically 1 to 5 μm), and then focusing the laser line on a spot size of around 1 μm on the sample surface through the objective lens of the microscope. The selected area is then scanned point by point, line by line, moving the sample vs the spot, the photocurrent being recorded (modulus and phase shift) at each point.

In this work, the experiments were done at various applied potentials and photon energies, depending on the specimens and on the macroscopic photoelectrochemical results. Image sizes and resolutions were also varied, to obtain the most pertinent informations.

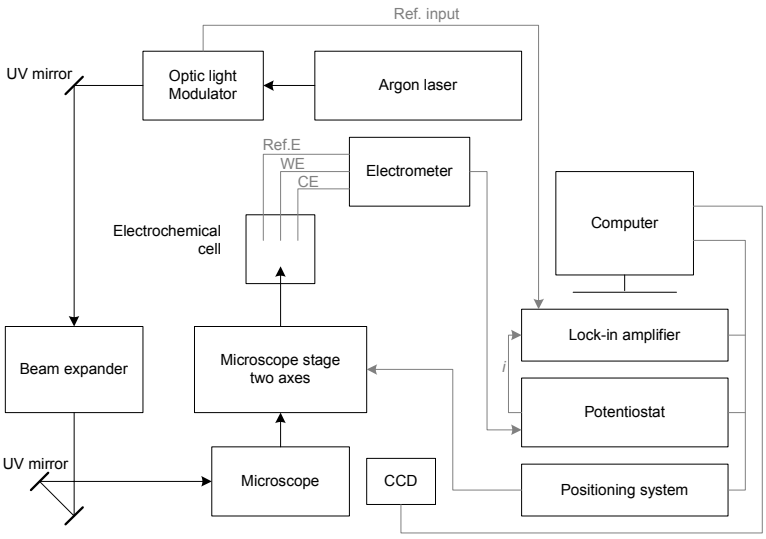

Figure 2.7 Schematic representation of the microscopic photoelectrochemical set–up

2.2.3 Mesoscopic photoelectrochemical characterizations

In macroscopic experiments, both photocurrent vs potential and photocurrent vs energy spectra may be recorded, but no local informations can be obtained. In microscopic experiments, local informations may be obtained, but only from photocurrent vs potential curves by the laser provided only a few wavelengths. One of the aims of the present work was to try to obtain photocurrent energy spectra also at a microscopic scale. The set–up developed here for mesoscopic PEC (Figure 2.8) is similar as the one used for photoelectrochemical imaging, but the light source is the Xenon arc bulb coupled to the monochromator as in macroscopic PEC.

Steps to operate in mesoscopic mode began from choosing an area on the optical image, and then working at focusing the noncoherent light of the Xenon arc light source on a spot with approximately 30 µm in diameter using a specific lens built in the microscope, which required sometimes a lot of efforts. Photocurrent energy spectra were then recorded in the same way as in macroscopic experiments. A most important thing of experiment is to put the spot on the right position, and to check regularly on the optical on–screen image always that the spot remains located inside the interesting area. Moreover the coupling of the light source to the monochromator, and the optical path from the monochromator output to the microscope input, were optimized to minimize light power losses and to obtain a parallel beam at the microscope input.

In this work, mesoscopic PEC was successfully applied to oxidized DSS and oxidized Ni–based alloy samples. However, due to the specific lens used, photon energies higher than 3.8 eV – 4.0 eV could not be tested.

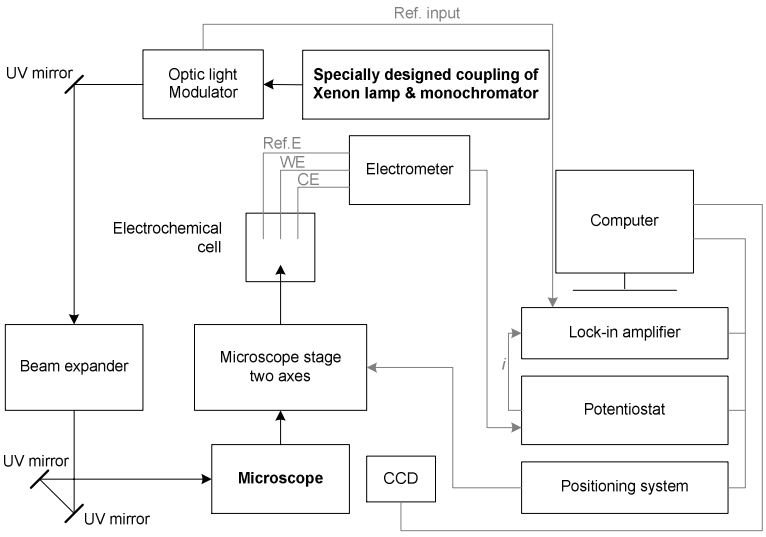

Figure 2.8 Schematic of mesoscopic photoelectrochemical set–up

2.2.4 Fitting model for the photocurrent energy spectra

As mentioned in Chapter 1, photocurrent energy spectra are usually analyzed by means of linear transforms to take benefit of the fact that, using the simplified form of the Gärtner–Butler model, the quantum yield, η, of the photocurrent is proportional to the light absorption coefficient and allows to write the following simple equation:

$$\left(\eta \times E\right)^{1/n} = C \times \left(E - E_G\right) \tag{2.2}$$

where E is the photon energy, n is 2 (resp. ½) for indirect (resp. direct) transitions and C is a constant, depending on the material, the applied potential (and of the modulation frequency of the light)

A lot of experimental works reported in the literature successfully used this classical analysis, as regards materials made of one or two constituents [2–5]. However, up to now, as regards complex oxide scales formed of several p–type and n–type phases, the complete description of the photocurrent energy spectra could not be achieved, and only semi–quantitative and/or partial informations could be obtained on the oxides present in the scales.

As J_{PH} was measured under modulated light conditions and thus actually was a complex number, it was proposed by our group [7] that the real ($Re(J_{PH})$) and the imaginary ($Im(J_{PH})$) parts of the photocurrent (or the modulus J_{PH} / and the phase shift θ) should be considered simultaneously when analyzing and fitting the photocurrent energy spectra, rather than their modulus ($|J_{PH}|$) only, as was made up to now. Therefore, the overall complex photocurrent, J_{PH}, was written as:

$$J_{PH} = \left|J_{PH}\right|\cos\theta + j\left|J_{PH}\right|\sin\theta = \sum_i J_{PH,i}\cos\theta_i + jJ_{PH,i}\sin\theta_i \tag{2.3}$$

where $J_{PH,i}$ and θ_i represent the modulus and phase shift, respectively, of the photocurrent issued from the i^{th} semiconducting constituent of the oxide layer. For thin semiconducting films such as those investigated in the present work, the space charge regions are low compared to penetration depth of the light. $J_{PH,i}$ may thus be expected, at a given applied potential (and at a given modulation frequency), to follow the simplified form of the Gärtner–Butler model by writing the equation as follows :

$$\left(J_{PH,i} \times E\right)^{1/n} = K_i \times \left(E - E_{G,i}\right) \tag{2.4}$$

where $E_{G,i}$ and K_i represent the energy gap and a value proportional to C (J_{PH} is proportional to but not equal to η) for the i^{th} semiconducting constituent. In addition, as the space charge regions are likely to extend over the whole thickness of each film constituent, it is assumed

that the recombinations of the photogenerated electron–hole pairs, and thus the phase shifts, θ_i, will not depend on the photon energy.

The J_{PH} (E) and θ(E) experimental data constituting a photocurrent vs energy spectrum have been fitted according to the above described model (with n = 2, for direct transitions have rarely been observed on disordered oxide scales) using a laboratory made software in the Matlab® environment (R2011b release). As the optimization tool, the latter software used the *fminsearch* procedure, which takes benefit of the simplex search method of Lagarias *et al.* [6] to find the minimum of a scalar function of several unconstrained variables, starting at an initial estimate of the latter.

In the present work, for a given vector of *m* ($E_{G,i}$, K_i, θ_i) triplets, *m* representing the supposed number of semiconducting phases contributing to the photocurrent, the scalar function to be minimized by the *fminsearch* function was defined as the product of the square roots of two quantities, D^2_{Re} and D^2_{Im}, where D^2_{Re} (resp. D^2_{Im}) is the sum of the squares at each photon energy of the difference between the real (resp. imaginary) parts of the experimental data and of the ones calculated using equation (2.2).

In the above cited lab made software, the *m* value is fixed by the user. The user is, however, free to decide for each of the 3 *m* variables, whether the variable will remain fixed to a user provided value, or will be allowed to be fitted. The user is also responsible for providing an initial estimate of the values of the *m* triplets, or for allowing random initial values for all variables of the fit. Finally, it is noteworthy that several successive calls of the *fminsearch* procedure were necessary to reach the minimum of the scalar function and a stable set of the output parameters of the latter procedure. In the case of successive calls, the output parameters of one call (except for the first one) were used as input parameters for the next call.

The fit results presented in Chapter 4 were mostly obtained allowing all parameters of the *m* triplets to be fitted, starting always from random initial values. Several runs were made for each spectrum, to ensure the stability of the final parameters.

2.3 Additional characterizations

Additional characterizations were performed to support the results obtained from photoelectrochemical experiments. Scanning electron microscopy (SEM) operated in secondary (SE) and backscattering (BSE) electron modes were used to observe the morphology of oxides and the distribution of chemical compositions over the surface whereas the element compositions were analyzed by energy–dispersive X–ray spectroscopy (EDS) mode. In addition, the oxide phases were analyzed using X–ray diffraction (XRD) and Raman spectroscopy. The basics of each technique are briefly recalled below.

2.3.1 Scanning electron microscopy

Scanning electron microscopy (SEM) is a well–known characterization technique which can reveal information about morphology, chemical compositions, and crystal structures and orientations. Focusing electron beam on the sample leads to electron–sample interaction and provides a variety of signals. In this work, secondary electrons and backscattered electrons which provide electron micrograph and characteristic X–rays which give an element analysis were used.

2.3.1.1 Secondary electrons

Signal of secondary electrons provides an image on a cathode–ray tube whose raster is harmonized with the raster of a point beam of electrons scanned over the sample surface. Morphology and topography of sample can be observed and analyzed. Image brightness at any point is proportional to the scattering secondary electron emission from the point on the sample being collided by electron beam.

2.3.1.2 Backscattered electrons

Backscattered electrons (BSE) are beam electrons which scattered back out from surface by elastic scattering when electrons strike the sample. Intensity of BSE is strongly related to the atomic number (Z) of the specimen that higher Z can deliver the higher intensity. Hence BSE images can provide information about the distribution of different elements in the sample.

2.3.1.3 Characteristic X–rays

Energy–dispersive X–ray spectroscopy or EDS, element analysis, is a common mode of SEM which get an information from characteristic X–ray signal. This analysis is widely used and highly confided in the qualitative data. However quantitative analysis of chemical composition is possibly performed by a solid state detector.

Scanning electron microscope, *SEM LEO Stereoscan S440*, was used in this study. Images were acquired with a beam–accelerating voltage of 20 keV. Elements analysis, EDS, were performed with Si(Li) semiconductor detector.

2.3.2 X–ray diffraction

X–ray diffraction, XRD, is a classical technique of phase identification via giving information about lattice spacing and crystal structure of material. Concept of this technique is the diffraction of a parallel reflected X–ray from atomic plane according to Bragg's law.

$$n\lambda = 2d_{hkl}\sin\theta \tag{2.5}$$

when n is an integer (1, 2, 3,..), λ is a wavelength of X–ray, d_{hkl} is a lattice spacing, and θ represents the angular locations of both X–ray source and detector to the specimen surface.

XRD data can be interpreted by comparing the obtained X–ray pattern with the joint committee on powder diffraction standards (JCPDS) database.

X–ray diffractometer, *Rigaku Miniflex II*, was used in this work. A copper target provides a K_α characteristic radiation at 1.5406 Å. Samples are normally scanned from 10° to 90° by 0.1° sampling width and 2.0°/minute scan speed. However the fine scan was done in necessary cases that scanned range was 32.5° to 37.5° by 0.005° sampling width and 0.1°/minute scan speed.

2.3.3 Raman spectroscopy

Raman spectroscopy is a vibrational spectroscopic technique based on inelastic scattering, or the frequency change, of monochromatic light typically delivered by laser. Monochromatic light interact with sample and reemit a spontaneous Raman scattering of incident light. Frequency of the reemitted photons is usually shifted up or down comparing with original frequency, which is named the Raman scattering or Raman effect. The intensity of Raman scattering for each frequency shift is recorded. The shift provides information about vibrational, rotational and other low frequency transitions in molecules.

Light scattering is possibly being in three types as showed in Figure 2.9. Rayleigh scattering is elastic scattering where reemitted photons have the same frequency as the incident ones. For spontaneous Raman scattering, a photon excites the molecule from the ground state to a virtual energy state. When the molecule relaxes it emits a photon and returns to a different rotational or vibrational state. The difference in energy between the original state and this new state leads to a shift in the emitted photon's frequency away from the

excitation wavelength. If the final vibrational state of the molecule is more energetic than the initial state, then the emitted photon will be shifted to a lower frequency in order for the total energy of the system to remain balanced. This scattering is defined as a Stokes scattering. When the final vibrational state is less energetic than the initial state and the emitted photon shift to a higher frequency, it is defined as an Anti–Stokes scattering.

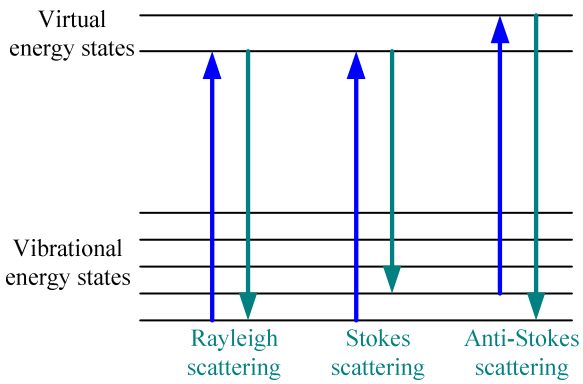

Figure 2.9 Possibility of light scattering: blue and green arrow represent incident and scattering light

Raman shifts are the shift of monochromatic light frequency and are generally presented in units of inverse length (cm^{-1}). In order to convert between spectral wavelength and wavenumbers of shift in the Raman spectrum, the following equation can be applied.

$$\Delta w = \left(\frac{1}{\lambda_0} - \frac{1}{\lambda_1} \right) \tag{2.6}$$

where Δw is the Raman shift expressed in wavenumber, λ_0 and λ_1 is the excitation wavelength and the Raman spectrum wavelength.

In this work, the analyzes were carried out using a Renishaw In–Via Raman spectrometer. This instrument is equipped with an argon laser which emits an excitation wavelength of 514 nm (green line), a CCD detector, and a peripheral network. An objective × 50 is used to focus the beam incident on a spot diameter around 1.5 µm. Beam power is 10 mW to avoid overheating which can damage the sample. Collection time of a spectrum is one or two minutes. Raman shift range was scanned from the 170 to 850 cm^{-1}. To be representative of each whole area on sample, the random five to ten points are performed. The spectra which were shown are the average of collected spectra. Raman imaging was performed on Ni-based alloys samples, and the analysis was done using software provided by Renishaw.

REFERENCES

[1] R. Benaboud, P. Bouvier, J.–P. Petit, Y. Wouters, and A. Galerie, Comparative study and imaging by photoelectrochemical techniques of oxide films thermally grown on zirconium and Zircaloy–4, *J. Nucl. Mater.* **360** (2007) 151–158.

[2] U. Stimming, Photoelectrochemical studies of passive films, *Electrochim. Acta* **31(4)** (1986) 415–429.

[3] Y. Wouters, A. Galerie and J.–P. Petit, Photoelectrochemical characterization of chromia scales thermally grown on various metal substrates, *Mater. Sci. Forum* **595–598** (2008) 1181–1188.

[4] L. Anicai, R. Masi, M. Santamaria and F. Di Quarto, A photoelectrochemical investigation of conversion coatings on Mg substrates, *Corr. Sci.* **47 (12)** (2005) 2883–2900.

[5] H. Tsuchiya, S. Fujimoto, O. Chihara and T. Shibata, Semiconductive behavior of passive films formed on pure Cr and Fe–Cr alloys in sulfuric acid solution, *Electrochem. Acta* **47 (27)** (2002) 4357–4366.

[6] J.C. Lagarias, J.A. Reeds, M.H. Wright and P. E. Wright, Convergence properties of the Nelde—Mead Simplex method in low dimension, *SIAM J. Optimiz.* **9 (1)** (1998) 112–147.

[7] J.–P. Petit, R. Boichot, A. Loucif, A. Srisrual, Y. Wouters, Photoelectrochemistry of oxidation layers: A novel approach to analyze photocurrent energy spectra, *Oxid. Met.* **79** (2013) 349–359.

CHAPTER 3
CHARACTERISTIC OF CHROMIA AND ITS SOLID SOLUTION

Chromia (Cr_2O_3), the only one stable oxide of chromium at high temperature, is well–acknowledged being able to be a protective oxide in high temperature oxidation conditions. Chromia–forming alloys are thus widely used in high temperature applications. However, chromia is not the unique oxide present in the oxidation layers of such alloys, oxides containing the other alloying elements are also formed, such as $Fe_{2-x}Cr_xO_3$ solid solutions.

The aim of the photoelectrochemical experiments presented in this chapter was to contribute clarifying the semiconducting properties (type of semiconduction, bandgap) of chromia and $Fe_{2-x}Cr_xO_3$ solid solutions with different Fe/Cr ratios, to help later analyzing photocurrent energy spectra of oxidation layers formed on alloys such as stainless steels.

This chapter is divided in two parts. The first one presents PEC characterizations of oxidation layers formed on pure chromium, the second focuses on the PEC behavior of chromia and $Fe_{2-x}Cr_xO_3$ solid solutions when prepared from powders.

3.1 Oxidation of pure chromium

Plenty of studies on pure chromium oxidation showed a strong dependence of the oxide properties on oxidation time, and temperature [1–7], and on the oxidation environment [3–11] (gaseous species, oxygen partial pressure, water vapor content). In the following, the effect of these parameters on electronic properties (semiconducting type and bandgap energy) of oxides formed on chromium is investigated.

3.1.1 Factors affecting the semiconducting type

This section focuses on the analysis of photocurrent vs potential curves (or photocurrent voltammograms), which ways, in simple cases reveal the semiconducting type of a semiconductor. Pure chromium oxidized under 20% oxygen in argon for 1 hour is used as the reference sample. Normalized voltammograms will be presented for convenience of analysis. These normalized voltammograms are obtained by dividing the measured photocurrent at a given applied potential by the value of the photocurrent measured at a selected applied potential (in our case, either 0 mV or 400 mV). The oxidizing conditions corresponding to “20% oxygen in argon” and “20% water vapor in argon” will be referred sometimes as “oxygen gas” and “water vapor” in the following text.

3.1.1.1 The presence of water vapor

Figure 3.1 illustrates photocurrent voltammograms, obtained when illuminating the sample at photon energies of 3.5 eV and 4.0 eV, in the case of pure chromium oxidized in oxygen gas (Figure 3.1(a)) and in water vapor (Figure 3.1(b)). It can firstly be pointed out that the two samples exhibit, whatever the photon energy, both cathodic and anodic photocurrents, at potentials respectively lower and higher than the potential corresponding to the minimum of the photocurrent on each photovoltammogram. At first sight, this could be interpreted as revealing a low–doped, near insulating, oxide.

However, in such a case, the photovoltammogram should be V–shaped, i.e. more or less symmetric vs the potential corresponding to the minimum of the photocurrent. This is clearly not observed. Moreover, the anodic part of the photovoltammogram exhibits a shape typical of an n–type semiconductor.

It is thus more likely that at least two oxides are present in the oxidation layer, one being n–type, another being either near insulating or p–type (to account for the cathodic photocurrents). It was indeed already reported in a previous work [10] that the oxidation scale on chromium was constituted of an internal equiaxed Cr_2O_3 and an external columnar Cr_2O_3, with proposed bandgaps of 3.0 eV and 3.5 eV respectively. The main defects implied in the formation of the internal and external layers were proposed to be interstitial chromium and chromium vacancies respectively [12–15].

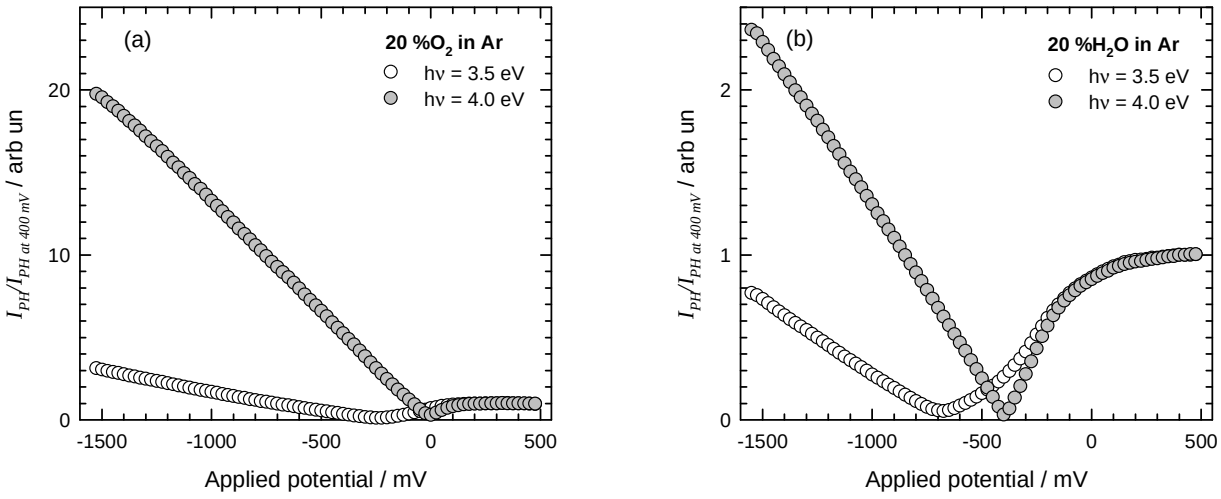

Figure 3.1 Photocurrent voltammograms obtained on pure chromium oxidized at 800°C during 1 hour under (a) 20% oxygen gas in argon and (b) 20% water vapor in argon

Finally, it can be observed that the contribution to the photocurrent of the n–type component is higher for the sample oxidized in water vapor, which is also in agreement with a more cathodic potential for the minimum of photocurrent. This could be due

to the doping of the corresponding oxide with inserted species (hydrogen? [10, 16–19]) acting as electron donor to the conduction band.

3.1.1.2 Influence of oxygen partial pressure

The photovoltammograms in Figure 3.1 are again presented in Figure 3.2(a) and (b) together with the curves obtained on samples oxidized in 3% H_2O in H_2 (Figure 3.2(c)). The oxygen partial pressure was varied at 2.0×10^{-1} atm (20% oxygen in argon gas), 2.9×10^{-6} atm (20% water vapor in argon gas), and 2.7×10^{-18} atm (3% water vapor in hydrogen gas). The comparison of the previous results with the ones obtained for the sample formed at the lowest oxygen partial pressure tends to indicate that the absence of oxygen promote (resp. disfavors) clearly the anodic (resp. cathodic) photocurrents together with a cathodic shift of the potential of the minimum photocurrent. This could suggest that the n–type oxide is favored in the case of Figure 3.2(c), and, considering the V–shape of the photovoltammograms near the minimum, that the other oxide is likely to be insulating and not p–type. However, the anomalous shape of the photovoltammograms at the most anodic potentials calls for caution. Photovoltammograms of non–ideal semiconductors remain hardly to be modeled, so photovoltammograms of layers constituted of multiple components remain hardly to be predicted.

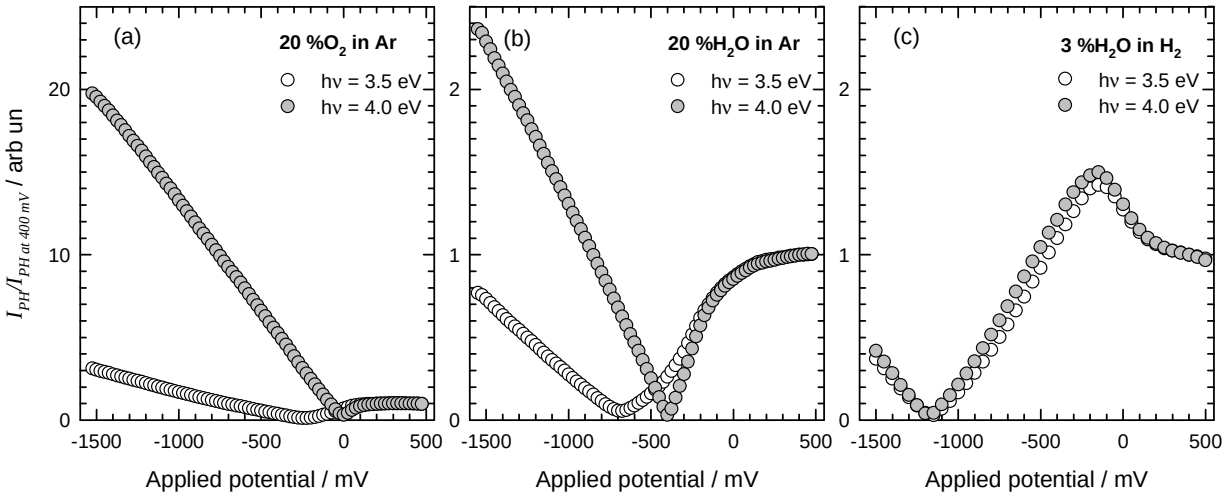

Figure 3.2 Photovoltammograms obtained for pure chromium oxidized at 800°C during 1 hour under (a) 20% oxygen gas in argon (b) 20% water vapor in argon and (c) 3% water vapor in hydrogen gas

3.1.1.3 Influence of nitrogen

In Figure 3.3, the photovoltammograms of pure chromium oxidized in oxygen gas dissolved in (a) argon and (b) nitrogen, are presented. It can be seen than the results are very similar, indicating that nitrogen has small effects on the properties of the layer

formed. Indeed, work reported in the literatures [4, 20] showed that nitrogen could be detected as traces at the metal/oxide interface but that no nitrogen could be detected within the oxide layer, owing to a low solubility of nitrogen in chromium oxide. Because of this, chromium transport is still the main defect for oxide growth and the oxide semiconducting behavior is not affected by the presence of nitrogen.

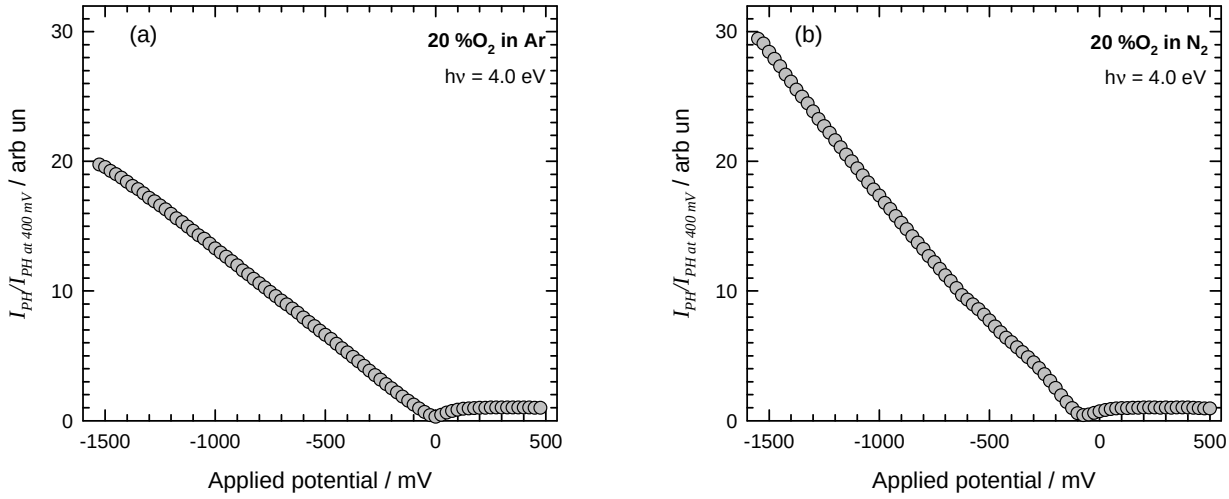

Figure 3.3 Photovoltammograms obtained for pure chromium oxidized at 800°C during 1 hour under (a) 20% oxygen gas in argon and (b) 20% oxygen gas in nitrogen gas

3.1.2 Bandgaps of the oxides formed

Bandgaps of semiconducting oxides can be evaluated from the photocurrent vs photon energy curves performed at a selected constant potential. When studying a single semiconductor, it is generally observed, as expected from the simplified Gärtner–Butler model, that the shape of photocurrent energy spectra remains unchanged when varying the applied potential. When dealing with samples constituted of multiple components, possibly of different semiconducting types, however, it may be anticipated that the shape of the photocurrent energy spectra will be potential dependent, due mainly to the consequences of differences in the flatband potentials of the components. For instance, changing the applied potential may increase the band bending (and the photocurrent) of one component whereas the contrary occurs for another one.

Thus, considering the results presented in the previous section, it was chosen to record photocurrent energy spectra at three potentials for each sample, i.e. in the cathodic range, around the minimum of photocurrent, and in the anodic range.

Figure 3.4 presents the corresponding photocurrent vs photon energy curves. It can be observed, as anticipated above, that the shapes of the spectra indeed strongly depend

on the applied potential. As expected for pure chromium oxide, all spectra exhibit very low photocurrents for photon energies less than 3.0 eV, likely to be attributed (to oxides of the trace impurities). Analyzing the spectra, it turns out that each of the latter exhibits the contributions to the photocurrents, considering in particular one of the spectra recorded near the minimum of photocurrent of the photovoltammograms. Indeed, these spectra exhibit a numerous of photocurrent near E = 3.8 eV. Again, if from thermodynamical point of view, only Cr_2O_3 is the stable oxide at high temperature [12], previous works in our team [10, 19, 21] and others [22–24] reported bandgaps values of Cr_2O_3 at both 3.0 eV and between 3.5 eV and 3.7 eV. Therefore the latter mentioned both two contributions could sign Cr_2O_3.

To try to assess roughly the bandgap values, E_g, the classical linear transform using the simplified form of Gärtner–Butler model [25–26] was applied to the photocurrent energy spectra, J_{PH}, using equation (3.1) (see Chapter 2),

$$\left(J_{PH} \cdot h\nu\right)^{1/2} = \text{const}\left(E_G - h\nu\right) \tag{3.1}$$

Note that J_{PH}, which presented on all photocurrent energy spectra and linear transform curves in this work, always refers to the modulus of J_{PH}.

Figure 3.5 shows the transformed spectra corresponding to the original spectra in Figure 3.4. A first bandgap value at around 3.0 $\pm$ 0.1 eV is easily found on each spectrum. The second bandgap however cannot easily be obtained on some spectra. Nevertheless the second bandgap at 3.8 eV is clearly indicated in Figure 3.5(a) at 0 mV and Figure 3.5(b) at –400 mV. However, the bandgap value assessed from the linear transform spectra does coincide with the 180° changes of dephasing angle (and thus the sign change of the photocurrent) in Figure 3.6(a) and (b) at this photon energy. When considering these results together with Figure 3.2, the first gap should correspond to n–type oxide whereas the second bandgap should correspond to p–type. In the other spectra, the difficulty to find bandgap still remains because there are no significant phase changes and the overall photocurrent does not change its sign. In those cases, the second bandgap can be estimated from the intercept of the first and the second linear lines. Tough the bandgap of Cr_2O_3 obtained from the linear transforms presented some dependence on the applied potential, it can be concluded that the oxidized pure chromium samples exhibited two constituents of Cr_2O_3 with bandgap 3.0 eV and 3.3–3.8 eV. Further work will deal with trying to fit the spectra of Figure 3.5 with the novel model developed in our team and whose application was focused on the modern alloys samples in Chapter 4. A more precise bandgap determination is expected from these fits, and hopefully more insights as concerns the semiconducting types.

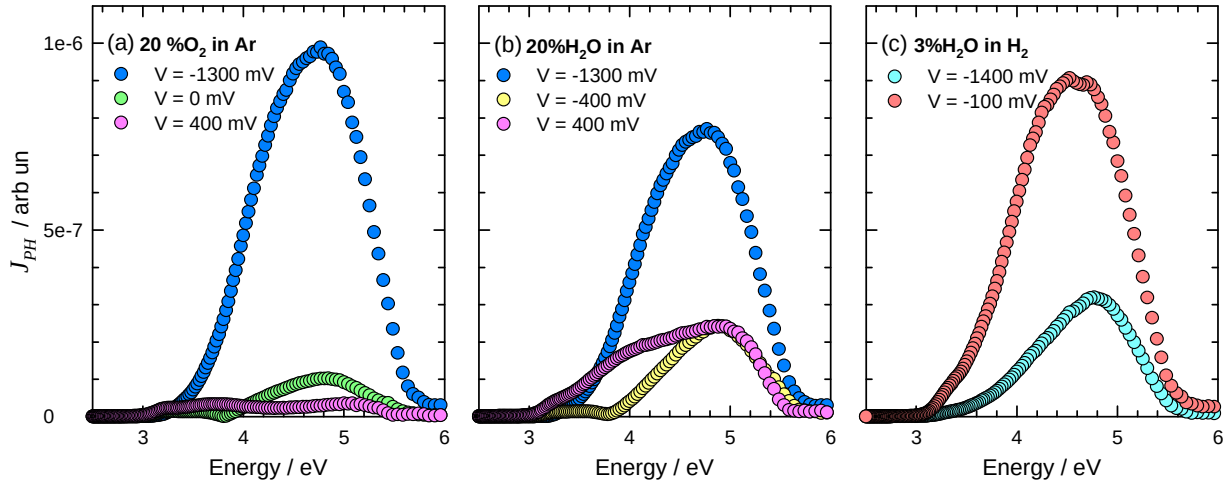

Figure 3.4 Photocurrent vs photon energy curves obtained at various applied potentials for pure chromium oxidized at 800°C for 1 hour under (a) 20% oxygen gas in argon (b) 20% water vapor in argon and (c) 3% water vapor in hydrogen gas

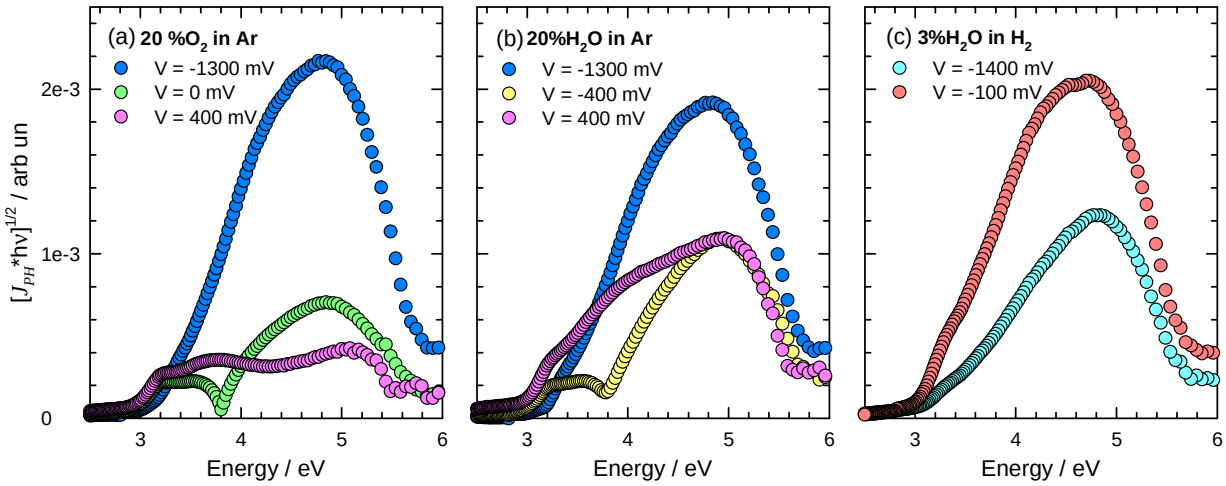

Figure 3.5 Linear transform spectra corresponded with photocurrent vs photon energy spectra in Figure 3.4

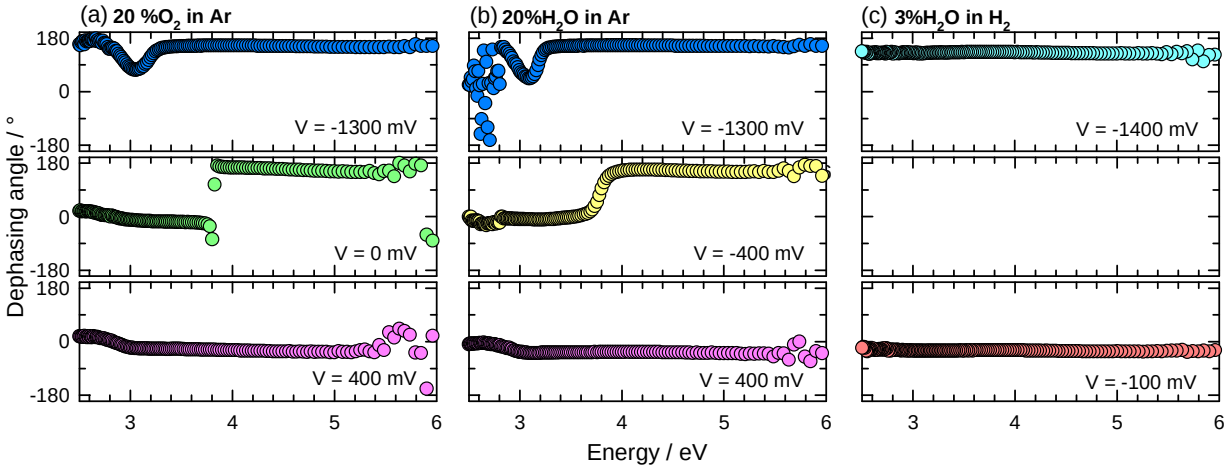

Figure 3.6 Dephasing angle corresponded with photocurrent vs photon energy spectra in Figure 3.4

3.2 $Fe_{2-x}Cr_xO_3$ solid solutions

In this section, corundum solid solution (or hematite chromia solid solutions), $Fe_{2-x}Cr_xO_3$, were prepared from powders by solid–state reaction, the presence and nature of oxide phases were identified by the conventional techniques as XRD and Raman spectroscopy while their electronic properties were checked by photoelectrochemical experiment. The optimal conditions, to obtain the desired solid solution, were first trialed on powders. Then, the mixed oxides were formed as circular pellets, and densified to obtain the samples suitable for photoelectrochemical characterizations.

3.2.1 Preparation of $Fe_{2-x}Cr_xO_3$ powder

$Fe_{2-x}Cr_xO_3$ powder was prepared by mixing the adequate mole fractions of hematite (Fe_2O_3) and chromia (Cr_2O_3) powders in a ball milling machine. The mixed powder was then allowed to react under air at 1100°C during 25 hours and/or 100 hours to check the completion of the solid state reaction. The tested x–values of $Fe_{2-x}Cr_xO_3$ were: 0.0, 0.4, 0.8, 1.0, 1.2, 1.3, 1.6, and 2.0.

The oxide phases presented in the mixtures obtained after ball milling were analyzed before high temperature reaction by XRD and Raman spectroscopy. An example of the results is given here for the case of a Fe_2O_3:Cr_2O_3 ratio equal to 2:3. Figures 3.7(a) and (c) shows diffractograms of pure Fe_2O_3 and Cr_2O_3 powder respectively: the patterns are very similar (but slightly differ in 2–theta) because the ionic radii of Fe^{3+} and Cr^{3+} are quite close and both oxides form in the same structure. Figure 3.7(b) shows the mixed patterns between Fe_2O_3 and Cr_2O_3, no other constituent is detected in the mixture.

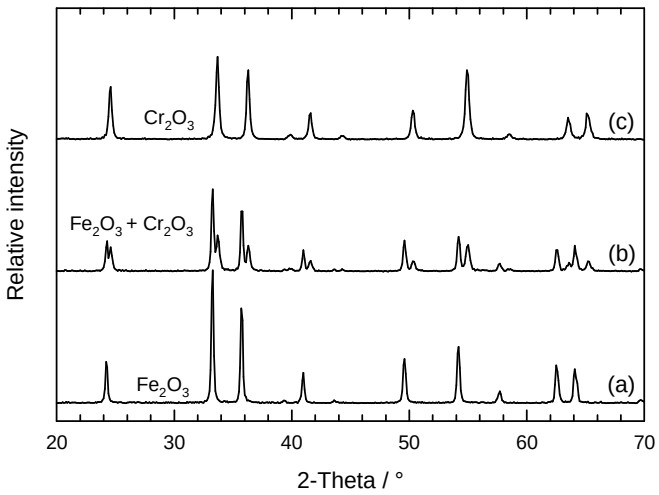

Figure 3.7 XRD patterns obtained from powders of (a) Fe_2O_3 (b) a mixture of Fe_2O_3:Cr_2O_3 at a 2:3 ratio and (c) Cr_2O_3

Raman spectra in Figure 3.8(a) exhibit the very strong characteristic peaks of hematite at 219.9 cm^{-1} and 284.9 cm^{-1} [27–31] whereas Figure 3.8(c) shows the sharp characteristic peak of chromia at 551.8 cm^{-1} [29–32]. Again, only peaks present in the spectra of Cr_2O_3 and Fe_2O_3 are observed in the spectrum of the mixture (Figure 3.8(b)).

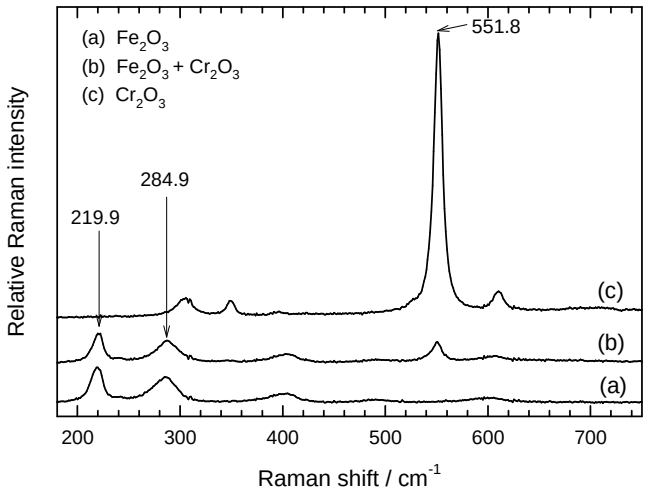

Figure 3.8 Raman spectra obtained from powders of (a) Fe_2O_3 (b) a mixture of Fe_2O_3:Cr_2O_3 at a 2:3 ratio and (c) Cr_2O_3

After sintering at 1100°C, the mixed powders were analyzed again to check whether the original oxides remained present or the solid state reaction was complete. Figure 3.10 shows XRD patterns of hematite chromia mixture at 2:3 ratios before (a) and after reaction time of 25 hours (b) and 100 hours (c). After heat treatment of the mixed powder, the patterns of both Fe_2O_3 and Cr_2O_3 vanished and replaced by the new pattern, similar to the original patterns but differing in 2–theta values, the diffraction peak angles being locate between the ones of the peaks of the material powders, as expected. From the diffractograms in Figure 3.9(b) and (c), it seems that the reaction was complete for both tested reaction times.

Figure 3.10 presents Raman spectroscopy results of the same mixed oxide before and after reaction. Peak shifts at more than 660 cm^{-1}, which correspond to the corundum solid solution phase [30], appear on spectra after sintering for 25 hours and for 100 hours (Figure 3.10(b) and (c)). However, Raman spectra revealed that 25 hours is an insufficient reaction time because some peaks of the original oxides still are presented. On the contrary, after 100 hours heat treatment, all strong peaks of original powders disappeared and only the Raman peak at 671 cm^{-1} of $Fe_{2-x}Cr_xO_3$ was presented.

From the above results, we concluded that the perfect solid solution, $Fe_{2-x}Cr_xO_3$, could be reasonably obtained by solid state reaction at 1100°C with 100 hours reaction time.

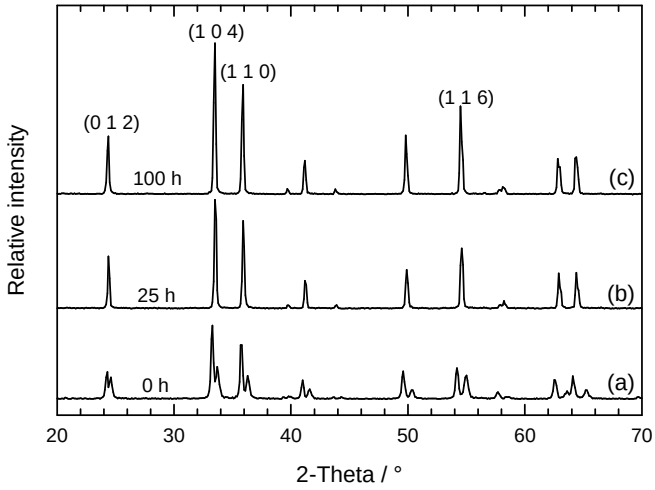

Figure 3.9 XRD patterns obtained from a mixture of Fe_2O_3 and Cr_2O_3 at the 2:3 ratio after (a) ball milling (b) 25 hours reaction time (c) 100 hours reaction time

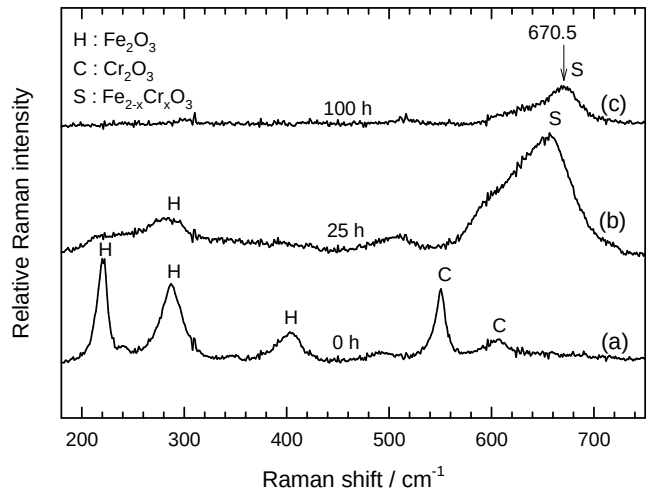

Figure 3.10 Raman spectra of Fe_2O_3 mixed with Cr_2O_3 in 2:3 ratios after (a) ball milling (b) 25 hours and (c) 100 hours reaction time

3.2.2 Correlation between x–value of $Fe_{2-x}Cr_xO_3$ and its lattice spacing

The correlation between the x–value of $Fe_{2-x}Cr_xO_3$ and the lattice spacings, d_{hkl}–spacings, was studied on the $Fe_{2-x}Cr_xO_3$ samples after 100 hours reaction time. Two main plans with high intensities on the diffractograms, (1 0 4) and (1 1 0), were chosen to run fine scans in the 32.5° to 37.5° range. Figure 3.11 shows diffractograms of the $Fe_{2-x}Cr_xO_3$ sample at various x–values, exhibiting higher 2–theta values at higher x–values. Conversely, d_{hkl}–spacings decreased with increasing x–values, according to Bragg's law.

It is also observed that our experimental data are close to the ones of JCPDS database. However, on both cases, the data do not exactly fit with a linear relation between x–values of $Fe_{2-x}Cr_xO_3$ and lattice spacing as predicted by Vegard's law though the fit could be

considered as reasonable for the (1 0 4) plane. The non–Vegardian behavior might be affected from the distortion of lattice spacing by the substitution of hematite with chromia (the replacement of Fe^{3+} with Cr^{3+}) [33], or by cation ordering and specific interactions between cations such as magnetic [34].

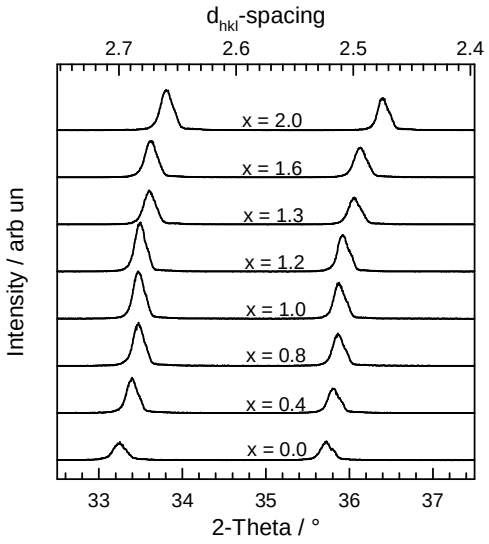

Figure 3.11 Fine–scanned XRD patterns obtained from $Fe_{2-x}Cr_xO_3$ powder at various chromium contents (x–values)

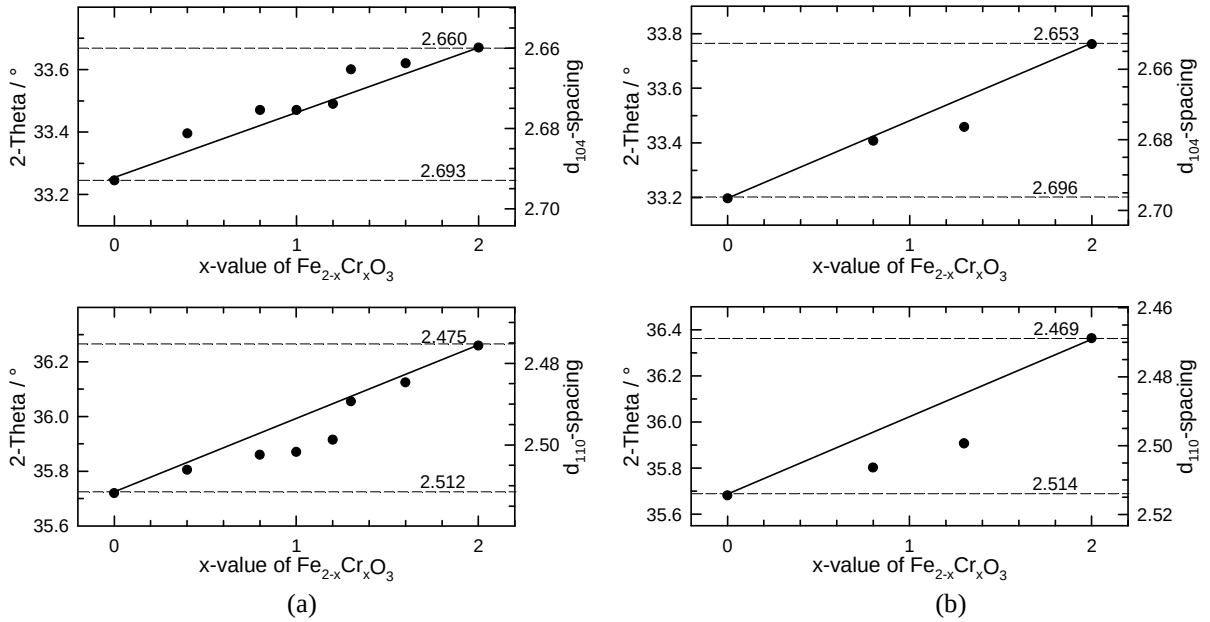

Figure 3.12 Correlation of 2–theta and d–spacings with the x–value of $Fe_{2-x}Cr_xO_3$, from (a) experimental values and (b) JCPDS database; the upper and lower plots correspond respectively to (1 0 4) and (1 1 0) planes

3.2.3 Correlation between x–value of $Fe_{2-x}Cr_xO_3$ and Raman shift

Typical Raman spectra of $Fe_{2-x}Cr_xO_3$ at x–value equals 0.0, 0.8, 1.2, and 2.0 are presented in Figure 3.13. The Raman shift of the characteristic peak of $Fe_{2-x}Cr_xO_3$ above 660 cm^{-1} was plotted as a function of the x–value (Figure 3.14). A linear correlation is obtained in the range x = 0.4 to x = 1.6, the Raman shift varying from 663.6 cm^{-1} up to 678.7 cm^{-1}. Our results seem to confirm, more accurately, the ones obtained previously by McCarty and coworkers [29]. So, we can conclude that it will be possible, from Raman spectra, to assess the x–value in $Fe_{2-x}Cr_xO_3$ solid solutions formed in oxidation layers of alloys.

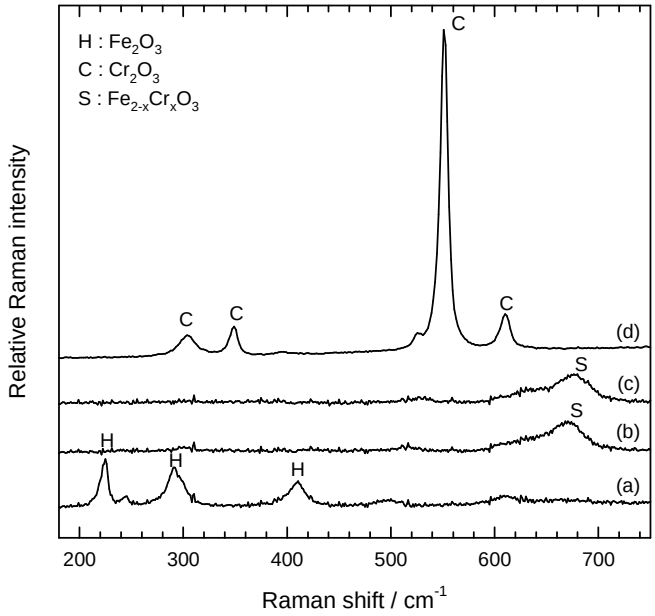

Figure 3.13 Typical Raman spectra obtained from (a) Fe_2O_3, x = 0.0, (b) and (c) $Fe_{2-x}Cr_xO_3$ at x= 0.8 and 1.2, and (d) Cr_2O_3, x = 2.0

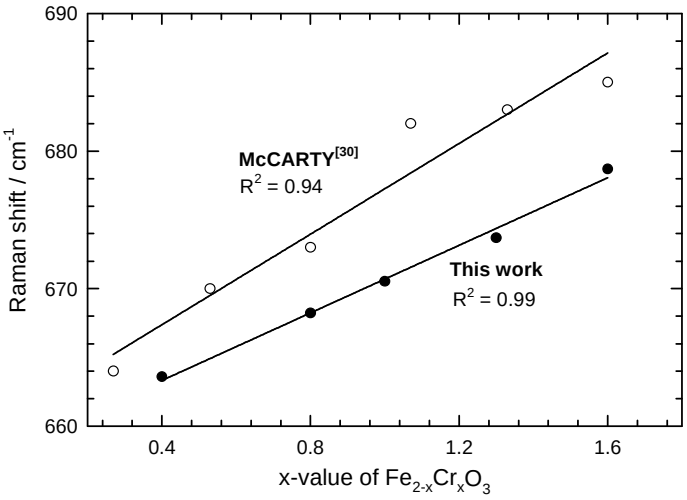

Figure 3.14 Shifts of the Raman main peak of $Fe_{2-x}Cr_xO_3$ as a function of the x–value

3.2.4 Semiconducting behavior of Fe_2O_3, Cr_2O_3, and $Fe_{2-x}Cr_xO_3$

Photoelectrochemical experiments were performed to investigate the semiconducting behavior of the solid solution samples, which were prepared as dense pellets.

3.2.4.1 Sample preparation

A diagram summarizing the procedure used to form these pellets is given in Figure 3.15. A green pellet of mixed powders with 10 mm diameter and 2 mm thickness was performed by hydraulic uniaxial pressing, and then was pressed at 300 MPa by cold isostatic pressing (CIP). After that, the green pellets were sintered at 1350°C for 20 hours to achieve the densification, and then hold at 1100°C for 100 hours to obtain complete solid state reaction in agreement with the above described previous experiments. The sintered pellet was then tested as concerns its resistance to electrolyte by visually inspecting the outcome of an electrolyte droplet deposited on the sample. From these trials, it turned out that dense pellets could only be obtained at x–value equal or less than 1.0, likely to be due to the very high melting point of chromia (about 2435°C) [35]. It is well–known that chromia has poor sinterability in air and requires special sintering conditions such as temperatures higher than 1600°C and reduced pressures to achieve high density ceramics.

Figure 3.16(a) and (b) show optical micrographs of pellet after sintering at 1350°C for 20 hours and x–values equaled 0.0 and 1.0 respectively. A dense pellet of pure hematite without any pore is evidenced in Figure 3.16(a). Since hematite has a low melting point (about 1565°C) [35] and the sintering temperature approached the melting point, so the necking and growing of the grains was easier at higher hematite fraction. In Figure 3.16(b), necking and grain growth could be observed but a part of porosity remains. Finally, an ohmic contact was applied on one side of the pellets using InGa eutectic and Ag paste. PEC characterization could perform on solid solution which x–values equal 0.0, 0.4, and 1.0.

In the following, photoelectrochemical studies of samples with x–values 0, 0.4, 1.0, and 2, will be presented. The sample corresponding to x = 2 (pure chromia) was obtained from TISTR (Thailand Institute of Scientific and Technology). It was prepared by hot isostatic pressing (HIP) at 1500°C 60 MPa for 2 hours. The pellet density was 87% of the theoretical density, but the penetration of the electrolyte was sufficiently slow to allow to record photocurrent energy spectrum before the electrolyte reached the ohmic back contact.

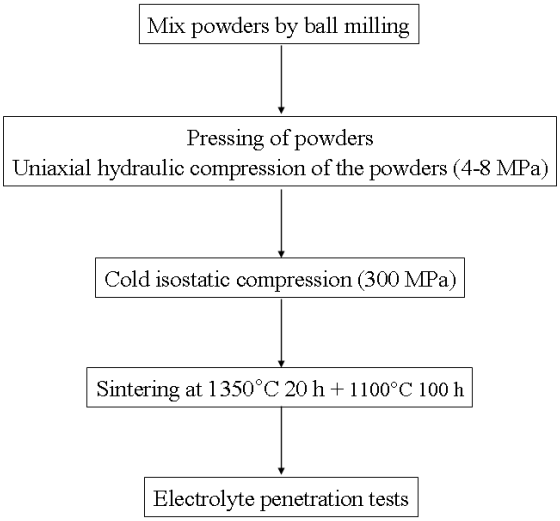

Figure 3.15 Diagram of the procedure used for forming pellets

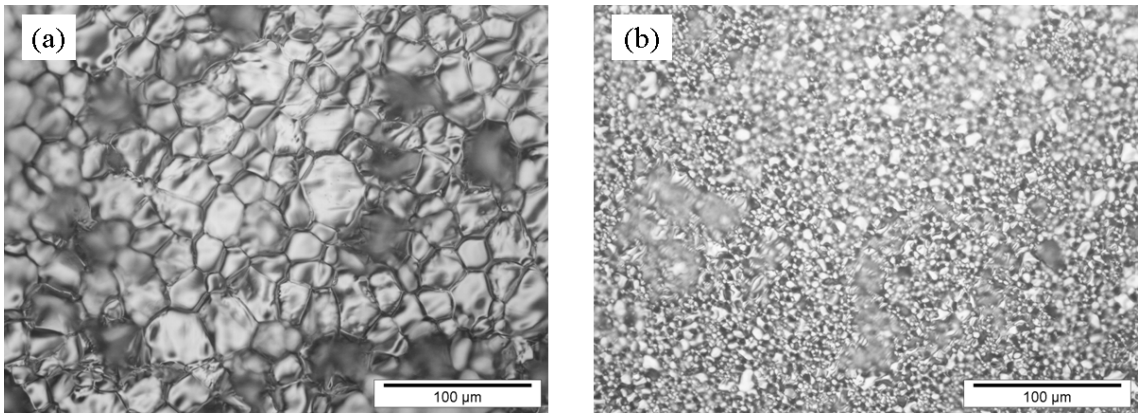

Figure 3.16 Optical micrographs of a pellet after sintering at 1350°C 20 hours obtained for $Fe_{2-x}Cr_xO_3$ (a) x = 0.0, and (b) x = 1.0

3.2.4.2 Photoelectrochemical characterizations

Samples with x = 0.0

Figure 3.18 presents, for the "hematite" pellet, *i.e.* the sample corresponding to x = 0.0, a photocurrent energy spectrum (Figure 3.17(a)) and its linear transform (Figure 3.17(b)). Only very low photocurrents could be obtained in the experimental conditions used for the recording of the spectrum, and the signal to noise ratio is poor. Nevertheless, a bandgap of 2.2 ± 0.1 eV may be assessed from the linear transform considering the linear part evidenced in Figure 3.17(b). Such a bandgap is in agreement with the values usually reported for Fe_2O_3 (from 1.9 to 2.3 eV).

However, when considering the values of the phase shifts of the photocurrents, or the spectra of the real and imaginary parts of the photocurrents (Figure 3.17(c)), it appears, by comparison to the ones obtained for a "model" p–type semiconductor such as p–GaP, it appears that the measured photocurrents of the x=0.0 sample are cathodic.

Moreover, using the 351 nm (3.53 eV) line of an argon laser as the light source, it was possible to measure directly the sign of the photocurrent by assessing the difference between the electrochemical currents, I_{stat}, measured both in dark and light conditions, as illustrated in Figure 3.17(d), and the photocurrent sign indeed was found negative. These observations are not in agreement with the usually reported n–type semiconduction of hematite [36–37]; they reveal either a p–type behavior, very surprising for Fe_2O_3, but usually reported for FeO (bandgap 2.3–2.4 eV [38], or perhaps a nearly Fe_2O_3 insulating sample which could exhibit both cathodic and anodic photocurrent depending on the applied potential.

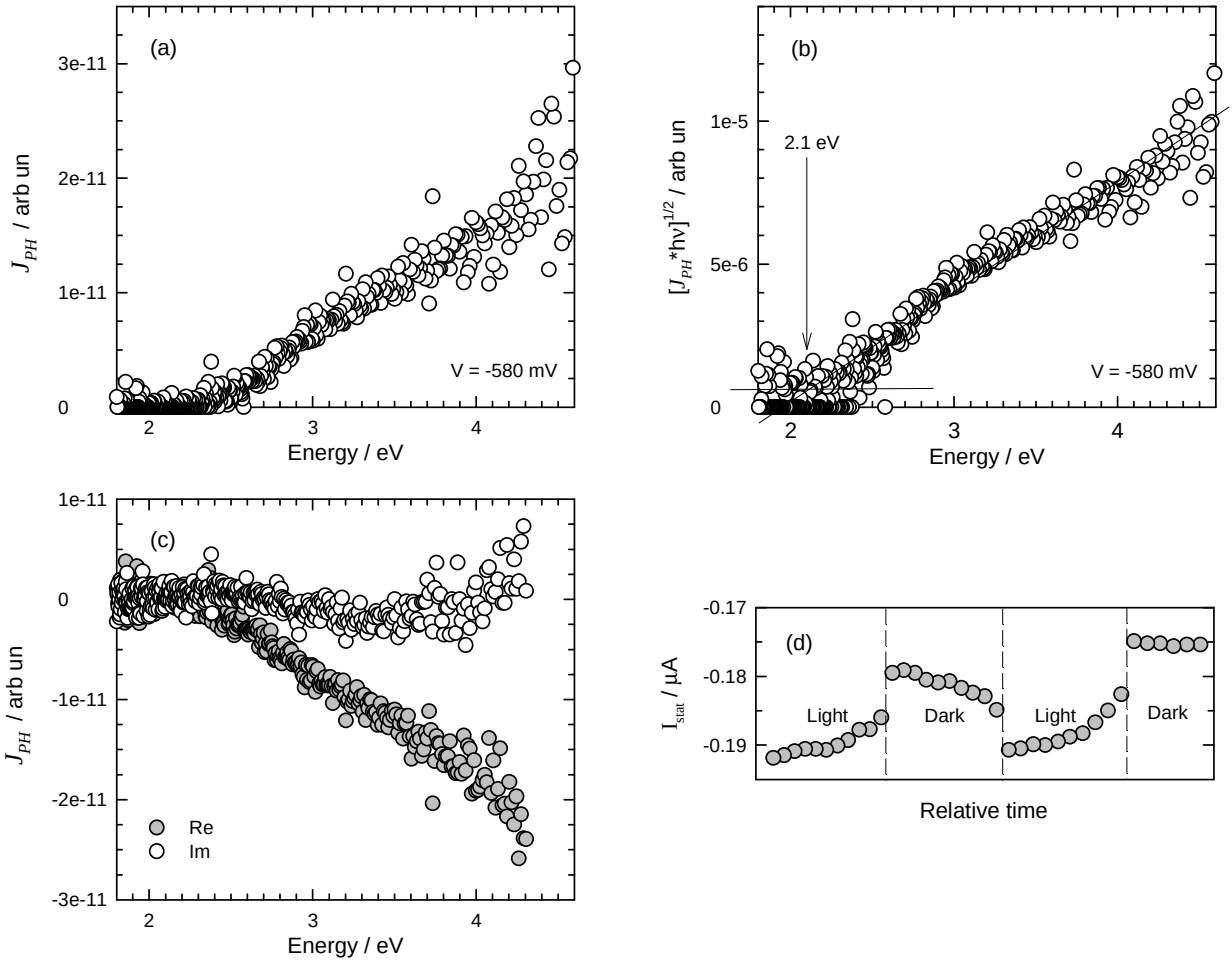

Figure 3.17 (a) Photocurrent vs photon energy, (b) Linear transform of data in (a), (c) the real (Re) and imaginary (Im) part of photocurrent in (a), and (d) the stationary current obtained under illuminated light (light) and non–illuminated (dark) condition for a pure hematite (x = 0.0) pellet

Samples with x = 2.0

Figure 3.18 presents, for the TISTR chromia pellet (x = 2.0), a photocurrent energy spectrum (Figure 3.18(a)) and its linear transform (Figure 3.18(b)); similar results were obtained when studying the chromia pellet provided by CEA Saclay. From the corresponding data, a bandgap of 3.1 ± 0.1 eV may be estimated for this sample, in

agreement with values reported in the literature for chromia [10, 19, 21]. The phase shifts or the spectra of the real and imaginary parts of the photocurrents (Figure 3.18(c)), compared to results obtained on a typical n–type semiconductor such as n–TiO_2, as well as the positive sign of the photocurrent allow to conclude that the x = 2.0 sample is n–type. Although the more often reported p–type behavior of Cr_2O_3 was expected, an n–type behavior indeed is possible (Cr_2O_3 is an amphoteric oxide [15]) and already were reported with a 3.0 eV bandgap in oxide layers grown on high temperature alloys [19, 21].

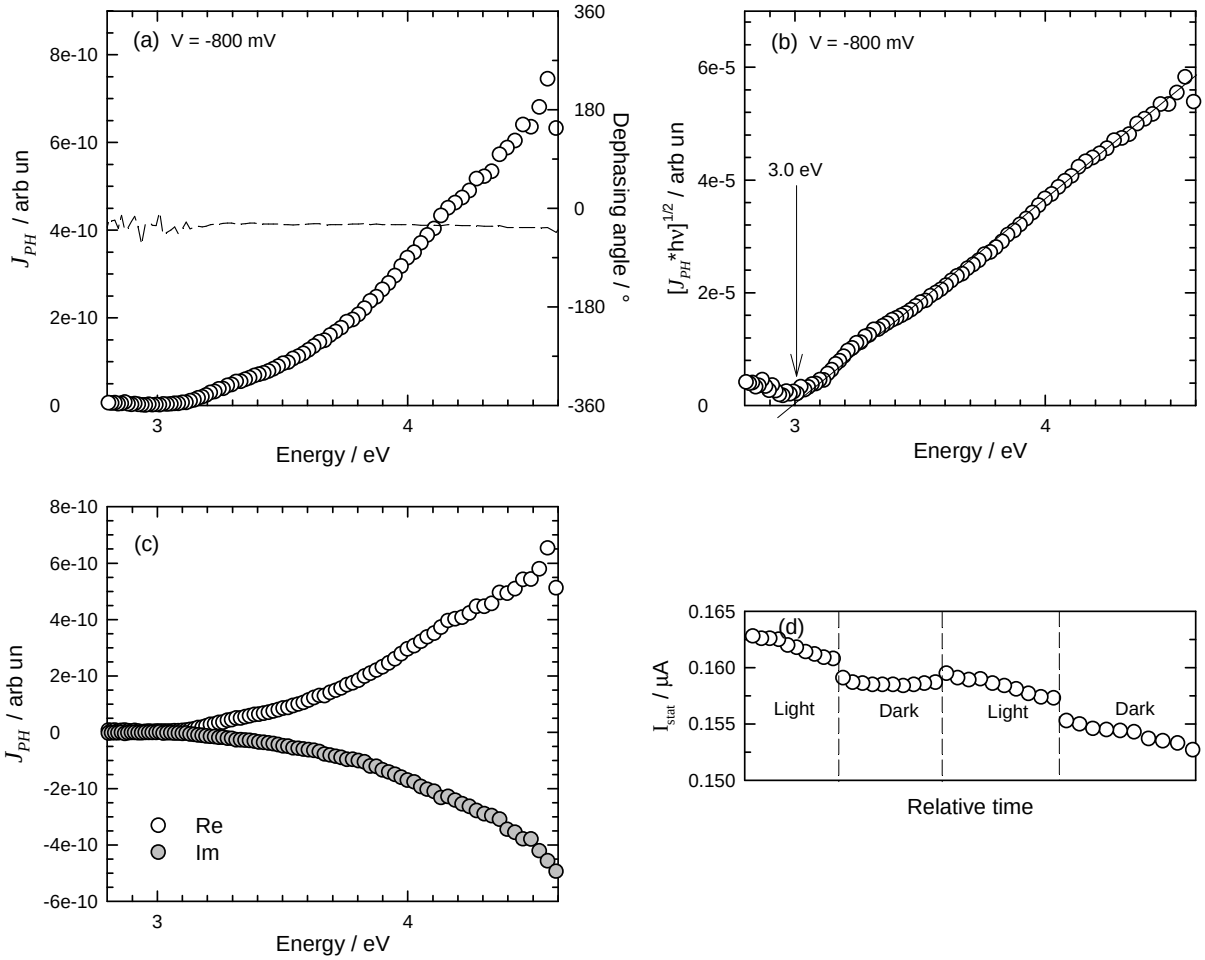

Figure 3.18 (a) Photocurrent vs photon energy in white circle and its dephasing angle (phase shift) in dashed line, (b) Linear transform of data in (a), (c) the real (Re) and imaginary (Im) part of photocurrent in (a), and (d) the stationary current obtained under illuminated light (light) and non–illuminated (dark) condition for a pure chromia (x = 2.0) pellet

Samples with x = 0.4 and x = 1.0

As concerns the x = 0.4 and x = 1.0 samples, their photocurrent energy spectra are presented in Figures 3.19(a) and 3.20(a) respectively, together with their linear transforms (Figures 3.20(b) and 3.21(b)). Analyzing these curves, it is clear on the one hand that the energy onset of the photocurrent is around 2 eV, indicating that the samples do still contain iron oxide, contrary to what was expected from the XRD and Raman characterizations

presented in the previous section for powders. On the other hand, slopes changes may be observed in the spectra and in their linear transforms:

- around 2.6 eV and between 3.0 eV and 3.5 eV for x = 0.4,
- around 2.8–2.9 eV and between 3.0 eV and 3.5 eV for x = 1.0.

These slopes changes are attributed to additional contributions to the photocurrents issuing from compounds having bandgaps close to these energy values. The values below 2.9 eV are likely to be attributed to the $Fe_{2-x}Cr_xO_3$ solid solutions, whose bandgaps are expected to be in–between the bandgaps of iron oxide and chromium oxide. The slope changes above 3.0 eV should correspond to photocurrents issued from residual chromia, which should also be present if iron oxide is present.

The sign of the photocurrent is negative for both samples, as evidenced in Figure 3.21. This suggests an overall p–type behavior of both samples. The latter conclusion is reinforced by the shapes of the photocurrent vs potential curves recorded on the samples and shown in Figures 3.22 (x = 0.4) and 3.23 (x = 1.0). It also can be understood if one considers that the x = 0.0 and x = 2.0 samples were found respectively p–type and n–type, and that the x = 0.4 and x = 1.0 samples correspond to iron/chromium ratio higher than or equal to 1.

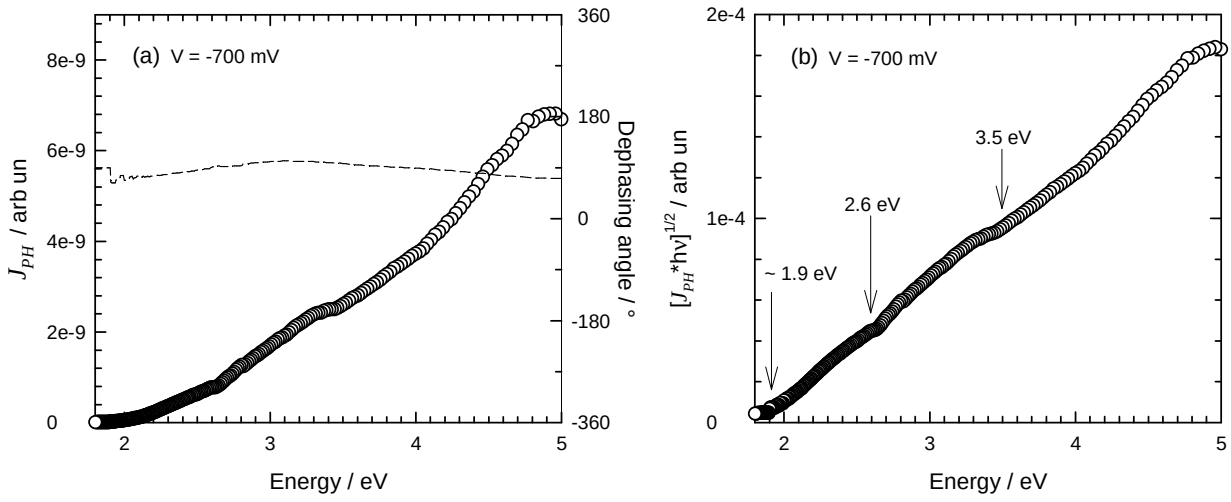

Figure 3.19 (a) Photocurrent vs photon energy and its dephasing angle in dashed line, and (b) Linear transform of data in (a) for a solid solution $Fe_{2-x}Cr_xO_3$ pellet at x = 0.4

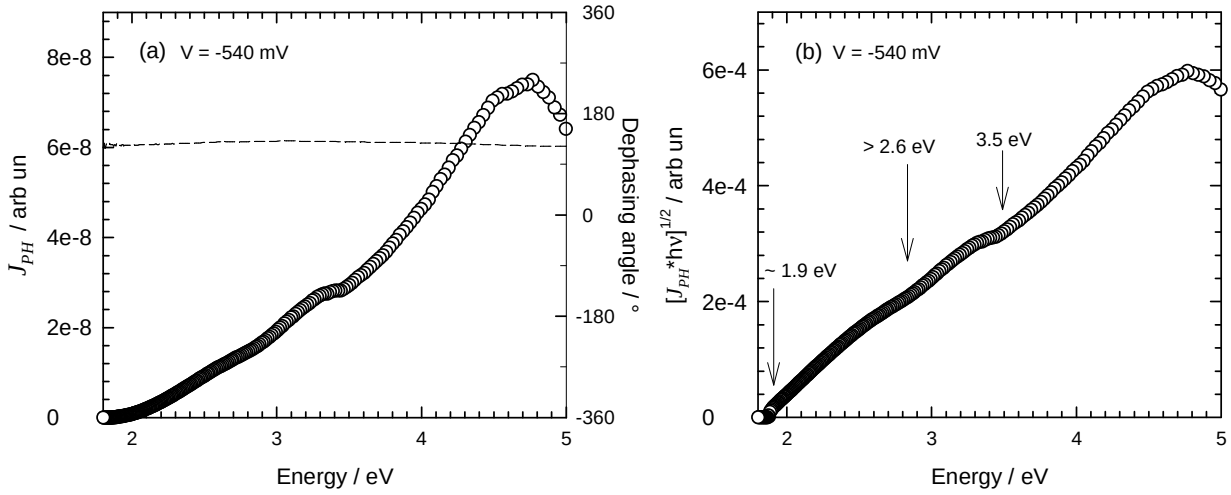

Figure 3.20 (a) Photocurrent vs photon energy and its dephasing angle in dashed line, and (b) Linear transform of data in (a) for a solid solution $Fe_{2-x}Cr_xO_3$ pellet at x = 1.0

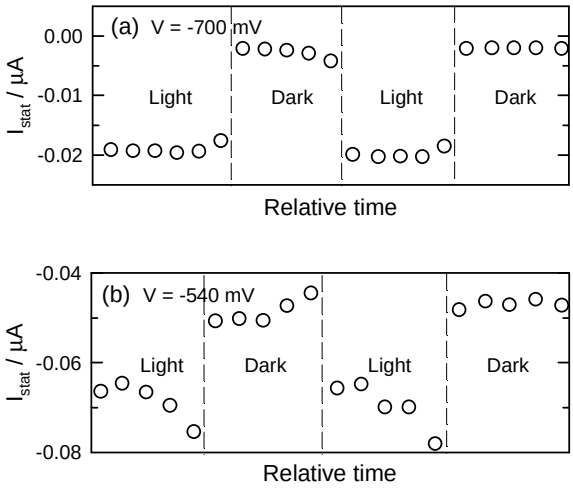

Figure 3.21 The stationary current obtained under illuminated (light) and non–illuminated (dark) condition; (a) x = 0.4, and (b) x = 1.0

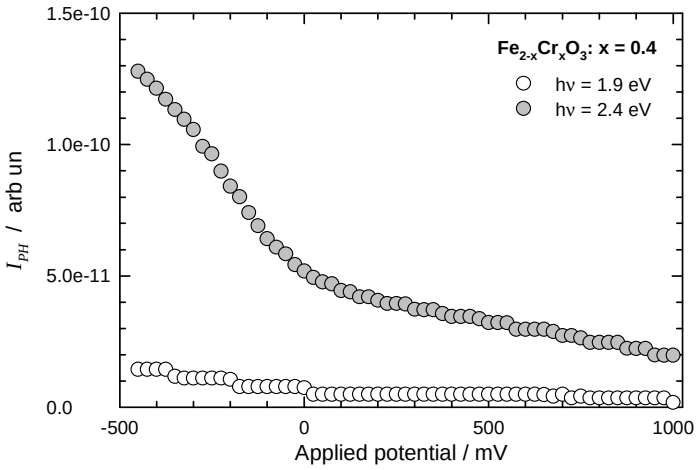

Figure 3.22 Photovoltammograms obtained on solid solution $Fe_{2-x}Cr_xO_3$ pellet with x = 0.4

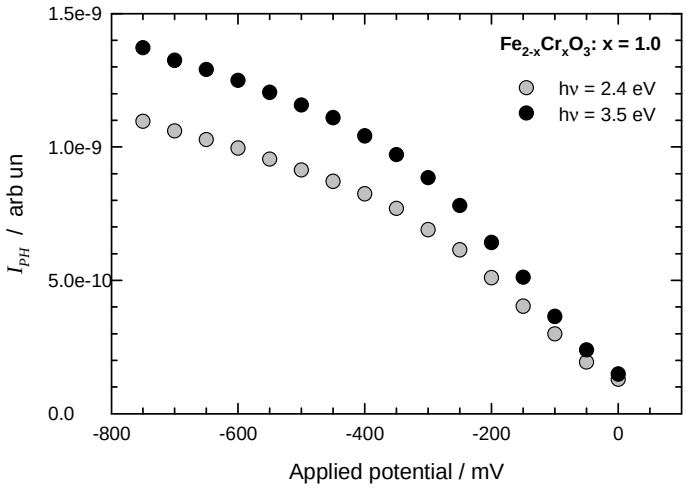

Figure 3.23 Photovoltammograms obtained on solid solution $Fe_{2-x}Cr_xO_3$ pellet with x = 1.0

To confirm or infirm the presence of iron oxides and chromia in the x = 0.4 and x = 1.0 pellets, complementary XRD and Raman characterizations of the latter samples were performed. Figures 3.24(a) and (b) present the corresponding XRD and Raman spectra of the pellets. From the diffractograms (Figure 3.24(a)), no other component as the iron/chromium solid solution may be evidenced. On the other hand, the Raman spectra in Figure 3.24(b) indeed show that Fe_2O_3 still present in the pellets, but no Cr_2O_3 evidence is found. However, it should be recalled that photoelectrochemical techniques often proved to be highly sensitive to minority components in oxidation layers [21].

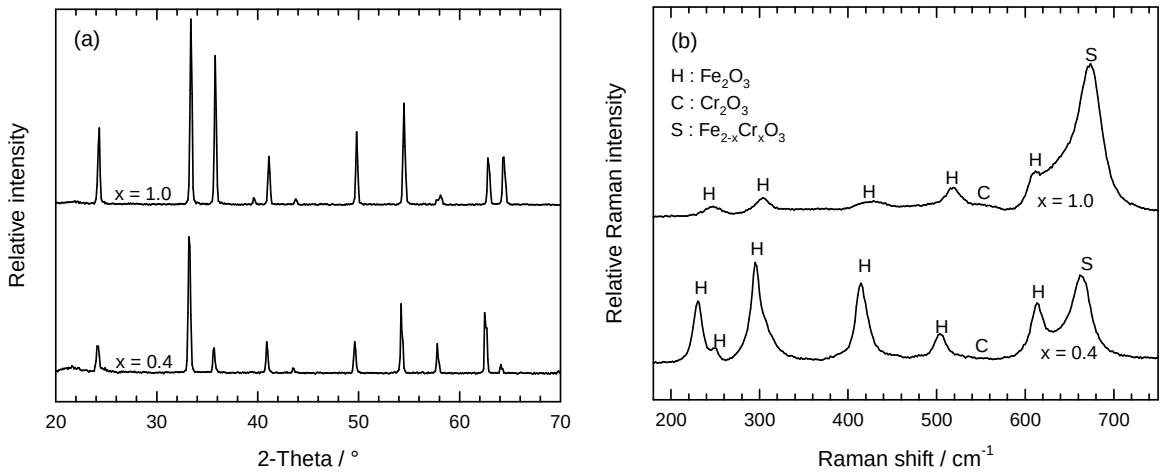

Figure 3.24 (a) Diffractograms and (b) Raman spectra obtained from $Fe_{2-x}Cr_xO_3$ pellet at various x–values

3.2.4.3 Bandgaps of $Fe_{2-x}Cr_xO_3$

Table 3.1 summarizes the results obtained by the photoelectrochemical study of the $Fe_{2-x}Cr_xO_3$ pellets elaborated in our work.

Even if the experiments did not allow to reach the initial goal, i.e. to establish a PEC database for $Fe_{2-x}Cr_xO_3$ compounds (type of semiconduction, bandgap value) because of the difficulty to prepare pellets of perfect and dense solid oxide solutions, the effect of the stoichiometry of $Fe_{2-x}Cr_xO_3$ on its bandgap energy could be roughly observed: the sample with the higher chromium content in $Fe_{2-x}Cr_xO_3$ (x = 1.0) appears to exhibit an higher bandgap value (around 2.8–2.9 eV) than the one (about 2.6 eV) of the sample with the lower chromium content (x = 0.4).

Following the literature [38–40], bandgap values may be estimated from thermodynamic extensive atomic data. It is proposed that the bandgap energies of a $Fe_{2-x}Cr_xO_3$ solid solution could be given by the following simple equation:

$$(2\text{-}x)\cdot E_G^{Fe_2O_3} + (x)\cdot E_G^{Cr_2O_3} = 2\cdot E_G^{Fe_{2\text{-}x}Cr_xO_3} \qquad (3.2)$$

Trying to test this equation on the results obtained in this work is difficult. First, due to the presence of iron oxide and likely of chromia in the $Fe_{2-x}Cr_xO_3$ samples, the determination of the bandgaps of these samples were quite approximated. Second, the bandgaps of the iron oxide (Fe_2O_3?) and of Cr_2O_3 were measured at 2.1 and 3.1 eV when the characterization was done on the pure pellet. But these values changed to 1.9 eV and 3.5 eV when the assessment was made from the PES of the mixed oxide pellets. Therefore the calculations were made for the two sets of bandgap values, and the results are presented in Table 3.2, together with the approximative experimental values.

Table 3.1 Summary of PEC studied on pellet

x–values of $Fe_{2-x}Cr_xO_3$	0.0	0.4	1.0	2.0*	2.0**
Bandgap (eV)	2.1	1.9 / 2.6 / 3.5	1.9 / 2.8–2.9 / 3.5	3.0	3.2
Semiconducting type	n.d.	p	p	n	n.d.

* pure chromia pellet performed at TISTR * CEA's pure chromia pellet n.d. is no data

Table 3.2 Summary of bandgaps of solid solution pellet

x–values of $Fe_{2-x}Cr_xO_3$		0.4	1.0
Experimental values		2.6	2.8–2.9
Calculation values	$E_G^{Fe_2O_3} = 2.1$, $E_G^{Cr_2O_3} = 3.1$	2.3	2.6
	$E_G^{Fe_2O_3} = 1.9$, $E_G^{Cr_2O_3} = 3.5$	2.22	2.7

3.3 Conclusions

The characteristic of chromia and its solid solution observed from both pure chromium metal and hematite–chromia solid solution experiments can be concluded as follows:

Chromia with n–semiconducting behavior obtained from powder sample indicated bandgap at around 3.0 eV whereas chromia generated on pure chromium metal showed two bandgaps relying on their microstructure which the one coincided with the powder while another alternated one was at 3.3-3.8 eV. From all above experiments, chromia at both bandgap seemed to be an insulator which inclined to be more either n– or p–type semiconducting depending on the original conditions. The presence of water vapor and/or hydrogen in oxidation atmosphere tended to promote n–type chromia owing to OH^- and H atom. At high oxygen partial pressure, chromia generally inclined to behave p–type due to oxygen interstitial.

The bandgap of pure hematite pellet was indicated at around 2.1 eV whereas the bandgap of hematite declines to 1.9 eV where it was in the mixed oxides (Fe_2O_3–$Fe_{2-x}Cr_xO_3$–Cr_2O_3) system. The anomalous results that pointed the p-hematite (it was often reported to be n-type oxide) could not image apart from either phase change or contamination but XRD and Raman spectroscopy indicated the phase of hematite, so, it was an ambiguous point for these experiments.

The mixed oxide pellets showed the dependence of chromium mole fraction on the bandgap of $Fe_{2-x}Cr_xO_3$. Since the pure $Fe_{2-x}Cr_xO_3$ did not obtain on pellets, the exact bandgap value could not be provided, however, it could be estimated using thermodynamics assumption.

REFERENCES

[1] I. V. Oryshich, N. E. Poryadchenko, I. G. Slys', N. P. Brodnikovskii, and A. V. Golovash, Air oxidation of chromium–based composites, *Powder Metallurgy and Metal Ceramics* **46** (3–4) (2007) 189–193.

[2] K. Shanker and P. H. Holloway, Atmospheric oxidation of chromium between 270 and 490°C, *Thin Solid Films* **105** (1983) 293–303.

[3] E.I. Alessandrini and V. Brusic, Effect of varying oxidizing and nitriding parameters on the surface of Cr thin films, J. *Vac. Sci. Technol. Journal of Vacuum Science and Technology* **9** (1) (1972) 83–86.

[4] Y. P. Jacob, V. A. C. Haanappel, M. F. Stroosnijder, H. Buscail, P. Fielitz, and G. Borchardt, The effect of gas composition on the isothermal oxidation behavior of PM chromium, *Corrosion Science* **44** (2002) 2027–2039.

[5] K.P. Lillerud and P. Kofstad, On high temperature oxidation of Chromium I. Oxidation of annealed, thermally etched chromium at 800°–1100°C, *J. Electrochem. Soc. Journal of The Electrochemical Society* **127** (11) (1980) 2397–2410.

[6] P. Kofstad and K.P. Lillerud, On high temperature oxidation of Chromium II. Properties of and the oxidation mechanism of chromium, *J. Electrochem. Soc.* **127** (11) (1980) 2410–2419.

[7] Y. Shu, F. Wang, and W. Wu, Corrosion behavior of pure Cr with a solid NaCl deposit in O_2 plus water vapor, *Oxidation of Metals* **54** (5/6) (2000) 457–471.

[8] J. Mougin, N. Rosman, G. Lucazeau, and A. Galerie, In situ Raman monitoring of chromium oxide scale, *J. Raman Spectrosc. Journal of Raman Spectroscopy* **32** (2001) 739–744.

[9] M. Michalik, M. Hänsel, J. Zurek, L. Singheiser, and W. J. Quadakkers, Effect of water vapour on growth and adherence of chromia scales formed on Cr in high and low pO_2–environments at 1000 and 1050°C, *Microscopy of Oxidation* (2001) 39–47.

[10] S. Henry, J. Mougin, Y. Wouters, J.–P. Petit, and A. Galerie, Characterization of chromia scales grown on pure chromium in different oxidizing atmospheres, *Microscopy of Oxidation* (2000) 231–234.

[11] E. A. Polman, T. Fransen, and P.J. Gellings, Oxidation kinetics of chromium and morphological phenomena, *Oxidation of Metals* **32** (5/6) (1989) 433–447.

[12] P. Kofstad, *High temperature corrosion*, London and New York: Elsevier applied science, 1988.

[13] P. Sarrazin, A. Galerie, J. Fouletier, *Mechanisms of high temperature corrosion a kinetic approach*, Zuerich: Trans Tech Publications Ltd, 2008.

[14] D. J. Young, *High temperature oxidation and corrosion of metals*, Oxford: Elsevier Ltd., 2008.

[15] ASM International Handbook Committee, *Metals Handbook Ninth Edition Volume 13, Corrosion*, Park (Ohio): ASM International, 1987.

[16] T. Norby, The influence of hydrogen defects on transport properties of oxides, *Advances in Ceramics* **23** (1987) 107.

[17] N. Bonanos, Oxide–based protonic conductors: point defects and transport properties, *Solid State Ionics* **145** (2001) 265–274.

[18] P. Kofstad, Defects and transport properties of metal oxides, *Oxidation of Metals* **44** (1/2) (1995) 3–27.

[19] Y. Wouters, A. Galerie, J–P. Petit, Photoelectrochemical characterisation of chromia scales thermally grown on various metal substrates, *Material Science Forum* **595–598** (2008) 1181–1188.

[20] C. Brunner, H. Hutter, P. Wilhartitz, and M. Grasserbauer, Investigation of the formation and properties of protective oxide layer on high purity chromium with SIMS imaging techniques, *Mikrochemica Acta* **125** (1997) 69–72.

[21] A. Srisual, S. Coindeau, A. Galerie, J.–P. Petit, and Y. Wouters, Identification by photoelectrochemistry of oxide phases grown during the initial stages of thermal oxidation of AISI 441 ferritic stainless steel, *Corrosion Science* **51** (2009) 562–568.

[22] F. Di Quarto, S. Piazza, and C. Sunseri, A photocurrent spectroscopic investigation of passive films on chromium, *Corrosion Science* **31** (1990) 721–726.

[23] F. Di Quarto, S. Piazza, and C. Sunseri, Photoelectrochemistry in corrosion studies: Achievements and perspectives, *Materials Science Forum* **192–194** (1995) 633–648.

[24] J. Portier, G. Campet, C. W. Kwon, J. Etourneau, M. A. Subramanian, Relationships between optical band gap and thermodynamic properties of binary oxides, *International Journal of Inorganic Materials* **3** (2001) 1091–1094.

[25] W. W. Gärtner, Depletion–layer photoeffects in semiconductors, *Physical Review* **116** (1) (1959) 84–87.

[26] M. A. Butler, Photoelectrolysis and physical properties of the semiconducting electrode WO_2, *Journal of Applied Physics* **48** (5) (1977) 1914–1920.

[27] D.L.A. de Faria, S.V. Silva, and M.T. de Oliveira, Raman Microspectroscopy of some iron oxide and oxyhydroxides, *Journal of Raman Spectroscopy* **28** (1997) 873–878.

[28] R.J. Thibeau, C.W. Brown, and R.H. Heidersbach, Raman spectra of possible corrosion products of iron, *Applied Spectroscopy* **32** (6) (1978) 532–535.

[29] K. F. McCarty and D. R. Boehme, A Raman study of the systems $Fe_{3-x}Cr_xO_4$ and $Fe_{2-x}Cr_xO_3$, *Journal of Solid State Chemistry* **79** (1989) 19–27.

[30] D.J. Gardiner, C. J. Littleton, K. M. Thomas, and K.N. Strafford, Distribution and characterization of high temperature air corrosion products on iron–chromium alloys by Raman microscopy, *Oxidation of* **27** (1987) 57–72.

[31] D. Renusch, B. Veal, K. Natesan, and M. Grimsditch, Transient oxidation in Fe–Cr–Ni alloys: a Raman–scattering study, *Oxidation of Metals* **46** (5/6) (1996) 365–381.

[32] G. Calvarin, A.M. Huntz, A. Hugot Le Goff, S. Joiret, and M.C. Bernard, Oxide scale stress determination by Raman spectroscopy application to the NiCr/Cr2O3 system and influence of Yttrium, *Scripta Materialia* **38** (11) (1998) 1649–1658.

[33] A.K. Bhattacharya, A. Hartridge, K.K. Mallick, C.K. MaJumdar, D. Das, S.N. Chintalapudi, An X–ray diffraction and Mössbauer study of nanocrystalline Fe_2O_3–Cr_2O_3 solid solutions, *Journal of Materials Science* **32** (1997) 557–560.

[34] T. Grygar, P. Bezdicka, J. Dedecek, E. Petrovsky, O. Schneeweiss, Fe_2O_3–Cr_2O_3 system revised, *Ceramics–Silikaty* **47** (1) (2003) 32–39.

[35] ASM International Handbook Committee, *Metals Handbook Ninth Edition Volume 13, Corrosion*, Park (Ohio): ASM International, 1987, p.64.

[36] S. Mohanty and J. Ghose, Studies on some α–Fe_2O_3 photoelectrodes, *J. Phys. Chem. Solids* **53** (1) (1992) 81–91.

[37] H. Asteman, E. Ahlberg, J.E. Svensson, Electric properties of alpha–Fe_2O_3, Cr_2O_3 and alpha–$(Cr,Fe)_2O_3$ and their relevance to corrosion, *Electrochemical society series* **99** (38) (2000) 17–25.

[38] F. di Quarto, C. Sunseri, S. Piazza, and M. C. Romano, Semiempirical correlation between optical band gap values of oxides and the difference of electronegativity of the elements. Its importance for a quantitative use of photocurrent spectroscopy in corrosion, *J. Phys. Chem. B* **101** (1997) 2519–2525.

[39] Y. Wouters, A. Galerie, J.–P. Petit, Photoelectrochemical study of oxides thermally grown on titanium in oxygen or water vapor atmospheres, *J. Electrochem. Soc.* **154** (10) (2007) C587–C592.

[40] A K Vijh, Correlation between bond energies and forbidden gaps of inorganic binary compounds, *J. Phys. Chem. Solids* **30** (1969) 1999–2005.

CHAPTER 4
MULTISCALE PHOTOELECTROCHEMICAL STUDIES ON MODERN ALLOYS

In high temperature corrosion, photoelectrochemical techniques are principally used to identify oxide phases via the value of their bandgaps, and to determine the semiconducting type of the oxides which may inform on the corrosion mechanism. Monochromatic issued from an incoherent source coupled to a monochromator was initially used to illuminate the whole surface of an oxidized sample, to perform macroscopic characterizations. A few decades later, the evolution of this technique lunched photoelectrochemical images which provided the informations at the microscopic scale and was useful to investigate a lateral oxides distribution. These microscopic characterizations could be performed by focusing a monochromatic light from a laser source (at a selected energy) on a micrometric spot of the selected sample area and by varying the position of the spot on the surface via microscopic stages.

This chapter aims to present novel possibilities of the PEC technique, as regards the introduction of the mesoscopic scale, and fitting of photocurrent energy spectra (PES), and to illustrate the latter in the case of high temperature oxidation layers of modern alloys. First, approval steps of mesoscopic photoelectrochemical characterizations, which were designed and developed as an original tool in our laboratory, will be presented. Then the performances of multiscale photoelectrochemical characterizations will be illustrated on two kinds of samples: oxidized duplex stainless steel and Ni–based alloys, using also more conventional characterizations such as SEM/EDS, XRD, and Raman spectroscopy. The corresponding results have already partly been published [1–3].

4.1 Photoelectrochemistry at the mesoscopic scale: approval steps

Over the past 40 years, photoelectrochemistry has attracted much deserved attention as a characterization tool of passive films and of thermal oxidation layers on metallic substrates [4–8]. The recording of photocurrents as a function of the potential applied to the oxidized metal electrode, and as function of the energy of the photons illuminating the latter, combined to the use of simple but robust models [9,10], allowed to obtain information on optical and electronic properties of the semiconducting oxides and on the material/electrolyte interface energetic, in connection with composition and (micro–) structure of these materials and use properties such as corrosion resistance.

Photoelectrochemical characterizations have been most often performed at the macroscopic scale, providing only an averaged view of the sample properties. The latter view may be completed at the microscopic scale by performing photoelectrochemical imaging, which is possible with a ca 1 µm resolution using the coherent light of lasers. But the photocurrent contrasts in the photoelectrochemical images may originate in spatial heterogeneities of numerous parameters, and difficulties often arise when analyzing these images. These problems could be partially solved if photocurrent energy spectra could be recorded at the microscopic scale. This was not obtained at the µm scale due to the few lines available on usual lasers. This work will show for the first time that focusing a beam issued from an incoherent light source on a ca 30 µm diameter spot is possible, and allows recording local photocurrent energy spectra at this mesoscopic scale, and thus provides informations complementary useful to the ones obtained from macroscopic and microscopic photoelectrochemical characterizations.

Duplex stainless steel was selected as an interesting test material, both to check the feasibility of photoelectrochemical experiments at the mesoscopic scale, and to assess the interest of such experiments when characterizing thermal oxidation layers. This choice was first guided by geometrical considerations: for both its austenitic and ferritic phases, duplex stainless steel exhibits numerous grains of sizes larger than around 30 µm. But also chemical composition issues were taken into account when selecting 2205 duplex stainless steel as the test material. The chromium content is higher in the ferritic phase than in the austenitic one of Table 2.2 (Chapter 2). It may be thus expected that the thermal oxidation layers grown on the alloy will be different, for instance as concerns the x–value of the $Fe_{2-x}Cr_xO_3$ solid solution which is generally observed in such oxidation layers.

In this section, the characterizations of a duplex stainless steel sample which was oxidized in 20 %water vapor at 650°C for 5 minutes will be reported. Initially, the results from the conventional photoelectrochemical in macroscopic and microscopic will be presented. After that mesoscopic photoelectrochemical characterizations will be presented to illustrate their performances and their usefulness in completing the informations provided by the macroscopic and microscopic photoelectrochemical characterizations. Finally, the results will be correlated to the ones obtained by Raman microscopy.

4.1.1 Macroscopic photoelectrochemical characterizations

Typical results of photoelectrochemical characterizations of the oxidized duplex stainless steel (ODSS) electrode at the macroscopic scale are presented in Figure 4.1. Figure 4.1(a) shows the dependence of the photocurrent on the applied potential, using several

photon energies. These curves provide mainly two informations. On the one hand, as the modulus of the photocurrent increases while increasing the applied potential, it can be concluded that the sample globally exhibits an n–type semiconducting behavior. On the other hand, two domains of potentials are observed on Figure 4.1(a). Below about V = –600 mV, very low photocurrents are measured for photon energies less than 3 eV. Above V = –600 mV, significant photocurrents values are measured at all tested photon energies. This evidences that the overall measured photocurrent arises from several photocurrent contributions, i.e. from several oxides present on the ODSS sample, whose respective amplitudes depend on the applied potential due to their different flatband potentials, and also depend on the photon energies due to their different band gap energies. The latter conclusions are also supported by the photocurrent energy spectra presented in Figure 4.1(b), which appear to be clearly different depending on the potential range where they were recorded.

Moreover, the photocurrent energy spectrum recorded at V = 0 mV could be fitted (the solid line present on the graph shows the fitted spectrum) using a model and fitting procedures developed in our group as described in Chapter 2. Fitting the photocurrent energy spectrum allowed to detect four contributions to the photocurrent, with the following indirect bandgap energies: $E_{G,1}$ = 2.0 eV, $E_{G,2}$ = 2.4 eV, $E_{G,3}$ = 3.1 eV, $E_{G,4}$ = 3.5 eV. $E_{G,1}$ is attributed to Fe_2O_3, $E_{G,4}$ to Cr_2O_3 [11] and, as explained in a following section, it is proposed that $E_{G,2}$ and $E_{G,3}$ should be attributed to $Fe_{2-x}Cr_xO_3$ compounds with different x–values.

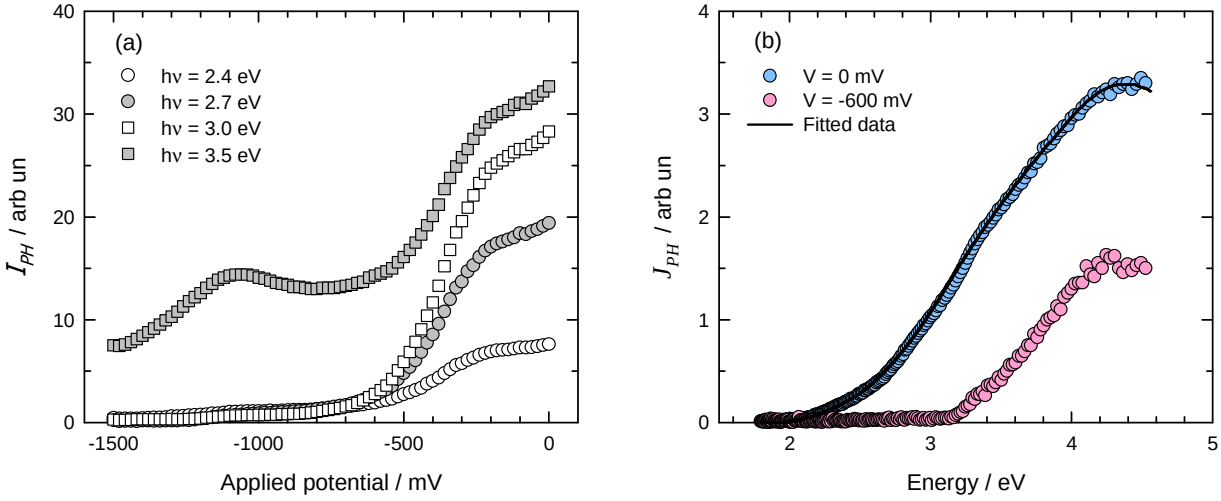

Figure 4.1 Typical photocurrents obtained by illuminating the whole oxidized DSS sample area: (a) plots of I_{PH} as a function of the applied potential, V, at several photon energies, and (b) plots of J_{PH} as a function of the photon energy at selected applied potential (the solid line shows the fitted spectrum)

4.1.2 Photoelectrochemical imaging

Photoelectrochemical images were recorded on a sample area covering both austenitic and ferritic grains (Figure 4.2(a)), using two photon energies: 2.60 eV (Figure 4.2(b)), an energy between $E_{G,2}$ and $E_{G,3}$, and 3.53 eV (Figures 4.2(c) and (d)), and also two values for the applied potential, V = –200 mV (Figures 4.2(b) and (d)) and V = – 700 mV (Figure 4.2(c)). It can be observed that the photocurrents exhibited by the oxidized austenitic grains are higher than the ones measured on ferritic grains. However, the photocurrent contrasts between these grains depend significantly on the photon energy and on the applied potential. At this point, this observation is hardly to be explained, although it could be suggested that the component with bandgap energy $E_{G,2}$ could be absent on ferritic grains.

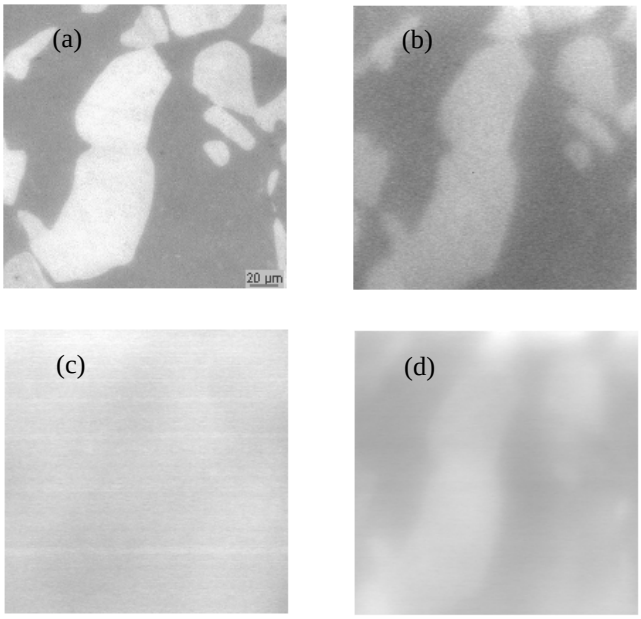

Figure 4.2 Optical and photoelectrochemical images of a 200 µm x 200 µm area of the oxidized DSS sample : (a) optical image ; (b) , (c), (d) : photoelectrochemical images obtained at : (b) V = –200 mV, hν = 2.6 eV, (c) V = –700 mV, hν = 3.53 eV, (d) V = –200 mV, hν = 3.53 eV

4.1.3 Mesoscopic photoelectrochemical characterizations

The individual oxidized ferritic and austenitic grains investigated in the experiments illustrated in Figure 4.2 have been characterized at the mesoscopic scale. The corresponding photocurrent energy spectra are presented in Figure 4.3. These results show firstly that photocurrent energy spectra actually can be recorded at the mesoscopic scales. But they also put in evidence the interest of such characterizations.

On the one hand, the data of Figure 4.3 allow to derive, at energies and potentials close to their values used in Figure 4.2, the ratios of the photocurrent values measured on austenitic grains to the ones measured on ferritic grains. These ratios are listed in

Table 4.1, and clearly account for the potential and photon energy dependent contrasts observed in the images of Figure 4.2.

On the other hand, when fitting the individual photocurrent energy spectra of austenitic and ferritic grains with our in–house model, it turns out (Table 4.2) that only 3 oxide components are found on each kind of grain. The bandgap energies of Fe_2O_3 and Cr_2O_3 are found whatever the metallurgic phase, but only one bandgap energy corresponding to a $Fe_{2-x}Cr_xO_3$ compound is found on each grain: 2.46 eV on the austenitic grain, 2.84 eV on the ferritic one.

As already written in Chapter 3, bandgap values may be estimated from thermodynamic extensive atomic data [8, 11–12], so it was proposed that the bandgap energies of a $Fe_{2-x}Cr_xO_3$ solid solution could be given by the following simple equation:

$$(2\text{-}x)\cdot E_G(Fe_2O_3) + x\cdot E_G(Cr_2O_3) = 2\cdot E_G(Fe_{2\text{-}x}Cr_xO_3) \qquad (4.1)$$

Considering the bandgap values found respectively on the austenitic and ferritic grains for $Fe_{2-x}Cr_xO_3$ (Table 4.2), the latter equation implies that the oxide solid solution formed on the austenitic phase exhibits a lower Cr content than the one grown on the ferritic phase, as indeed could be anticipated from data of metallurgical element of each phase.

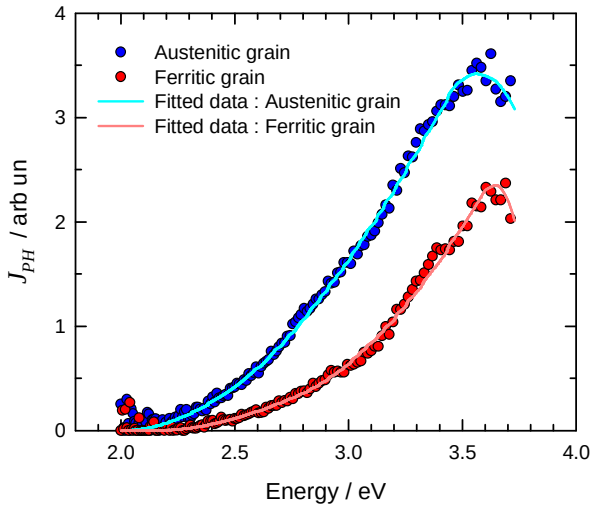

Figure 4.3 Photocurrent energy spectra obtained by illuminating individual austenitic (blue circle) or ferritic (red circle) grains of the oxidized DSS sample at V = 0 mV (the solid lines show the fitted spectra)

Table 4.1 Ratios of the photocurrent values measured on austenitic grains to the ones measured on ferritic grains, as obtained from experimental data of Figure 4.3

Applied potential		V = 0 mV	V = –600 mV
Photon energy	hν = 2.60 eV	3.3	– –
	hν = 3.53 eV	1.7	1.1

4.1.4 Raman spectroscopy characterizations

The Raman spectra recorded on individual oxidized ferritic and austenitic grains are presented in Figure 4.4. Both spectra show the characteristic peaks of hematite at 411 cm^{-1}, and chromia at 550 cm^{-1}. The broad peak observed at the highest Raman shift values is characteristic of $Fe_{2-x}Cr_xO_3$ [13–16]. It can be seen that this peak is shifted from 668 cm^{-1} (austenitic grains) to 674 cm^{-1} (ferritic grains), which, according to the previous work in Chapter 3 and the work of McCarty et al. [13], signs a lower x–value in the oxide solid solution formed on austenite, as deduced above from mesoscopic photocurrent energy spectra. Moreover, a strong correlation between the x–value and the Raman shift corresponding to the $Fe_{2-x}Cr_xO_3$ peak was pointed out by the experimental results in section 3.2.3 (Chapter 3) and also by the study of McCarty et al. From the experimental results, an x–value of 0.8 (resp. 1.3) could be assessed in the case of oxidized austenite (resp. ferrite). The corresponding bandgap energies calculated from these x–values, using bandgap value of Fe_2O_3 at 2.0 eV and bandgap value of Cr_2O_3 at 3.5 eV, are given in Table 4.2 and appear to be very close of the ones obtained by fitting the mesoscopic photocurrent energy spectra.

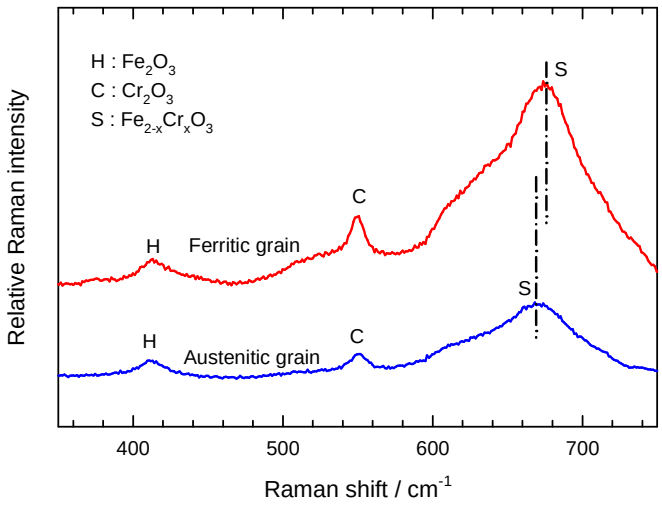

Figure 4.4 Raman spectra recorded on individual austenitic (lower curve) and ferritic (upper curve) grains of the oxidized DSS sample

Table 4.2 Summary of the bandgap energies, E_G, obtained by fitting the photoelectrochemical energy spectra of the oxidized duplex stainless steel sample, and of the E_G values of $Fe_{2-x}Cr_xO_3$ derived from Raman characterizations of the latter sample (values are given in eV)

			Fe_2O_3	$Fe_{2-x}Cr_xO_3$		Cr_2O_3
As obtained by fitting photocurrent energy spectra	Macroscopic		2.0	2.4	3.1	3.5
	Mesoscopic	austenitic grain	2.0	2.4(6)		3.4
		ferritic grain	2.1		2.8(4)	3.5
As obtained from Raman spectra derived x–values		austenitic grain		2.6		
		ferritic grain			2.9	

4.1.5 Conclusions

It was shown here that the whole set of photoelectrochemical tools available at the macroscopic scale may now be used at the mesoscopic scale, to obtain local information but complete photoelectrochemical informations of different (30 µm diameter) zones of a unique sample. The results obtained at the mesoscopic scale in the case of oxidized duplex stainless steel provided interesting complementary information to the ones of microscopic and macroscopic studies. In particular, the origin of the potential and photon energy dependent contrasts in the photoelectrochemical images was elucidated. It could also be shown that, whereas the macroscopic results suggested the presence of four oxides (Fe_2O_3, Cr_2O_3 and two $Fe_{2-x}Cr_xO_3$ compounds) in the thermal scale, the mesoscopic photocurrent energy spectra showed that Fe_2O_3 and Cr_2O_3 were present on all grains, but that the scale on each grain (oxidized in exactly the same conditions) was likely to contain an unique $Fe_{2-x}Cr_xO_3$ compound, its x–value depending on the metallurgic nature of the grain. Finally, it should also be pointed out that the novel approach developed in our group for the fitting of photocurrent energy spectra could be applied both for macroscopic and mesoscopic PES.

4.2 Oxidation of duplex stainless steel: multiscale photoelectrochemical study

As presented in the above section, photoelectrochemical characterizations at the mesoscopic scale allows to obtain complementary information to the ones obtained from the macroscopic and/or microscopic photoelectrochemical analyses. To go further on the study of the oxidation of duplex stainless steel (DSS2205) using multiscale photoelectrochemistry, the oxidation conditions, such as the oxidation atmospheres, temperatures, and times were varied. Additional analyzes of the sample, were made by SEM/EDS, XRD, and Raman spectroscopy.

4.2.1 Morphology of the oxidized samples

Electron micrographs presented in Figure 4.5 do illustrate the surface morphology of the oxidized duplex stainless steel, and show the different oxides grown on individual ferritic and austenitic grain due to the differences in chemical compositions and in the structure of the alloy matrix. Traces of oxides are observed on the sample oxidized at low temperature (Figures 4.5(a) and (b)); the topology of this "initial" state is not obviously recognized at higher temperature (Figures 4.5(c) and (d)) because the oxidation rate is higher at high temperature. Indeed, the propagation of oxide at longer oxidation time reveals clearly oxide shapes which strongly depend on metallurgical variables of the base alloys and of the oxidizing gas. In water vapor (Figure 4.5(a) – (d)) thermal oxides exhibit either flake or polyhedral forms on austenitic grains while they appear as whiskers on ferritic grains. At low oxygen partial pressure (in water vapor), the formation of whiskers on ferritic area could be explained by the diffusion of cations along a tunnel centered round the core of a screw dislocation or a bundle of dislocation where surface diffusion is very fast, comparing to lattice diffusion [17]. In oxygen gas (Figure 4.5(e) and (f)), a granular oxide could be observed on both kinds of grains: a smaller and more homogenous oxide is presented on austenitic grains due to the fact that the structure of austenitic (FCC) phase is denser than that of the ferritic phase (BCC), providing a lower diffusion rate that lunched more homogenous oxide topology. From these micrographs, it can be concluded that the difference in oxide morphologies were affected not only from the oxidizing gas but also from the crystalline structure of the alloy due to different atomic densities and preferred orientations on the surface.

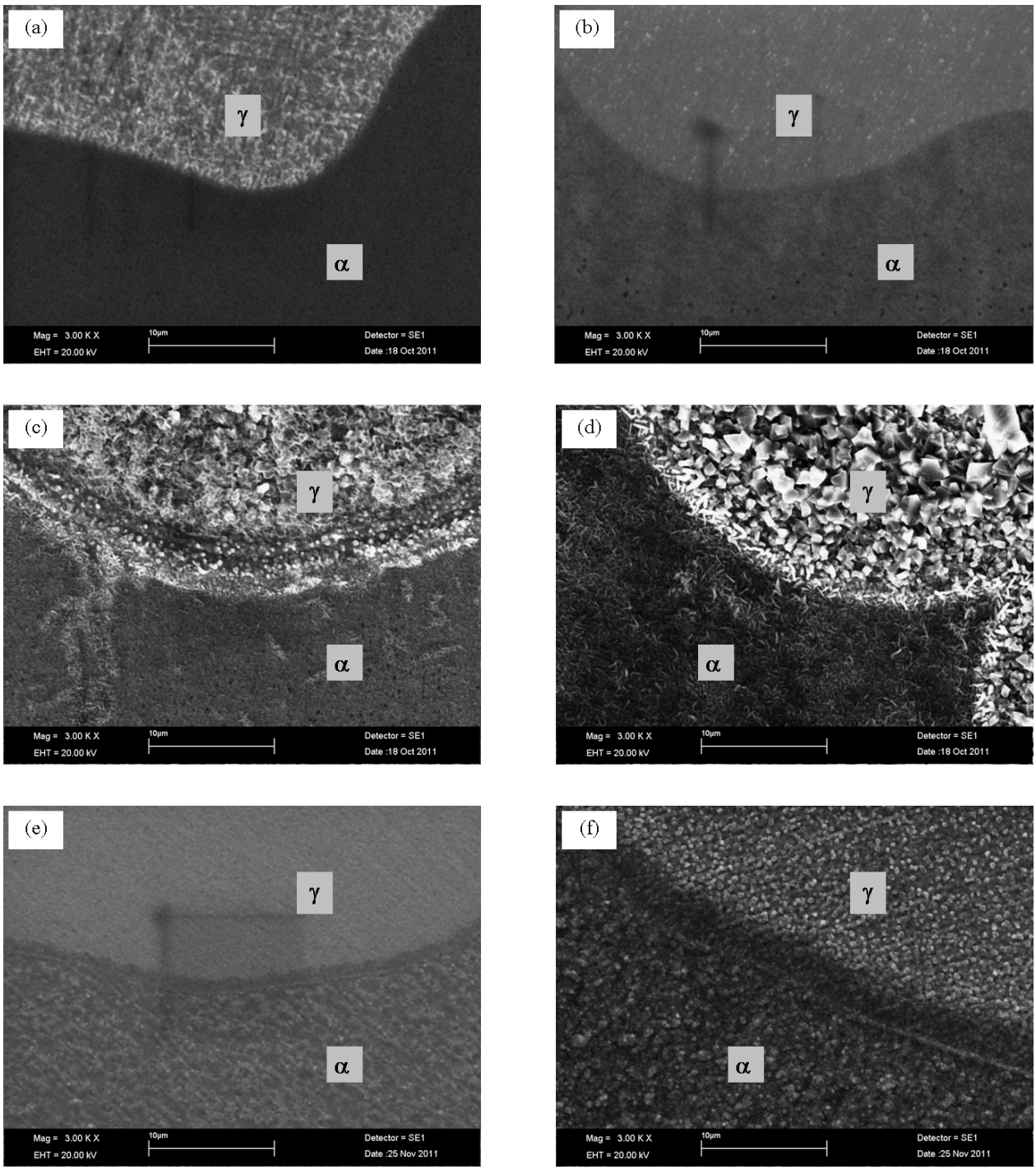

Figure 4.5 SEM micrographs of the thermal oxides grown on DSS2205 oxidized in water vapor; (a) 650°C for 5 min (b) 650°C for 60 min (c) 850°C for 5 min (d) 850°C for 60 min, and in oxygen; (e) 850°C for 5 min (f) 850°C for 60 min

4.2.2 Oxide phase identification

4.2.2.1 X–ray diffraction characterizations

Figure 4.6 presents X–ray diffractograms of DSS before, (a), and after, (b) to (e), oxidation. The oxidized samples typically exhibited oxides of corundum structure (Fe_2O_3 and/or Cr_2O_3 and/or $Fe_{2-x}Cr_xO_3$), and partly of spinel structure ($Mn_{3-y}Cr_yO_4$). In the case of short time oxidation at lower temperature (Figure 4.6(b)), oxide phases could not clearly be put in evidence because of the sensitivity limits of the instrument. The increase of oxidation time and temperature do increase the oxide thickness as can be seen from the signal increase on the patterns. The nature of the oxidizing gas also affects the oxidation rate as shown by Figures 4.6(d) and (e): the ratio of the peaks of the oxide phase to the ones of the base alloy was higher in water vapor atmosphere, so a thicker oxide (faster oxidation rate) forms in water vapor.

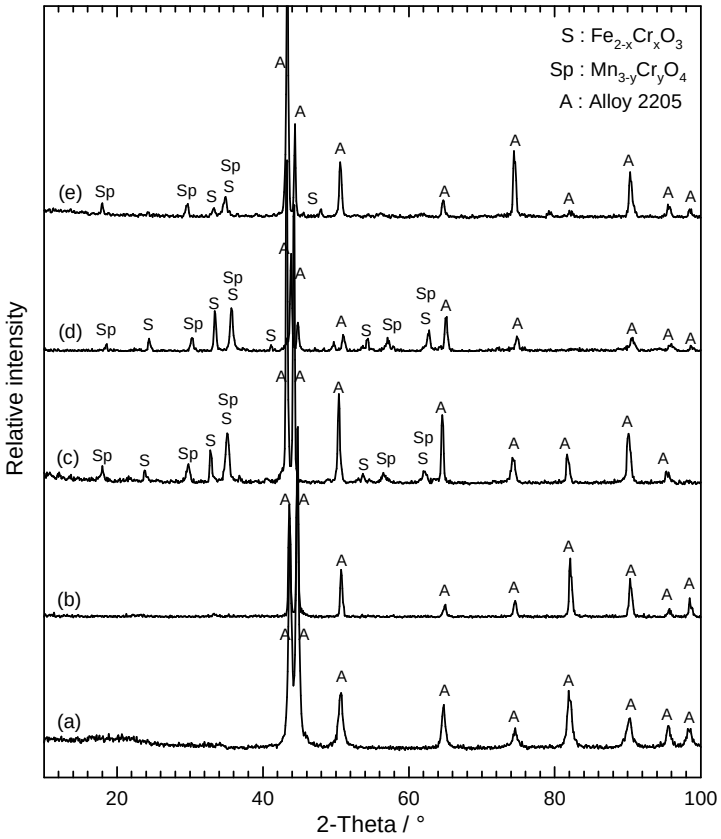

Figure 4.6 X–ray patterns obtained from duplex stainless steel (a) before and (b) – (e) after oxidation; in water vapor (b) 650°C for 5 min (c) 850°C for 5 min (d) 850°C for 60 min, and (e) in oxygen gas at 850°C for 60 min

4.2.2.2 Raman spectroscopy characterizations

The Raman spectra recorded on individual ferritic and austenitic grains which were oxidized at 850°C for 60 minutes in water vapor and in oxygen are presented in Figure 4.7. In water vapor, Figure 4.7(a), the characteristic peaks of hematite (resp. chromia) at around 411 cm^{-1} (resp. 554 cm^{-1}) were only detected on the austenitic (resp. ferritic) grains whereas Raman shift at 659 and/or 680 cm^{-1} corresponding to the spinel phases were observed on both grains. Since literature reported that the characteristic peak of $Fe_{2-x}Cr_xO_3$ should be located at 664–685 cm^{-1} [13] while the characteristic peaks of $MnCr_2O_4$ should appear at 660 and 680 cm^{-1} [18–21], it is difficult to affirm the observed peaks correspond to $Fe_{2-x}Cr_xO_3$ or $Mn_{3-y}Cr_yO_4$. According to the Raman peaks of the austenitic grain and XRD results, it could imply that the spinel phase only present on ferritic grain. Moreover, the absence of chromium oxide on the austenitic grain in this case (in water vapor during longer oxidation time) could imply iron–rich solid solutions. In oxygen atmosphere, Raman peaks on both types of grains show the presence of $Fe_{2-x}Cr_xO_3$ and Cr_2O_3 without evidence of Fe_2O_3, indicating chromium–rich solid solutions. Furthermore, characteristic peak of $Fe_{2-x}Cr_xO_3$ shifts from 665 cm^{-1} (on ferritic grains) to 673 cm^{-1} (on austenitic grains) which signs a lower x–value of the corundum solid solution oxide formed on the ferritic grain.

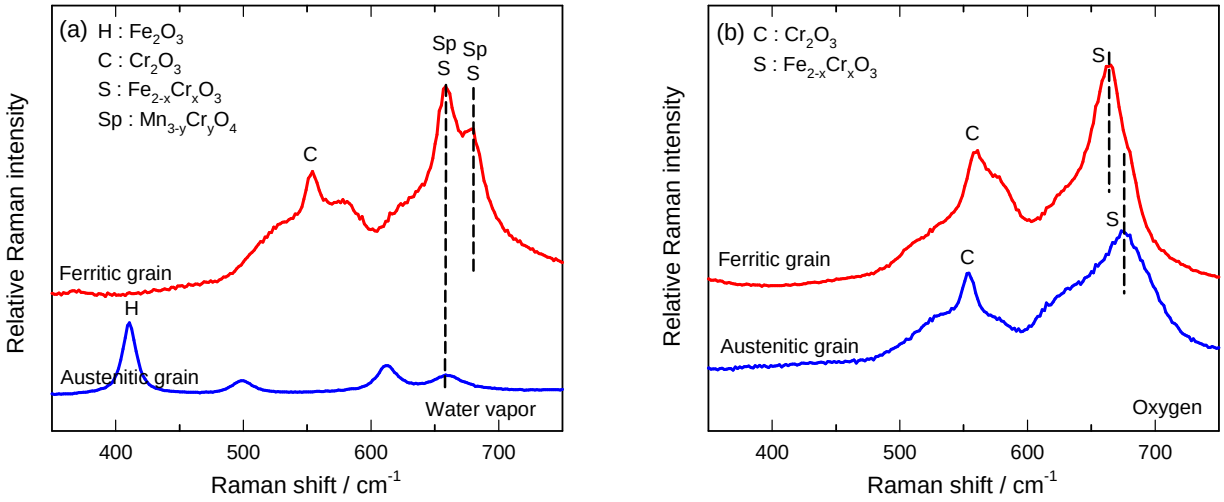

Figure 4.7 Raman spectra recorded on individual austenitic (lower curve) and ferritic (upper curve) grains of the DSS sample oxidized at 850°C 60 min (a) in water vapor (b) in oxygen

4.2.3 Photoelectrochemical characterizations

4.2.3.1 Macroscopic photoelectrochemical characterizations

All macroscopic scale photocurrent voltammograms (i.e. photocurrent vs potential curves) recorded on ODSS samples could be classified in 3 patterns, as illustrated in Figure 4.8. Figure 4.8(a) shows the typical pattern obtained for samples oxidized in water vapor (except for the sample oxidized at 850°C for 60 min). The modulus of the photocurrent increases as the applied potential increases. It is concluded that the sample globally exhibits an n–type semiconducting behavior. Moreover, when considering the sharp increase in the photovoltammogram at about –500 mV, where the phase shift does not vary significantly around this potential, it may be suggested that 2 n–type components are present in the oxidized layer, having different flatband potentials (i.e. having different positions of their valence and conduction band on the electronic energy scale, and thus on the electrochemical potential scale). In contrast, DSS samples oxidized in oxygen all exhibited the pattern shown in Figure 4.8(c), where the photocurrent modulus decreases as the applied potential increases, revealing an overall p–type behavior of the scales. The particular shape of the photocurrent voltammogram in Figure 4.8(b) was obtained only for the sample oxidized in water vapor at 850°C for 60 min; it signs the presence of at least 2 components in the scale, one being n–type as evidenced by the curve recorded at 2.41 eV, the other being more or less insulating as suggested by the V–shaped part of the photocurrent voltammogram recorded at 3.53 eV.

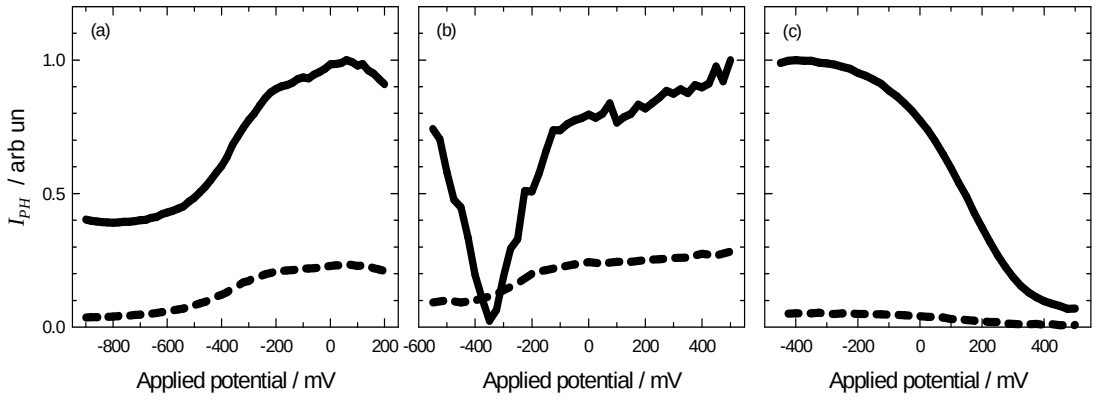

Figure 4.8 Typical as measured photocurrent amplitude vs applied potential curves obtained at hν = 2.41 eV (dashed line) and 3.53 eV (solid line) on the whole surface of DSS sample oxidized in water vapor (a) at 650°C for 5 min, (b) at 850°C for 60 min, and in oxygen (c) at 850°C for 60 min

Figure 4.9 presents macroscopic photocurrent energy spectra (i.e. photocurrent vs photon energy curves) measured at several applied potentials for the same ODSS samples as in Figure 4.8. The shape of these photocurrent energy spectra appears to be strongly potential dependent. This again can be explained by the fact that the oxidized

samples are constituted of several semiconducting components, having different bandgaps and different flatband potentials: varying the applied potential does not change the bandgap but induces changes in the band bending of the individual components, and consequently relative changes of the complex photocurrents issued from each component. This significant dependence of the photocurrent energy spectra on the applied potential is interesting, considering all the spectra and the slopes changes therein. It allows to conclude that each spectrum is the combination of at least three contributions to the global photocurrent, with approximate bandgap values of 2 eV, 2.6 to 3.0 eV, and around 3.4 eV; the bandgap values are in agreement with the ones which could be expected for layers formed of Fe_2O_3, $Fe_{2-x}Cr_xO_3$, and Cr_2O_3 respectively, and with the fitted values of a previous work on an ODSS sample in section 4.1.

The question of the semiconducting type of each of the components remains difficult to discuss. Even with the help of the fitting model for the photocurrent energy spectra, the analysis of the signs of the individual contributions to the photocurrent will require to consider the interfaces at which a given contribution could be generated (metal/scale, scale/electrolyte, oxide/oxide in the scale), before concluding on the semiconducting type of a given component. However, Fe_2O_3 has always been reported as an n–type semiconductor. The semiconducting type of $Fe_{2-x}Cr_xO_3$ depends on the surrounding nevertheless, at the same environment, the value of x switched from n at low x values to p at high x values [22]. Chromia is known to present a low deviation from the stoichiometry, but can exhibit rather n–type or p–type semiconduction depending on the oxygen activity in the oxidizing atmosphere [23]. The formation of p–type oxide in oxygen should arise from metallic vacancies or oxygen interstitial as the main defect, while the presence of n–type oxide in water vapor should correspond to metallic interstitials or oxygen vacancies as the main defect [24–25]. In addition, in water vapor atmosphere, a change from n–type to p–type Cr_2O_3 was observed as the effect of changing oxidation time and temperature; as in previous works, the latter transition could be attributed to the presence of hydrogen [26] or hydroxide ion [27–28], which however was not investigated here. From the above observations, it could be concluded that the change from overall n–type behavior for samples oxidized in water vapor to overall p–type for samples formed in oxygen could be due to a change of the semiconducting type of Cr_2O_3 and/or $Fe_{2-x}Cr_xO_3$, and that the nearly insulating behavior observed in Figure 4.8(b) at high photon energy is likely to be attributed to Cr_2O_3.

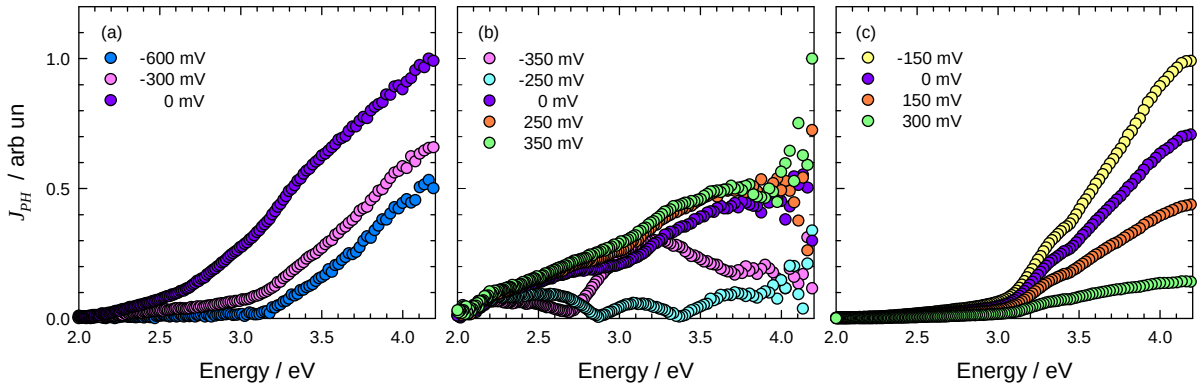

Figure 4.9 Photocurrent energy spectra at several applied potentials obtained on the whole surface of ODSS in water vapor (a) at 650°C for 5 min, (b) at 850°C for 60 min, and in oxygen (c) at 850°C for 60 min

The influence of atmosphere, oxidation time and temperature on the photoelectrochemical results is illustrated in Figure 4.10. Figure 4.10(a) exhibits clearly that water vapor promotes the development of iron–rich oxide, i.e. a higher photocurrent contribution at low photon energy (E < 3.0 eV), contrary to what can be observed in presence of oxygen. Iron–rich oxides are undoubtedly localised at the metal/oxide interface [28]. Figure 4.10(b) presents the oxidation time effect, at 850°C in oxygen, on the well known competition between iron and chromium oxide development. The ratio of the photocurrents in the high energy domain to the ones in the low energy range increases with time, signing, as expected, an increase with time of the relative amount of Cr_2O_3 and chromium rich $Fe_{2-x}Cr_xO_3$ in the scale. In addition, while in oxygen little effect of the temperature is observed (Figure 4.10(d)), one should notice that increasing the temperature in water vapor leads to a higher development of iron–rich oxide (Figure 4.10(c)). Again, this result is consistent with numerous kinetic studies on stainless steels showing a breakaway observed sooner when temperature increases.

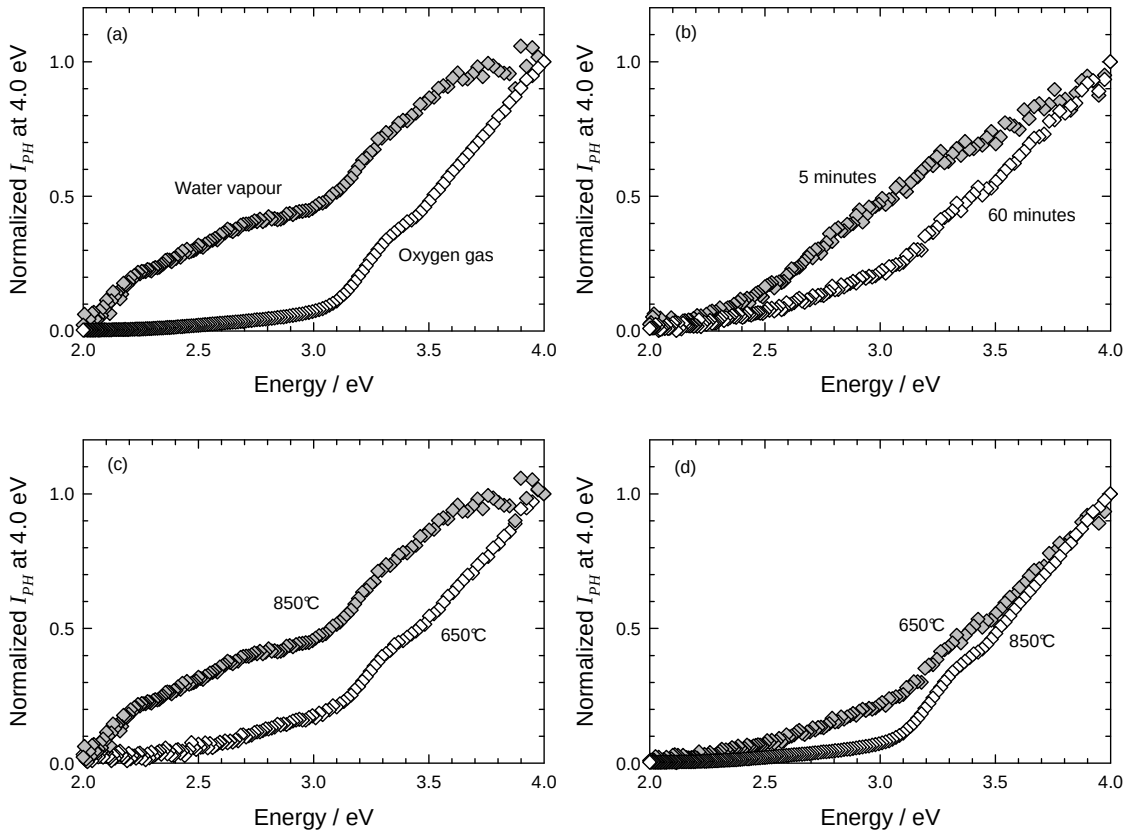

Figure 4.10 Energy spectra normalized at 4.0 eV; specimens oxidized (a) at 850°C for 60 min, (b) in oxygen at 650°C and (c) in water vapor for 60 min and (d) in oxygen for 60 min (V = 0 mV)

4.2.3.2 Mesoscopic photoelectrochemical characterizations

Mesoscopic photovoltammograms and photocurrent energy spectra were recorded on individual austenitic or ferritic grains. Figure 4.11 shows typical photovoltammograms measured on the whole sample area, and on individual grains of ODSS sample, at a photon energy value of 3.53 eV, i.e. higher than the bandgap energy of chromia. In oxygen, whatever the grain, p–type semiconduction is clearly observed as the result of the thermal growth of chromia at high oxygen activity in the atmosphere. On the contrary, in water vapor (i.e. low oxygen activity), chromia is now close to an insulator, as shown by the V–shaped curve. In addition, the flatband potential assessed as the potential of the minimum photocurrent is located on the macroscopic spectra at around –350 mV, an intermediate value between the ones of the individual grains (Figure 4.11(a)), putting in evidence that the macroscopic response averages the ones of the different grains.

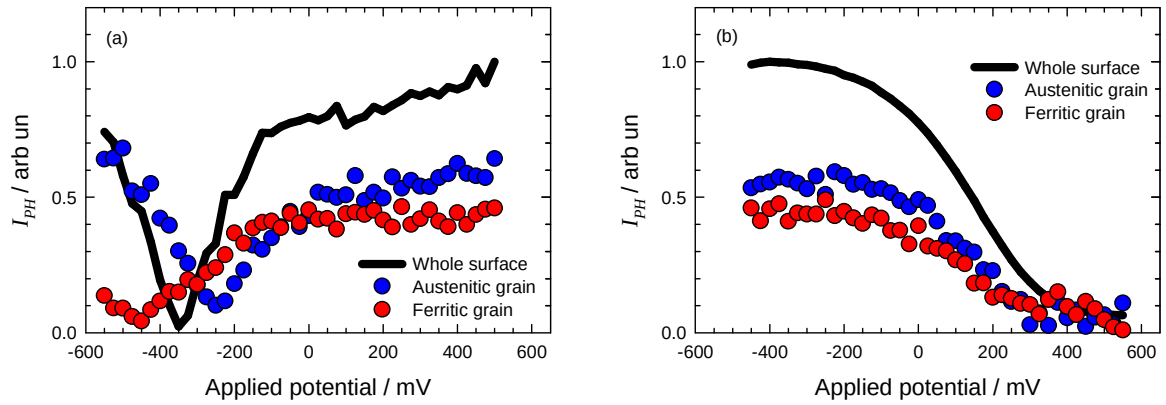

Figure 4.11 Typical photovoltammogramms obtained at hν = 3.53 eV on the whole surface of ODSS sample and the individual oxidized grain of austenitic and ferritic phases at 850°C for 60 min (a) in water vapor and (b) in oxygen

Figure 4.12 presents the dependences of the photocurrent amplitude and of the phase shifts on the photon energy, at the applied potential value of –350 mV, which corresponds to the cathodic (resp. anodic) branch of the V–shaped curve for the austenitic (resp. ferritic) grain. It is observed, both on Figure 4.12(a) and Figure 4.12 (b) that the phase shifts have a similar behavior in the [2.0 – 2.7] eV and in [2.7 – 3.3] eV ranges on both kinds of grains, whereas a phase shift difference of about 180° (a change of the sign of the photocurrent) is observed at higher energies. The latter trends reinforce the idea that the near insulating behavior should be attributed to chromia. The strong difference between the phase shifts in the [2.0 – 2.7] eV and in [2.7 – 3.3] eV ranges indicate photocurrents of different signs for Fe_2O_3 and iron–rich $Fe_{2-x}Cr_xO_3$ compared to chromium rich $Fe_{2-x}Cr_xO_3$, but as stated above, the question of their semiconducting type remains unclear. In addition, the less marked changes in the phase shift observed around 2.5 eV in Figure 4.12(a) and 2.7 eV in Figure 4.12(b) appear to be in agreement with the 2.4 eV and 2.8 eV values determined at the beginning part of this chapter for the bandgaps of $Fe_{2-x}Cr_xO_3$ on austenitic and ferritic grains respectively, i.e. with an x value higher on ferritic grains.

Additional features may be pointed out, as illustrated by the results presented in Figure 4.13 and Table 4.3. At low oxygen activity (Figure 4.13(a)), the differences in the photocurrent energy spectra of the ferritic and austenitic oxidized grains are mainly located in the low photon energy range, with higher photocurrents issued from the iron rich oxides on the austenitic grains. On the contrary, at high oxygen activity (Figure 4.13(b)), the differences in the photocurrent energy spectra of the ferritic and austenitic oxidized grains are mainly located in the high photon energy range, with higher photocurrents issued from the chromium rich oxides on the austenitic grains. These results coincided with the Raman

characterization which tended to present hematite (resp. chromia) on sample oxidized in water vapor (resp. in oxygen), including Fe–rich (resp. Cr–rich) solid solution on austenitic phase.

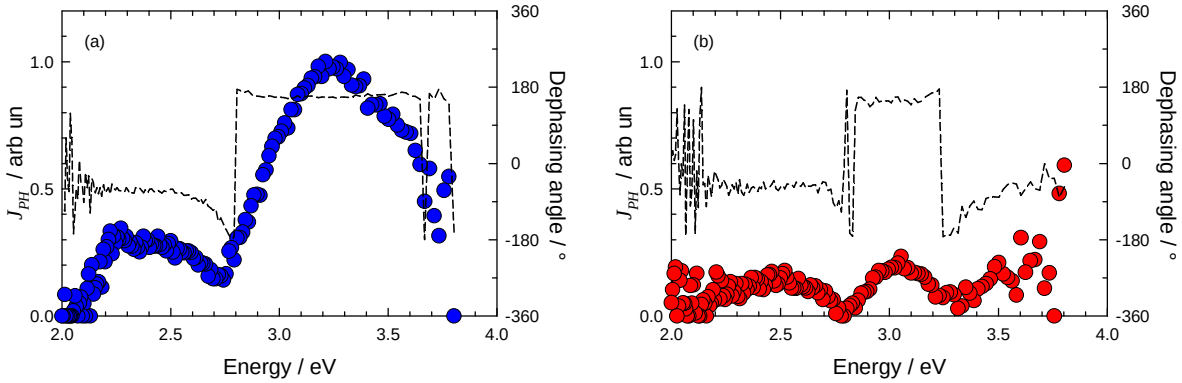

Figure 4.12 Photocurrent amplitude (white or gray circle) and dephasing angle (dashed line) vs energy spectra obtained on individuals (a) austenitic and (b) ferritic grains at an applied potential of –350 mV of ODSS sample in water vapor at 850°C for 60 min

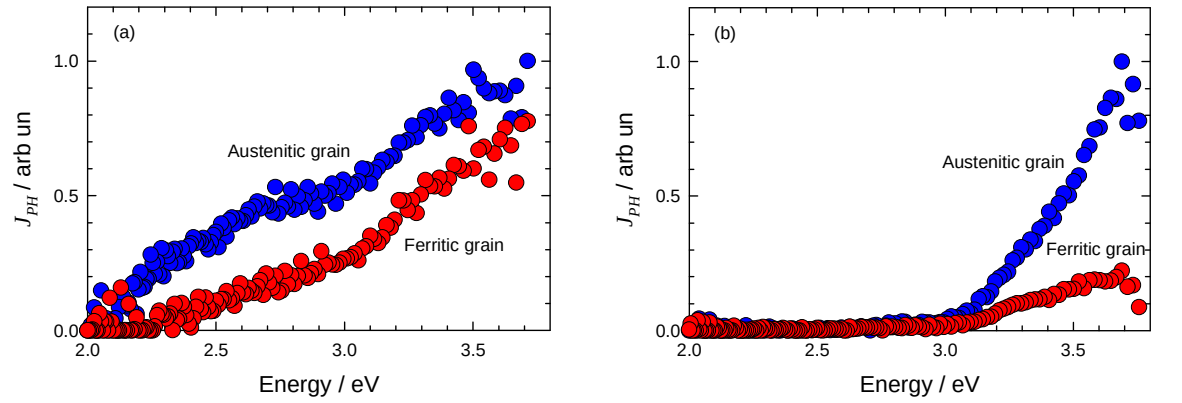

Figure 4.13 Photocurrent energy spectra obtained on individuals austenitic (●) and ferritic (●) grains of DSS oxidized at 850°C for 60 min (a) in water vapor at 350 mV (b) in oxygen at 0 mV

Table 4.3 Ratios of the photocurrent values measured on austenitic grains to the ones measured on ferritic grains, as obtained from experimental data of Figure 4.13

Oxidation atmosphere		Water vapor	Oxygen
Photon energy	hν = 2.60 eV	2.89	1.48
	hν = 3.53 eV	1.40	3.18

4.2.3.3 Microscopic photoelectrochemical characterizations

Also photoelectrochemical images were recorded on ODSS samples. Figure 4.14 shows a set of images obtained from samples oxidized both in water vapor (top images) and in oxygen (bottom images) at 850 °C for 60 min, respectively at the same applied potential as in Figure 4.13. Images (d) and (h) were obtained by dividing point by point, for each sample, the photocurrent measured at 2.60 eV by the one measured at 3.53 eV. In Figure 4.14(a) (resp. 4.14(b)) the austenitic grains (γ) correspond to the darker (resp. lighter) areas, the ferritic grains (α) to the lighter (resp. darker) areas.

Higher image contrasts are obtained when using the visible laser line for water vapor samples, whereas higher contrasts are obtained using the UV laser line in the case of oxygen samples that because of the major oxide in water vapor was hematite and/or iron–rich solid solution whereas the major oxide in oxygen was chromia and/or chromium–rich solid solution. The latter observations are in agreement with the above presented mesoscopic results (Table 4.3). In addition, the photoelectrochemical images always show higher photocurrents on the oxidized austenitic grains than on the ferritic ones. For Raman analyses suggested thicker layers on ferritic grains, in agreement with higher chromium supplies at the metal/oxide interface, the phenomena responsible for higher photocurrents on austenitic grains is likely to be related to lower doping, or electron–hole recombination centers, concentrations, but the question remains open.

Since the photocurrent values measured at 2.60 eV are due to contributions of Fe_2O_3 and $Fe_{2-x}Cr_xO_3$ whereas the values recorded at 3.53 eV are due to the latter oxides and also to Cr_2O_3, images (d) and (h) are expected to give a rough relative estimation of the Cr_2O_3 fraction in the scales. On this basis, in the case of water vapor oxidation (Figure 4.14(d), the Cr_2O_3 fraction appears to be higher on ferrite than on austenite. This can be explained considering that the chromium content in the ferritic phase is higher than in the austenitic one, inducing more protective chromia formation on ferrite at the initial oxidation stage; moreover, the high temperature diffusion of chromium in ferritic phase is known to be faster than in austenitic phase, and a higher iron content in austenite induces higher iron diffusion in corundum oxide, reducing the chromia fraction. In oxygen atmosphere, higher oxygen partial pressure plays a negative role and opposite results is observed (Figure 4.14(h)).

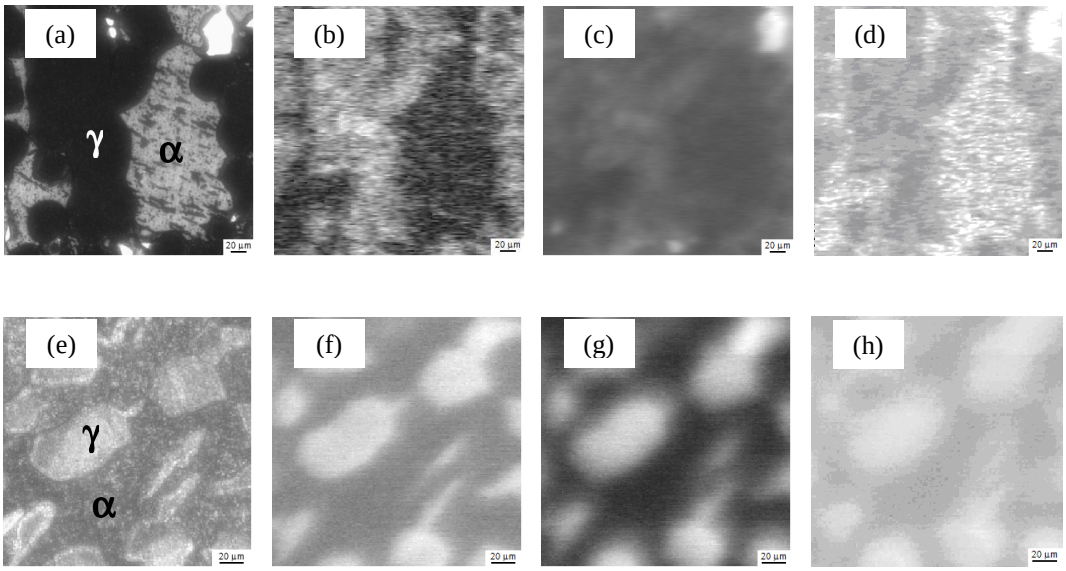

Figure 4.14 Image set of ODSS at 850°C for 60 min in water vapor (top images) and in oxygen (bottom images): (a) and (e) optical image, (b) and (f) PEC image at hυ = 2.60 eV, (c) and (g) PEC image at hν = 3.53 eV, and (d) and (h) processed image

4.2.4 Conclusions

Oxidation time, oxidation temperature, and gases affected on oxide type, its quantity, and also the morphology. Furthermore, it affected on both thermal oxide type and semiconducting behavior of the oxide. Macroscopic results which is an average of all different grain, allowed to point out at the major effects induced by changes in the atmosphere, time or temperature of oxidation. Mesoscopic experiments evidenced differences in the layers grown on ferritic and austenitic grains, also allowing to account for the contrasts observed on the photoelectrochemical images. The latter images showed atmosphere dependent differences in the chromia relative fraction in oxidized ferritic and austenitic grains.

The corundum oxide phases of Fe_2O_3, $Fe_{2-x}Cr_xO_3$, and Cr_2O_3 were always detected either on austenitic or on ferritic grains, that a chromium content in $Fe_{2-x}Cr_xO_3$ depended not only on nature of materials but also on oxidizing atmospheres. Whatever the grain, ferritic or austenitic, semiconduction of chromia was affected in the same way, and was proven to be very sensitive to the oxygen activity in the oxidation atmosphere. At low oxygen partial pressure like in water vapor, chromia appeared as an insulator, i.e. a protective oxide exhibiting a low deviation from stoichiometry. On the contrary at a high oxygen partial pressure like in oxygen, chromia clear exhibited p–type semiconduction.

4.3 Oxidation of Ni–based alloys: multiscale photoelectrochemical study

Nickel based alloys are well considered materials for uses in high temperature applications. In this work, we did focus on Inconel 690, a high–chromium content nickel alloy, which is generally used in thermal exchangers between primary and secondary circuits. The oxidation of the latter alloy was conducted here at 900°C in several atmospheres. The aims of this section are partly, on the one hand, to investigate the possibilities offered by investigating oxidized samples using multiscale photoelectrochemical characterizations, but, mainly, on the second hand, to show the interest, when analyzing PES, of the model developed in our lab in the course of the present work.

To support the results obtained by photoelectrochemistry, additional characterizations of the thermal scales have been performed using SEM/EDS and Raman spectroscopy.

4.3.1 Morphology of oxidized Ni–based alloys

Figure 4.15 presents the secondary (SE) and backscattered (BSE) electron micrographs of Alloy 690 oxidized in various conditions. On the SE micrographs, an homogeneous thermal oxide can be observed on the sample oxidized in water vapor (Figure 4.15(e)) while the oxidized samples in oxygen and in air, especially at longer oxidation time (Figures 4.15(c) and (g)) reveal heterogeneities between grains of diverse orientations and at grain boundaries. In oxygen and in air, both different orientations on some grains are revealed by the presence of both black (darker) and white (brighter) areas in the same grain. BSE micrographs confirm the homogeneities of the oxide on samples oxidized in water vapor (Figure 4.15(f)) and the heterogeneities on the ones oxidized in oxygen and in air (Figure 4.15(d) and (h)) and significantly show that the oxides grown on grain boundaries can be distinguished from the ones on grain bulk. A darker zone at grain boundary (resp. a brighter in grain area) corresponds to a lower (resp. a higher) flux of backscattered electrons due to a lower (resp. a higher) atomic number (Z) element located at grain boundary (resp. in grain area). Since thermal oxide grown on Ni–based alloys mainly contains Ni, Fe, and Cr [29–33], chromium, which has the lowest atomic number among these three elements should be the major element forming oxide at grain boundary. Furthermore, the BSE images can also distinguish the difference on each orientation of grain area, which should correspond to the difference in chemical composition or amounts of the oxides. For the case of the sample oxidized in oxygen 30 h (Figure 4.15(c) and (d)), SE and BSE micrographs show the coincidence between the black and the white areas in each grain. The black and the white in BSE can suggest that the black area refers to be more chromium rich while the white ones

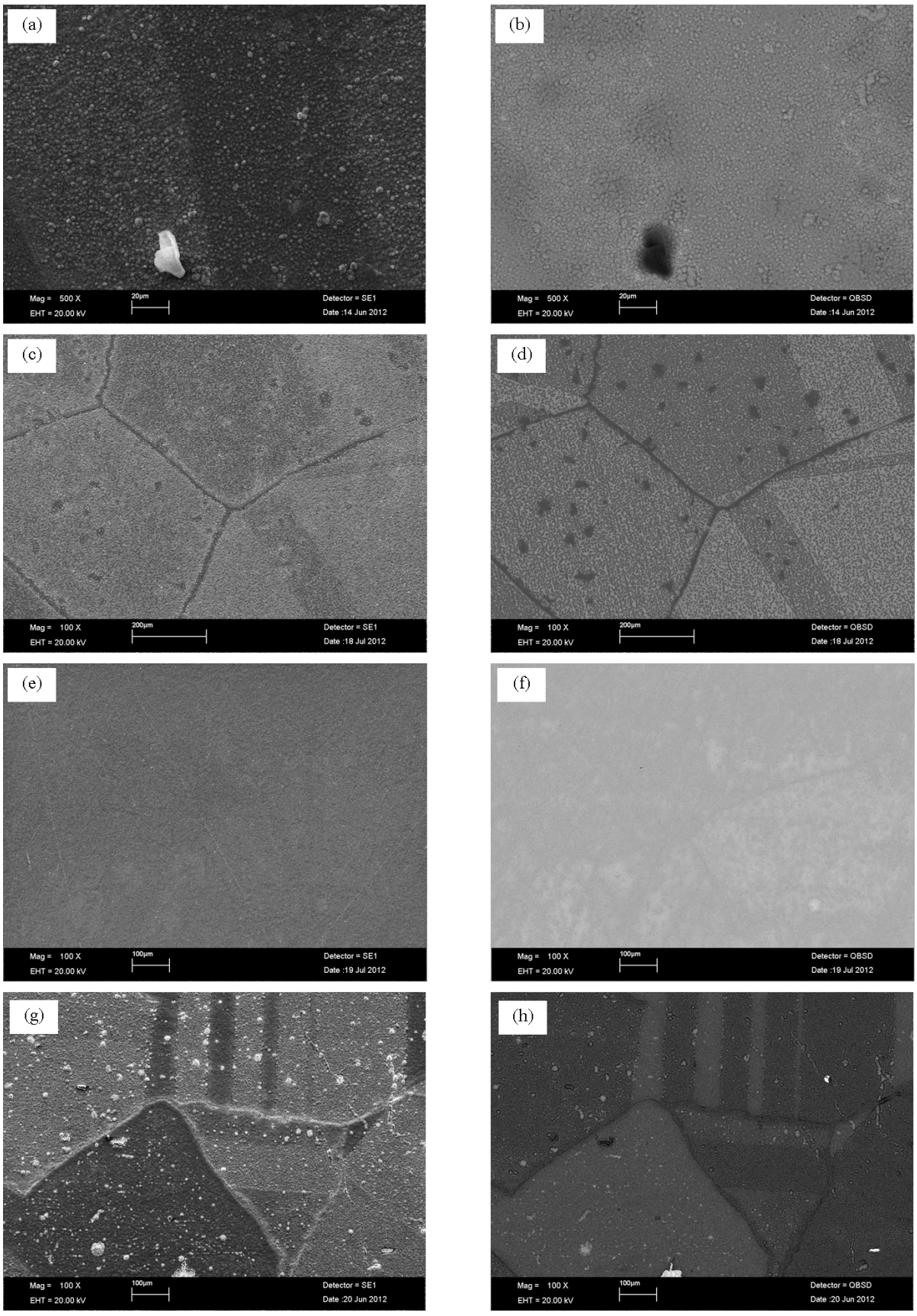

Figure 4.15 Secondary (images in left hand side) and backscattering (images in right hand side) electron micrograph of thermal oxide grown on oxidized Alloy 690: (a) (b) in oxygen for 2 h, (c) (d) in oxygen for 30 h, (e) (f) in water vapor for 30 h, and (g) (h) in air for 21 h

could include more nickel and/or iron components. The orientation plays an inversed role compared to the case of the sample oxidized in air (Figure 4.15(g) and (h)) by revealing chromium rich (resp. nickel and iron rich) oxides on the white (resp. the black) areas on the SE micrographs.

Figure 4.16 illustrates a possible organization of the oxide scales based on the EDS results obtained on the oxidized samples of Figure 4.15. In oxygen, especially in Figure 4.16(b), the elemental analysis at grain boundaries entirely differs from that of the ordinary grain, tending to show pure chromium oxide at grain boundary while the combination of Cr, Ni, Fe oxides is observed on grains. These results are in agreement with those of the preceding paragraph. Major oxide of Cr is generally detected while Ni and Fe become more in quantity when time increases. The orientations differences result in nodules with different compositions. However the case of the sample oxidized in oxygen 30 h remains unclear because the oxide (Figure 4.16(b)) shows a more chromium–rich oxide on the white area contrary the BSE micrographs which presented chromium–rich oxide on the black one. In water vapor (Figure 4.16(c)), the homogeneous oxide matrix contains more Cr than Ni and more Ni than Fe; the nodules are composed of the same elements but with more Fe than Ni. In air (Figure 4.16(d)), on heterogeneous oxide is again observed. At grain boundary, the main oxide is chromium oxide with traces of Ni and Fe signals, while, on grain areas, oxides in the matrix and nodules exhibit mainly Cr but also Ni and Fe in low concentrations. Furthermore, the signals of Ni and Fe elements compared to the ones of Cr in grain areas are higher in black zones which suggest that a more chromium–rich oxide is presented on the white areas as observed on the above SEM micrographs.

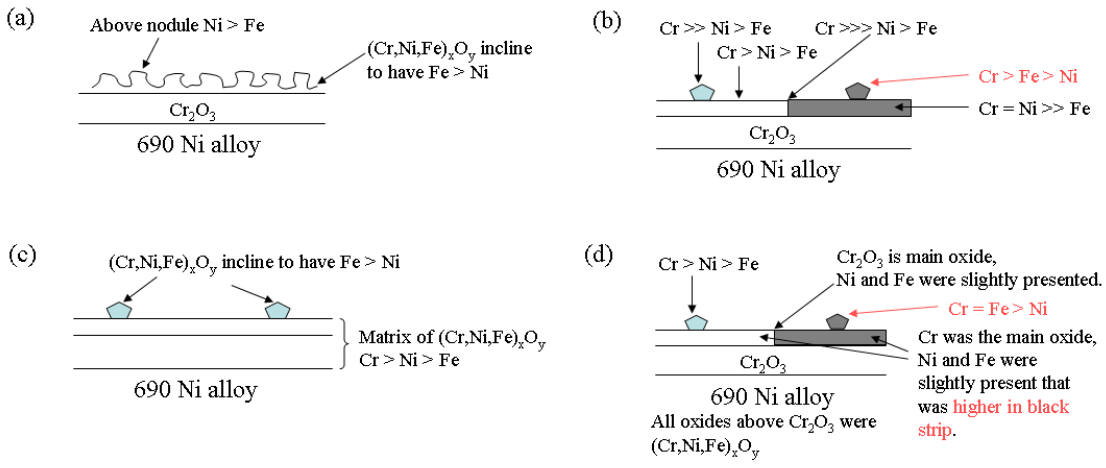

Figure 4.16 Model of oxide scales aspects based on X–ray analysis (EDS) of oxidized Alloy 690: (a) in oxygen for 2 h, (b) in oxygen for 30 h, (c) in water vapor for 30 h, and (d) in air for 21 h

At this point, it is clear that, as expected, the oxidation of Ni–based alloy 690 depends on the oxidizing atmospheres, on the exposure time, and on the surface orientation of the metallic grains. Chromium is the major metallic constituent of the oxides overall on the surface, but oxides containing Ni and Fe are also present. In oxygen and in air, a heterogeneous film is observed with most of chromia at grain boundary. Oxides combining the presence of Cr, Fe, and Ni oxides were found on the grains surfaces. Surface orientation plays a role on the chemical compositions and quantities of the oxides. In water vapor, the mixture of oxides formed homogeneously over the surface with mainly chromium oxide and a slight distribution of nodules of the mixed oxides of Cr, Fe, and Ni over the surface. From all these results, it could be assumed that chromia (or Cr–rich oxide) was the first oxide which developed on surface, and that Fe and Ni then diffused through chromia and formed their oxides as an outer layer with a propagation of oxide nodules depending on the oxidation conditions and the surface orientations.

It has also to be pointed out that such thermal scales appear very complex, for their contained various components and for the latter are more or less heterogeneously distributed both in the depth of the scale (perpendicularly to the scale's surface) and laterally (parallel to the to the scale's surface). The choice of such samples, although being very challenging, was made to assess the limits of multiscale photoelectrochemical characterizations.

4.3.2 Overview of the photovoltammograms and of the semiconducting behavior of the oxide layers

Figure 4.17 exhibits macroscopic photocurrent voltammograms recorded at several photon energies on samples oxidized in several oxidation conditions.

The shapes observed on the curves corresponding to short time oxidation in oxygen (Figure 4.17(a)) show both n–type (at energies below 3.1 eV) and p–type (at energies above 3.1 eV) behaviors. For samples oxidized in the same atmosphere but for longer time (Figure 4.17(b)), if the high energy behavior still seems to sign p–type behavior, the V–shaped form observed in the low energy range around the minimum of photocurrent tends to indicate a more insulating sample.

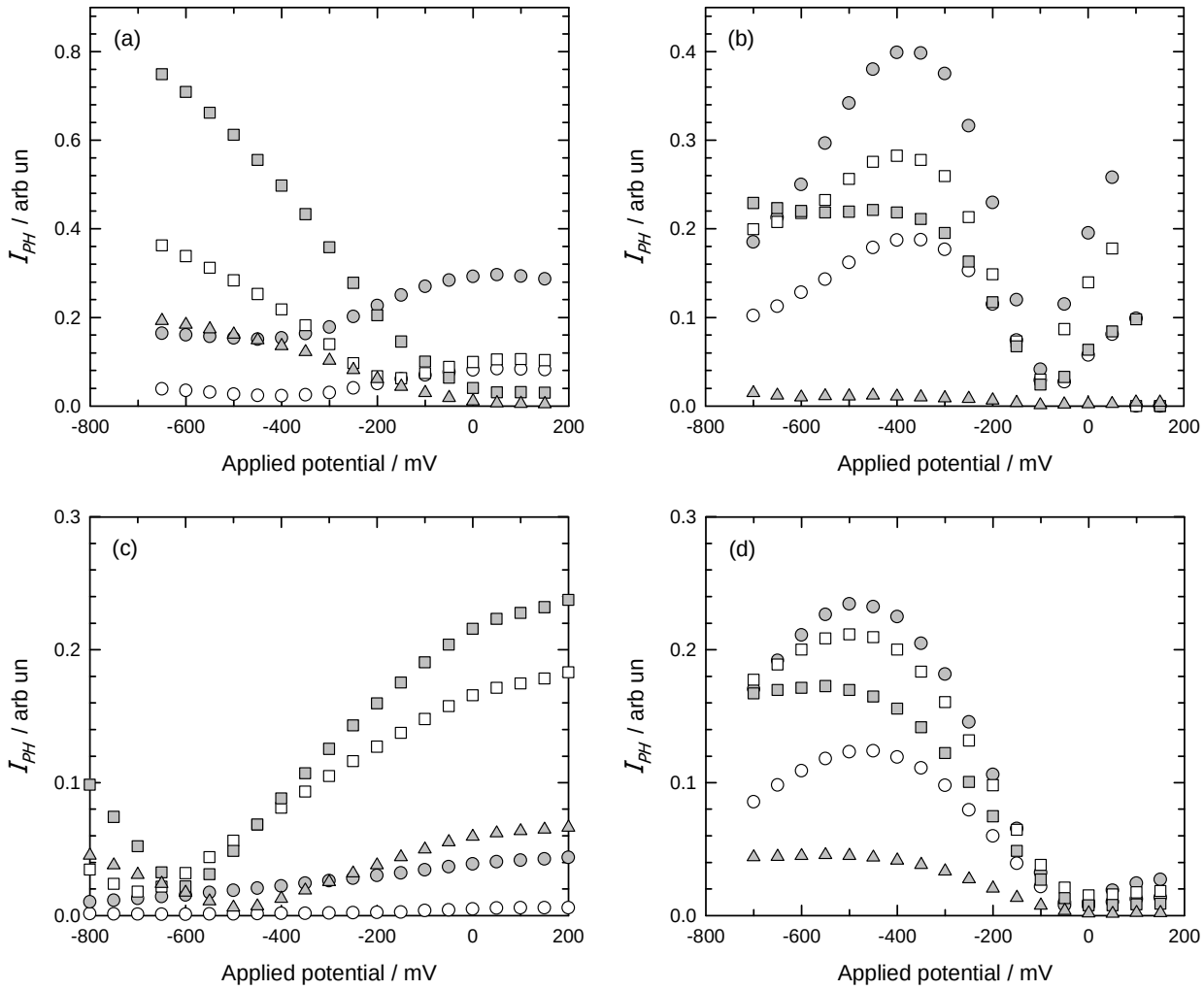

Figure 4.17 Typical as measured photocurrent amplitude (modulus) versus applied potential curves obtained at hν = 2.54 eV (○), hν = 3.10 eV (●), hν = 3.54 eV (□), hν = 4.08 eV (■), and hν = 4.66 eV (△), on the whole surface of Alloy 690 oxidized (a) in oxygen for 2 h, (b) in oxygen for 30 h, (c) in water vapor for 30 h, and (d) in air for 21 h

On the contrary, in the case of the samples oxidized for 30 hours in water vapor (Figure 4.17(c)), the photovoltammograms tend to indicate the overall combination of insulating and n–type behaviors, which confirms that the presence of water vapor promotes n–type semiconduction in some of the oxides.

Besides, it should be noted that potential of the minimum of the photocurrent modulus is cathodically shifted for the "water vapor" samples compared to the "oxygen" samples, which could be attributed to that flatband potentials of n–type semiconductors are more negative than those of p–type, at least for a same semiconductor.

The results obtained for the case of the sample grown in air for 21 hours (Figure 4.17(d)) are very similar to those obtained for the sample grown in oxygen for 30 hours,

except that the V–shaped contribution appears to be lower, perhaps due to the shorter time of oxidation.

To conclude this section, we would like to mention that the above remarks should be considered only as rough, averaged trends, for the number of components in the layers certainly is higher than two.

4.3.3 Photocurrent energy spectra of oxide layers: bandgap assessment of their components

4.3.3.1 Macroscopic characterizations: usual analysis of the linear transforms

Figure 4.18 collects the macroscopic photocurrent energy spectra measured at several applied potentials on each sample (left hand side) and their linear transforms (right hand side) for the samples oxidized over more than 21 hours. Indeed, the shape of all the spectra strongly depends on the applied potential, always showing the presence of more than one constituent in the layers.

In oxygen (Figure 4.18(a) and (b)), the spectra allow to distinguish at least four components with the bandgap at around 1.8 eV, 2.7–2.8 eV, 3.5–3.6 eV, and > 4.0 eV.

In air (Figure 4.18(c)), the spectra recorded at –600 mV and –300 mV exhibit similar shapes whereas the one recorded at 0 mV has a different shape (Figure 4.17(d)). Linear transforms in Figure 4.18(d) revealed three or four components with bandgap energies located at around 1.8 eV, above 3.5 eV, and some between them, when the applied potentials were –600 mV and –300 mV, while bandgaps of less than 2 eV, 2.3 eV, and 3.1 eV are suggested when the applied potentials was 0 mV.

In water vapor (Figure 4.18(e)), the photocurrent contributions below 3.0 eV became very low, showing that water vapor promoted high bandgap energy (above 3.0 eV) oxide phases but disfavored the development of lower bandgap energy oxide phases. Figure 4.18 (b) tends to account for at least four oxides with bandgap at < 2.9 eV, 2.9–3.1 eV, 3.7–3.9 eV and > 4.0 eV.

However, the high complexity of the shapes of the above presented PES and of their linear transforms prevents us from giving definitive conclusions neither on the number of components in each thermal scale nor on the bandgap values of the components. Therefore, each of the spectra was analyzed and fitted using the novel method described in Chapter 2. The corresponding results will be presented in the next section.

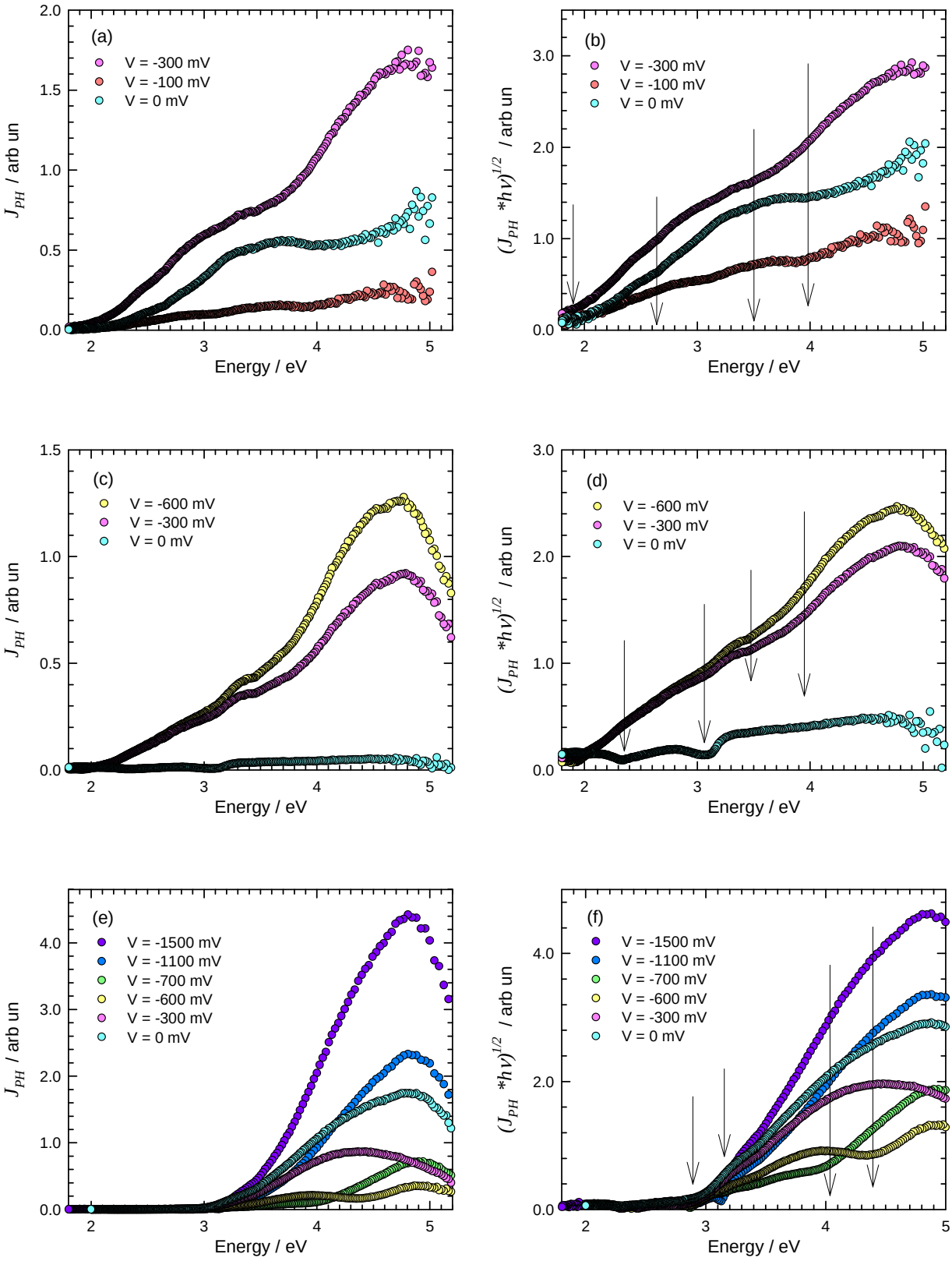

Figure 4.18 Photocurrent versus photon energy (left hand side) and its linear transform (right hand side) obtained on the whole surface of oxidized Alloy 690 (a) (b) in oxygen for 30 h, (c) (d) in air for 21 h, and (e) (f) in water vapor for 30 h

4.3.3.2 Macroscopic characterizations: fitting of the photocurrent energy spectra

For each photocurrent energy spectrum, the real ($Re(J_{PH})$) and imaginary ($Im(J_{PH})$) parts of the complex photocurrents, J_{PH}, were first calculated, at each tested energy, E, from the experimental values of the modulus $| J_{PH} |$ and of the phase shift, θ.

Then, several values of the possible number of components, *m*, in the scale, were successively assumed. For each *m* value, 50 to 100 fit attempts were run, according to the fit conditions given in Chapter 2, to ensure the stability of the final parameters obtained from the fits. The latter final parameters, including the m value, were validated when corresponding, among the whole set of fits, to the minimum distance between the experimental real and imaginary spectra and the corresponding spectra calculated from the fit final parameters, and when not obviously duplicating components with very close bandgaps [3].

It has to be emphasized that, excepted in a very few cases which will be identified in the text, all the PES fits were run allowing all parameters to be fitted, starting from random values, and that, consequently, the PES spectra measured at several applied potentials for the same sample were fitted independently.

In the following of present section, only the bandgap values obtained from the fits will be given and discussed. For each presented fit result, the value obtained for m will be given, together with three linear correlation coefficients (LCC), C–M, C–Re, C–Im, expressing the correlation between the experimental and the calculated values for the curves : $| J_{PH} | = f(E)$, $Re(J_{PH})$ an $Im(J_{PH})$ respectively.

4.3.3.2.1 Samples oxidized in oxygen for 30 hours

Figure 4.19 shows the experimental and fitted spectra at each tested potential value for Alloy 690 oxidized in oxygen for 30 h. Eight semiconducting phases (*m* = 8) were found when polarizing at 0 mV whereas seven semiconducting phases (*m* = 7) were found at –100 mV and –300 mV. The latter difference is not surprising knowing all the semiconducting components do not necessary yield photocurrent at every tested potential, it has to be noted that *m* is twice the number of components which could be more or less clearly assessed from the usual linear transform analysis in section 3.3.1. Figure 4.20 summarizes the fitted bandgap values; among them, appear to be six present at each potential with bandgap at around 1.5 eV, 2.0 eV, 2.7 eV, 3.1 eV (which could be n–type because it is only observed at the most anodic potentials), 3.5 eV (which could be p–type because it only appeared at the cathodic potential), and 4 .0 eV.

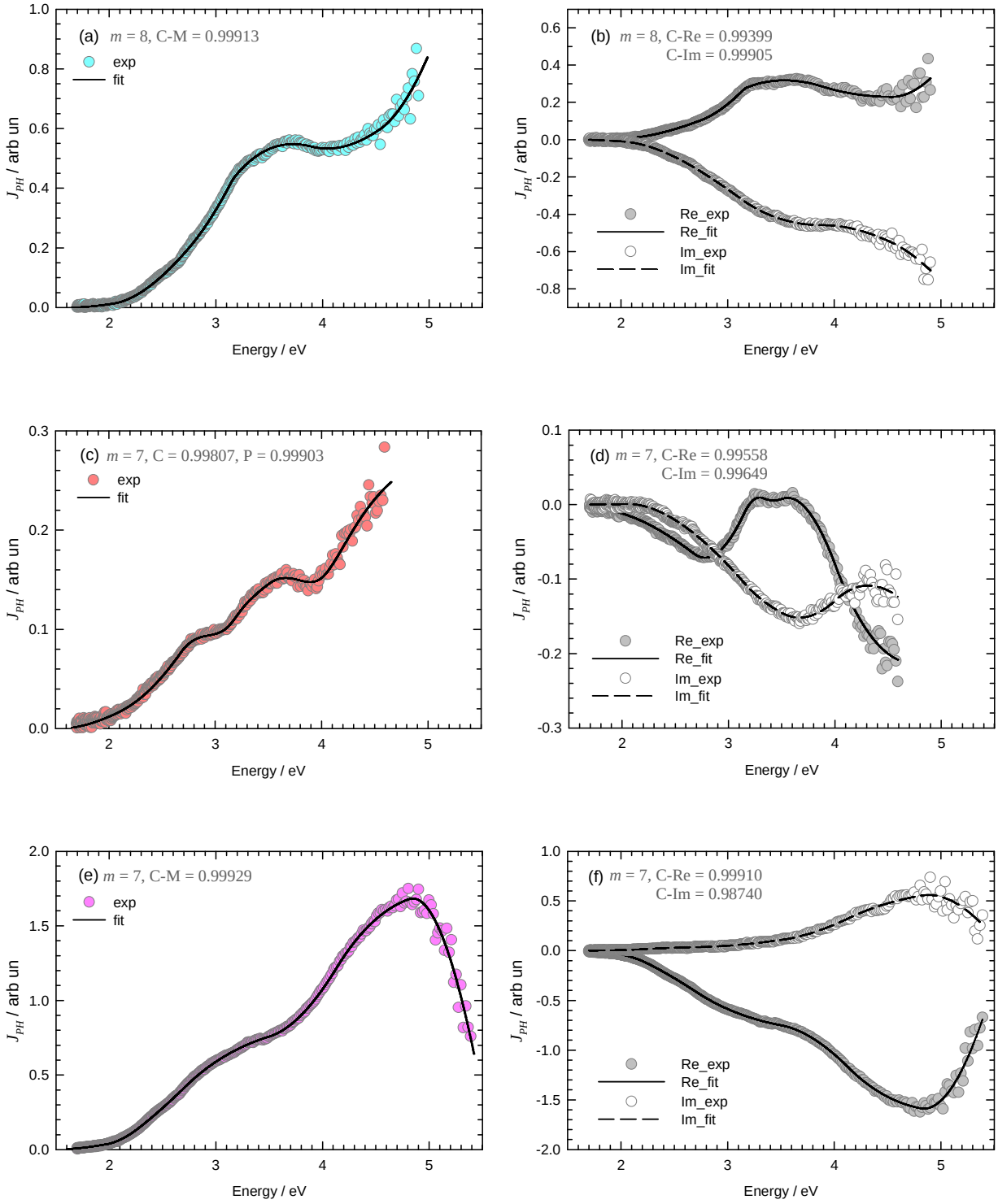

Figure 4.19 Photocurrent energy spectra of Alloy 690 oxidized in oxygen for 30 h (left hand side), and its real part and imaginary part (right hand side): (a) (b) at 0 mV, (c) (d) at –100 mV, and (e) (f) at –300 mV. "exp" and "fit" account for experimental and fitted data. "Re" and "Im" are used for the real and imaginary parts of J_{PH}.

From literatures, the bandgap of $NiFe_2O_4$ was reported at 1.7 eV by Peng et al. [34] whereas other studies located its value at 2.5 eV [35, 36]. The bandgap of Cr_2O_3 is usually given as 3.5 eV [37–40], but also reported at 3.0 eV for the internal subscale [41]. The bandgap of $NiCr_2O_4$ was reported at 4.1 eV, according to the work

of Marchetti et al. [35] and Zhang et al. [36]. In addition, due to the high sensitivity of the photoelectrochemical techniques, it is likely that corundum oxide [42], Fe_2O_3 (E_G = 1.9 eV – 2.3 eV) and $Fe_{2-x}Cr_xO_3$ (E_G = 2.4 eV – 2.9 eV), should also be taken into account. Therefore it can be proposed that the oxide layer on this sample is composed of either Fe_2O_3 or $NiFe_2O_4$ ($E_G \cong$ 2.0 eV), Cr_2O_3 (E_G = 3.1 eV and 3.5 eV), and $NiCr_2O_4$ (E_G = 4.0 eV). The nature of the oxides with bandgaps at 1.5 eV and 2.7 eV still remains unclear, however the second has a possibility to represent a Cr–rich solid solution of corundum $Fe_{2-x}Cr_xO_3$ or a solid solution of spinel $NiFe_2O_4$–$NiCr_2O_4$ with unknown ratio.

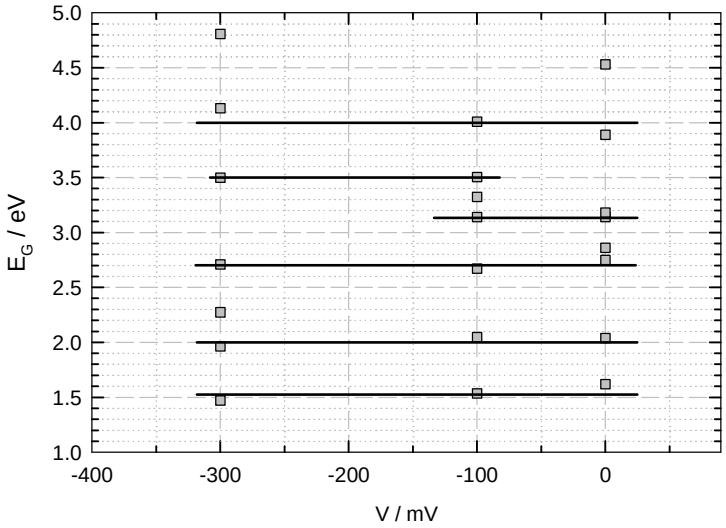

Figure 4.20 Plot summarizing the bandgap (E_G) obtained from the fits presented in Figure 4.19

4.3.3.2.2 Samples oxidized in air for 21 hours

Figure 4.21 shows the experimental and fitted spectra at each tested potential value for Alloy 690 oxidized in air for 21 h. To minimize the distance between experimental and calculated spectra, and to obtain convincing fitted curves, especially for the spectrum recorded at 0 mV, the number of components clearly need to be increased. Eleven semiconducting phases (m = 11) were necessary for the spectrum recorded at 0 mV whereas ten semiconducting phases (m = 10) were found at –300 mV and –600 mV. The fitted bandgap values shown in Figure 4.22 appear very close together for the PES obtained at –300 mV and –600 mV. They however are slightly different from the ones obtained at 0 mV. This spectrum was the most difficult to fit correctly. Nevertheless the presence of nine oxide phases can be assumed with bandgap at 1.2 eV, 1.8 eV, 2.2 eV, 2.7 eV, 3.0 eV, 3.2 eV, 3.4 eV, 4.1 eV, and 4.7 eV.

The bandgaps obtained for alloy oxidized in air for 21 h could refer to constituents such as either Fe_2O_3 or $NiFe_2O_4$ (E_G = 1.8 eV and 2.2 eV), Cr_2O_3 (E_G = 3.0 eV, 3.2 eV and 3.4 eV), and $NiCr_2O_4$ (E_G = 4.1 eV). The bandgap at 2.7 eV could

be supposed to be Cr–rich $Fe_{2-x}Cr_xO_3$ or $NiFe_2O_4$–$NiCr_2O_4$ solid solution whereas the bandgap at 1.2 eV and 4.7 eV are still blind.

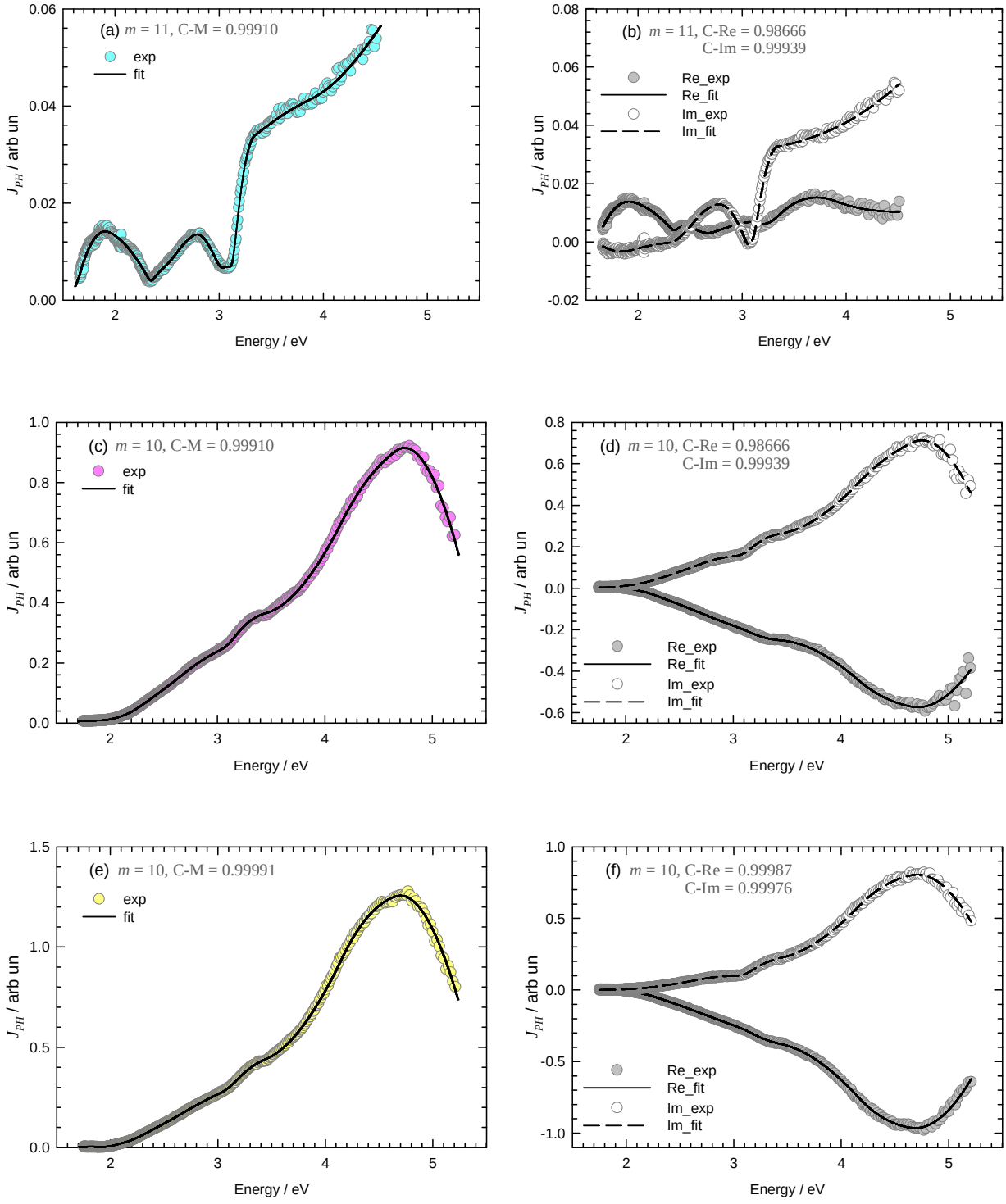

Figure 4.21 Photocurrent energy spectra of Alloy 690 oxidized in air for 21 h (left hand side), and its real part and imaginary part (right hand side): (a) (b) at 0 mV, (c) (d) at –300 mV, and (e) (f) at –600 mV. "exp" and "fit" account for experimental and fitted data. "Re" and "Im" are used for the real and imaginary parts of J_{PH}.

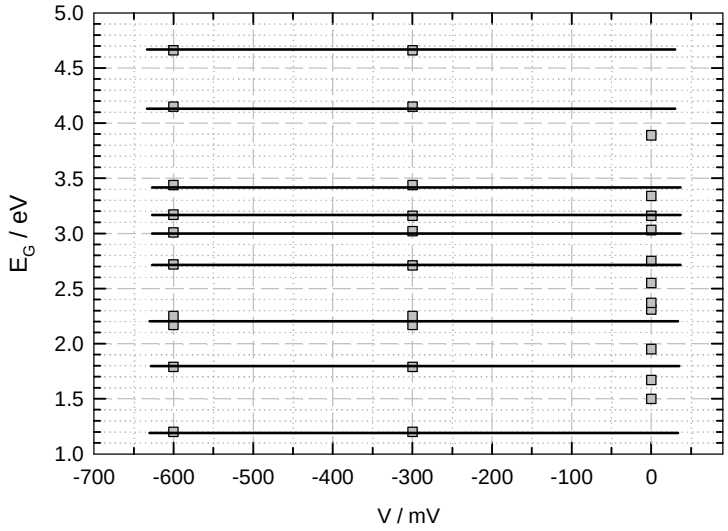

Figure 4.22 Plot summarizing the bandgap (E_G) obtained from the fits presented in Figure 4.21

4.3.3.2.3 Samples oxidized in water vapor for 30 hours

Figure 4.23 shows the experimental and fitted spectra at each tested potential value for Alloy 690 oxidized in water vapor for 30 h. Using m = 13 for all the tested potentials allowed to fit all the PES, and the fitted bandgap values at each potential are very close together as evidence in Figure 4.24. At any applied potential, the fit provided the same twelve bandgaps at 2.2 eV, 2.3 eV, 2.4 eV, 2.7 eV, 2.8(5) eV, 3.0 eV, 3.1(5) eV, 3.3 eV, 3.5 eV, 3.8 eV, 4.3 eV, and 4.7 eV (although there was some slight shifts at –600 mV which corresponds to the minimum of photocurrent on the photovoltammograms). Hence the whole evaluated bandgaps may be considered as reliable.

The fitted bandgaps obtained on alloy oxidized in water for 30 h again suggest the presence of Fe_2O_3 or $NiFe_2O_4$ (E_G = 2.2 – 2.4 eV), Cr_2O_3 (E_G = 3.0 – 3.5 eV), and $NiCr_2O_4$ (E_G = 4.3 eV). The bandgap at 2.7 eV and 2.8(5) eV could assume to be the corundum solid solution of with Cr–rich or the spinel solid solution oxide as the preceding results, and also the bandgap at 3.8 eV has a possibility to be Cr_2O_3 or spinel solid solution of $NiFe_2O_4$–$NiCr_2O_4$ with Cr–rich, whereas the bandgap at 4.7 is an unknown.

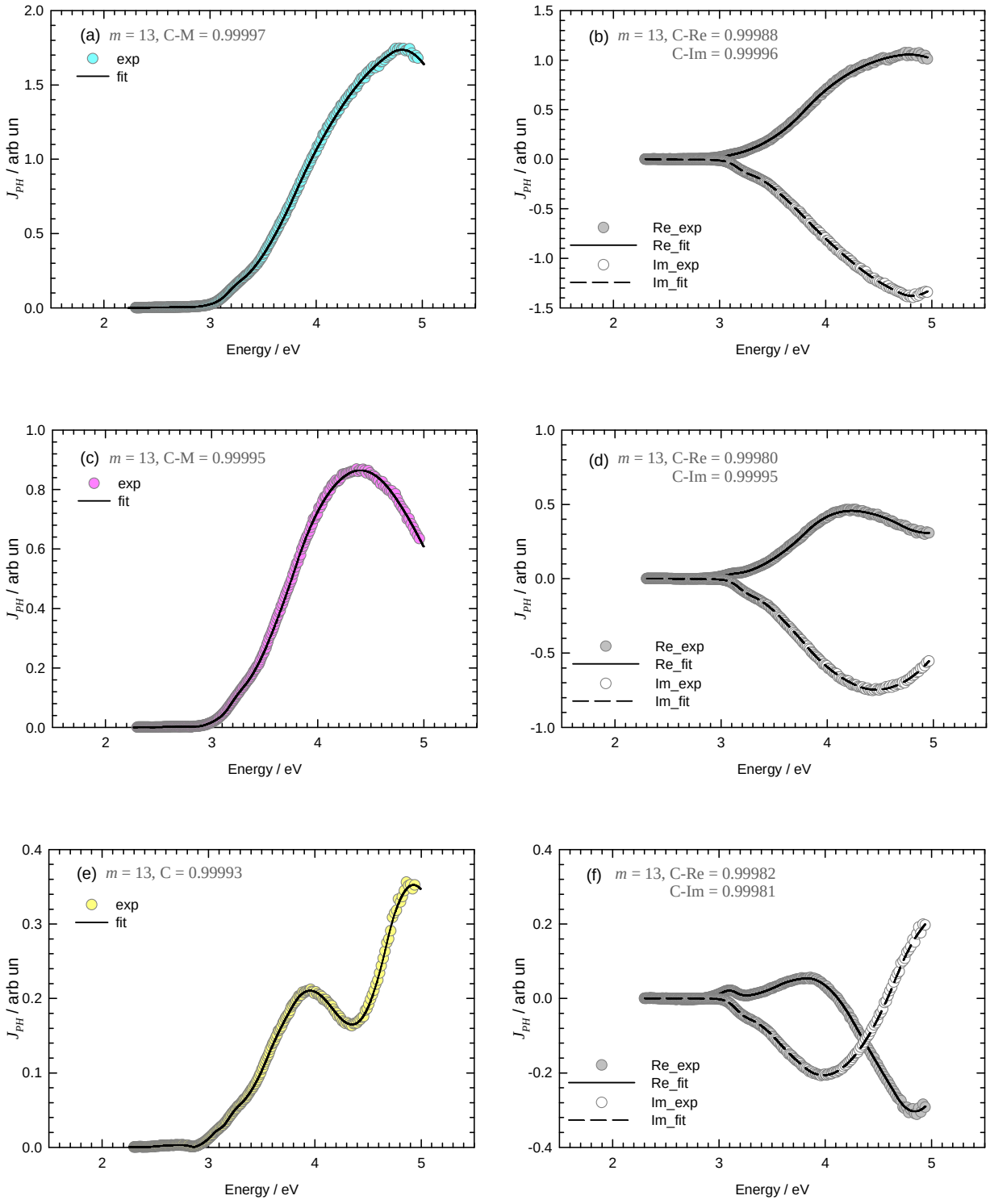

Figure 4.23 Photocurrent energy spectra of Alloy 690 oxidized in water vapor for 30 h (left hand side), and its real part and imaginary part (right hand side): (a) (b) at 0 mV, (c) (d) at –300 mV, (e) (f) at –600 mV, (g) (h) at –700 mV, (i) (j) at –1100 mV, and (k) (l) at –1500 mV. "exp" and "fit" account for experimental and fitted data. "Re" and "Im" are used for the real and imaginary parts of J_{PH}.

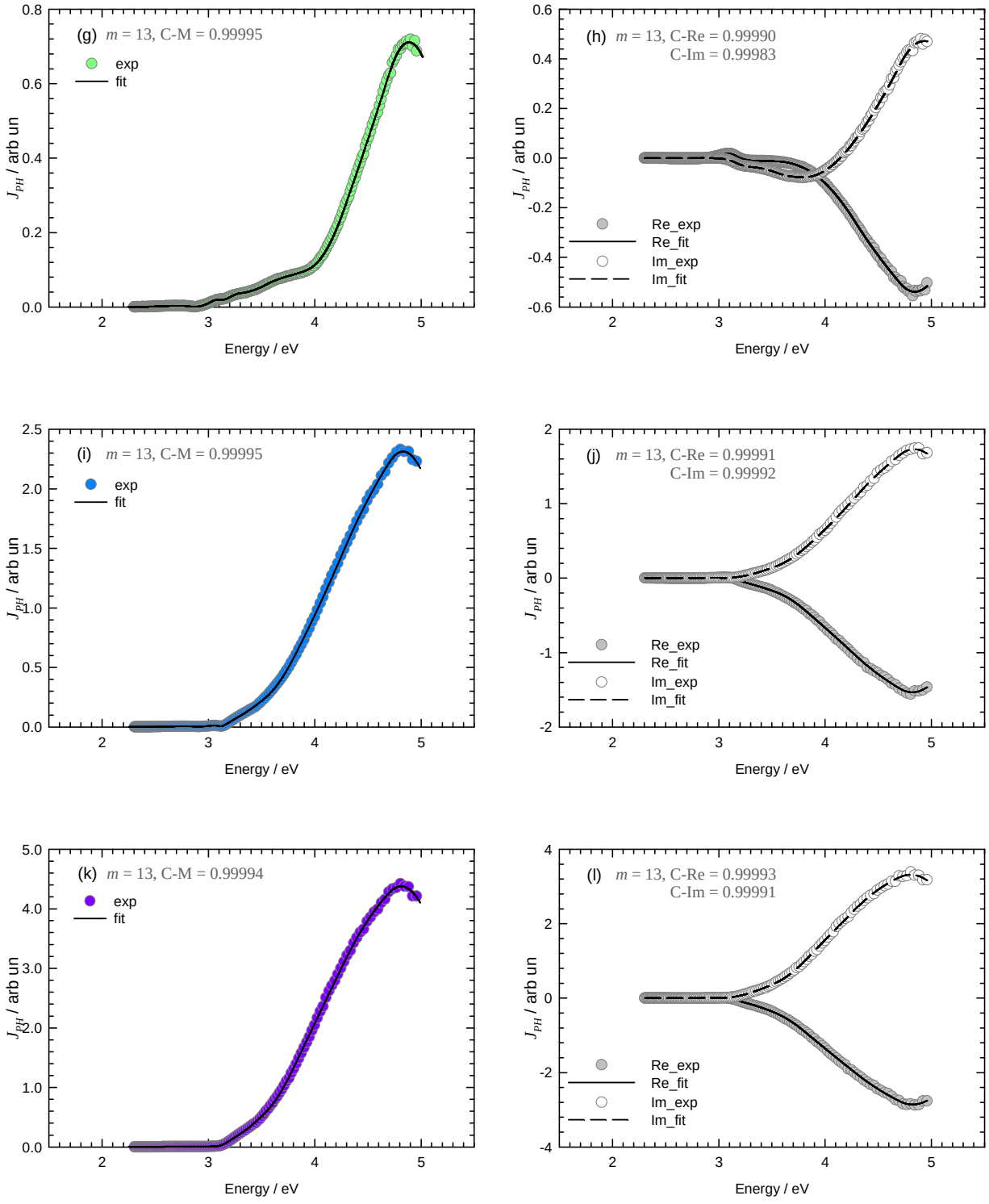

Figure 4.23(cont.) Photocurrent energy spectra of Alloy 690 oxidized in water vapor for 30 h (left hand side), and its real part and imaginary part (right hand side): (a) (b) at 0 mV, (c) (d) at –300 mV, (e) (f) at –600 mV, (g) (h) at –700 mV, (i) (j) at –1100 mV, and (k) (l) at –1500 mV. "exp" and "fit" account for experimental and fitted data. "Re" and "Im" are used for the real and imaginary parts of J_{PH}.

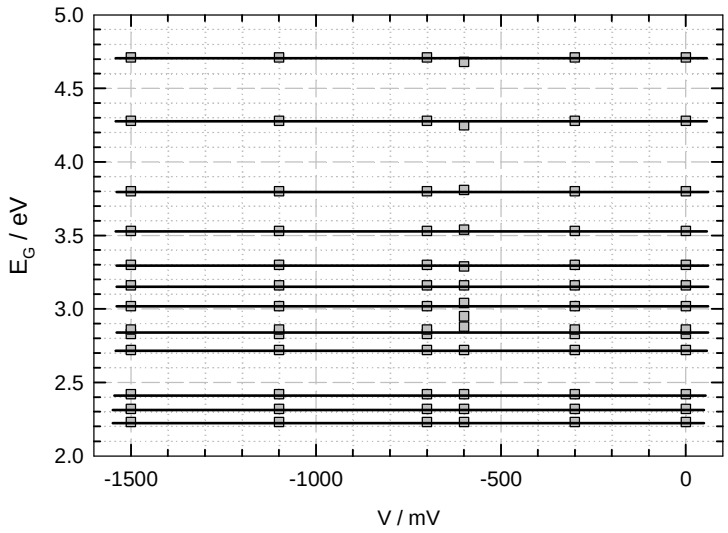

Figure 4.24 Plot summarizing the bandgap (E_G) obtained from the fits presented in Figure 4.23

From all the above results obtained at the macroscopic scale, two major trends can be stated:

– The PES model and the fitting procedure did apply on all samples, and yielded convincing fits and bandgap values.

– The number of semiconducting phases allowing convincing fits is high.

The latter trend was tought to be due to the presence of slightly different solid solutions $Fe_{2-x}Cr_xO_3$ from one zone to another on the surface. Mesoscopic investigations were thus under taken.

4.3.4 Mesoscopic photoelectrochemical characterizations

These experiments have been conducted on samples oxidized in oxygen for 30 hours, and in water vapor for 21h.

4.3.4.1 Samples oxidized in oxygen for 30 hours

Mesoscopic photocurrent energy spectra obtained on individual black and white area of an oxidized grain and also on a grain boundary of Alloy 690 oxidized in oxygen 30 h are presented in Figure 4.25. Figure 4.25(a) and (b) shows photocurrent obtained at 0 mV and –300 mV, these potentials being located respective above and below the potential corresponding to the minimum of photocurrent on the macroscopic photovoltammograms. The spectra obtained on grain boundary always showed in curve between the curves of the black and white areas because the beam size was bigger than the grain boundary area, providing the photocurrents issued from not only the grain boundary but also it issued from the neighboring grains. Hence the study at a definite grain boundary was not possible.

At V = 0 mV, the photocurrents obtained on the white area always to be higher than the one on black area, conversely with the photocurrents obtained at V = –300 mV that are higher on black area. The latter results also confirm the potential dependence of the PES shapes. Mesoscopic photocurrent energy spectra appeared also complex and difficult to analyze by means of calculated their linear transforms. Our model was thus applied again on the black and white spectra. The calculated spectra obtained from the fits and parameters are plotted and compared with the experimental data in Figure 4.26 and Figure 4.27. The corresponding assessed bandgap values are collected in Figure 4.28.

Since the photon fluxes available in mesoscopic mode were clearly lower than the macroscopic level, and for the specific lens added to the microscope did cut light above 4 eV, the energy spectra could only be recorded with an acceptable signal/noise ratio for photon energies lower than 3.6 eV. The data in Figure 4.28 indicate similar bandgaps on the black and white areas with values at around 1.8 eV, 2.0 eV, 2.7 eV, 3.1 eV, and 3.5 eV. The first (resp. the last) two bandgaps correspond with Fe_2O_3 and/or $NiFe_2O_4$ (resp. Cr_2O_3). From thermodynamics point of view, the higher Cr content in $Fe_{2-x}Cr_xO_3$ (E_G at around 2.7 eV) is pointed on the white area with a slight higher E_G value. Moreover, at –300mV, E_G = 3.1 eV absents on black area that can be implied more inward diffusion of Cr on white area.

Table 4.4 reports the ratio of photocurrent values measured on the white area to the one measured on the black area at two photon energies. In oxygen for 30 h, at V = 0 mV, the ratios are higher than 1.0, which indicates higher photocurrent obtained on white area, moreover, the higher ratio at low photon energy implies a lower Cr_2O_3 fraction on white area. Conversely, at V = –300 mV, the ratios are less than 1.0 which correspond to lower photocurrents obtained on white area, furthermore, the lower ratios at low photon energy suggests higher Cr_2O_3 fraction on white area.

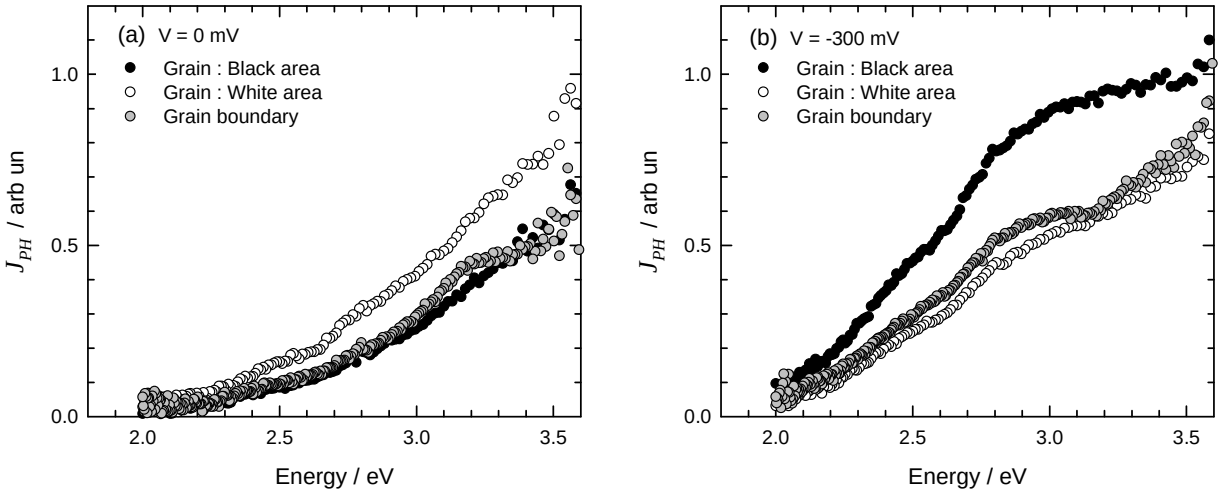

Figure 4.25 Mesoscopic photocurrent energy spectra obtained on specific areas of the sample surface: a grain boundary (gray circle), black (black circle) and white (white circle) areas of a grain for Alloy 690 oxidized at 900°C in oxygen for 30 h at: (a) V = 0 mV and (b) V = –300 mV

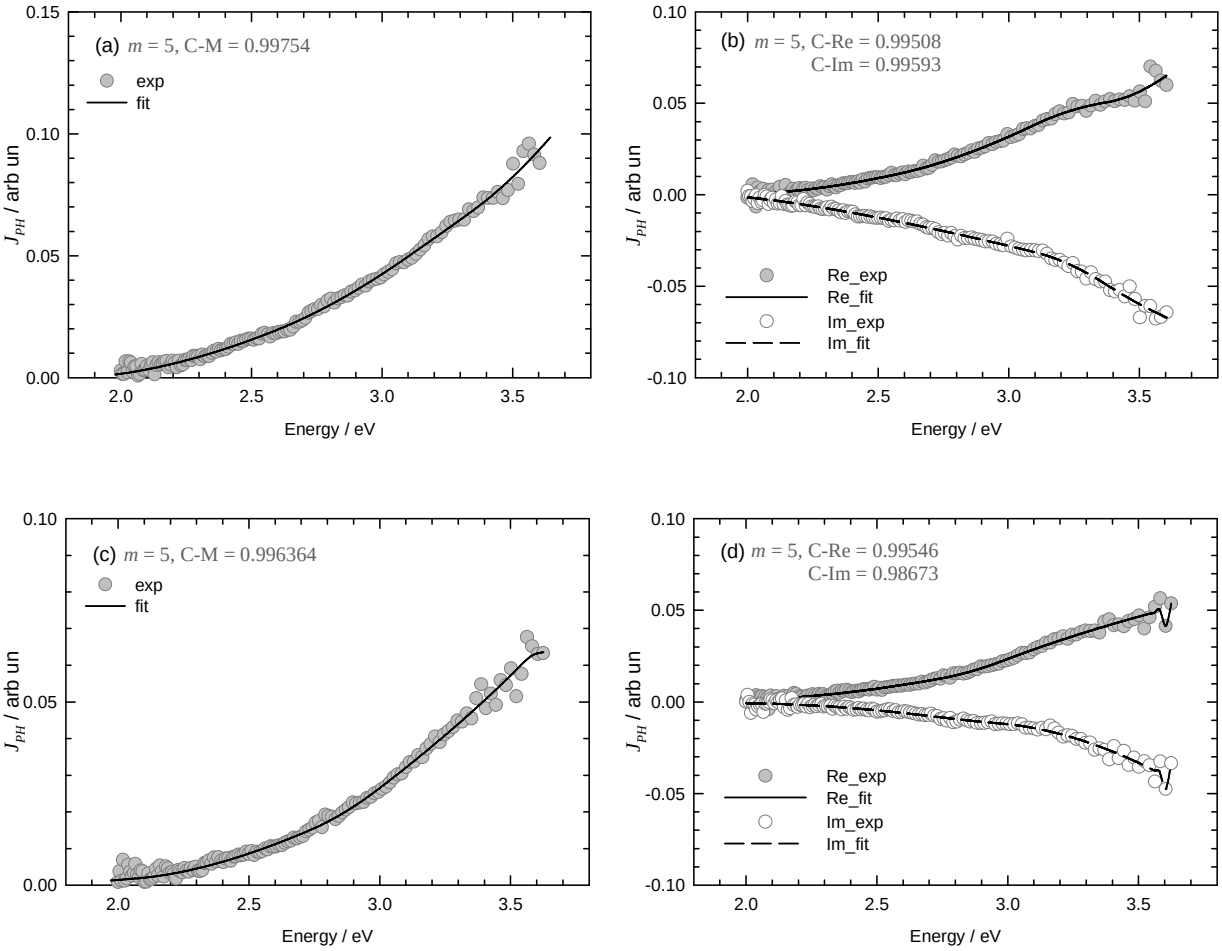

Figure 4.26 Mesoscopic photocurrent energy spectra measured at V = 0 mV Alloy 690 oxidized in oxygen for 30 h: plots of the modulus of the photocurrent (left hand side) and of its real and imaginary parts (right hand side): (a) (b) black area, and (c) (d) white area. "exp" and "fit" are for experimental and fitted curves. "Re" and "Im" correspond to the real and imaginary parts of the photocurrent.

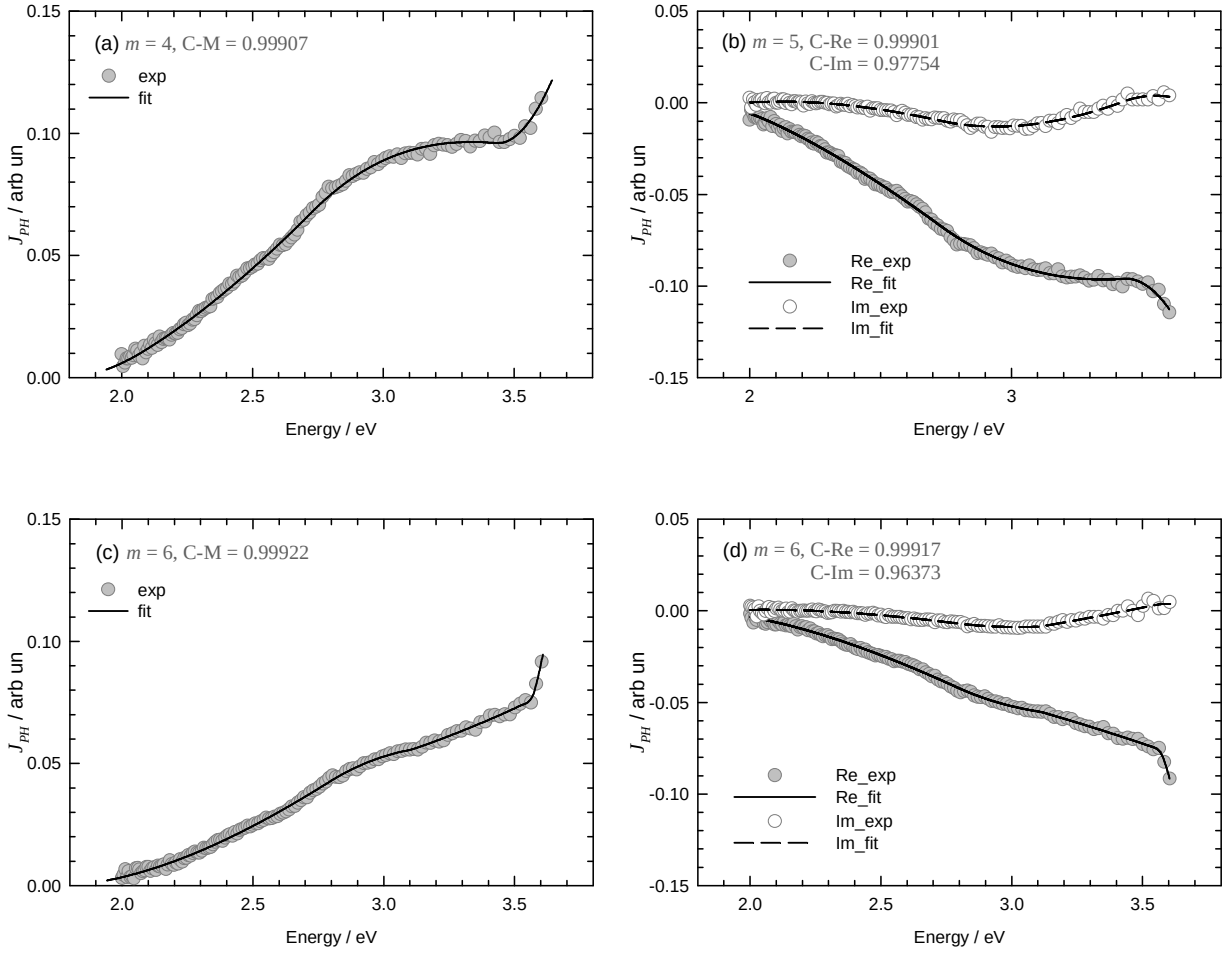

Figure 4.27 Mesoscopic photocurrent energy spectra measured at V = –300 mV Alloy 690 oxidized in oxygen for 30 h: plots of the modulus of the photocurrent (left hand side) and of its real and imaginary parts (right hand side): (a) (b) black area, and (c) (d) white area. "exp" and "fit" are for experimental and fitted curves. "Re" and "Im" correspond to the real and imaginary parts of the photocurrent.

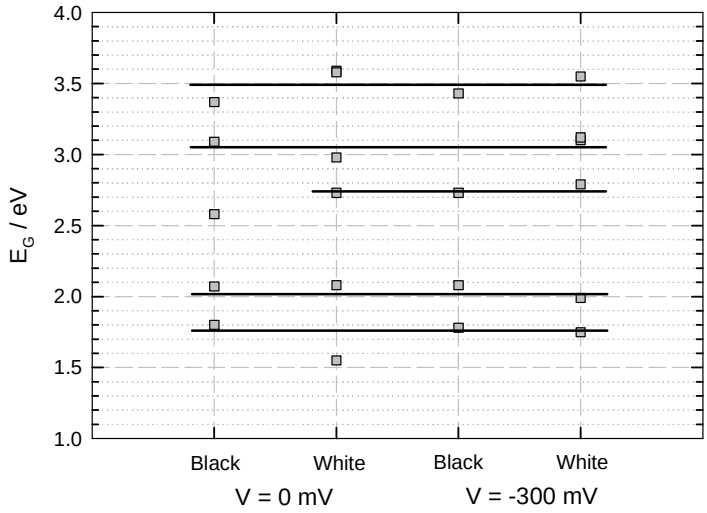

Figure 4.28 Bandgap values obtained from the fits, according to the results in Figure 4.26 and Figure 4.27

Table 4.4 Ratios of the photocurrent values measured on grain at white area to the ones measured at black area, as obtained from experimental data of Figure 4.25 and Figure 4.29

Oxidation conditions		In oxygen for 30 h		In air for 21 h
Applied potential		0 mV	–300mV	–300 mV
Photon energy	hν = 2.54 eV	1.9	0.5	3.1
	hν = 3.53 eV	1.6	0.7	1.7

4.3.4.2 Samples oxidized in air for 21 hours

Mesoscopic photocurrent energy spectra obtained on individual black and white areas of the sample oxidized in air for 21 h are illustrated in Figure 4.29. The PES clearly show different shapes between black and white photocurrents, and also that the white area provides higher photocurrents, as expressed by the ratio given in Table 4.4. When dividing the values at 3.53 eV by the ones at 2.54 eV, it can be so defined ratio is twice higher on the black grain, which could suggest that Cr_2O_3 (resp. $NiFe_2O_4$) is more present on the black grain (resp. the white grain).

The spectra could be recorded and fitted the energy range [2.1 – 3.75 eV], as illustrated in Figure 4.30. The obtained *m* values were 4 and 5 for black and white areas respectively; however, the highest bandgap value found on the white area, 3.66 eV, is so close to the limit of the available photon energy range that it prevents us to affirm that a component having this bandgap is really present in the scale. The obtained bandgap values (Figure 4.31) are different from one zone to the other but some close values are found between zones. Bandgap at around 2.7 eV also presents a slightly higher value on the white area, referring the higher Cr content in $Fe_{2-x}Cr_xO_3$.

Table 4.5 reports fitted bandgap energies obtained from macroscopic and mesoscopic mode. Since the photocurrents in macroscopic scale issued from all parts of the sample surface, so the bandgap provided by the whole surface should include the bandgaps observed at the meso–scale. Table 4.5 shows a reasonable agreement, hence indicating that the presence of diverse bandgaps obtained from macroscopic PEC refers either to different oxides or oxides with different stoichiometries that can be located on the same and/or the different surface areas.

Even though mesoscopic photoelectrochemical could not cover the whole energy range that would have allowed to examine the cases of the higher bandgaps, the above results confirm the surface orientation dependence of Alloy 690 as concerns the oxidation products.

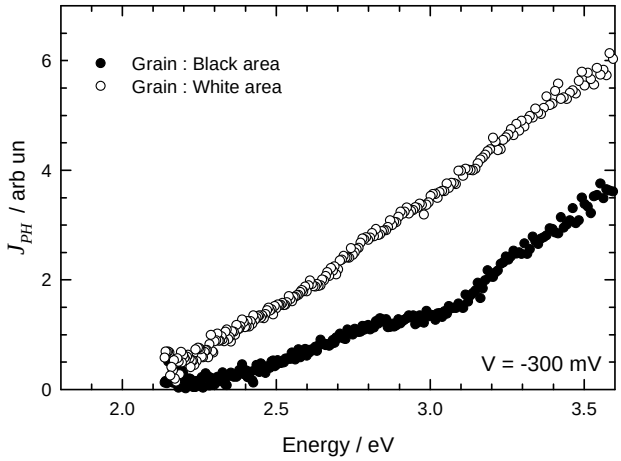

Figure 4.29 Mesoscopic photocurrent energy spectra obtained on individual black (black circle) and white (white circle) area of alloy 690 oxidized in air for 21 h

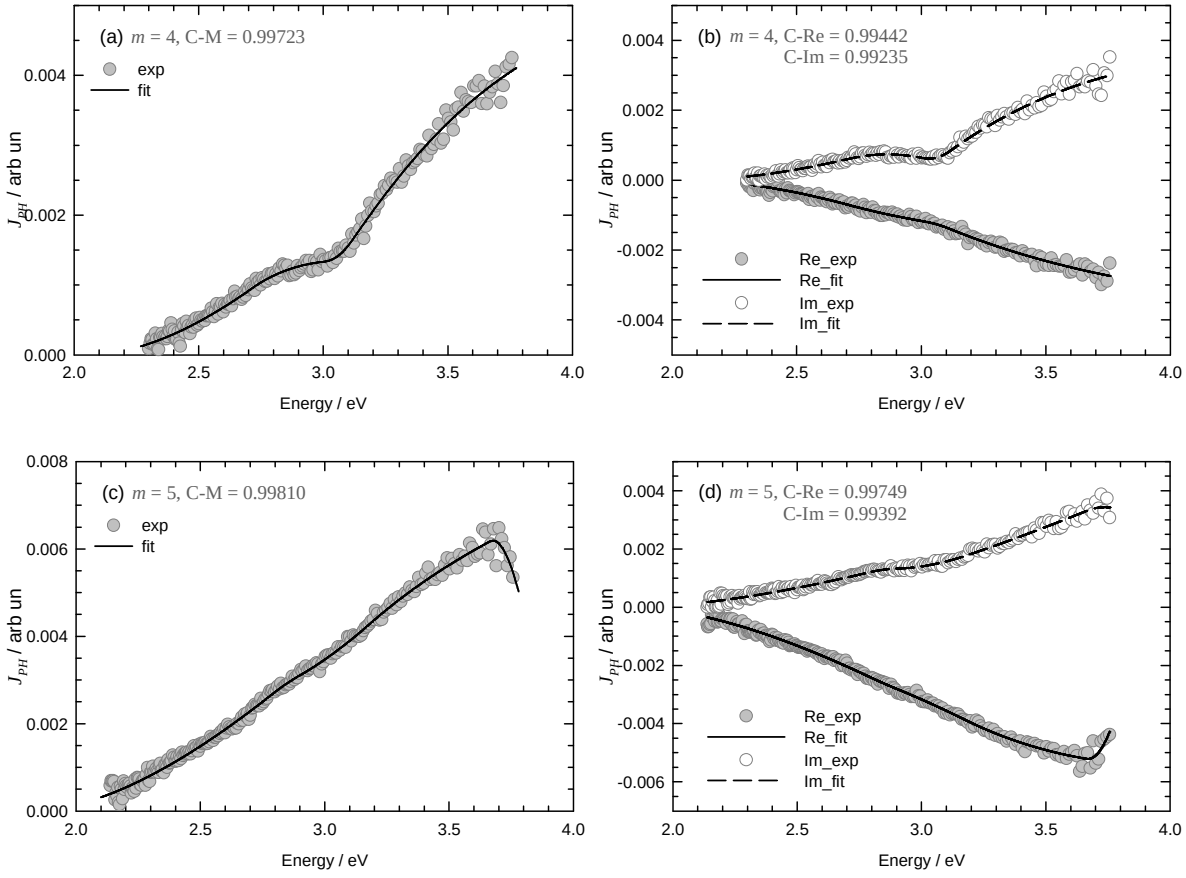

Figure 4.30 Mesoscopic photocurrent energy spectra measured at V = –300 mV Alloy 690 oxidized in air for 21 h: plots of the modulus of the photocurrent (left hand side) and of its real and imaginary parts (right hand side): (a) (b) black area, and (c) (d) white area. "exp" and "fit" are for experimental and fitted curves. "Re" and "Im" correspond to the real and imaginary parts of the photocurrent.

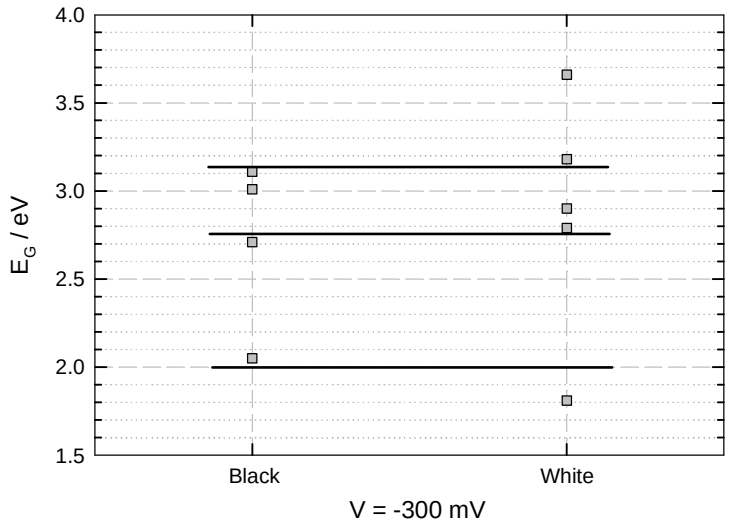

Figure 4.31 Bandgap values obtained from the fits, according to the results in Figure 4.30

Table 4.5 Summary of the bandgap energies, E_G, obtained by fitting the photoelectrochemical energy spectra of Alloy 690 oxidized in air for 21 h (values are given in eV). The bandgap range covers from 1.5 eV to 3.7 eV. The characterizations are performed at –300 mV.

macroscopic		1.79	2.17	2.25	2.71	3.02	3.16	3.44
mesoscopic	Black		2.05		2.71	3.01	3.11	
	white	1.81			2.79	2.90	3.18	3.66

4.3.5 Microscopic photoelectrochemical characterizations

The coherent light of laser lines at 2.54 eV and 3.53 eV were used to record photoelectrochemical images. The lower energy line can produce photocurrent from $NiFe_2O_4$, Fe_2O_3 and $Fe_{2-x}Cr_xO_3$ (Fe–rich) whereas the higher one can generate photocurrent from all previous oxides and also from the ones with higher bandgap energies such as Cr_2O_3. However these laser lines can not activate $NiCr_2O_4$ whose bandgap energy is above 4.0 eV.

A sufficiently contrast could not always be obtained, only the case of samples oxidized in air for 21 h will be presented here.

Figure 4.32 displays typical optical image and photoelectrochemical images obtained for such samples. Both photoelectrochemical images in Figure 4.32(b) and (c) illustrate lower photocurrents at grain boundary and also on black area. According to the PEC image performed by 2.54 eV laser line, low bandgap oxides are more presented on the white area than on the black area and on grain boundary. Furthermore, the half decreasing of image contrast at 3.54 eV, which is an agreement with the mesoscopic results in Table 4.4, infers that the Cr_2O_3 fraction on the white area is lower than on the black area.

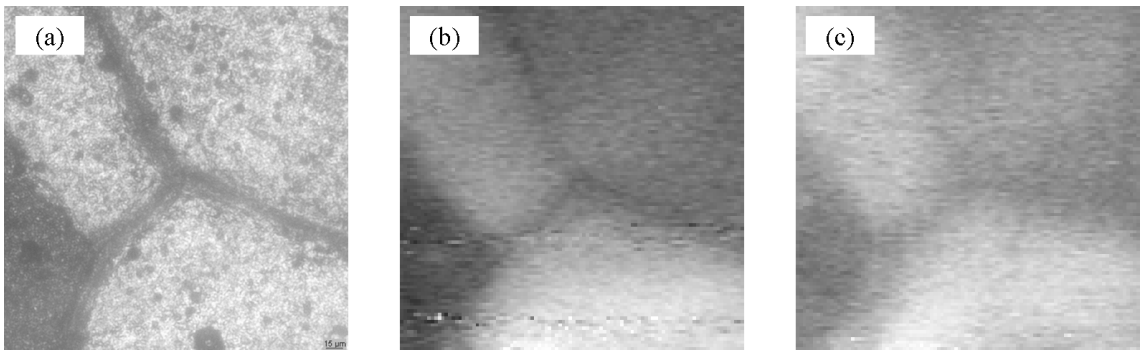

Figure 4.32 Image set of Alloy 690 oxidized in air for 21 h; (a) optical images, (b) and (c) photoelectrochemical images recorded at –300 mV: (b) hν = 2.54 eV, and (c) hν = 3.54 eV

4.3.6 Raman spectroscopy characterizations

Works reported in the literature indicated a predominant characteristic Raman peak at around 550 cm^{-1} for Cr_2O_3 [43–46], from 694 to 706 cm^{-1} for $NiFe_2O_4$ [47–49], and from 682 to 687 cm^{-1} for $NiCr_2O_4$ [49–51]. Raman spectra of Alloy 690 oxidized under various atmospheres which are presented in Figure 4.33. All these spectra sign the presence of corundum oxides of Cr_2O_3 and of spinel oxide (either $NiFe_2O_4$ or $NiCr_2O_4$). Since thermal oxide grown in oxygen and in air obviously exhibit surface heterogeneities, Raman spectra were recorded on five specific zones: grain boundary, matrix and nodule on a black grain, and matrix and nodule on a white grain.

Raman spectra of sample oxidized in oxygen for 30 h (Figure 4.33(a)) obviously showed very strong signals of Cr_2O_3 with a lack of spinel oxide at grain boundary. Concerning the grain matrix of both black and white zones, the spectra evidenced the presence of Cr_2O_3 (around 556 cm^{-1}) as well as $NiFe_2O_4$ (around 693 cm^{-1}). Identical Raman shifts of spinel oxide were pointed at 680 cm^{-1} and 707 cm^{-1} for the nodules on the white grain and the black grain, which could correspond to with $NiCr_2O_4$ and $NiFe_2O_4$ respectively.

Raman spectra of samples oxidized in air for 21 h (Figure 4.33(b)) presented both Cr_2O_3 and spinel oxide phase on the grain and its boundary. Cr_2O_3 plays an important role at grain boundary whereas the spinel oxide evidently is more present on grain area. On both black and white areas, Raman shifts of all spinel oxides presented quite the same value at around 707 cm^{-1}, excepted on the black matrix which locates at 695 cm^{-1}. The Cr_2O_3 peak was absent on both black and white nodules whereas it was present on the matrix: the stronger peak of Cr_2O_3 observed on the black revealed a higher Cr_2O_3 fraction in this area, again in agreement with the mesoscopic PEC results.

Raman spectra of the homogeneous oxide on sample oxidized in water vapor for 30 h (Figure 4.33(c)) showed a major contribution of Cr_2O_3 at around 558 cm^{-1} and a minor one of $NiFe_2O_4$ at around 695 – 709 cm^{-1}.

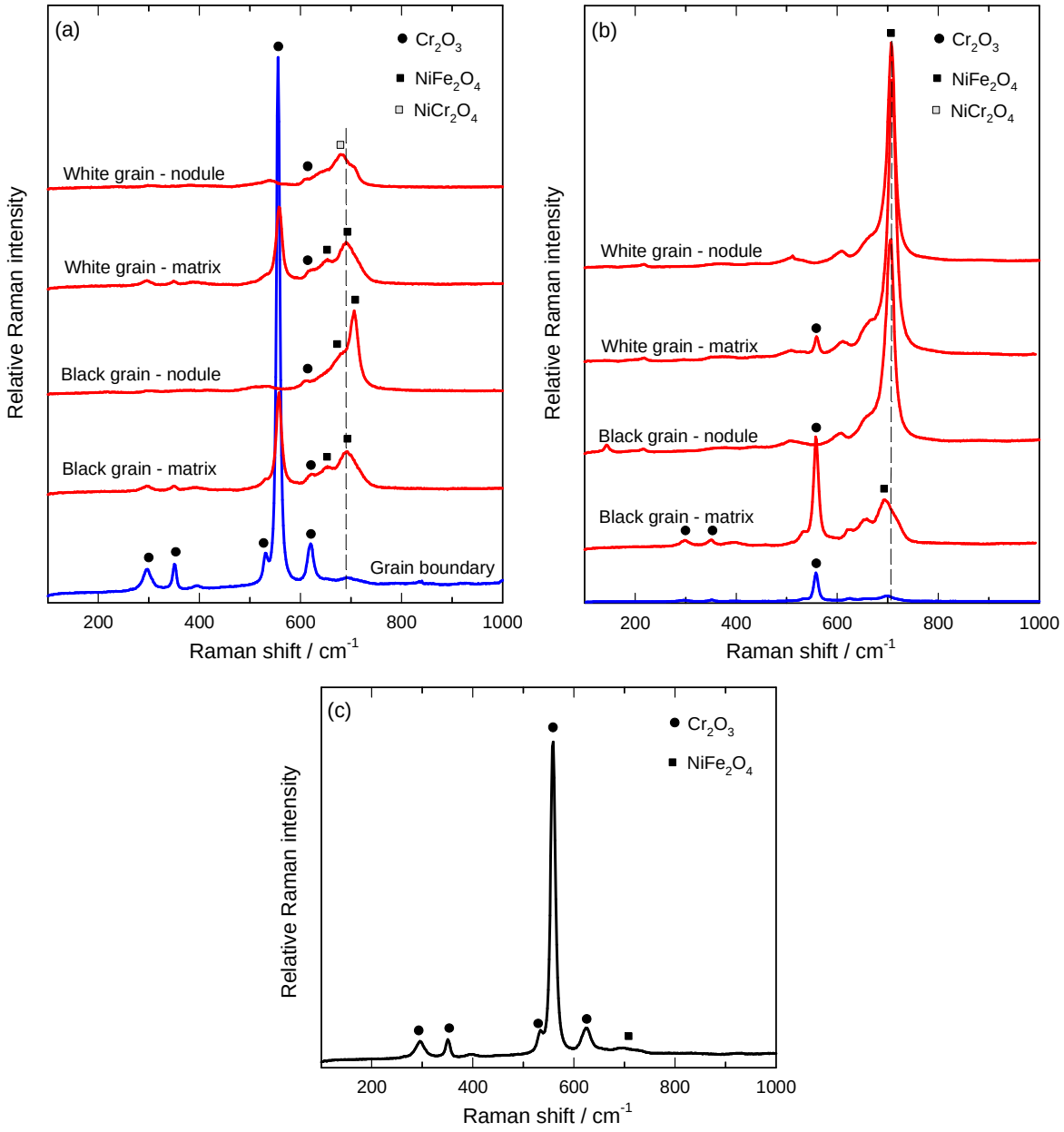

Figure 4.33 Raman spectra of thermal oxides grown on Alloy 690 oxidized at 900°C: (a) in oxygen for 30 h, (b) in air for 21 h , and (c) in water vapor for 30 h

The latter results indicated that the oxides developed on Alloy 690 under oxygen, air, and water vapor were composed of corundum Cr_2O_3, either $NiFe_2O_4$ or $NiCr_2O_4$, and perhaps the solid solution of $NiFe_2O_4$–$NiCr_2O_4$ whose Raman shift should locate between the corresponding shifts of $NiFe_2O_4$ and $NiCr_2O_4$. In oxygen, Cr_2O_3 was more evidenced than $NiFe_2O_4$ at grain boundary, while the amount of Cr_2O_3 was reduced and replaced by either $NiFe_2O_4$ or $NiCr_2O_4$ on grain area. Spinel oxides were more observed on grain areas,

especially on nodules where the fraction of Cr_2O_3 appeared to diminish. Furthermore, surface orientation evidently affected on the chemical composition (and amounts) of spinel oxide which could perhaps be due to different diffusion rates of metal cations through the different planes of the crystal structure.

At this stage it turned out that the complexity of our samples attracted the interest of the Raman teams at CMTC –SIMaP (Dr A.Crisci) and LEPMI (Dr M. Mermoux). Additional characterizations by Raman imaging could thus be carried out, on samples oxidized in oxygen for 30 hours, and in air for 21 hours. The latter case is illustrated in Figure 4.34.

It is beyond the scope of the present work to discuss how the images set in the latter figure were obtained. Briefly, a multivariate analysis of the whole set of the individual Raman spectra which recorded on each point of the selected area was conducted by our colleagues. Two treatments were tested. In the first one, all spectra were considered as the linear combination of the individual spectra of two "pure" components (Cr_2O_3, spinel oxide) assumed to be the ones shown in Figure 4.35(a). In the second one, all spectra were considered as the linear combination of the individual spectra of four "pure" components (two "forms" of Cr_2O_3, two spinel oxides) assumed to be the ones shown in Figure 4.35(b). This allowed to draw images of the lateral distributions of these components on the surface, as shown together with the optical image in Figure 4.34.

Results of the first treatment showed that Cr_2O_3 exhibited intense signals at grain boundary, and a light dispersion on grain matrix. Conversely, spinel oxide, possibly $NiFe_2O_4$ or $NiCr_2O_4$, presented the highest signals above grain matrix, and smaller ones at grain boundary. Besides, a visible difference was observed between the black and white matrixes. When using the second treatment, the resulting mappings showed, in agreement with what was deduced from the first treatment, that Cr_2O_3 covers the whole surface but is more present at grain boundaries. The superposition image of spinel oxide certainly showed a lack of this kind of oxide at grain boundary. Moreover the image pointed out that the spinel oxide #1 with higher Raman shift and the spinel oxide #2 with lower Raman shift preferred the different surface orientation. Since the "identity" peaks of spinel oxides in the second treatment located at 703 cm^{-1} and 710 cm^{-1}, one could suggest that this could at least partly arise from orientation dependent stoichiometries of $Ni_{1-x}Fe_xCr_2O_4$ (solid solutions between $NiFe_2O_4$ and $NiCr_2O_4$).

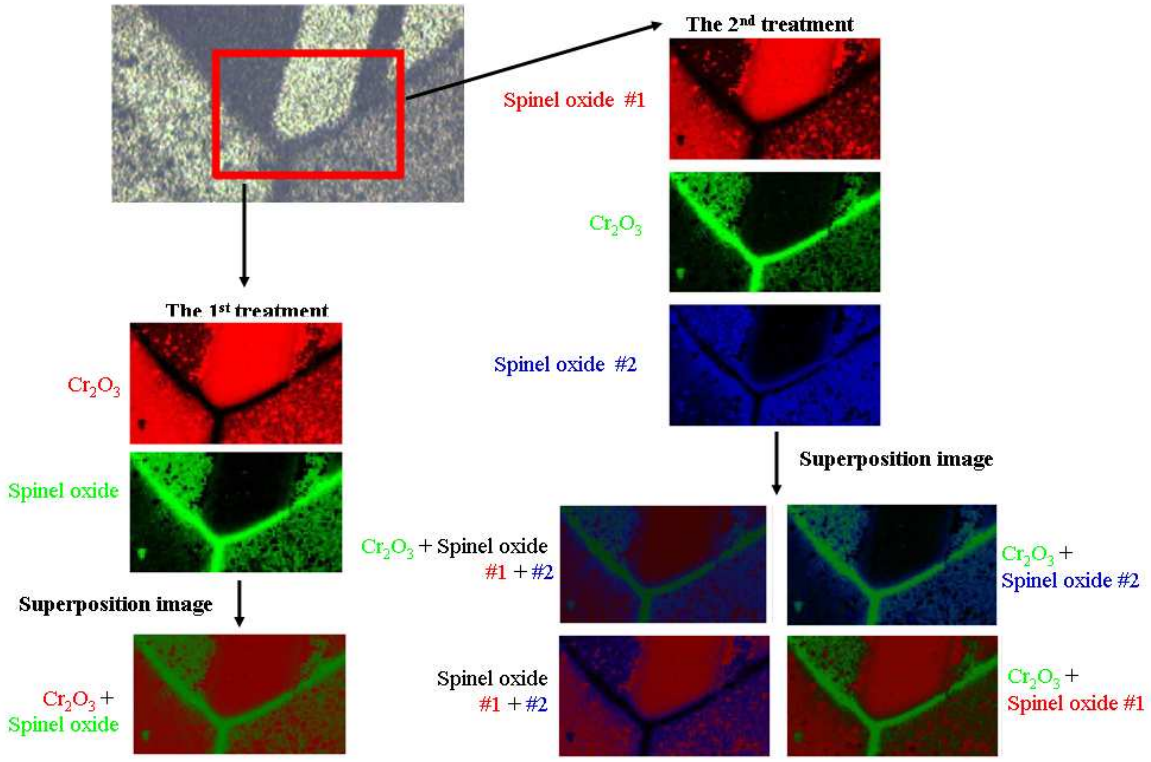

Figure 4.34 Raman spectral images of Alloy 690 oxidized at 900°C in air for 21 h

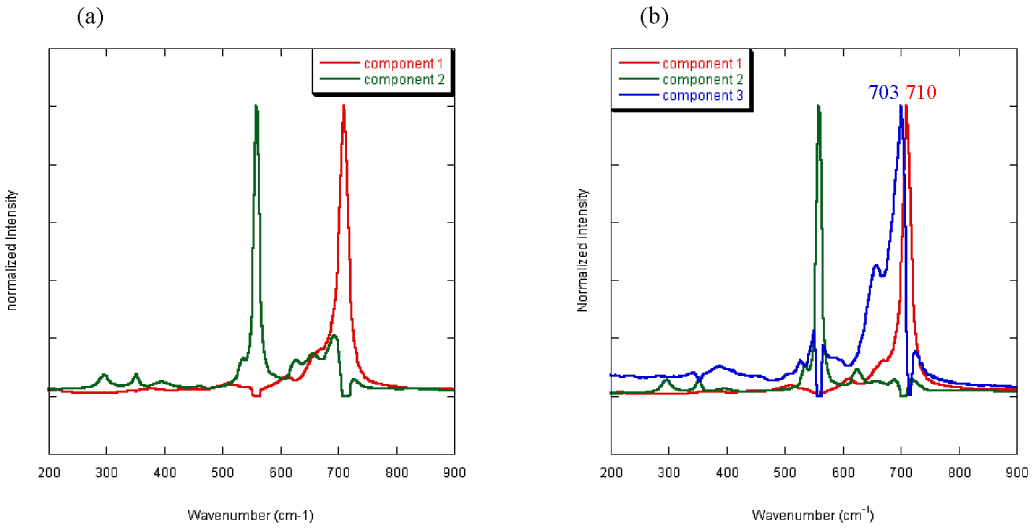

Figure 4.35 Spectra of the "pure" the components assumed for the multivariable analysis of the Raman spectral images in Figure 4.34: (a) first treatment and (b) second treatment

4.3.7 Study of the sample oxidized in oxygen for short time

The PES of the thermal layer grown on oxidized Alloy 690 for 2 h were very complex to model. If the great majority of the recorded PES did apparently yielded at first sight convincing fits with absent 6 to 8 components, it appeared impossible to obtain such results, in the case of samples oxidized in oxygen for 2 h, without increasing the member of components to more to 12 or 13, as will be shown in the next section.

The success obtained by increasing *m* for this particular case, lead to reexamine the cases of the other samples and to even better fits (in the case of water vapor, see above).

However, such a high member of components brought some doubts about the reality of all the latter. This section intends to make this question clear.

4.3.7.1 Macroscopic photoelectrochemical characterizations

Photocurrent energy spectra obtained on the whole surface of the sample and their linear transforms are presented in Figure 4.36. Clearly again, the shapes of the spectra depend on the applied potential, and revealed more than one constituent in the scale. Linear transforms suggested at least four components with bandgaps at around 1.8 eV, 2.5–2.6 eV, 3.0–3.3 eV, and > 4.0 eV.

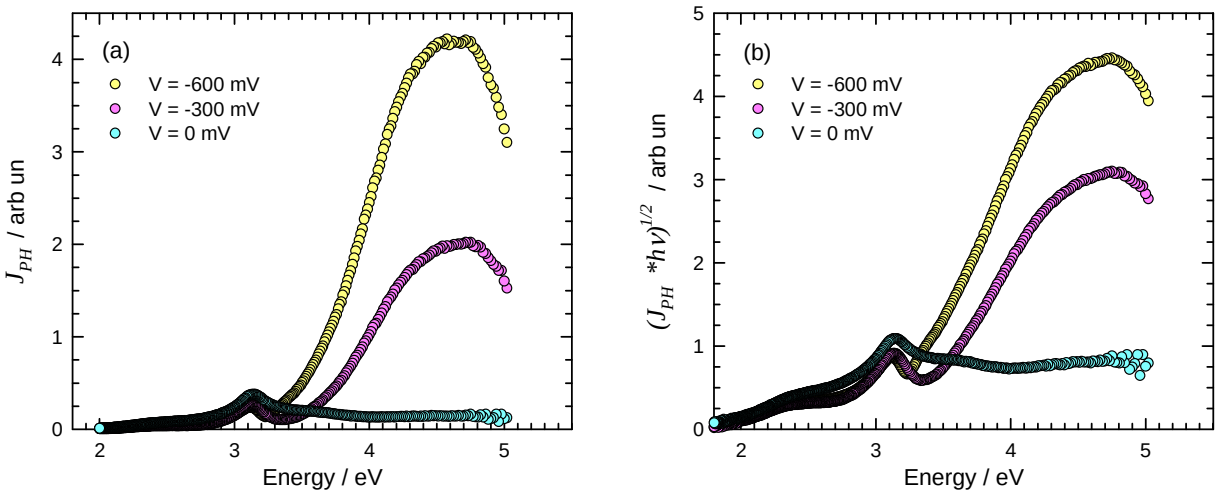

Figure 4.36 (a) Photocurrent versus photon energy and (b) linear transform obtained on the whole surface of oxidized Alloy 690 in oxygen for 2 h

Figure 4.37 illustrates the high quality of the fit results. Twelve semiconducting phases (m = 12) were found at 0 mV whereas eleven semiconducting phases (m = 11) were found at –300 mV and –600 mV. For each energy curve, the fit was done many times with various random initial parameters, the best fits (minimum distance) giving stable final parameter values as illustrated in Figure 4.38.

Figure 4.39 shows that the fitted bandgap values depended only slightly on the applied potential.

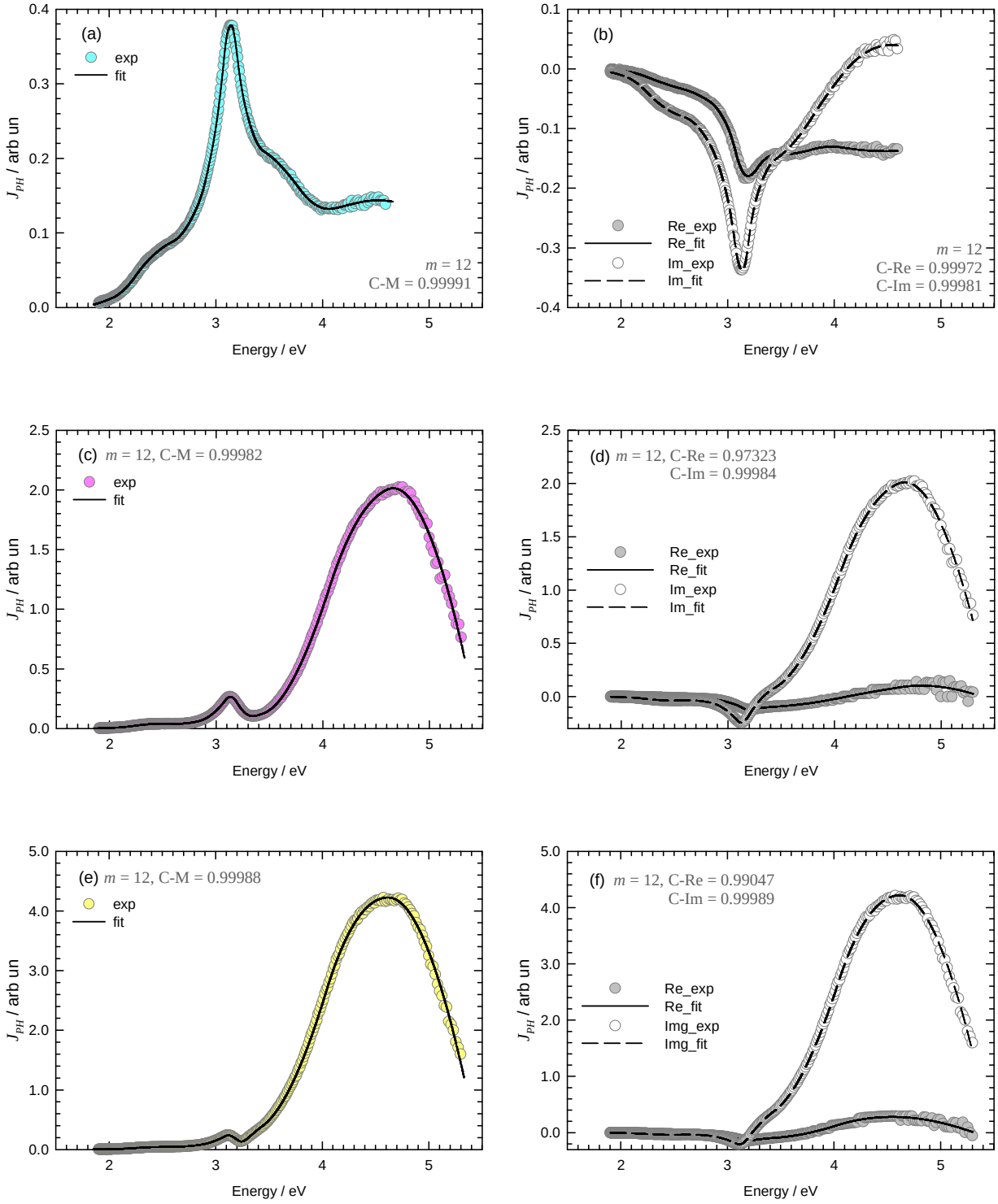

Figure 4.37 Photocurrent energy spectra of Alloy 690 oxidized in oxygen for 2 h (left hand side), and its real part and imaginary part (right hand side): (a) (b) at 0 mV, (c) (d) at –300 mV, (e) (f) at –600 mV. "exp" and "fit" account for experimental and fitted data. "Re" and "Im" are used for the real and imaginary parts of J_{PH}.

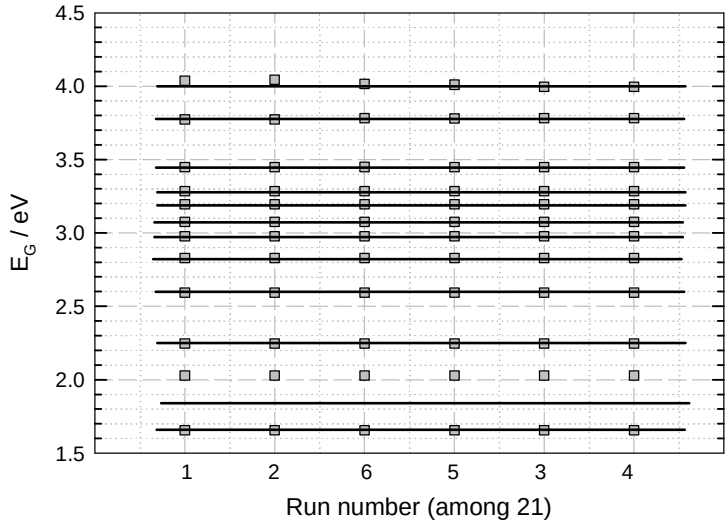

Figure 4.38 Bandgaps ($E_{G,i}$) obtained for the 6 best fits (data of Figure 4.37(a) and (b))

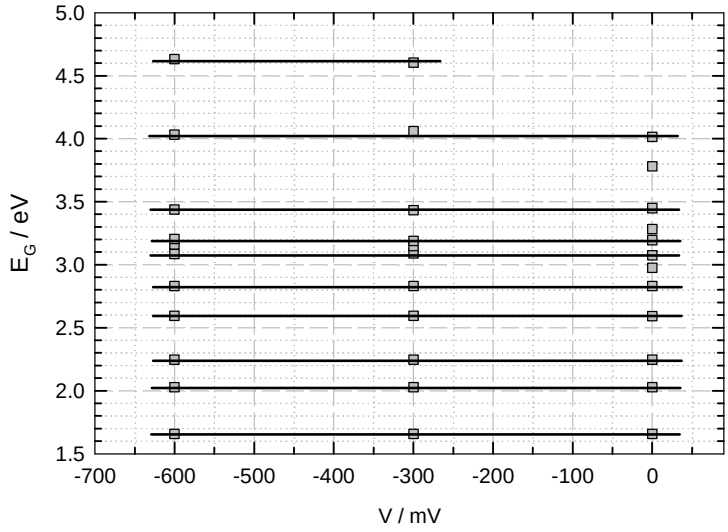

Figure 4.39 Bandgaps obtained from the fits presented in Figure 4.37

From the above results, it is concluded that 12 semiconducting components should indeed be present in the thermal scale.

4.3.7.2 Results from Raman imaging characterizations

Fortunately, the samples shortly oxidized in oxygen in the present work were independently analyzed using Raman spectral imaging by the above cited colleagues of the Raman team. A Raman microscopic mapping of the selected area shown in Figure 4.40 was performed with a 2 µm resolution in both x and y directions (the Raman probe was the light of a 514 nm laser line focused on a spot of 1 µm diameter spot on the sample), providing more than 50000 individual spectra.

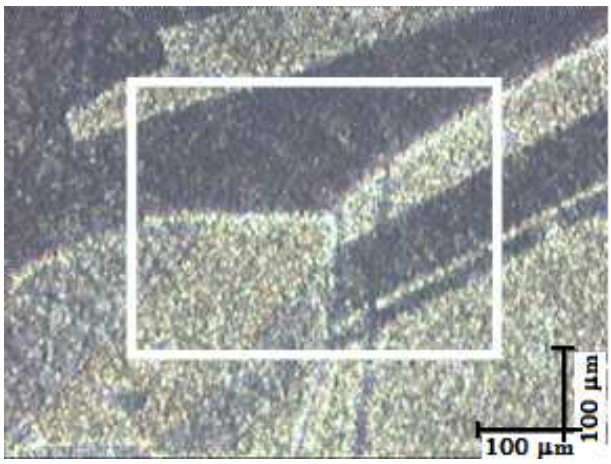

Figure 4.40 Optical image of the sample surface: the white border square presents the selected area where the Raman spectra image was recorded (Alloy 690 oxidized in oxygen for 2 h).

This set of spectra was first submitted to Principal Components Analysis (PCA), using a software provided by Renishaw, the manufacturer of the Raman set–up used. This PCA showed that the whole set of spectra was constituted of 12 components, whose signatures are presented in Figure 4.41 together with the images of their relative intensities in the selected areas.

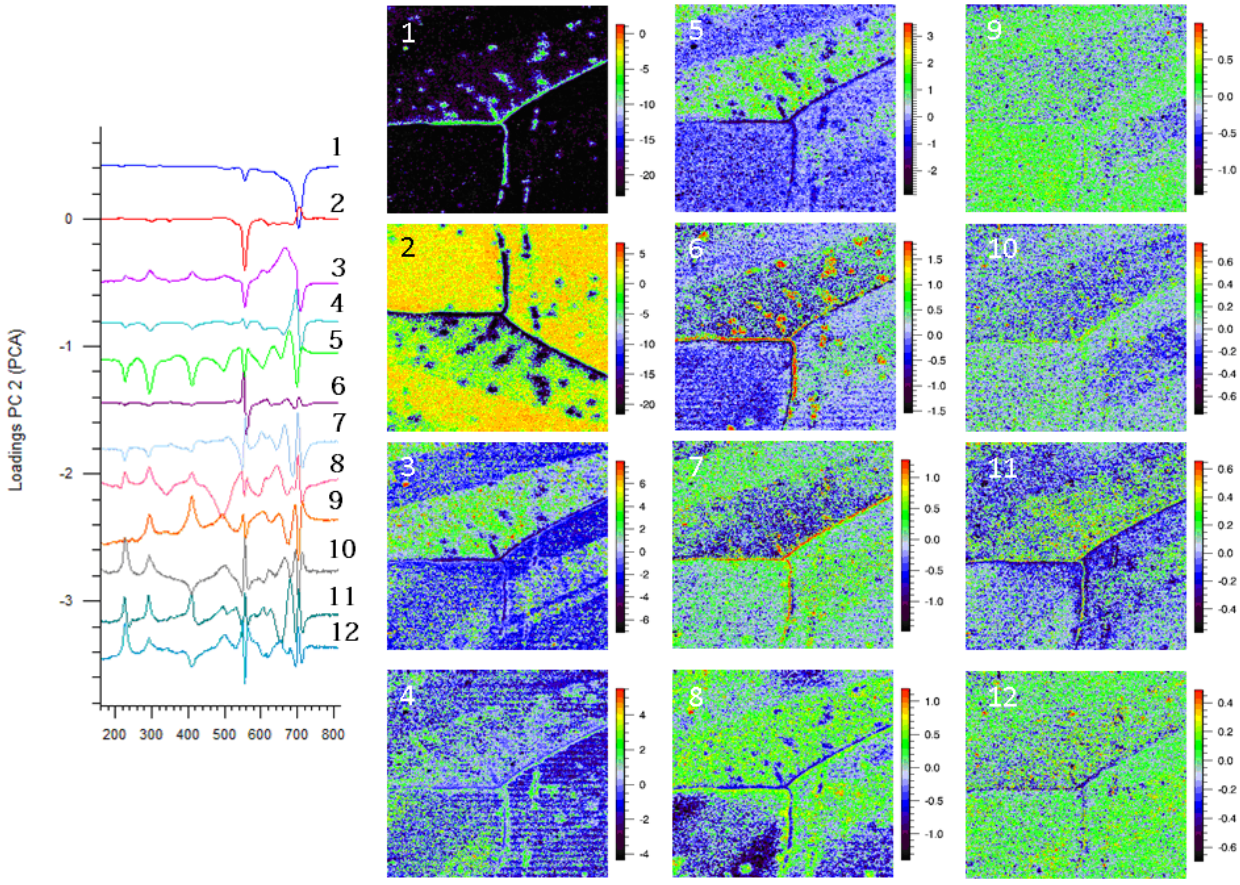

Figure 4.41 Results of the principal components analysis

Then two multivariate analyses were performed, using first 5 (Figure 4.42), then 10 (Figure 4.43) of the 12 detected principal components. It turned out that the first analysis showed that 98% of the more than 50000 spectra could indeed be obtained by a linear combination of the 5 “pure” spectra. And the second analysis showed that 10 components were necessary to reach a percentage equal to 99.5%.

It appears thus very likely that the thermal scale indeed consists in more than 10 oxide phases, and that 5 of the latter could be considered as main constituents. And, at our sense, these results do cross–correlate with the results obtained in the preceding section when fitting the PES using our new approach (necessity of twelve SCs to account for the PES).

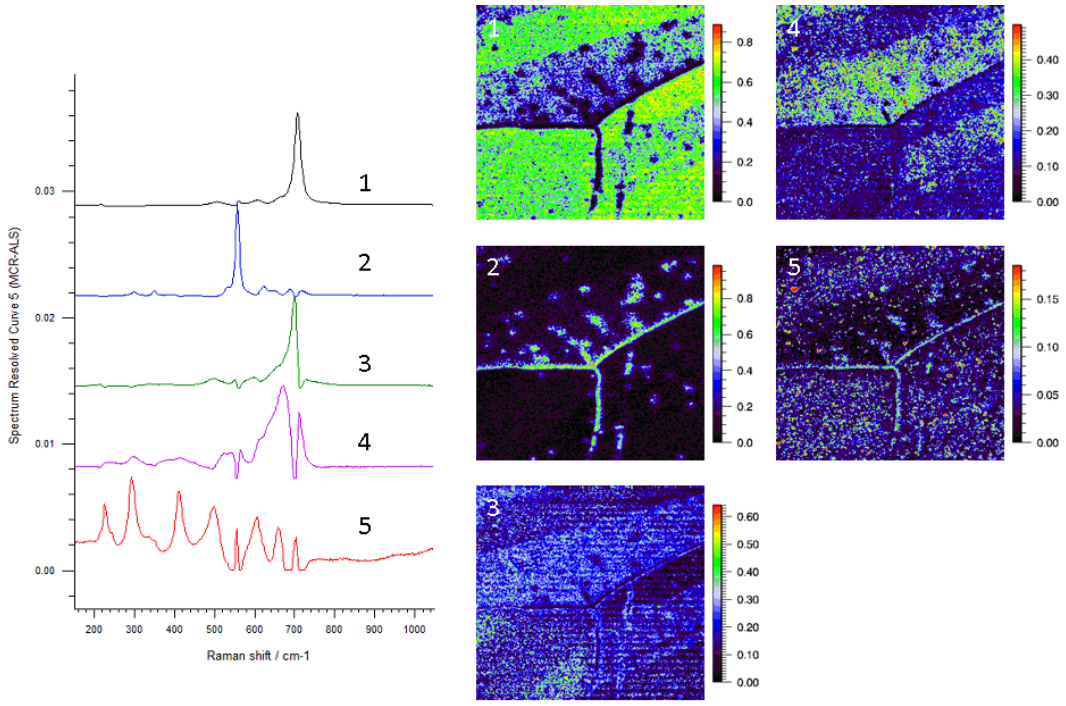

Figure 4.42 Mapping of the results of the multivariate analysis performed with 5 of the 12 principal components obtained from PCA

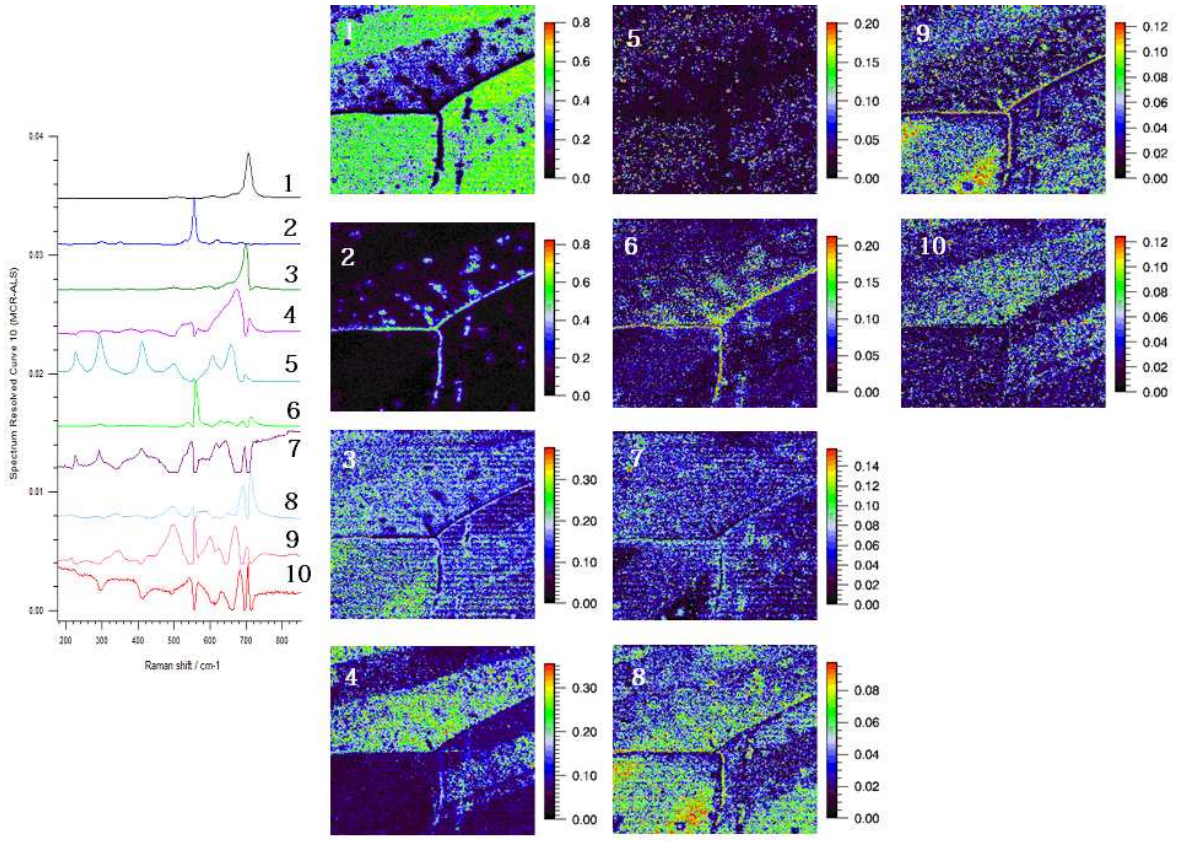

Figure 4.43 Mapping of the results of the multivariate analysis performed with 10 of the 12 principal components obtained from PCA

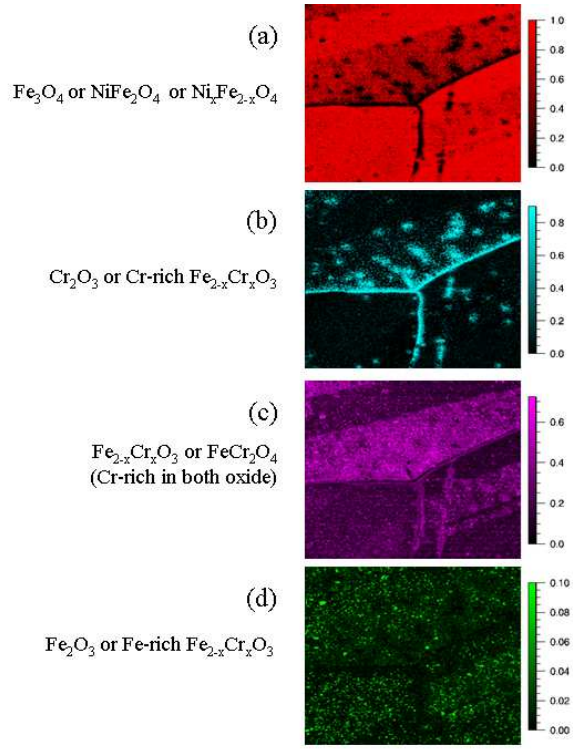

Figure 4.44 Raman spectral images map with four components of (a) Fe_3O_4 or $NiFe_2O_4$ or $Ni_xFe_{2-x}O_4$ (b) Cr_2O_3 or Cr–rich $Fe_{2-x}Cr_xO_3$ (c) $Fe_{2-x}Cr_xO_3$ or $FeCr_2O_4$ and (d) Fe_2O_3 or Fe–rich $Fe_{2-x}Cr_xO_3$

4.3.8 Concluding remarks

Oxidation of Ni–based alloy, Inconel 690, certainly depended on oxidation atmosphere, oxidation time, and also nature of substrate (that is surface orientation in this work). All characterizations coincidently reported general thermal oxides grown on Alloy 690 composed of Cr, Fe, Ni, in forms of Cr_2O_3, $NiFe_2O_4$, $NiCr_2O_4$, $Ni_{1-y}Fe_yCr_2O_4$, Fe_2O_3, and $Fe_{2-x}Cr_xO_3$. Photocurrent voltammograms obtained from macroscopic experiments indicated most of thermal oxides could behave as either n– or p– semiconducting, and also insulating, depending on oxidizing conditions. Photocurrent obtained on the whole surface reported that the presence of water vapor promote n–type oxide. Moreover, mesoscopic and microscopic results showed an agreement about the effect of surface orientation and the influence of a few amount of water vapor (in air) on the main defects of oxidation (relating with semiconducting behavior). Photocurrent energy spectra obtained on individual grain orientation were given the precise information which differed in orientation and showed their orientation dependence on Cr content in $Fe_{2-x}Cr_xO_3$ and on oxide semiconducting behavior, and also presented the effect of surface orientation on oxide species by constructed the diverse oxides observed in macroscopic one. Furthermore, photoelectrochemical images always revealed the intense Cr_2O_3 at grain boundary, contrast with the grain are which present more spinel oxides. Finally, the fitting on energy spectra of thinner layer affirmed the complexity of oxide layer by showing the repeatability and the reliability of the model. The whole results get from photoelectrochemical characterizations were ensured with Raman spectroscopy characterization which always shows the coincident results.

4.4 Conclusions

In the present chapter, we presented and validated a novel photoelectrochemical tool, developed for the first time in this work, allowing to record both photovoltammograms and photocurrent energy spectra at a mesoscopic scale, i.e. on surface areas of about 30 µm in diameter.

The concomitant use of the photoelectrochemical techniques at the macroscopic, mesoscopic and microscopic levels was then shown to be useful when investigating the thermal scales grown at high temperature on complex alloy matrixes, such as duplex stainless steels and high chromium content Ni–based alloys.

The novel approach to analyze photocurrent energy spectra developed in our group was also presented. The latter approach was already proven to be successful, but only on quite simple oxidation layers [2–3]. It was proven in this chapter to be also applicable and precious

in the case of samples consisting in more than ten laterally and heterogeneously distributed components, and that a quite simple analysis of PES would now allow to assess the number of semiconducting phases in oxidation layers, and to determine their bandgaps values.

Among the final parameter values, only the bandgap values have been looked at. Other informations were initially expected from the K_i and θ_i values of each component, such as insights in the semiconducting type of each component. Up to now, however, this could not be undoubtly obtained.

Nevertheless, it is yet possible to take more benefit from the fitted photocurrent spectra. As a concluding example, the mesoscopic PES obtained for the sample oxidized in air for 21 hours again are presented in Figure 4.45(a), together with the plot of the black to white ratios of both spectra (Figure 4.45(b)). Based on these ratios, it was proposed in section 4.3.4.2 that the oxides on the white areas contained more the low bandgap components than the black areas, and, conversely, less high bandgap ones. For each PES in Figure 4.45(a), using the complete set of the fit's end parameter values, we recalculated two spectra, which would have been obtained if only the bandgaps below (resp. above) 3.0 eV would have been present in the layer. These calculated pseudo–spectra are presented in Figure 4.46. They undoubtly confirm the suggestions brought by the curve in Figure 4.45(b).

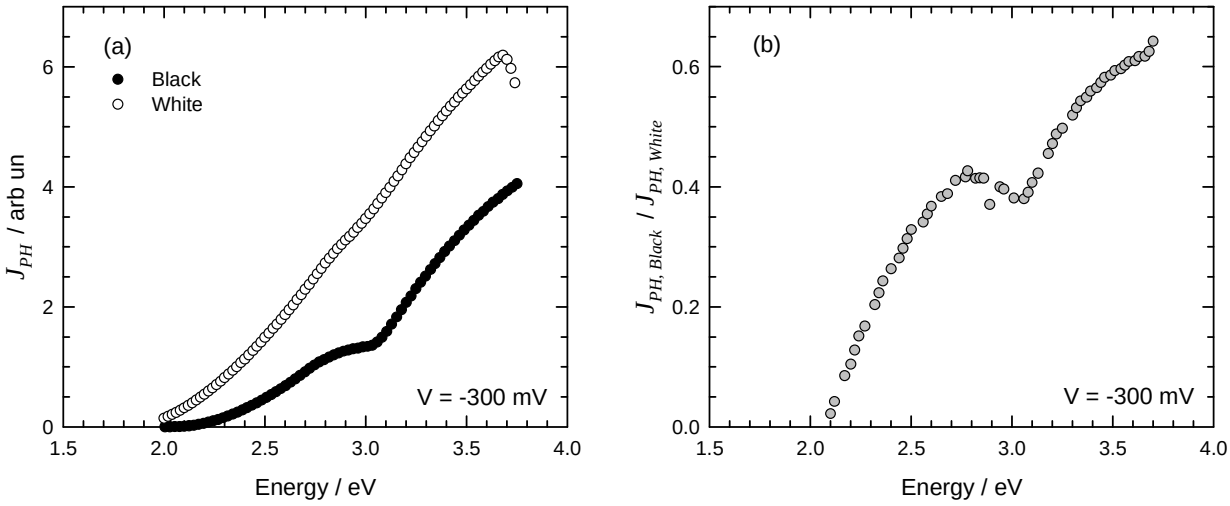

Figure 4.45 (a) Fits data of mesoscopic PES obtained on individual black (black circle) and white (white circle) area of Alloy 690 oxidized in air for 21 h, and (b) Plot of the black to white ratios of both spectra in (a)

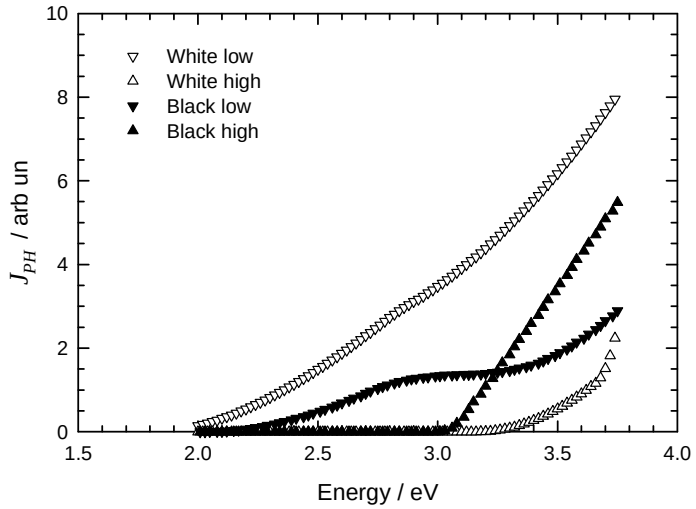

Figure 4.46 Pseudo–PES corresponding to PES in Figure 4.45(a)

REFERENCES

[1] A. Srisrual, J.–P. Petit, Y. Wouters, C. Pascal, and A. Galerie, Photoelectrochemical investigations on individual ferritic and austenitic grains of a duplex stainless steel oxidized in water vapour, *Mater. High Temp.* **28 (4)** (2011) 349–354.

[2] A. Srisrual, J.–P. Petit, Y. Wouters, and A. Galerie, Multiscale photoelectrochemical studies on oxidized duplex stainless steels, *Oxid. Met.* **79** (2013) 337–347.

[3] J.–P. Petit, R. Boichot, A. Loucif, A. Srisrual, and Y. Wouters, Photoelectrochemistry of oxidation layers: a novel approach to analyze photocurrent energy spectra, *Oxid. Met.* **79** (2013) 349–359.

[4] S.R. Morrison, *Electrochemistry at semiconductor and oxidized metal electrodes*, Plenum Press, NY, 1980.

[5] U. Stimming, Photoelectrochemical studies of passive films, *Electrochemica Acta* **31 (4)** (1986) 415–429.

[6] R. Benaboud, P. Bouvier, J.–P. Petit, Y. Wouters, A. Galerie, Comparative study and imaging by PhotoElectroChemical techniques of oxide films thermally grown on zirconium and Zircaloy–4, *J. Nucl. Mater.* **360** (2007) 151–158.

[7] F. Atmani, Y. Wouters, A. Galerie, J.–P. Petit, Y. Dali, M. Tupin, P. Bossis, Imaging by photoelectrochemical techniques of Laves–phases γ–$Zr(Fe,Cr)_2$ thermally oxidized on Zircaloy–4, *Mater. Sci. Forum.* **595–598** (2008) 571–579.

[8] Y. Wouters, A. Galerie, J.–P. Petit, Photoelectrochemical study of oxides thermally grown on titanium in oxygen or water vapor atmospheres, *J. Electrochem. Soc.* **154 (10)** (2007) C587–C592.

[9] W. W. Gärtner, Depletion–layer photoeffects in semiconductors, *Phys. Rev.* **116 (1)** (1959) 84–87.

[10] M. A. Butler, Photoelectrolysis and physical properties of the semiconducting electrode WO_3, *J. Appl. Phys.* **48 (5)** (1997) 1914–1920.

[11] F. di Quarto, C. Sunseri, S. Piazza, and M. C. Romano, Semiempirical correlation between optical band gap values of oxides and the difference of electronegativity of the elements. Its importance for a quantitative use of photocurrent spectroscopy in corrosion studies, *J. Phys. Chem. B* **101** (1997) 2519–2525.

[12] A K Vijh, Correlation between bond energies and forbidden gaps of inorganic binary compounds, *J. Phys. Chem. Solids* **30** (1969) 1999–2005.

[13] K. F. McCarty and D. R. Boehme, A Raman study of the systems $Fe_{3-x}Cr_xO_4$ and $Fe_{2-x}Cr_xO_3$, *J. Solid State Chem.* **79** (1989) 19–27.

[14] N. Karimi, F. Riffard, F. Rabaste, S. Perrier, R. Cueff, C. Issartel, H. Buscail, Characterization of the oxides formed at 1000 °C on the AISI 304 stainless steel by X–ray diffraction and infrared spectroscopy, *Appl. Surf. Sci.* **254** (2008) 2292–2299.

[15] A. Galerie, S. Henry, Y. Wouters, M. Mermoux, J.–P. Petit, L. Antoni, Mechanisms of chromia scale failure during the course of 15–18Cr ferritic stainless steel oxidation in water vapour, *Mater. High Temp.* **22 (1/2)** (2005) 105–112.

[16] J. Mougin, *Tenue mécanique de couche d'oxyde thermique générées sur le chrome et sur quelques aciers inoxydables ferritiques*, PhD Thesis, Institut National Polytechnique de Grenoble, France, 2001 (in French).

[17] E. A. Polman, T. Fransen, and P. J. Gellings, Oxidation kinetics of chromium and morphological phenomena, *Oxidation of Matals* **32 (5/6)** (1989) 433–447.

[18] R. L. Farrow, R. E. Benner, A. S. Nagelberg, and P. L. Mattern, Characterization of surface oxides by Raman spectroscopy, *Thin Solid Films* **73** (1980) 353–358.

[19] J. C. Hamilton, R. J. Anderson, Oxidation of Fe–18Cr–3Mo: an in–situ Raman study, *High Temp. Science* **19** (1985) 307–321.

[20] R. L. Farrow, A. S. Nagelberg, Raman spectroscopy of surface oxides at elevated temperatures, *Appl. Phys. Lett.* **36(12)** (1980) 945–947.

[21] Y. Matsuda, S. Hinotani, and K. Yamanaka, Characterization of oxide layers on SUS410Ti stainless steel grown in low oxygen pressures by Raman spectroscopy, *Tetsu to Hagane* **82 (3)** (1996) 208–213.

[22] X. Yang, N. Chen, S. Shen, E. Lui, and J. Huang, Preparation, characterization and gas–sensitive properties of nano–crystalline Cr_2O_3–Fe_2O_3 mixed oxides, *Science in China (Series B)* **41 (4)** (1998) 442–448.

[23] A. Holt, P. Kofstad, Electrical conductivity and defect structure of Cr2O3, *Solid State Ionics* **69** (1994) 137–143.

[24] ASM International Handbook Committee, *Metals Handbook Ninth Edition Volume 13, Corrosion*, Park (Ohio): ASM International, 1987, p. 66.

[25] P. Sarrazin, A. Galerie, J. Fouletier, *Mechanisms of high temperature corrosion a kinetic approach*, Zuerich: Trans Tech Publications Ltd, 2008, p.148.

[26] A. Loucif, J.–P. Petit, Y. Wouters, P. Combrade, "Effect of Dissolved Hydrogen, Surface Condition and Composition on the Electronic Properties of the Oxide Films Formed on Nikel–base Alloys in PWR Primary Water", in *15th International Conference on Environmental Degradation*, edited by J.T. Busby et al., TMS Conference Proceeding 2011, pp. 953–963.

[27] A. Galerie, J.–P. Petit, Y. Wouters, J. Mougin, A. Srisrual, P.Y. Hou, Water vapour effects on the oxidation of chromia–forming alloys, *Materials Science Forum* **696** (2011) 200–205.

[28] A. Galerie, S. Henry, Y. Wouters, M. Mermoux, J.–P. Petit and L. Antoni, Mechanism of chromia scale failure during the course of 15–18Cr ferritic stainless steel oxidation in water vapour, *Mater. High Temp.* **22 (1/2)** (2005) 105–112.

[29] J. Panter, B. Viguier, J.–M. Cloué, M. Foucault, P. Combrade, E. Andrieu, Influence of oxide films on primary water stress corrosion cracking initiation of alloy 600, *Journal of Nuclear Materials* **348** (2006) 213–221.

[30] P. Xu, L.Y. Zhao, K. Sridharan, T.R. Allen, Oxidation behavior of grain boundary engineered alloy 690 in supercritical water environment, *Journal of Nuclear Materials* **422** (2012) 143–151.

[31] M. Sun, X. Wu, Z. Zhang, E.–H. Han, Analyses of oxide films grown on alloy 625 in oxidizing supercritical water, *Journal of Supercritical Fluids* **47** (2008) 309–317.

[32] S. Zhang, Y. Tan, K. Liang, Photoelectrochemical study on semiconductor properties of oxide films on alloy 600 in high temperature water with ZnO addition, *Journal of Nuclear Materials* **434** (2013) 43–48.

[33] L. Marchetti, S. Perrin, Y. Wouters, F. Martin, M. Pijolat, Photoelectrochemical study of nickel base alloys oxide films formed at high temperature and high pressure water, *Electrochimica Acta* **55** (2010) 5384–5392.

[34] F. Bergmann, M. Handschuh, W. Lorenz, Charge transfer dynamics of electrochemical dark and photoprocesses on semiconductors part II: Fermi energy characteristics and photoadmittance functions, *Chem. Phys.* **215 (1)** (1997) 157–166.

[35] L. P. Bonfrisco and M. Frary, Effects of crystallographic orientation on the early stages of oxidation in nickel and chromium, *J. of Materials Science* **45 (6)** (2010) 1663–1671.

[36] A. R. J. Kucernak, R. Peat, and D. E. Williams, Dissolution and reaction of sulfide inclusions in stainless steel imaged using scanning laser photoelectrochemical microscopy, *J. Electrochem. Soc.* **139 (8)** (1992) 2337–2340.

[37] F. Di Quarto, S. Piazza, and C. Sunseri, A photocurrent spectroscopic investigation of passive films on chromium, *Corr. Sci.* **31** (1990) 721–726.

[38] F. Di Quarto, S. Piazza, and C. Sunseri, Photoelectrochemistry in corrosion studies: Achievements and perspectives, *Materials Science Forum* **192–194** (1995) 633–648.

[39] J. Portier, G. Campet, C. W. Kwon, J. Etourneau, M. A. Subramanian, Relationships between optical band gap and thermodynamic properties of binary oxides, *International Journal of Inorganic Materials* **3** (2001) 1091–1094.

[40] Y. Wouters, A. Galerie, J–P. Petit, Photoelectrochemical characterisation of chromia scales thermally grown on various metal substrates, *Material Science Forum* **595–598** (2008) 1181–1188.

[41] C.–S. Chang, H. Gomi, H. Sakata, Electric and optical properties of Cr_2O_3 films prapared by chemical vapour deposition, *Phys. Stat. Sol.* (a) **155** (1996) 417-425.

[42] A. Srisrual, S. Coindeau, A. Galerie, J.–P. Petit, Y. Wouters, Identification by photoelectrochemistry of oxide phases grown during the initial stages of oxidation of AISI 441 ferritic stainless steel in air or in water vapour, *Corr. Sci.* **51** (2009) 562–568.

[43] K. F. McCarty and D. R. Boehme, A Raman study of the systems $Fe_{3-x}Cr_xO_4$ and $Fe_{2-x}Cr_xO_3$, *Journal of Solid State Chemistry* **79** (1989) 19–27.

[44] D.J. Gardiner, C. J. Littleton, K. M. Thomas, and K.N. Strafford, Distribution and characterization of high temperature air corrosion products on iron–chromium alloys by Raman microscopy, *Oxidation of* **27** (1987) 57–72.

[45] D. Renusch, B. Veal, K. Natesan, and M. Grimsditch, Transient oxidation in Fe–Cr–Ni alloys: a Raman–scattering study, *Oxidation of Metals* **46** (5/6) (1996) 365–381.

[46] G. Calvarin, A.M. Huntz, A. Hugot Le Goff, S. Joiret, and M.C. Bernard, Oxide scale stress determination by Raman spectroscopy application to the NiCr/Cr2O3 system and influence of Yttrium, *Scripta Materialia* **38** (11) (1998) 1649–1658.

[47] R. Benrabaa, H. Boukhlouf, A. Löfberg, A. Rubbens, R.–N. Vannier, E. Bordes–Richard, A. Barama, Nickel ferrite spinel as catalyst precursor in the dry reforming of methane: Synthesis, characterization and catalytic properties, *J. of Natural Gas Chemistry* **21** (2012) 595–604.

[48] P. Sivakumar, R. Ramesh, A. Ramanand, S. Ponnusamy, C. Muthamizhchelvan, Preparation and properties of nickel ferrite ($NiFe_2O_4$) nanoparticles via sol–gel auto–combustion method, *Materials Research Bulletin* **46** (2011) 2204–2207.

[49] J. H. Kim, I. S. Hwang, Development of an in situ Raman spectroscopic system for surface oxide films on metals and alloys in high temperature water, *Nuclear Engineering and Design* **235** (2005) 1029–1040.

[50] G. J. Abraham, R. Bhambroo, V. Kain, R. Shekhar, G.K. Dey, V.S. Raja, Electrochemical characterization of oxide film formed at high temperature on alloy 690, *Nuclear Engineering and Design* **243** (2012) 69–75.

[51] Z. Wang, S.K. Saxena, P. Lazor, H.S.C. O'Neill, An in situ Raman spectroscopic study of pressure induced dissociation of spinel $NiCr_2O_4$, *Journal of Physics and Chemistry of Solids* **64** (2003) 425–431.

GENERAL CONCLUSIONS AND PERSPECTIVES

From the preceding chapters, it may be concluded that some, but, due to experimental difficulties, not all, of the initial goals of the present work were reached.

General conclusions

The conclusions are divided in three main categories following the aim of research.

Photoelectrochemical characterizations of $Fe_{2-x}Cr_xO_3$

The bandgaps of chromia were confirmed to be located at around 3.0 eV and/or [3.3-3.8] eV. Chromia was again shown to behave as n– or p–type semiconductor, or to be an insulator, depending on oxidation conditions (such as oxidation times, and atmospheres). In high temperature applications of chromia–forming alloys, chromia initially presents an n– or p–semiconducting oxide, and it always become more insulating when the oxidation time increases. The presence of water vapor and/or hydrogen in the oxidation atmosphere tends to promote n–type chromia. The presence of nitrogen insignificantly influences the semiconducting behavior. At high (resp. low) oxygen partial pressure, chromia generally inclines to behave p–type (resp. n–type).

Only the corundum hematite–chromia solid solutions corresponding to x = 0.4 and x = 1.0 could be studied, but unfortunately not as pure phases. The influence of x on the bandgap energy of $Fe_{2-x}Cr_xO_3$ could be observed and roughly correlated to values expected from thermodynamic models. The semiconducting behavior of the x = 0.4 and x = 1.0 solid solutions was shown to be p–type. This can be understood when considering that the x = 0 (Fe_2O_3) and x = 2 (Cr_2O_3) samples were found to be respectively p-type and n-type, but the question of why the x = 0 sample, expected to be n-type, appeared in fact p-type, or why it turned to FeO (known as p-type), was not understood.

Progresses in photoelectrochemical characterizations

On the one hand, the feasibility and the interest of performing photoelectrochemical characterizations at the mesoscopic scale was demonstrated for the time on oxidized duplex stainless steel samples. Mesoscopic characterizations provided local PES on micro–areas (30 µm in diameter) that allowed to distinguish the oxides grown on individual ferritic and austenitic grains, in particular as concerned the x ratio in $Fe_{2-x}Cr_xO_3$. From now, photoelectrochemical tools, at least in our laboratory, can be operated in three

modes: (1) at the macroscopic scale, providing an averaged view of the sample properties, (2) at the microscopic level, showing the lateral photocurrents (and thus heterogeneities) distribution with a ca 1 µm resolution, and (3) at the mesoscopic scale, giving local information on specific areas of heterogeneous samples.

On the other hand, the novel approach to analyze photocurrent energy spectra developed in our group was shown to be suitable even for highly complex oxidation layers, allowing to assess the number of semiconducting components in the layer, and the bandgaps of the latter.

Multiscale photoelectrochemical characterizations in the HTC field

Preceding results reported the influence on the thermally oxidized layer of the oxidation conditions and of the nature and structure of the metallic substrate. Multiscale (macroscopic, mesoscopic, and microscopic) photoelectrochemical experiments showed high ability to identify oxides in thermal layers, to detect and to distinguish them, both in the case of duplex stainless steels and of Ni–based alloys. Moreover, the results suggested a different main defect to be implied for oxidations in oxygen and in water vapor atmospheres.

In the case of oxidized duplex stainless steels, photoelectrochemical always revealed the presence of corundum oxide phases of Fe_2O_3, $Fe_{2-x}Cr_xO_3$, and Cr_2O_3 both on austenitic and on ferritic grains. Differences in the chromium content in $Fe_{2-x}Cr_xO_3$ on austenitic and ferritic grains were distinguished, which depended on not only the composition of the underlying alloy, but also on the oxidizing atmosphere. Semiconduction of chromia on both grains is affected in the same way, and sensitive to the oxygen activity in the oxidation atmosphere that prefers to exhibit p–type semiconduction in a high oxygen partial pressure.

In the case of oxidized Ni–based alloys, photoelectrochemistry revealed the presence of Cr_2O_3, $NiFe_2O_4$, $NiCr_2O_4$, $Ni_{1-z}Fe_zCr_2O_4$, Fe_2O_3, $Fe_{2-x}Cr_xO_3$, and some yet unknown oxides. Most of thermal oxides can behave as either n– or p– semiconducting, and also insulating, depending on oxidizing conditions. The presence of water vapor actually promoted n–type oxide. The surface orientation dependence was observed both in photoelectrochemical and Raman characterizations. Mesoscopic and microscopic results showed the effect of surface orientation on oxide species, and their electronic properties. Moreover, photoelectrochemical images revealed the intense Cr_2O_3 at grain boundary whereas spinel oxide inclines to present only on grain.

Perspectives

From all of difficulties and interesting points during the frame of research, some perspectives should be proposed to reach the successful experiments and also it should be good for the evaluation of the technique.

(1) Since the difficulty to make the dense sample, which is suitable to perform PEC experimental, the sample preparation for the Cr_2O_3 and its solid solution should be tried by the other technique such as the physical vapor deposition like a sputtering on the metal substrate, or chemical co−precipitation method.

(2) The surface orientation on each area should be analyzed in parallel with PEC characterization to mention the correlation between orientation plane and thermal oxide grown on Ni−based alloy.

(3) According to the complexity (12 oxide species detectable) of thermal oxide grown on Ni−based alloys oxidized in oxygen for 2 h sample, mesoscopic PEC should be applied to obtain more exact information on each surface orientation, confirming and comparing with Raman spectroscopy results.

APPENDIX

APPENDIX A

Element analysis (EDX) of oxidized Ni–based alloy samples

Ni–based alloy oxidized at 900°C in oxygen for 30 h

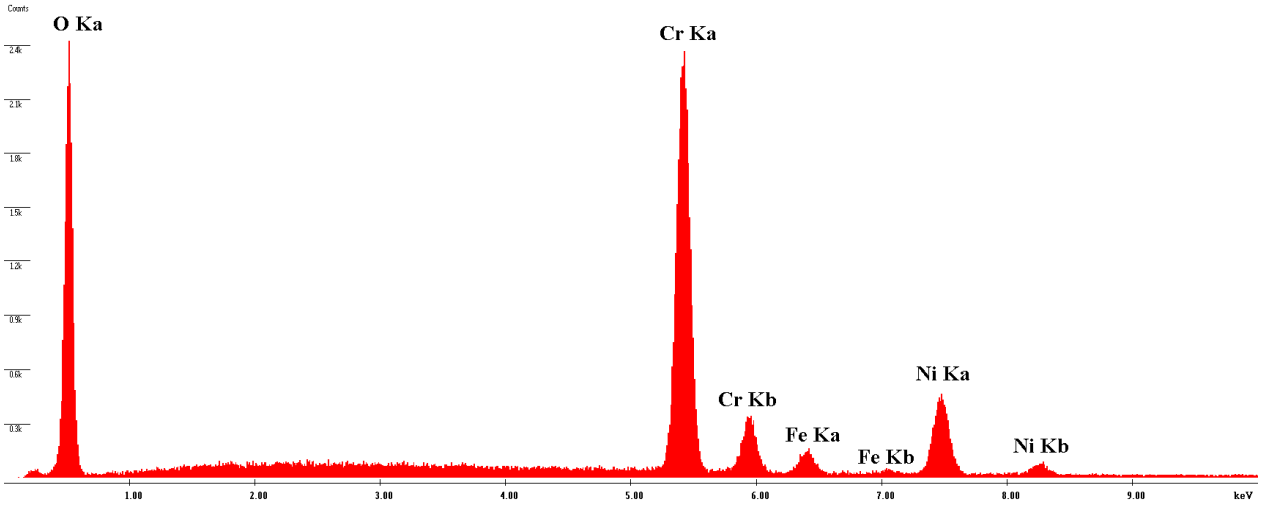

Figure A.1 EDX spectra obtained on Alloy 690 oxidized at 900°C in oxygen for 30 h: at grain boundary

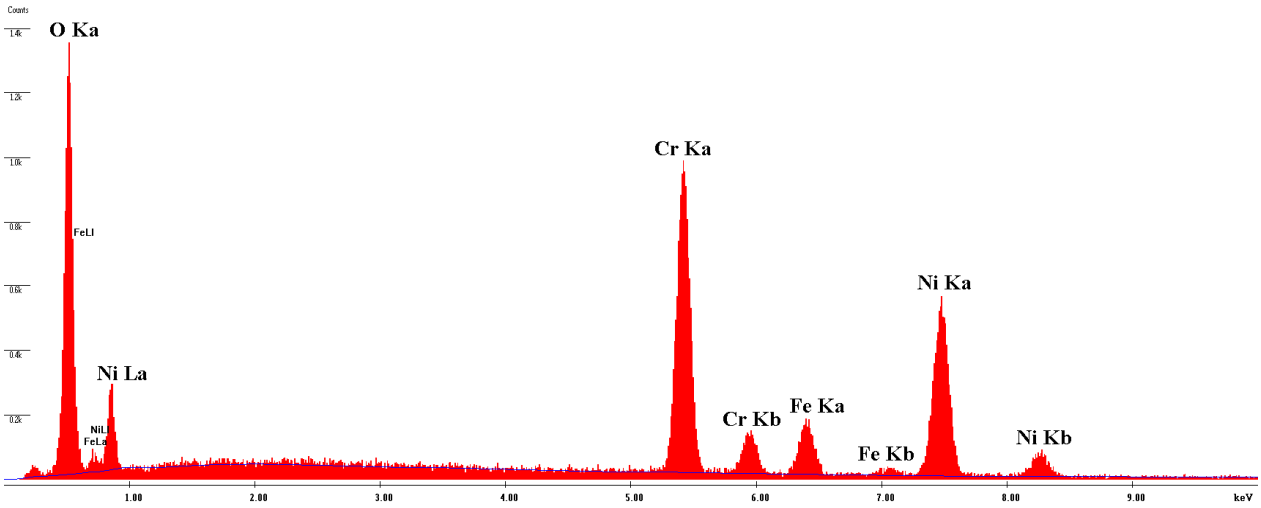

Figure A.2 EDX spectra obtained on Alloy 690 oxidized at 900°C in oxygen for 30 h: on matrix of white area (on grain)

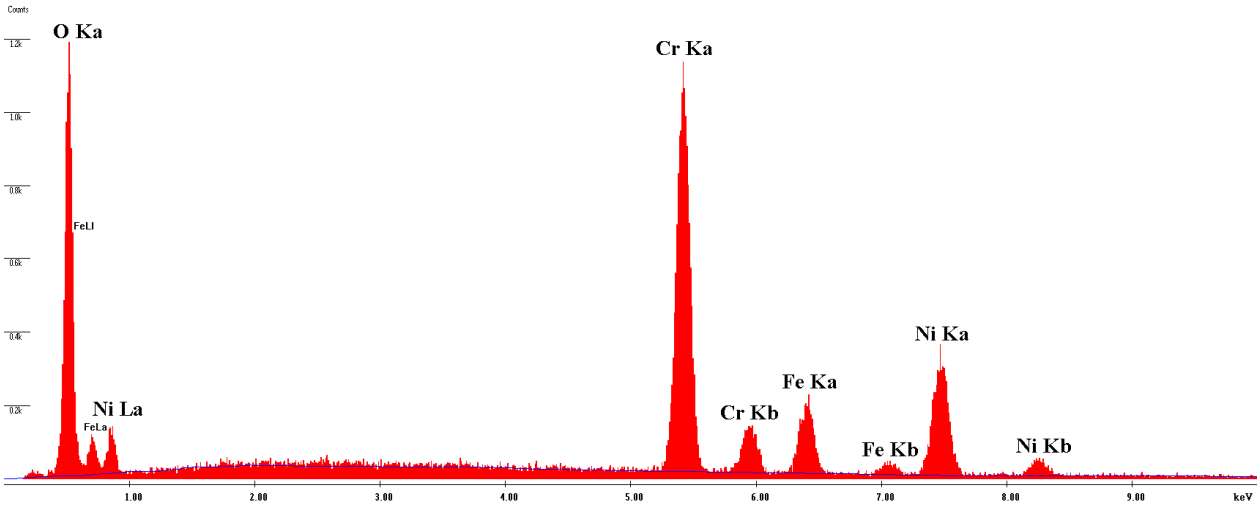

Figure A.3 EDX spectra obtained on Alloy 690 oxidized at 900°C in oxygen for 30 h: on nodule of white area (on grain)

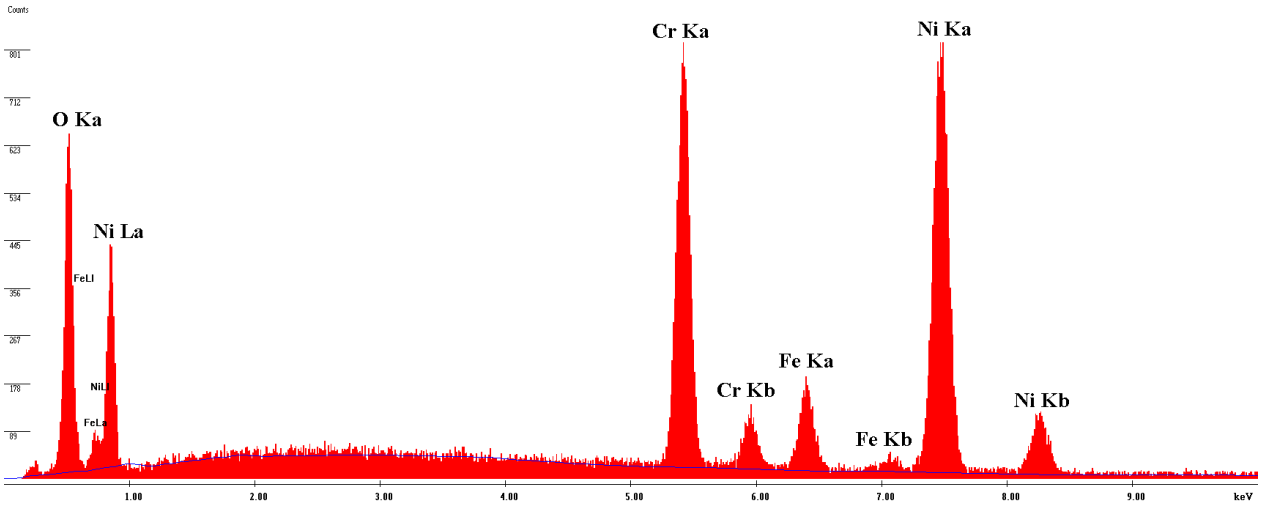

Figure A.4 EDX spectra obtained on Alloy 690 oxidized at 900°C in oxygen for 30 h: on matrix of black area (on grain)

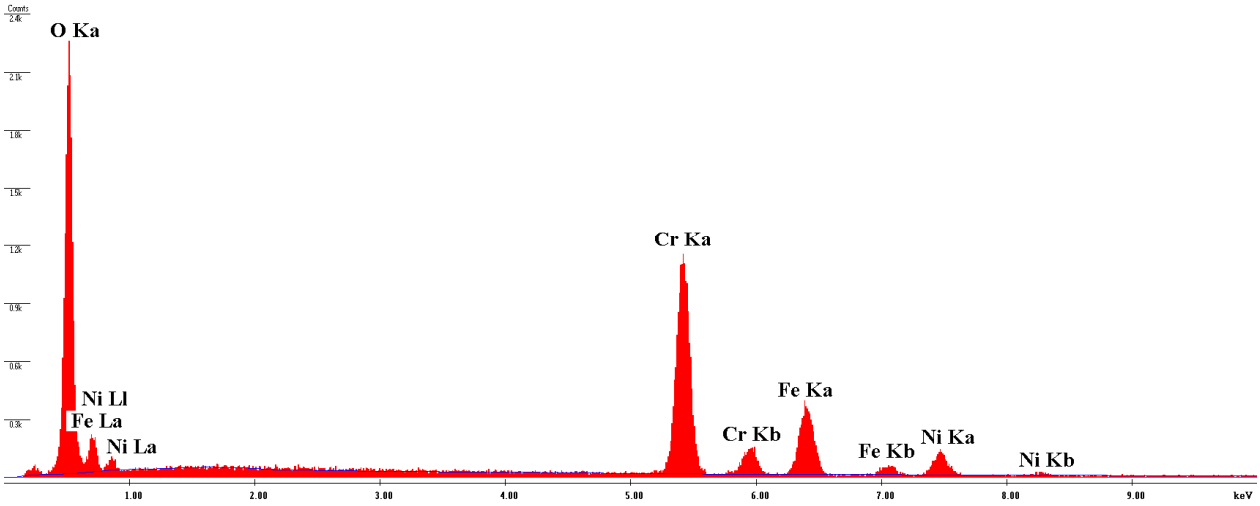

Figure A.5 EDX spectra obtained on Alloy 690 oxidized at 900°C in oxygen for 30 h: on nodule of black area (on grain)

Ni–based alloy oxidized at 900°C in water vapor for 30 h

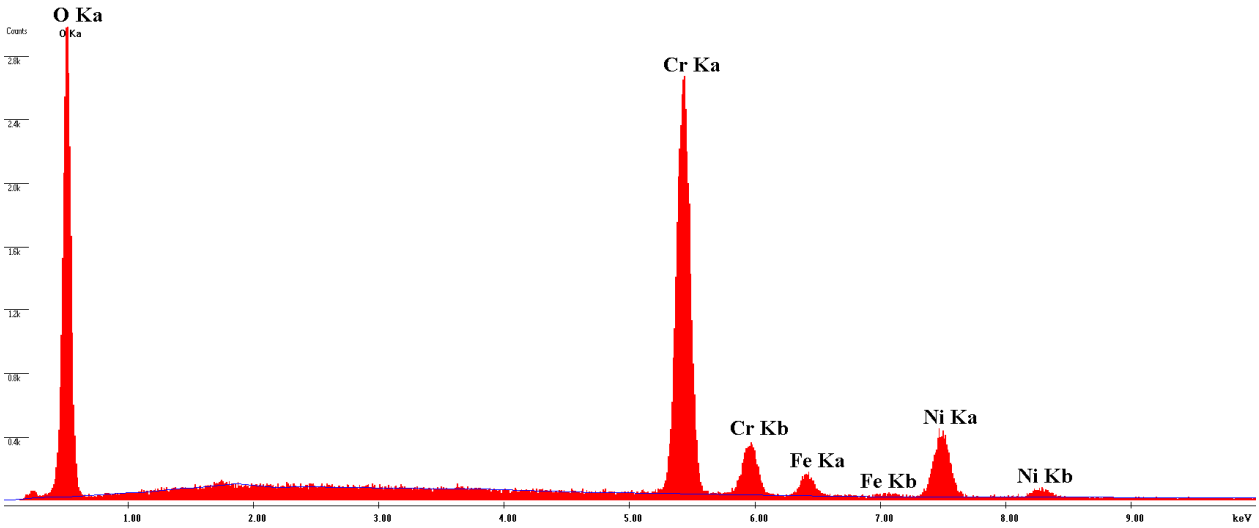

Figure A.6 EDX spectra obtained on Alloy 690 oxidized at 900°C in water vapor for 30 h: on matrix of grain area

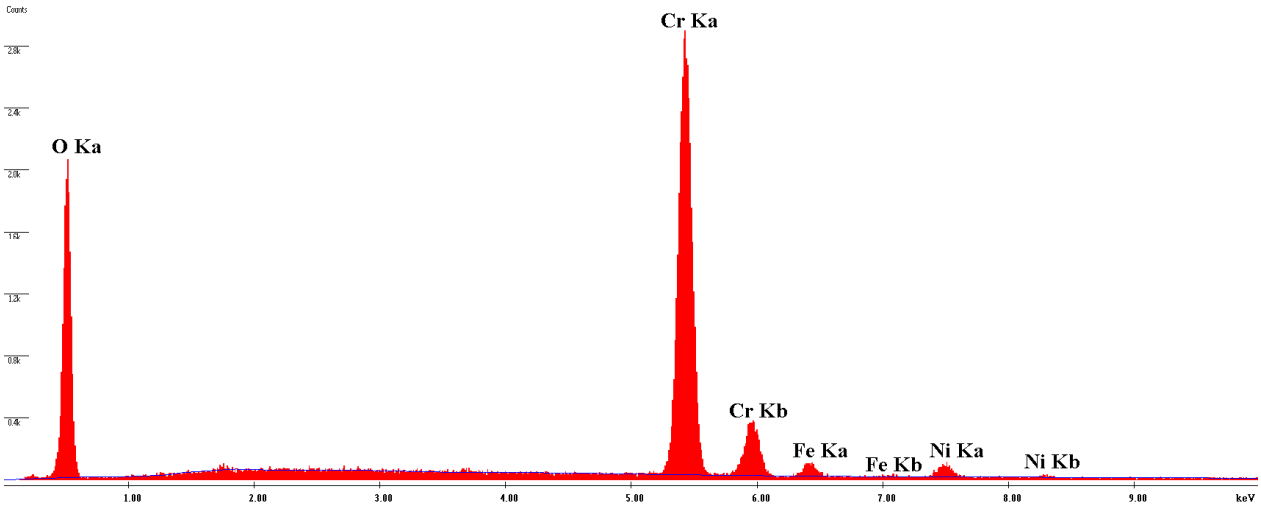

Figure A.7 EDX spectra obtained on Alloy 690 oxidized at 900°C in water vapor for 30 h: on nodule of grain area

Ni–based alloy oxidized at 900°C in air for 21 h

Grain boundary

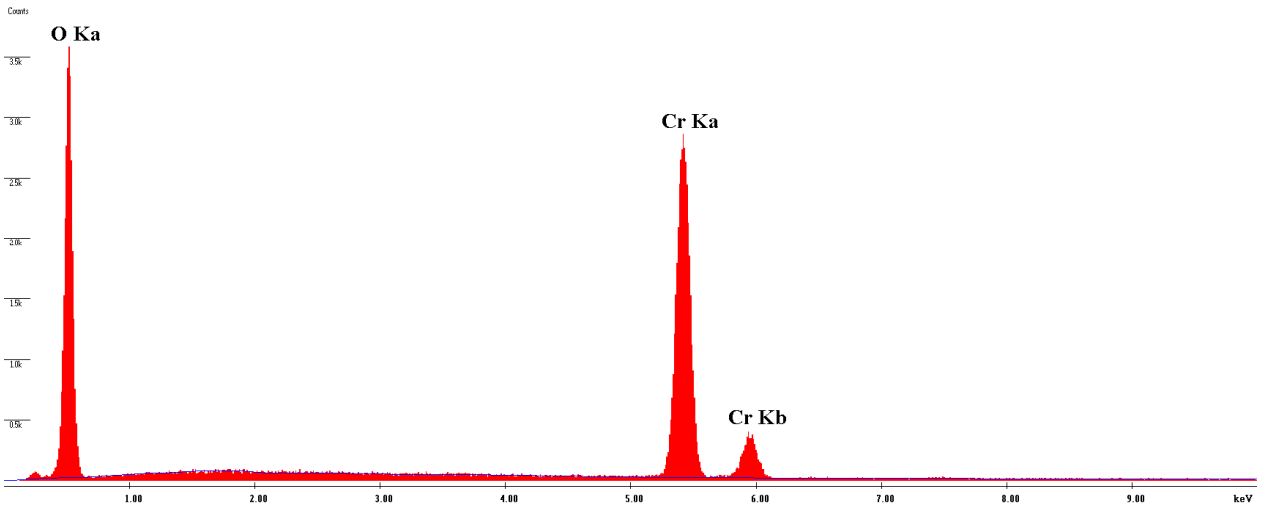

Figure A.8 EDX spectra obtained on Alloy 690 oxidized at 900°C in air for 21 h: at grain boundary

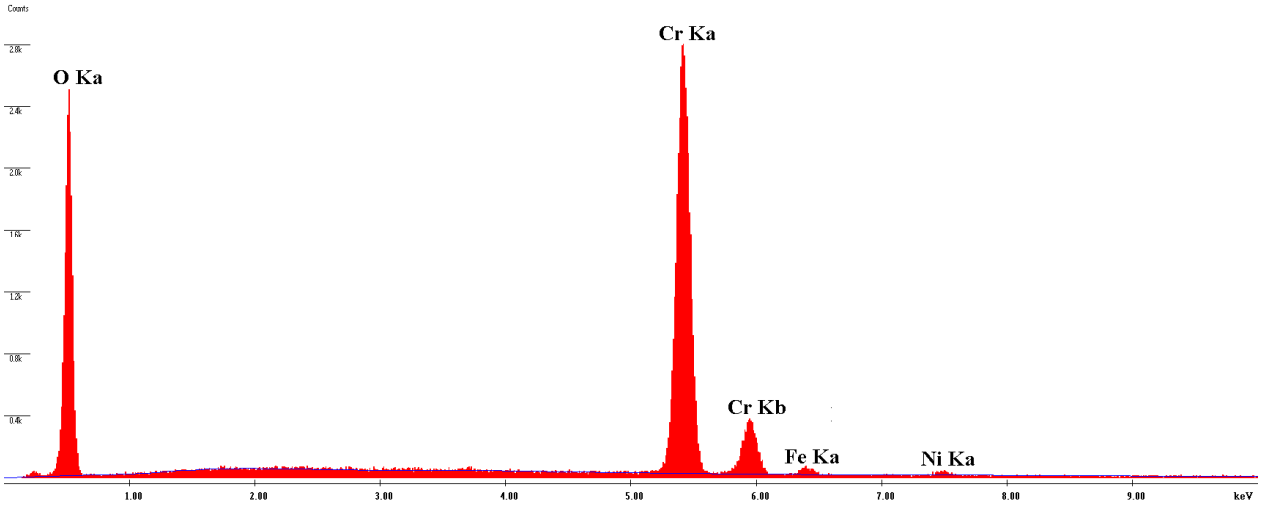

Figure A.9 EDX spectra obtained on Alloy 690 oxidized at 900°C in air for 21 h: on matrix of white area (on grain)

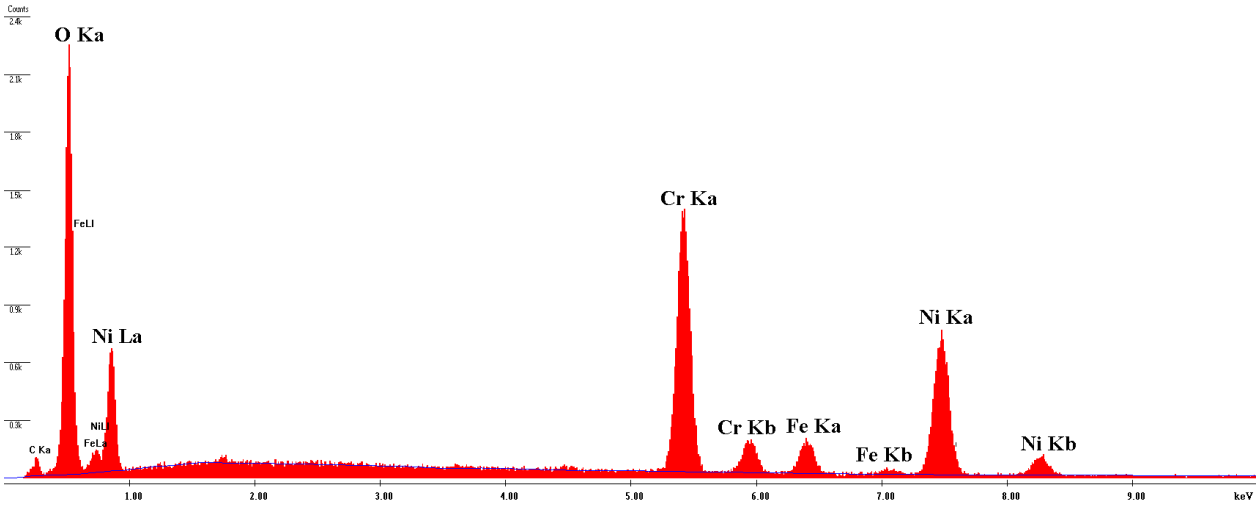

Figure A.10 EDX spectra obtained on Alloy 690 oxidized at 900°C in air for 21 h: on nodule of white area (on grain)

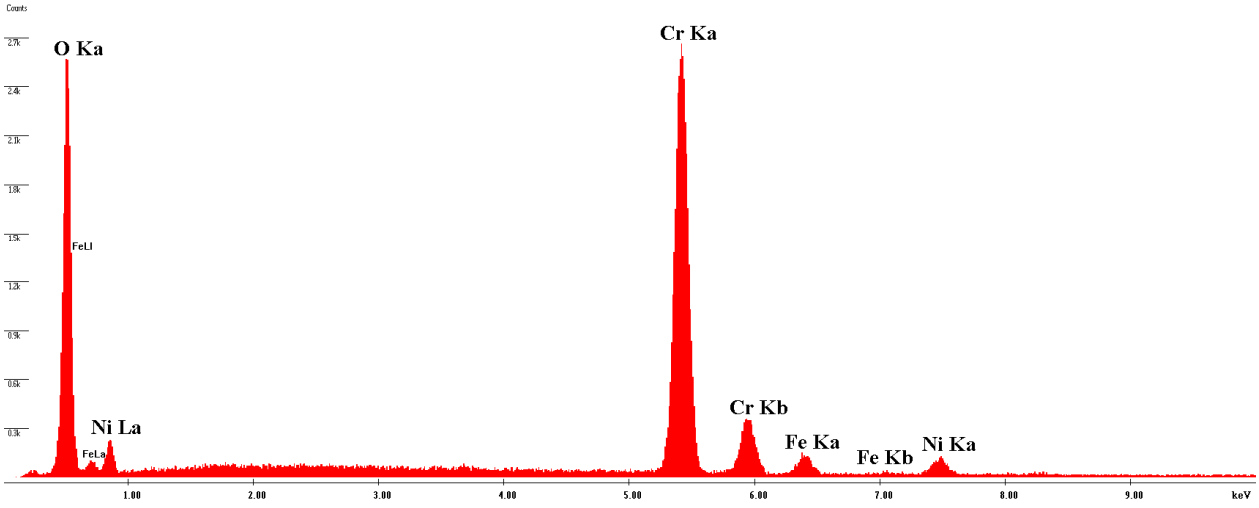

Figure A.11 EDX spectra obtained on Alloy 690 oxidized at 900°C in air for 21 h: on matrix of black area (on grain)

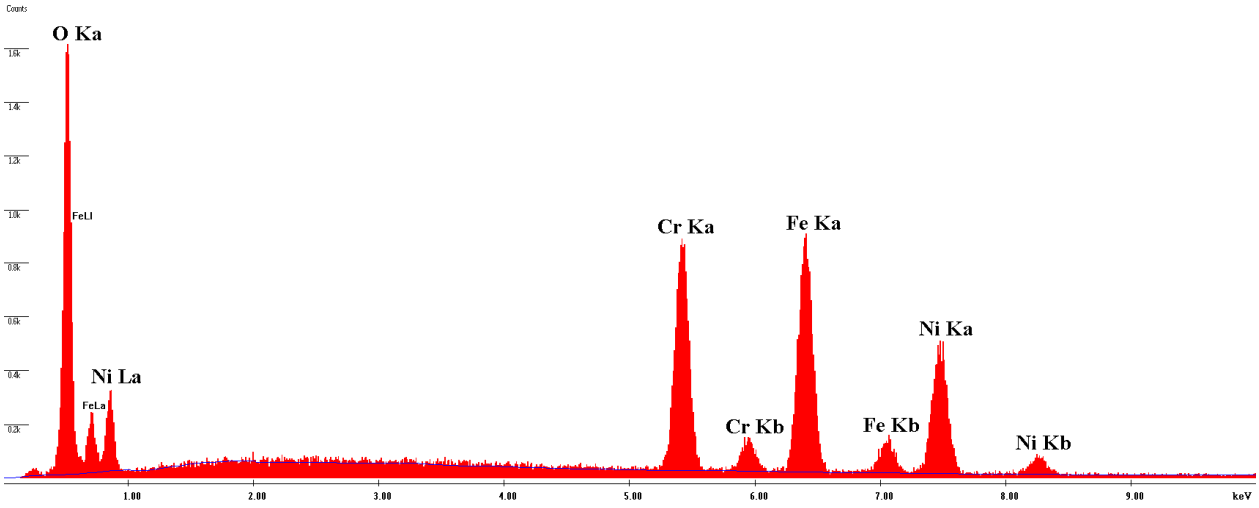

Figure A.12 EDX spectra obtained on Alloy 690 oxidized at 900°C in air for 21 h: on nodule of black area (on grain)

APPENDIX B

Résumé en français

B.1 Introduction

La Corrosion à Haute Température (High Temperature Corrosion, HTC) des métaux et alliages métalliques est le principal phénomène responsable de la défaillance des matériaux ; c'est aujourd'hui un phénomène d'une haute importance industrielle (nécessité d'accroître les durées de services dans des environnements de plus en plus sévères) mais dont la complexité augmente. Cette complexité trouve son origine dans des mécanismes d'oxydation très influencés par les conditions de services très diverses des matériaux. Elle est due également au fait que les paramètres métallurgiques des alliages sont aujourd'hui finement ajustés, une part croissante de ces matériaux étant maintenant micro−structurée, ce qui leur confère de meilleures performances, mais accroît la difficulté de l'étude de leur oxydation. Les couches d'oxydation formées, dont la structure et les propriétés physic−chimiques contrôlent le processus de corrosion, sont très hétérogènes, tant dans leur composition chimique que la distribution spatiale de leurs composants.

Pour caractériser les propriétés des couches d'oxydation, de nombreuses techniques ont été utilisées, telles que la microscopie électronique à balayage (Scanning Electron Microscopy, SEM) associée à l'analyse X (Energy–Dispersive X–ray Spectroscopy, EDS) pour les observations morphologiques et l'analyse élémentaire, et la diffraction X (X–Ray Diffraction, XRD) ou la spectroscopie Raman pour identifier les phases oxydées.

Les techniques PhotoElectroChimiques (PEC), qui ont été particulièrement développées à SIMaP, sont moins communément utilisées dans le domaine HTC. Cependant, ces techniques ont déjà fait leurs preuves en fournissant, aux échelles macroscopique et microscopique, des résultats intéressants en termes de propriétés chimiques et électroniques des couches d'oxydation, et en se révélant particulièrement sensibles à de très faibles variations d'un même paramètre entre deux échantillons.

Il apparaissait donc intéressant de poursuivre le développement des outils photoélectrochimiques, tant en termes d'acquisition des mesures que de modélisation des résultats, de manière à pouvoir continuer à caractériser des couches d'oxydation de plus en plus complexes. Trois directions ont été choisies.

Le premier objectif était d'obtenir une base de données photoélectrochimiques pour les oxydes simples ou mixtes présents simultanément dans les couches d'oxydation formées à

haute température sur aciers et autres alliages, tels que : hématite, chromine, and solutions solides hématite/chromine ($Fe_{2-x}Cr_xO_3$) à différents ratios, pour faciliter ensuite l'identification de ces oxydes dans les couches formées sur des aciers chromino−formeurs.

Le second objectif était de mettre au point et de valider un dispositif original de mésoscopie PEC, permettant de mettre en oeuvre, sur des zones sélectionnées de 30−40 µm en diamètre, tous les outils disponibles pour les études macroscopiques; de fait, si des dispositifs d'imagerie PEC (résolution spatiale : 1 µm) ont déjà été mis au point et utilisés, les études menées ne concernaient qu'un petit nombre d'énergies de photons, en raison du nombre restreint de raies monochromatiques disponibles sur un laser classique.

Le troisième objectif était de contribuer à développer et valider des modèles et/ou des procédures pour améliorer les outils d'analyse des spectres en énergie des photocourants (Photocurrent Energy Spectra, PES) tels qu'utilisés au laboratoire et dans la littérature.

B.2 Caractérisations de la chromine et de ses solutions solides

B.2.1 Oxydation du chrome pur

Des coupons de chrome pur à 99.7% (pour les impuretés résiduelles, cf Tableau B.1), fournis par Goodfellow, ont été oxydés à 850°C dans différentes atmosphères (20% O_2 ou 20% H_2O dans Ar ou 3% H_2O dans H_2). Les durées d'oxydation allaient de 30 minutes à 16 heures, fournissant des couches d'épaisseur comprise entre 0.3 µm et 2.0 µm.

Tableau B.1 Impuretés résiduelles du chrome utilize dans l'étude (en ppm)

	Al	C	Ca	Cu	Fe	K	Mg	Mo	Na	P	Pb	S	Si	W
ppm	10	40	20	5	2000	< 5	< 5	50	10	5	5	5	80	100

B.2.1.1 Paramètres influant sur le type de semiconduction

La Figure B.1 montre les voltammogrammes de photocourants obtenus en illuminant l'échantillon avec des photons d'énergie 3.5 eV et 4.0 eV, pour le cas du chrome pur oxydé dans (a) 20% O_2 dans Ar, (b) 20% H_2O dans Ar, et (c) 3% H_2O dans H_2. On peut tout d'abord remarquer que ces trois échantillons montrent, quelle que soit l'énergie des photons, à la fois des photocourants cathodiques et des photocourants anodiques, aux potentiels respectivement inférieurs and supérieurs au potentiel correspondant au minimum de photocourant sur chaque photovoltammogramme. A première analyse, cela pourrait être interprété comme révélant un oxyde peu dopé, proche de l'isolant. Par ailleurs, ces

photovoltammogrammes montrent clairement l'influence de l'atmosphère d'oxydation sur le comportement semiconducteur des couches formées.

La présence de vapeur d'eau, Figure B.1(b), conduit à un comportement de type n, ce qui est d'ailleurs en accord avec le fait que le potential du minimum de photocourant est plus cathodique. Cela pourrait être dû à un dopage de l'oxyde par des espèces insérées (hydrogène? [1–5]) agissant comme états donneurs à la bande de conduction.

Les pressions partielles d'oxygène utilisées étaient de : 2.0×10^{-1} atm (20% O_2 dans Ar), 2.9×10^{-6} atm (20% H_2O dans Ar), et 2.7×10^{-18} atm (3% H_2O dans H_2). L'absence d'oxygène favorise (resp. défavorise) clairement les photocourants anodiques (resp. cathodiques), et s'accompagne d'un déplacement cathodique du potentiel du minimum de photocourant. Cela pourrait suggérer que la formation de l'oxyde de type n est favoriséedans le cas de la Figure B.1(c), et, au vu de la forme en V des photovoltammogrammes au voisinage du minimum, que l'autre oxyde est probablement isolant plutôt que de type p. Cependant, l'allure inhabituelle des photovoltammogrammes aux potentiels les plus anodiques appelle à la prudence. Les photovoltammogrammes de semiconducteurs non idéaux restent difficiles à modéliser, de sorte que les photovoltammogrammes de couches thermiques constitutéed de multiples composants restent difficiles à prédire.

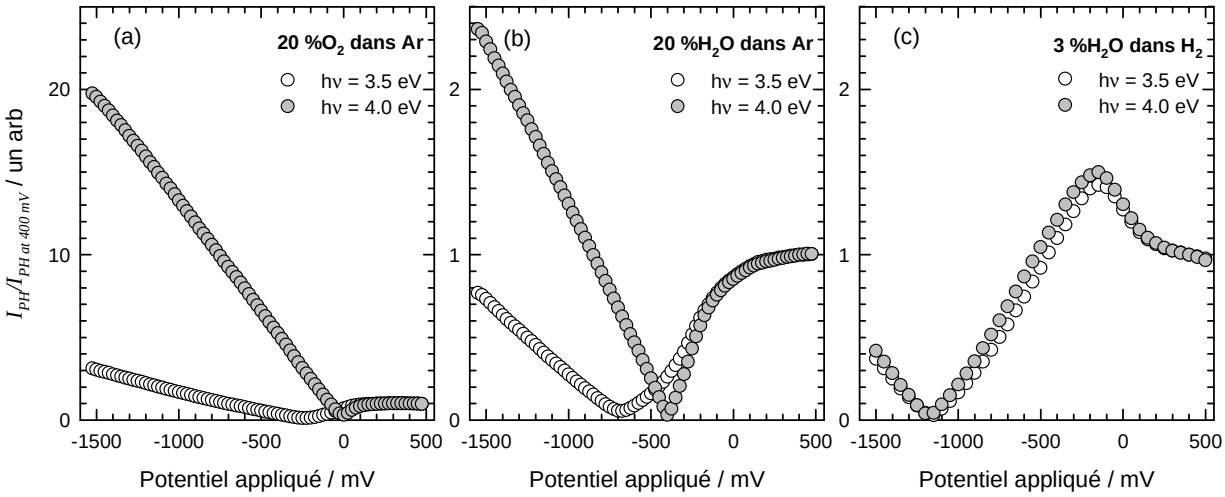

Figure B.1 Photovoltammogrammes obtenus pour le chrome pur oxydé à 800°C pendant 1 heure dans (a) 20% O_2 dans Ar (b) 20% H_2O dans Ar et (c) 3% H_2O dans H_2

B.2.1.2 Largeurs de bande interdite des oxydes formés

Les largeurs de bande interdite (bandgaps) des oxides semiconducteurs peuvent être évaluées à partir de mesures du photocourant en fonction de l'énergie des photons (Photocurrent Energy Spectra, PES) effectuées à potential appliqué constant. Pour un semiconducteur unique, on observe généralement, comme prévu par le modèle simplifié de

Gärtner–Butler, que la forme des PES reste inchangée lorsque l'on fait varier le potential appliqué. Lorque l'on s'intéresse à des échantillons formés de multiples composants, eux–mêmes potentiellement de types de semiconduction different, cependant, l'on peut s'attendre à ce que la forme des PES dépende du potential appliqué, principalement en raisons des conséquences des différences entre les potentiels de bande plate des composants. Par exemple, changer le potential appliqué peut augmenter la courbure de bande (et le photocourant) d'un composant et la diminuer pour un autre.

De ce fait, et au vu des resultants exposés à la section précédente, nous avons décidé de mesurer des PES à trois potentiels pour chaque échantillon, i.e. dans le domaine cathodique, au voisinage du minimum de photocourant, et dans le domaine anodique.

La Figure B.2 présente les PES ainsi obtenus. On peut observer, comme anticipé plus haut, que l'allure des spectres depend effectivement fortement du potentiel appliqué. Comme attendu pour la chromine pure, tous les spectres montrent de très faibles photocourants pour les énergies de photons inférieures à 3.0 eV (ces photocourants étant très probablement attribuables aux oxydes des impuretés résiduelles). A l'examen des spectres, il apparaît que chacun d'entre eux montrent (au moins) deux contributions au photocourant, en particulier ceux mesurés au voisinage de minimum de photocourant des photovoltammogrammes. De fait, ces spectres présentent un minimum de photocourant près de E = 3.8 eV. D'autre part, si d'un point de vue thermodynamique, seul Cr_2O_3 est un oxyde stable à haute température [6], de precedents travaux dans notre équipe [1, 5, 7] et dans d'autres [8–10] ont révélé des valeurs de bandgaps pour Cr_2O_3 tant à 3.0 eV qu'entre 3.5 eV et 3.7 eV. En conséquence, les deux contributions au photocourant évoquées ci–dessus pourraient signer toutes les deux Cr_2O_3.

Pour essayer d'évaluer les valeurs de bandgaps, E_G, la transformée linéaire classique issue du modèle simplifié de Gärtner–Butler [11–12] a été appliquée aux PES, selon l'équation (B.1),

$$\left(J_{PH} \cdot h\nu\right)^{1/2} = \text{const}\left(E_G - h\nu\right) \qquad \text{(B.1)}$$

où J_{PH}, hν, and E_G représentent le photocourant, l'énergie du photon, et le bandgap repectivement. Signalons en passant que la notation J_{PH}, utilisée dans ce manuscrit pour tous les PES et toutes les transformées linéaires, désigne toujours le module du photocourant.

La Figure B.3 montre les transformées linéaires des PES de la Figure B.2. Une première valeur de gap est facilement obtenue sur chaque spectre, à environ 3.0 $\pm$ 0.1 eV. La seconde valeur de bandgap n'est par contre pas aisée à obtenir sur certains spectres.

Néanmoins, ce second bandgap est clairement vu à 3.8 eV en Figure B.3(a) à 0 mV et en Figure B.3(b) à –400 mV. Par ailleurs, cette valeur d'énergie coïncide avec un changement de 180° du déphasage du photocourant (et donc un changement de signe du photocourant) en Figure B.4(a) and (b). En rapprochant cela des resultants de la Figure B.1, on peut conclure que le premier gap correspond à l'oxyde de type n, tandis que le second correspondrait à un oxide de type p. Pour ce qui concerne les autres spectres, la difficulté à évaluer la valeur du second gap persiste en l'absence de ce changement de signe du photocourant. Dans ces cas, le second bandgap peut être évalué comme l'intersection des deux parties linéaires. Bien que le gap de Cr_2O_3 obtenu à partir des transformées linéaires soit légèrement dependant du potential, nous pouvons conclure que les échantillons de chrome pur oxides comportment deux composants de bandgaps 3.0 eV et 3.3 à 3.8 eV.

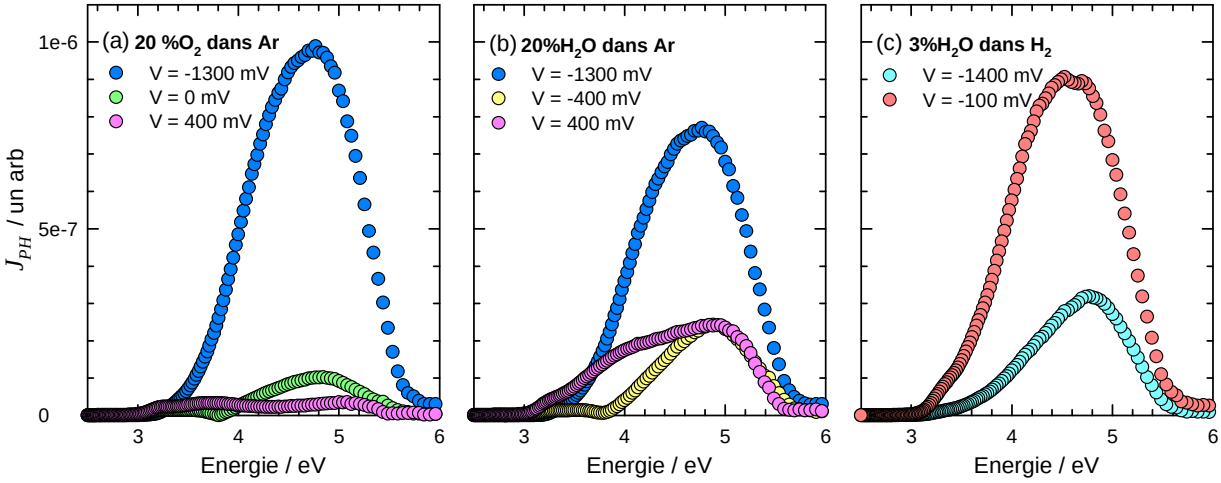

Figure B.2 Spectres en énergie du photocourant obtenus à different potentiels pour du chrome pur oxydé à 800°C pendant 1 heure dans (a) 20% O_2 dans Ar (b) 20% H_2O dans Ar et (c) 3% H_2O dans H_2

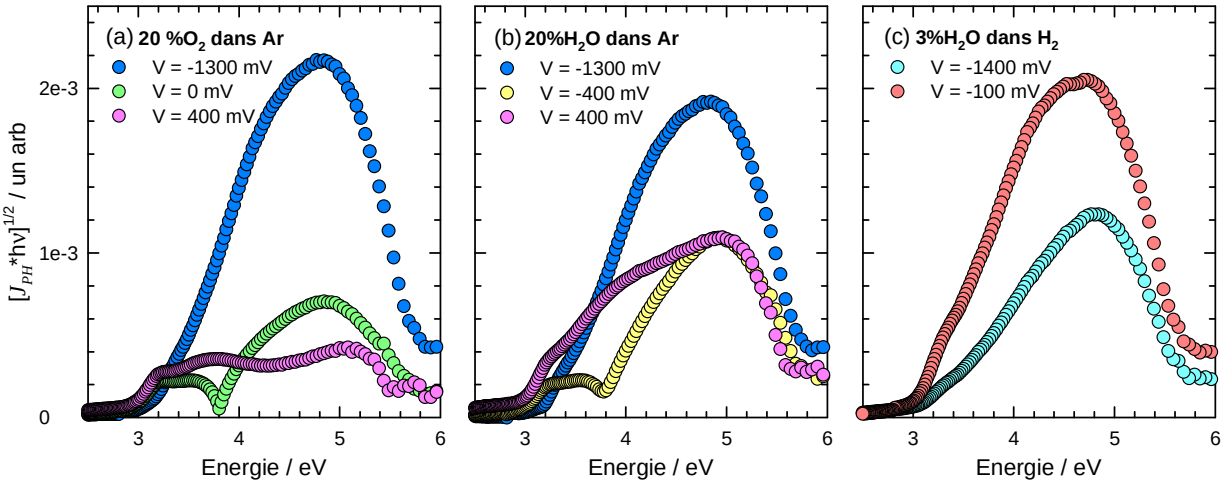

Figure B.3 Transformées linéaires des PES de la Figure B.2

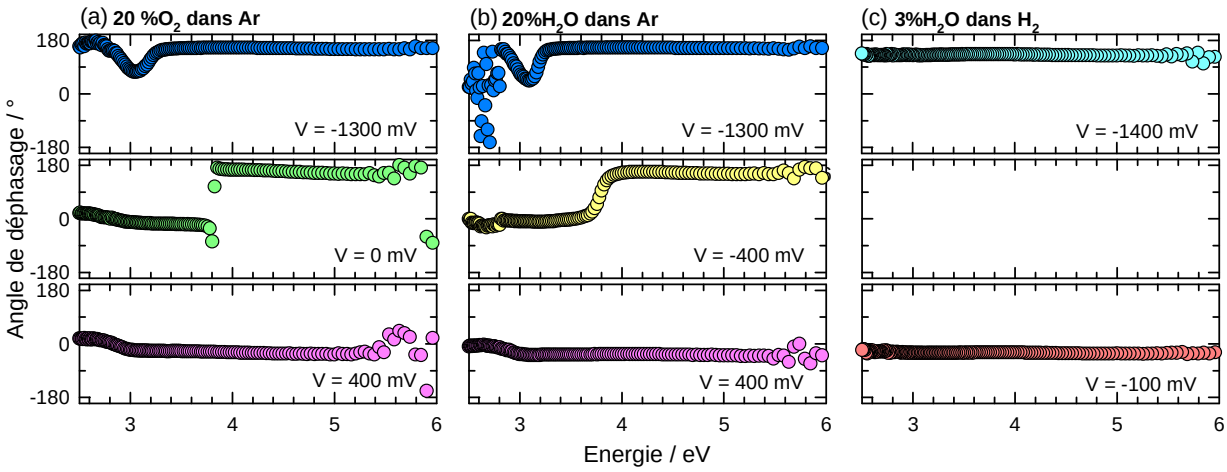

Figure B.4 Déphasages du photocourant en fonction de l'énergie des photons pour les PES de la Figure B.2

B.2.2 Solutions solides $Fe_{2-x}Cr_xO_3$

Des solutions solides hématite–chromine ont été préparées par reaction à l'état solide de mélanges de poudres d'hématite et de chromine. Les poudres de Fe_2O_3 ont été fournies par Chimie–Plus (Ref: 28312) tandis que celles de Cr_2O_3 ont été obtenues auprès de PROLABO (No. 22.798).

B.2.2.1 Corrélation entre la valeur de x dans $Fe_{2-x}Cr_xO_3$ et le shift Raman

Le shift Raman du pic caractéristique de $Fe_{2-x}Cr_xO_3$ (en poudre) autour de 660 cm^{-1} [13–17] a été porté en fonction de x en Figure B.5. Une corrélation linéaire est observée dans l'intervalle allant de x = 0.4 à x = 1.6, le shift Raman variant de 663.6 cm^{-1} jusqu'à 678.7 cm^{-1}. Nos résultats confirment, mais aussi précisent, ceux obtenus auparavant par McCarty and coworkers [14]. Ainsi donc, il sera possible, à partir de spectres Raman, d'estimer x dans les solutions solides $Fe_{2-x}Cr_xO_3$ formées dans les couches d'oxydation des alliages.

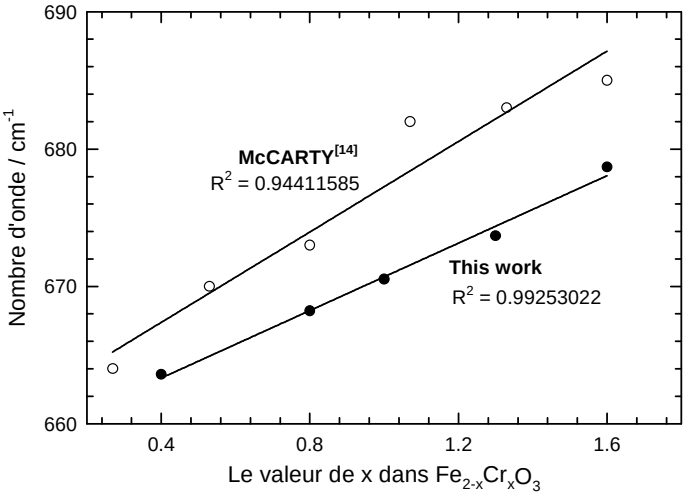

Figure B.5 Shifts Raman du pic principal de $Fe_{2-x}Cr_xO_3$ en fonction de x.

B.2.2.2 Comportement semiconducteur de $Fe_{2-x}Cr_xO_3$

Echantillon correspondant à x = 2.0 (pur Cr_2O_3)

La Figure B.6 présente (a) le PES et (b) la transformée linéaire de ce PES, pour une pastille de chromine (x = 2.0). Un bandgap de 3.1 ± 0.1 eV est obtenu pour cet échantillon, en accord avec les valeurs de la littérature pour la chromine [1, 5, 7]. Le test de photocourant stationnaire illustré en Figure B.6(c) révèle un comportement de type n (photocourant positif) comme celui de la couche interne isotrope formée thermiquement sur le chrome pur. [1]. Bien que l'on se soit davantage attendu au type p, plus fréquemment rapporté dans la littérature, un comportement de type n ne peut être exclu, (Cr_2O_3 est un oxyde amphotère oxide [18]) et a déjà été mentionné avec un gap à 3 eV dans des couches d'oxydes formées à haute température sur des alliages [5, 7].

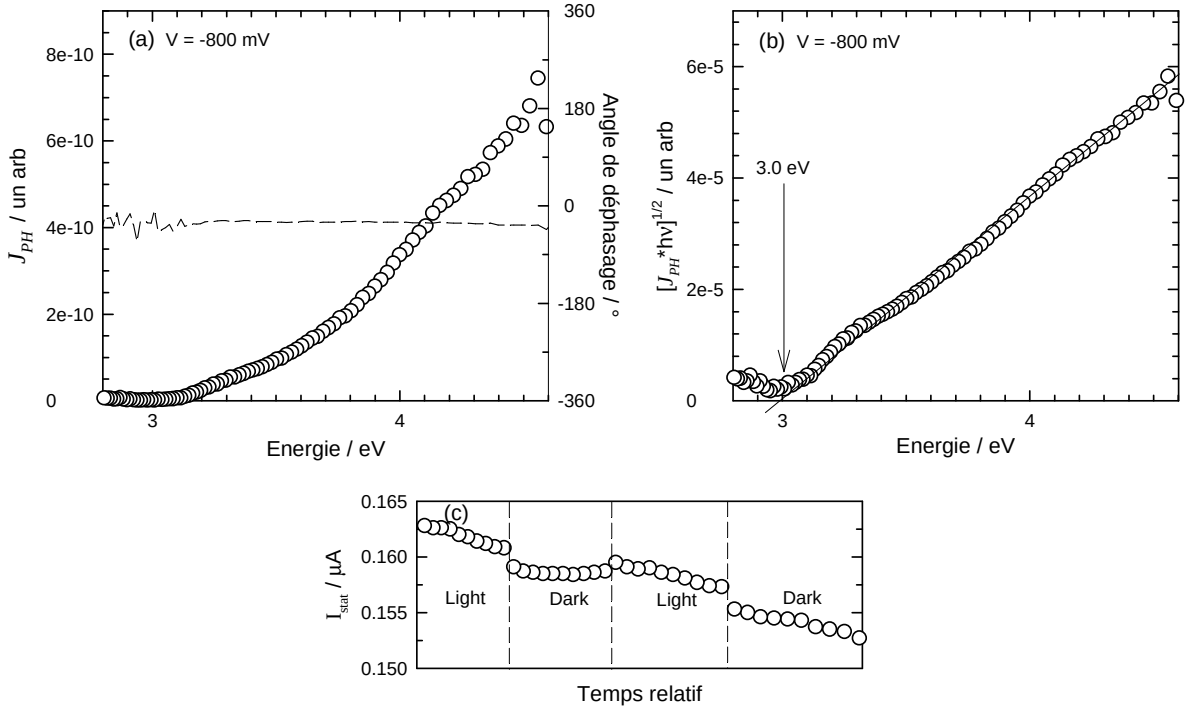

Figure B.6 (a) Photocourant et déphasage (en pointillé) en fonction de l'énergie de photon, (b) Transformée linéaire du PES en (a), et (c) courant direct mesuré sous illumination (light) et dans le noir (dark) pour une pastille de pure chromine (x = 2.0).

Echantillons correspondant à x = 0.4 et x = 1.0

Les PES de ces échantillons, ainsi que leurs transformées linéaires, ont été analysés, de même que les mesures de photocourant stationnaires. Ces spectres ne sont pas présentés ici, mais les principaux résultats sont rassemblés dans le Tableau B.2. Dans les deux cas (x = 0.4 et x = 1.0), trois contributions au photocourant sont mises en évidence, le bandgap le plus faible et le bandgap le plus élevé correspondant pour chauqe échantillon à

celui de l'hématite et celui de la chromine respectivement, alors que le gap intermédiaire, de valeur inférieure à 2.9 eV, est attributable à la solution solide $Fe_{2-x}Cr_xO_3$. Le photocourant est négatif pour les deux échantillons, suggérant un comportement de type p des deux échantillons.

Même si ces expériences n'ont pas permis d'atteindre le but initial, i.e. d'établir une base de données PEC pour les composants de type $Fe_{2-x}Cr_xO_3$ (type de semiconduction, valeur de bandgap), en raison de la difficulté à préparer des pastilles de $Fe_{2-x}Cr_xO_3$ denses et sans phases chromine et hématite résiduelles, l'effet de la stoechiométrie de $Fe_{2-x}Cr_xO_3$ sur la valeur de son gap a été noté: l'échantillon à x = 1.0 montre une valeur de bandgap plus élevée (2.8–2.9 eV) que l'échantillon à x = 0.4 (environ 2.6 eV).

Selon la littérature [19–21], les valeurs de gaps peuvent être estimées à partir de grandeurs thermodynamiques extensives. Il est proposé que le gap de $Fe_{2-x}Cr_xO_3$ peut être estimé à partir de la simple équation:

$$(2\text{-}x)\cdot E_G^{Fe_2O_3} + (x)\cdot E_G^{Cr_2O_3} = 2\cdot E_G^{Fe_{2\text{-}x}Cr_xO_3} \qquad (B.2)$$

Tableau B.2 Résumé des résultats PEC

La valeur de x dans $Fe_{2-x}Cr_xO_3$	0.4	1.0	2.0
La bande interdite (eV)	1.9 / 2.6 / 3.5	1.9 / 2.8–2.9 / 3.5	3.0
Le type de semiconduction	p	p	n

*B.2.3 **Conclusions:** caractéristiques de la chromine et des solutions solides hématite–chromine*

Les caractéristiques de la chromine et des solutions solides hématite–chromine, telles que déduites des résultats la section B.2 peuvent être résumées comme suit:

La chromine présente 2 largeurs de bande interdite: une à 3.0 eV, l'autre dans l'intervalle [3.5–3.8] eV. Elle peut se comporter comme un semiconducteur de type n, ou de type p, ou comme un isolant selon les conditions dans lesquelles elle a été formée.

La valeur de x dans $Fe_{2-x}Cr_xO_3$ peut être obtenue à partir de spectres Raman.

La valeur de x dans $Fe_{2-x}Cr_xO_3$ influe sur le gap de la solution solide.

B.3 Photoélectrochimie à l'échelle mésoscopique: mise au point

Les aciers inox duplex (Duplex Stainless Steel, DSS) nous sont apparus comme des matériaux d'étude intéressants, à la fois pour tester la faisabilité de mesures photoélectrochimiques à l'échelle mésoscopique, et pour évaluer l'intérêt de telles

expériences dans la caractérisation de couches thermiques d'oxydation. Notre choix a d'abord été guidé par des considérations géométriques: aussi bien pour la phase austénitique que la ferritique, le DSS présentait de nombreux grains de taille supérieure à environ 30 µm. Mais des particularités de composition chimiques ont été aussi prises en compte dans notre choix. En effet, les échantillons de notre étude étaient un DSS2205, fourni par APERAM Stainless France, et dont les compositions chimiques sont données dans le tableau B.3. On note que la teneur en chrome est plus élevée dans la phase ferritique que dans la phase austénitique. On peut donc s'attendre à ce que les couches d'oxydation forméessur l'alliage diffèrent selon la nature du grain, par exemple en ce qui concerne la valeur de x dans la solution solide $Fe_{2-x}Cr_xO_3$ généralement observée dans de telles couches d'oxydation. Les échantillons de DSS ont été découpés sous formes de carrés de 10 × 10 (× 2) mm^3, polis jusqu'à 3 µm, ensuite rincés dans une cuve à ultra–sons successivement dans l'éthanol et l'eau distillée, puis conservés en dessicateur pendant 24 heures avant d'être oxydés dans un four tubulaire à 650°C ou 850°C. Des atmosphères d'oxydation sèches et humides ont été utilisées, en l'occurence 20% O_2 ou 20% H_2O dans N_2. Les oxydations ont été conduites pendant 5 minutes et 1 heure dans chacune des conditions d'atmosphère et de température, ce qui a fourni des couches d'oxydation d'épaisseur entre 20 nm et 200 nm.

Dans cette partie, sont présentées les caractérisations d'un échantillon DSS oxydé dans 20 % H_2O dans N_2 à 650°C pendant 5 minutes.

Tableau B.3 Composition chimique de l'acier inox duplex DSS2205 (% massiques)

Elément	Cr	Ni	Mo	Mn	Si	Cu	P	C	N	S	Fe
En moyenne	22.77	5.69	3.09	1.76	0.47	0.17	0.0348	0.035	0.1810	< 0.01	Bal.
Austénite	21.61	7.11	2.42	2.10	0.52	0.27		0.29	0.52		Bal.
Ferrite	26.00	3.80	4.15	1.74	0.64	0.12		0.08	0.05		Bal.

B.3.1 Caractérisations PEC macroscopiques

Des résultats typiques des caractérisations photoélectrochimiques macroscopiques d'un échantillon DSS oxydé (oxidized duplex stainless steel, ODSS) sont présentés en Figure B.7. La Figure B.7(a) montre la dépendance du photocourant au potentiel appliqué, pour diverses énergies de photons. Ces courbes fournissent principalement deux informations. D'une part, comme le module du photocourant augmente lorsque le potentiel appliqué croît, on peut conclure que l'échantillon montre globalement un comportement semiconducteur de type n. D'autre part, deux domaines de potentiel peuvent être observés sur la Figure B.7(a). En–dessous d'environ V = –600 mV, de très faibles photocourants

seulement sont mesurés pour des énergies de photons inférieures à 3 eV. Au–delà de V = –600 mV, des valeurs significatives de photocourants sont obtenues quelle que soit l'énergie des photons. Cela met en évidence le fait que le photocourant global mesuré est la combinaison de plusieurs contributions au photocourant, i.e. est issu de plusieurs oxydes présents dans l'échantillon ODSS. L'amplitude de chaque contribution dépend du potentiel appliqué car ces oxydes n'ont pas le même potentiel de bande plate, et dépend aussi de l'énergie des photons car ces oxydes n'ont pas le même gap. La validité de ces dernières conclusions est aussi confirmée les PES présentés en Figure B.7(b), qui se modifient clairement avec le potentiel appliqué.

En outre, le PES mesuré à V = 0 mV a pu être fitté (la ligne continue sur le graphe correspond au spectre fitté) en utilisant un modèle et des procédures d'ajustement développées dans notre groupe. Ce fit a permis de détecter quatre contributions au photocourant, avec les énergies de gaps indirects suivantes: $E_{G,1}$ = 2.0 eV, $E_{G,2}$ = 2.4 eV, $E_{G,3}$ = 3.1 eV, $E_{G,4}$ = 3.5 eV. $E_{G,1}$ ett $E_{G,4}$ sont attribués à Fe_2O_3 et Cr_2O_3 [19] et, comme expliqué dans ce qui suit, nous pensons que $E_{G,2}$ and $E_{G,3}$ sont à attribuer à deux composants de type $Fe_{2-x}Cr_xO_3$, avec des x différents.

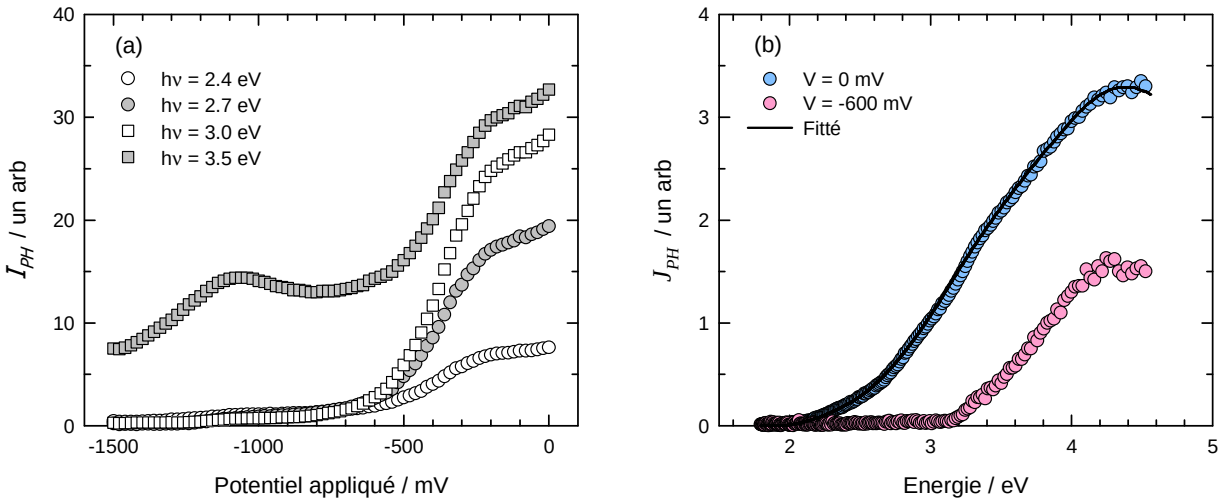

Figure B.7 Photovoltammogrammes typiques obtenus en illuminant tout l'échantillon ODSS: (a) photocourant brut, I_{PH}, en fonction du potentiel appliqué, V, à différentes énergies de photons, et (b) photocourant, J_{PH}, en fonction de l'énergie des photons à un potentiel appliqué donné (la ligne continue montre les spectres fittés)

B.3.2 Imagerie photoélectrochimique

Des images photoélectrochimiques ont été prises sur une zone de l'échantillon comportant à la fois des grains austénitiques et des grains ferritiques (Figure B.8(a)), à deux énergies de photon: 2.60 eV (Figure B.8(b)), une valeur entre $E_{G,2}$ and $E_{G,3}$, et 3.53 eV (Figures B.8(c) et (d)), et aussi à deux valeurs de potentiel appliqué, V = –200 mV (Figures

B.8(b) et (d)) et V = – 700 mV (Figure B.8(c)). On observe que les photocourants fournis par les grains austénitiques oxydés sont plus élevés que ceux mesurés sur les grains ferritiques oxydés. Cependant, les contrastes de photocourant entre grains dépendent sensiblement de l'énergie des photons et du potentiel appliqué. A ce point de notre discours, cette observation est difficile à expliquer, bien que l'on puisse suggérer que le composant correspondant à $E_{G,2}$ pourrait être absent sur les grains ferritiques.

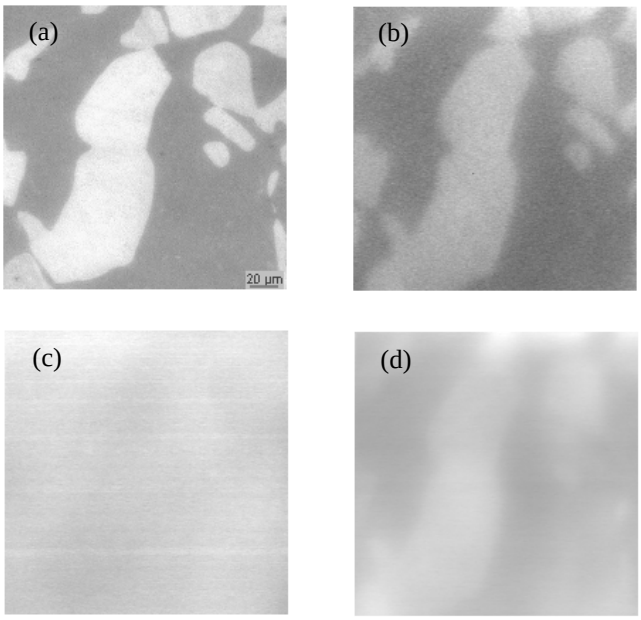

Figure B.8 Images optiques et photoélectrochimiques d'une zone 200 µm x 200 µm de l'échantillon ODSS: (a) image optique; (b), (c), (d) : images PEC obtenues à : (b) V = –200 mV, hν = 2.6 eV, (c) V = –700 mV, hν = 3.53 eV, (d) V = –200 mV, hν = 3.53 eV

B.3.3 Caractérisations photoélectrochimiques mésoscopiques

Les grains ferritiques et austénitiques oxydés étudiés dans les expériences illustrées en Figure B.8 ont été caractérisés individuellement à l'échelle mésoscopique. Les PES correspondants sont présentés en Figure B.9. Ces résultats montrent premièrement que des PES peuvent effectivement être mesurés à l'échelle mésoscopique. Mais ils mettent aussi en évidence l'intérêt de caractérisations PEC à cette échelle.

D'une part, les données de la Figure B.9 permettent d'évaluer, à des énergies et des potentiels proches des valeurs utilisées en Figure B.8, les rapports des valeurs de photocourant mesurées sur les grains austénitiques à celles mesurées sur les grains ferritiques. Ces rapports sont compilés dans le Tableau B.2, et rendent clairement compte de la dépendance des contrastes des images de la Figure B.8 avec le potentiel appliqué ou l'énergie des photons.

D'autre part, lorsque l'on fitte les PES individuels des grains oxydés d'austénite et de ferrite, il s'avère (Tableau B.4) que seulement 3 oxydes sont détectés sur chaque type de grain. Les énergies de gap de Fe_2O_3 et Cr_2O_3 sont trouvées quelle que soit la phase métallurgique du grain, mais un seul gap correspondant à un composé de type $Fe_{2-x}Cr_xO_3$ est observé sur chaque grain: 2.46 eV sur les austénitiques, 2.84 eV sur les ferritiques.

Comme déjà évoqué avec l'équation (B.2), les valeurs de gaps peuvent être estimées à partir de données thermodynamiques atomiques. Au regard des valeurs de gaps obtenues respectivement sur les grains austénite et ferrite pour $Fe_{2-x}Cr_xO_3$ (Tableau B.4), l'équation (B.2) implique que la solution solide oxyde formée sur la phase austénite est moins riche en chrome que celle formée sur la phase ferrite, comme on pouvait d'ailleurs le prévoir connaissant les copositions métallurgiques de chaque phase.

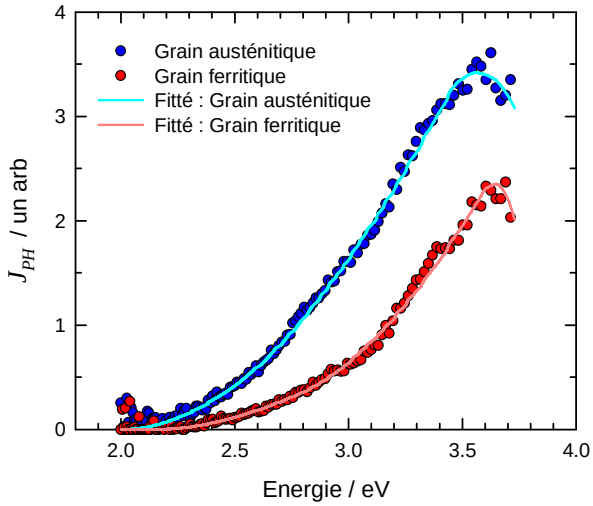

Figure B.9 PES obtenus en illuminant individuellement des grains oxydés austénitiques (cercles bleus) ou ferritiques (cercles rouges) à V = 0 mV (les lignes continues correspondent aux spectres fittés)

Tableau B.4 Rapports des valeurs de photocourant mesurées sur des grains austénitiques à celles mesurées sur des grains ferritiques (données de la Figure B.9)

		V = 0 mV	V = –600 mV
	hν = 2.60 eV	3.3	– –
	hν = 3.53 eV	1.7	1.1

B.3.4 Spectroscopie Raman

Les spectres Raman mesurés individuellement sur des grains oxydés de ferrite et d'austénite sont présentés en Figure B.10. Ces spectres montrent tous deux les pics caractéristiques de l'hématite à 411 cm^{-1}, et de la chromine à 550 cm^{-1}. Le pic large observé aux valeurs les plus élevées de shift Raman est typique de $Fe_{2-x}Cr_xO_3$ [14–17]. On note que ce pic est déplacé de 668 cm^{-1} (austénite) à 674 cm^{-1} (ferrite), ce qui, d'après la section B.2.2.1

et les travaux de McCarty et al. [13], signe une valeur de x plus faible pour la solution solide oxyde formée sur l'austénite, comme déjà déduit plus haut des PES mésoscopiques. De plus, d'après les résultats de B.2.2.1 et les spectres de la Figure B.10, une valeur de x=0.8 (resp. x=1.3) peut être estimée pour le cas l'austénite oxydée (resp. de la ferrite oxydée). Les énergies de gap correspondant à ces valeurs de x (en prenant le gap de Fe_2O_3 à 2.0 eV, et celui de Cr_2O_3 à 3.5 eV) sont données dans le Tableau, elles sont très proches de celles obtenues en fittant les PES mésoscopiques.

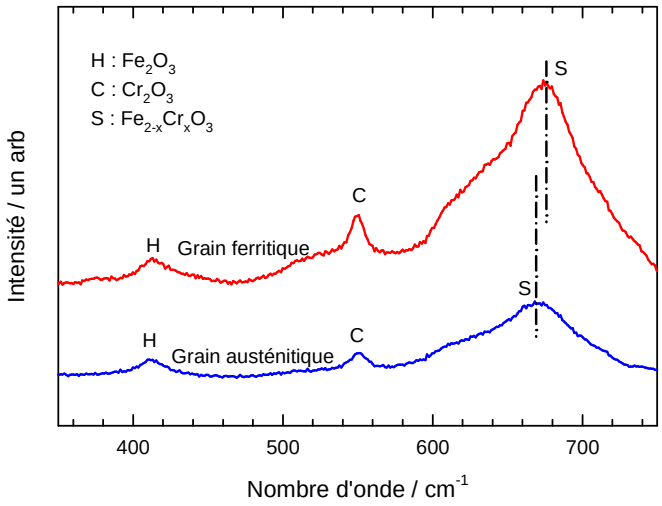

Figure B.10 Spectres Raman mesurés individuellement sur des grains austénitiques (en bas) et ferritiques (en haut) de l'échantillon ODSS

Tableau B.5 Récapitulatif des gaps, E_G, obtenus par fit des PEC mésoscopiques de l'échantillon ODSS (a), et des valeurs de E_G de $Fe_{2-x}Cr_xO_3$ calculées à partir des valeurs de x obtenues par spectroscopie Raman (b) (en eV)

			Fe_2O_3	$Fe_{2-x}Cr_xO_3$		Cr_2O_3
(a) Comme obtenue par fit des spectres en énergie du photocourant	Macroscopique		2.0	2.4	3.1	3.5
	Mésoscopique	le grain austénitique	2.0	2.4(6)		3.4
		le grain ferritique	2.1		2.8(4)	3.5
(b) Comme obtenue par spectroscopie Raman (des valeurs de x)		le grain austénitique		2.6		
		le grain ferritique			2.9	

B.3.5 PEC à l'échelle mésoscopique : conclusions

Il a été montré ici que l'ensemble des outils photoélectrochimiques disponibles à l'échelle macroscopique peut maintenant être aussi mis en œuvre à l'échelle mésoscopique, pour obtenir localement des informations photoélectrochimiques complètes sur différentes zones (30 µm en diamètre) d'un même échantillon.

Les résultats obtenus à l'échelle mésoscopique dans le cas d'un acier inox duplex oxydé ont fourni des résultats intéressants complémentaires à ceux des études micro– et macroscopiques. En particulier, la question de l'origine de la dépendance en potentiel et énergie des contrastes des images photoélectrochimiques a pu être élucidée. Il a également être observé que, alors que les résultats macroscopiques suggéraient la présence de 4 oxydes (Fe_2O_3, Cr_2O_3 et 2 composés de type $Fe_{2-x}Cr_xO_3$) dans la couche thermique, les PES mésoscopiques ont montré que Fe_2O_3 et Cr_2O_3 étaient présents sur tous les grains, mais que la couche formée sur chaque grain (oxydé exactement dans les mêmes conditions) ne contenait très probablement qu'un unique composé de type $Fe_{2-x}Cr_xO_3$, la avleur de x étant fixée par la nature métallurgique du grain.

Enfin, il faut remarquer que la nouvelle approche développée dans notre groupe pour l'ajustement des PES a pu être appliquée aussi aux PES mésoscopiques.

B.4 Oxydation des aciers inox duplex: une étude photoélectrochimique multi–échelle

Pour aller plus loin dans l'étude de l'oxydation de l'acier DSS2205, tous les échantillons ODSS préparés comme indiqué au début de B.3 ont été caractérisés par photoélectrochimie multi–échelle.

B.4.1 Caractérisations macroscopiques

L'ensemble des photovoltammogrammes obtenus sur les échantillons ODSS peut être classé entre 3 groupes, comme illustré en Figure B.11. La Figure B.11(a) montre les résultats typiques obtenus pour les échantillons oxydés en vapeur d'eau (à l'exception de celui oxydé à 850°C pendant 60 min) : les échantillons ont globalement un comportement semiconducteur de type n. En outre, si l'on considère l'accroissement brusque du photocourant vers –500 mV, alors que le déphasage ne varie pas significativement dans cette zone de potentiel, on peut suggérer que composants de type n sont présents dans la couche d'oxydation, de potentiels de bande plate différents. Au contraire, les échantillons DSS oxydés dans l'oxygène ont généralement l'allure de la Figure B.11(c), typique d'un comportement global de type p pour les couches. La forme particulière du photovoltammogramme de la Figure B.11(b) n'a été observée que pour l'échantillon oxydé en vapeur d'eau à 850°C pendant 60 min; elle signe la présence d'au moins deux composants dans la couche d'oxydation, l'un de type n comme le montre la courbe mesurée à 2.41 eV, l'autre étant plus ou moins isolante comme le suggère l'allure en V du photovoltammogramme mesuré à 3.53 eV.

La Figure B.12 présente les PES macroscopiques mesurés à plusieurs valeurs de potentiel appliqué pour les mêmes échantillons ODSS que ceux de la Figure B.11. L'allure ces spectres est très dépendante du potentiel appliqué. Cela, à nouveau, peut être expliqué par le fait que les échantillons oxydés sont constitués de plusieurs composants semiconducteurs, de bandgaps et potentiels de bande plate différents: changer le potentiel appliqué ne change pas le gap de ces composants, mais induit des modifications de la courbure de bande de chaque composant, et par conséquent, des changements relatifs des photocourants complexes fournis par cahque composant. Cette dépendance du photocourant au potentiel appliqué est intéressante car, l'examen de tous les spectres et des changements de pentes dans ces spectres, permet de conclure que chaque spectre est la combinaison d'au moins trois contributions au photocourant global, dont les gaps seraient approximativement 2 eV, 2.6 à 3.0 eV, et environ 3.4 eV; ces valeurs de gap sont en accord avec ce qu'on attendrait pour des couches formées de Fe_2O_3, $Fe_{2-x}Cr_xO_3$, et Cr_2O_3 respectivement, et avec les valeurs fittées en section B.3.

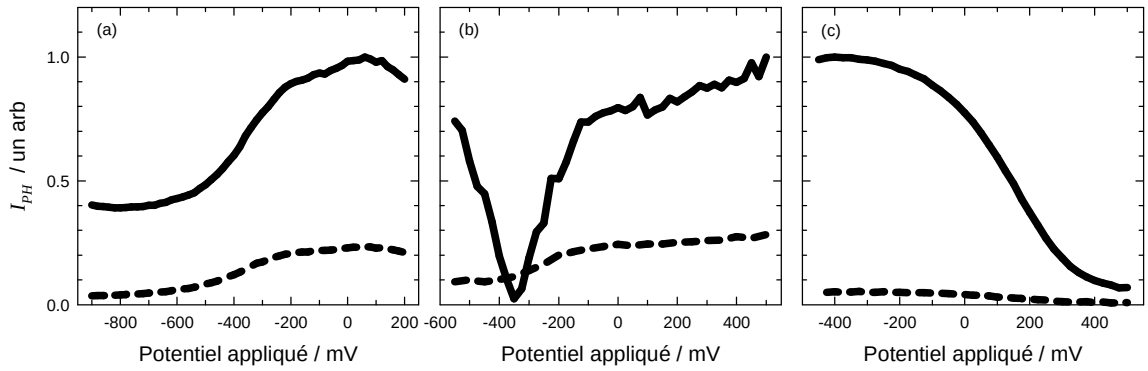

Figure B.11 Photovoltammogrammes typiques obtenus à hν = 2.41 eV (pointillés) et 3.53 eV (ligne continue) sur l'ensemble de la surface d'un DSS oxydé vapeur d'eau (a) à 650°C pendant 5 min, (b) à 850°C pendant 60 min, et en oxygène (c) à 850°C pendant 60 min

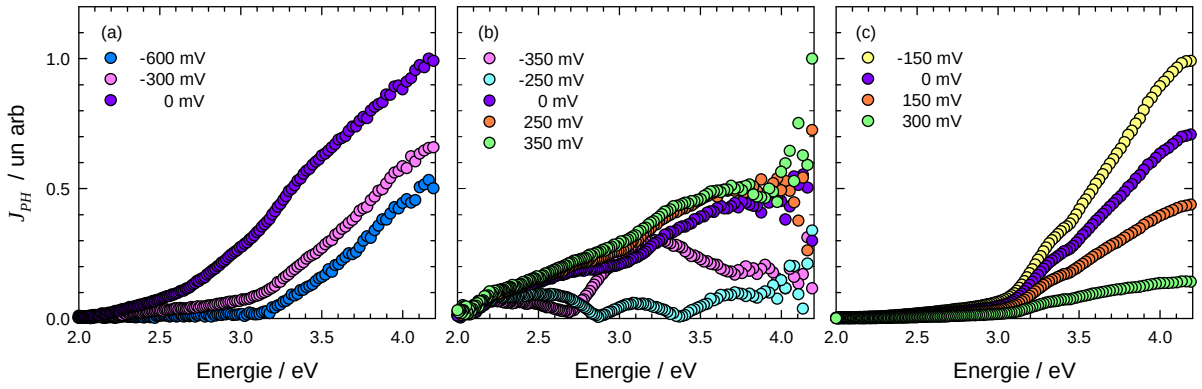

Figure B.12 PES mesurés à divers potentiels sur l'ensemble de la surface d'un DSS oxydé en vapeur d'eau (a) à 650°C pendant 5 min, (b) à 850°C pendant 60 min, et en oxygène (c) à 850°C pendant 60 min

B.4.2 Caractérisations mésoscopiques

Des photovoltammogrammes et des PES à l'échelle mésoscopique ont été mesurés individuellement sur des grains austénitiques et ferritiques. La Figure B.13 montre des photovoltammogrammes typiques obtenus sur toute la surface, et sur des grains individuels, d'échantillons ODSS, à une énergie de photon de 3.53 eV, i.e. plus grande que le gap de la chromine. En atmosphère oxygène (Figure B.13(b)), quel que soit le grain, un comportement semiconducteur de type p est clairement observé, résultat de la croissance d'une couche thermique de chromine dans un milieu à forte activité d'oxygène. Au contraire, en vapeur d'eau (Figure B.13(a)), la chromine est proche de l'isolant, comme l'indique l'allure en V du photovoltammogramme. De plus, le potentiel de bande plate, correspondant au potentiel du minimum de photocourant est situé sur les photovoltammogrammes macroscopiques à environ –350 mV, une valeur intermédiaire entre celles des grains indiciduels, ce qui met en évidence que la réponse macroscopique moyenne celles des différents grains.

On notera que l'atmosphère d'oxydation affecte de la même façon le comportement semiconducteur des grains austénitiques et ferritiques.

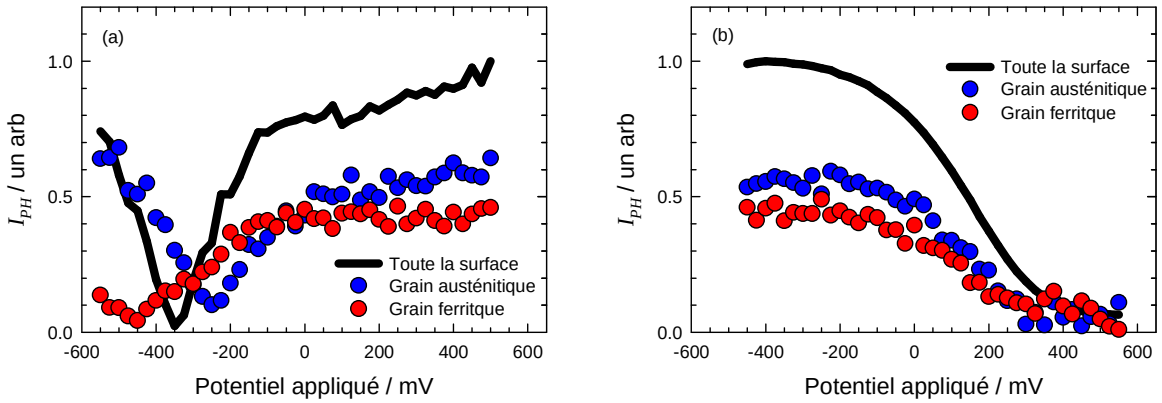

Figure B.13 Photovoltammogrammes typiques obtenus à hν = 3.53 eV sur l'ensemble de la surface et sur les grains individuels d'un DSS oxydé à 850°C pendant 60 min (a) en vapeur d'eau et (b) en oxygène

Quelques points particuliers peuvent également être notés, comme illustré par les résultats présentés en Figure B.14 et dans le Tableau B.6. A faible activité en oxygène (Figure B.14(a)), les différences entre les PES des grains ferritiques et austénitiques sont principalement observées à basse énergie, avec des photocourants plus élevés issus d'oxydes riches en fer sur les grains d'austénite. Au contraire, à forte activité en oxygène (Figure B.14(b)), ces différences sont principalement visibles à haute énergie, avec des photocourants plus forts issus des oxydes riches en chrome sur les grains austéniques.

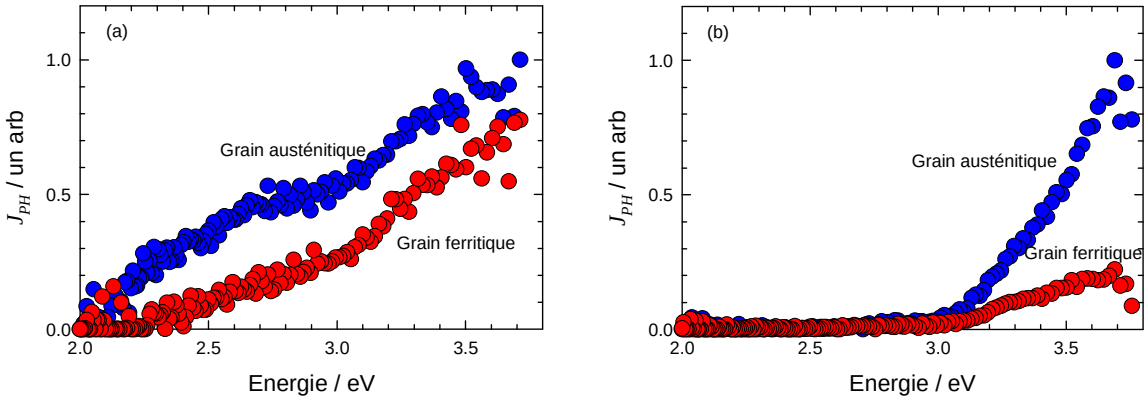

Figure B.14 PES obtenus sur des grains austénitiques (●) et ferritique (●) d'un DSS oxydé à 850°C pendant 60 min (a) en vapeur d'eau, à 350 mV (b) en oxygène, à 0 mV

Tableau B.6 Rapports des photocourants mesurés sur l'austénite à ceux mesurés sur la ferrite (données de la Figure B.14)

Les atmosphères d'oxydation		La vapeur d'eau	L'oxygène
	hν = 2.60 eV	2.89	1.48
	hν = 3.53 eV	1.40	3.18

B.4.3 Caractérisations microscopiques

La Figure B.15 montre une série d'images photoélectrochimiques obtenues pour des échantillons oxydés en vapeur d'eau (images du haut) et en oxygène (images du bas) à 850 °C pendant 60 min, au même potentiel que pour la Figure B.14. Les images (d) et (h) ont été obtenues en divisant, point par point, pour chaque échantillon, le photocourant mesuré à 2.60 eV par celui mesuré à 3.53 eV. En Figure B.15(a) (resp. B.15(b)) les grains d'austénite (γ) correspondent aux zones plus foncées (resp. plus claires), les grains ferritiques (α) aux zones plus claires (resp. plus sombres).

Des contrastes plus élevés sont obtenus dans le visible pour les échantillons formés en vapeur d'eau, alors que de meilleurs contrastes sont obtenus en UV pour les échantillons formés en oxygène, parce que l'oxyde majoritaire en vapeur d'eau est l'hématite et/ ou une solution solide riche en fer, alors qu'en oxygène l'oxyde majoritaire est la chromine et/ou une solution solide riche en chrome. Ces dernières observations sont en accord avec les résultats mésoscopiques présentés plus haut (Figure B.14). De plus, les images photoélectrochimiques montrent toujours des photocourants plus élevés sur les grains oxydés d'austénite que sur ceux de ferrite. Comme la spectroscopie Raman suggère des couches un peu plus épaisses sur la ferrite (en accord avec un apport de chrome plus important à l'interface métal/oxyde), le fait que les photocourants soient plus élevés sur l'austénite est

plutôt à relier à un moindre dopage, ou à un taux de recombinaisons moindre des paires électron–trou photogénérées, mais la question reste ouverte.

Puisque les valeurs de photocourant mesurées à 2.60 eV sont dues aux contributions de Fe_2O_3 et $Fe_{2-x}Cr_xO_3$ alors que celles mesurées à 3.53 eV sont dues à ces mêmes oxydes mais aussi à Cr_2O_3, il est attendu des images (d) et (h) qu'elles donnent une estimation grossière de la fraction de Cr_2O_3 dans les couches. Sur cette base, dans le cas de l'oxydation en vapeur d'eau (Figure B.15(d), la fraction de Cr_2O_3 fraction apparaît plus élevée sur la ferrite que sur l'austénite. Cela peut être expliqué si l'on considère que la teneur en chrome dans la phase ferritique est plus élevée que dans la phase austénitique, conduisant à la formation de davantage de chromine protectrice sur la ferrite au début de l'oxydation; en outre, la diffusion à haute température du chrome est connue pour être plus rapide dans la ferrite que dans l'austénite, et une teneur en fer plus élevée dans l'austénite induit une diffusion plus importante du fer dans l'oxyde corundum et réduit la fraction de chromine. En atmosphère oxygène, la pression partielle élevée d'oxygène joue un rôle négatif, et on observe des résultats opposés. (Figure B.15(h)).

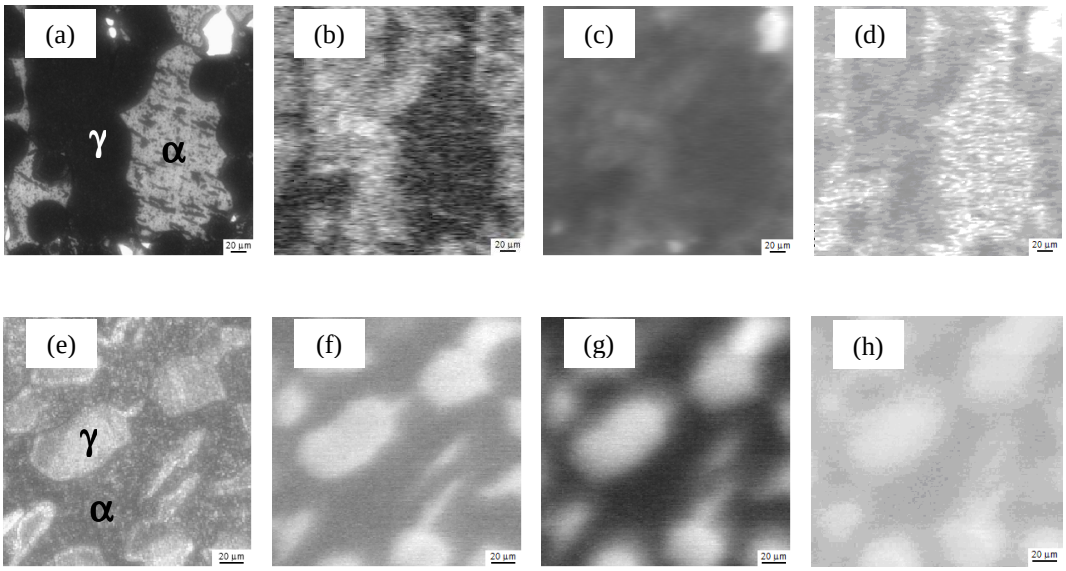

Figure B.15 Jeu d'images pour un ODSS obtenu à 850°C pendant 60 min en vapeur d'eau (images du haut) et en oxygène (images du bas): (a) et (e) images optiques, (b) et (f) images PEC à hυ = 2.60 eV, (c) et (g) images PEC à hν = 3.53 eV, et (d) et (h) images composites (voir texte)

B.4.4 Conclusions sur l'oxydation de l'acier inox duplex

La durée d'oxydation, la température d'oxydation, et les atmosphère d'oxydation influent à la fois sur la nature des oxydes formés et sur leur type de semiconduction. Les caarctérisations macroscopiques, qui moyennent le comportement des garins individuels, ont néanmoins permis de pointer les effets principaux des variations des paramètres d'oxydation.

Les expériences à l'échelle mésoscopique ont mis en évidence les différences entre les couches formées sur les grains ferritiques et austénitiques, et permis de rendre compte des contrastes observés sur les images photoélectrochimiques. Ces dernières ont montré des différences dans la fraction relative de chromine sur les deux types de grain, différences sensibles à l'atmosphère d'oxydation.

Les phases corundum de Fe_2O_3, $Fe_{2-x}Cr_xO_3$, et Cr_2O_3 ont toujours été détectées sur les deux types de grains, la teneur en chrome de $Fe_{2-x}Cr_xO_3$ ne dépendnat pas seulement de la nature des grains, mais aussi de l'atmosphère d'oxydation. Quelle que soit la nature du grain, la semiconduction de la chromine est affectée de la même façon, et dépend nettement l'activité en oxygène dans l'atmosphère d'oxydation. A faible pression partielle d'oxygène, (eg en vapeur d'eau), la chromine est isolante, i.e. constitue un oxyde protecteur proche de la stoechiométrie. Au contraire, à forte pression partielle d'oxygène (e.g. en oxygène), la chromine ets clairement de type p.

B.5 Oxidation of Ni–based alloys: multiscale photoelectrochemical study

Les objectifs de cette partie ne sont pas seulement d'évaluer les performances de caractérisations photoélectrochimiques multi–échelles, mais aussi de montrer l'intérêt du modèle développé au laboratoire pour l'analyse des PESdans le cas de couches d'oxydes complexes. Des alliages base nickel (Inconel 690) modèles développés et fournis par le CEA Saclay ont été polis jusqu'au μm, et nettoyés dans l'éthanol puis l'eau distillée dans une cuve à ultra–sons. Les expériences d'oxydation ont été menées dans une thermobalance SETARAM (modèle B24) à 900°C. Des atmosphères d'oxydation sèche et humide ont été utilisées, constituées respectivement de flux de 20% O_2 et 20% H_2O dans l'azote. Les oxydations ont été conduites pendant 2 heures et/ou 30 heures. Par ailleurs, des oxydations à l'air ambiant ont été aussi réalisées, dans un four conventionnel, à 900°C pendant 21 heures. Toutes les couches d'oxydes obtenues avaient une épaisseur inférieure à 2 μm.

Tableau B.7 Composition chimique de l'Inconel 690 utilisé (% massique)

Elément	Cr	Fe	C	S	O	N	Ni
% massique	29.79	10.14	0.0059	< 0.0005	< 0.0010	< 0.0005	Bal.

B.5.1 Aperçu général des photovoltammogrammes et du comportement semiconducteur des couches d'oxydes

La Figure B.16 présente les photovoltammogrammes macroscopiques mesurés à plusieurs énergies de photons pour des échantillons diversement oxydés.

L'allure des courbes correspondant à une oxydation sur un temps court en oxygène (Figure B.16(a)) montre à la fois des comportements de type n (énergies inférieures à 3.1 eV) et de type p (énergies supérieures à 3.1 eV). Pour les échantillons oxydés dans la même atmosphère mais plus longtemps (Figure B.16(b)), si le comportement aux plus hautes énergies est toujours de type p, la forme en V observée aux plus basses énergies au voisinage du minimum de photocourant suggère un comportement plus proche de l'isolant.

Au contraire, dans le cas des échantillons oxydés 30 heures en vapeur d'eau (Figure B.16(c)), les photovoltammogrammes montrent une combinaison isolant/type n, ce qui à nouveau confirme que la présence de vapeur d'eau promeut une semiconduction de type n de certains des oxydes formés.

Les résultats obtenus pour l'échantillon oxydé à l'air pendant 21 heures (Figure B.16(d)) sont très similaires à ceux obtenus pour l'échantillon oxydé 30 heures en oxygène, excepté que la contribution en forme de V–shaped est moins nette.

Pour conclure cette section, nous voudrions mentionner que les remarques ci–dessus doivent être considérées comme des tendances brutes, moyennées, car le nombre de composants dans les couches est certainement plus grand que deux.

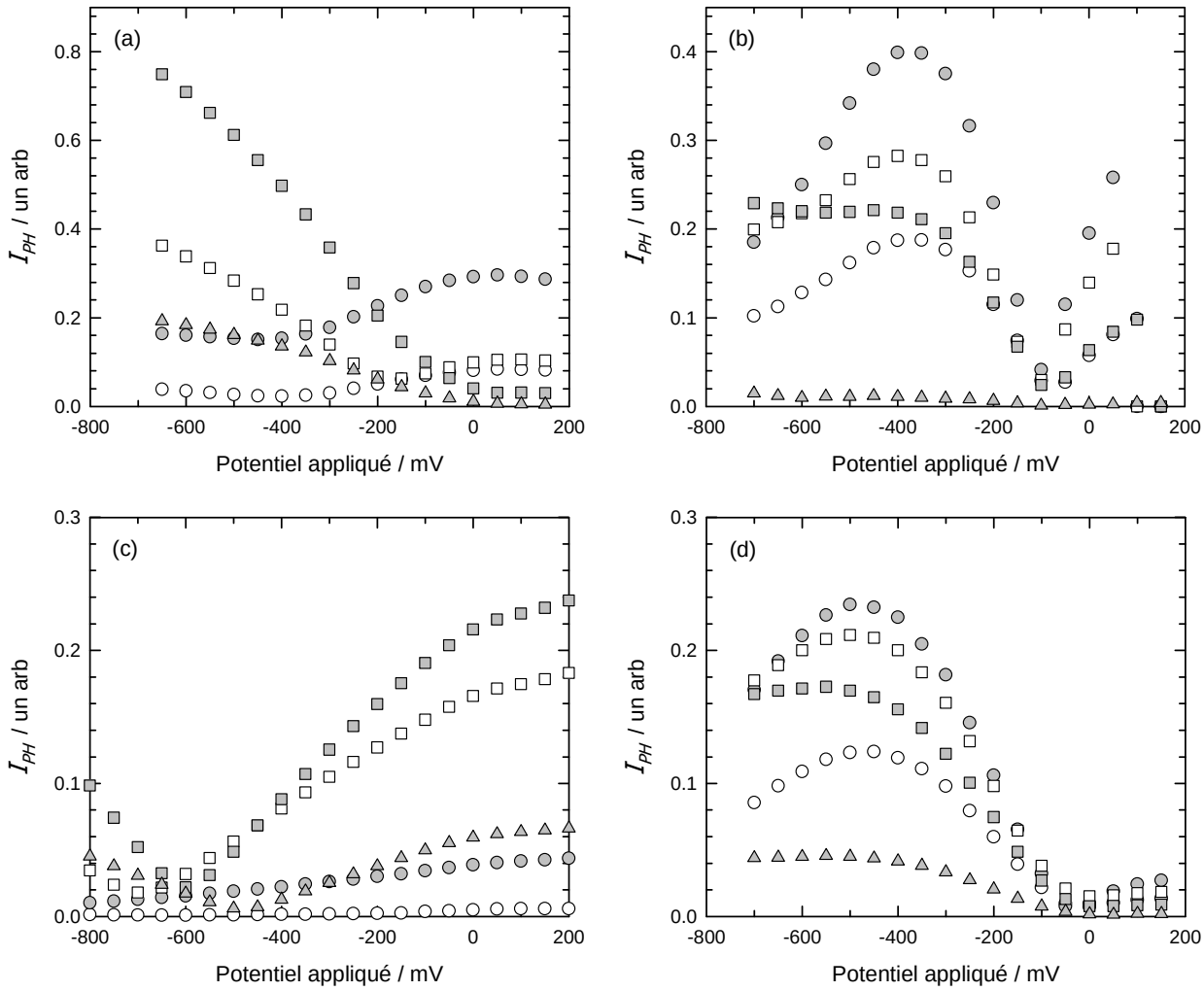

Figure B.16 Photovoltammogrammes typiques (modules) obtenues pour hν = 2.54 eV (○), hν = 3.10 eV (●), hν = 3.54 eV (□), hν = 4.08 eV (■), and hν = 4.66 eV (△), sur l'ensemble de la surface de l'alliage 690 oxydé (a) en oxygène pendant 2 h, (b) en oxygène pendant 30 h, (c) en vapeur d'eau pendant 30 h, et (d) à l'air pendant 21 h

B.5.2 PES des couches oxydées : évaluation des gaps de leurs composants

B.5.2.1 Caractérisations macroscopiques: analyse classique en transformées linéaires

Tous les PES obtenus pour les alliages base nickel oxydés ont montré un meêm comportement : l'allure des spectres dépend fortement du potentiel appliqué, et ils montrent toujours la présence de plus d'un composant dans les couches. La Figure B.17 présente l'exemple des PES mesurés pour l'échantillon oxydé 30 heures en vapeur d'eau et les transformées linéaires correspondantes. En Figure B.17(a), les contributions au photocourant pour les énergies en–dessous de 3.0 eV sont très faibles, ce qui montre que la vapeur d'eau favorise les phases oxyde à fort gap ($\geq$ 3.0 eV), et défavorise le développement

d'oxydes de gaps plus faibles. La Figure B.17(b) suggère la présence d'au moins 4 oxydes de gaps < 2.9 eV, 2.9–3.1 eV, 3.7–3.9 eV et > 4.0 eV.

Cependant, la grande complexité des PES ci–dessus, et celle de leurs transformées linéaires doit nous prévenir de tirer des conclusions définitives tant sur le nombre de composants que sur le gap des ces composants. En conséquence, chacun de ces PES a été analysé et fitté à l'aide de notre nouveau modèle. Les résultats correspondants sont présnetés dans la suite.

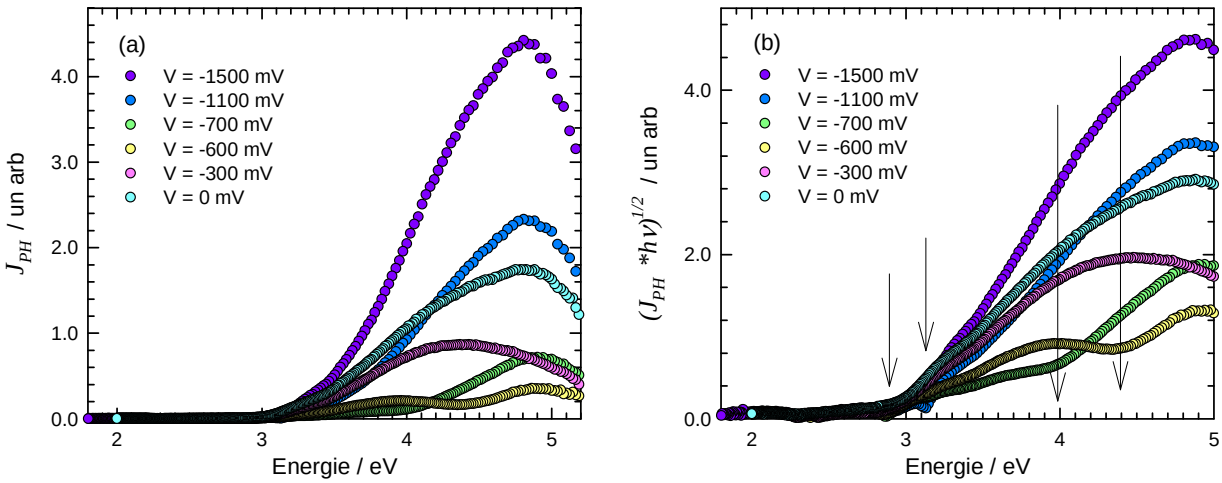

Figure 4.17 (a) PES et (b) leurs transformées linéaires obtenus pour l'ensemble de la surface de l'alliage 690 oxydé en vapeur d'eau pendant 30 h

B.5.2.2 Caractérisations macroscopiques: fit des PES

Les PES sont habituellement analysés au moyen de transformées linéaires pour tirer parti du fait que, dans la forme simplifiée du modèle de Gärtner–Butler, le rendement quantique, η, du photocourant est proportionnel au coefficient d'absorption de la lumière, ce qui permet d'écrire l'équation simple suivante:

$$(\eta \times E)^{1/n} = C \times (E - E_G) \qquad \text{(B.3)}$$

où E est l'énergie du photon, n vaut 2 (resp. ½) pour une transition indirecte (resp. directe) et C est une constante, dépendant du matériau, du potentiel appliqué (et de la fréquence de modulation de la lumière).

Beaucoup de travaux expérimentaux décrits dans la littérature ont utilisé avec succès cette analyse classique, pour des matériaux faits d'un ou deux composants [22–25]. Mais, jusqu'à aujourd'hui, pour des couches complexes d'oxydes constituées de plusieurs composants de type n et p, aucune description complète des PES n'a pu être proposée, et seules des informations semi–quantitatives et/ou partielles ont pu être obtenues sur les composants de ce type de couches oxydées.

Mais, comme J_{PH} est mesuré sous illumination modulée, et de ce fait est une grandeur complexe, notre groupe a proposé [26] de considérer simultanément les parties réelle ($Re(J_{PH})$) et imaginaire ($Im(J_{PH})$) du photocourant (ou le module $|J_{PH}|$ / et le déphasage θ) pour l'analyse et le fit des PES, plutôt que seulement le module ($|J_{PH}|$), comme fait jusqu'à présent. Ainsi, le photocourant complexe global, J_{PH}, s'écrit:

$$J_{PH} = |J_{PH}|\cos\theta + j|J_{PH}|\sin\theta = \sum_i J_{PH,i}\cos\theta_i + jJ_{PH,i}\sin\theta_i \qquad (B.4)$$

où $J_{PH,i}$ et θ_i représentent le module et le déphasage, respectivement, du photocourant issu du $i^{ème}$ composant semiconducteur de la couche d'oxydes. Pour des semiconducteurs de faible épaisseur comme ceux étudiés ici, les régions de charge d'espace sont faibles par rapport à la profondeur de pénétration de la lumière. $J_{PH,i}$ est donc supposé, à un potentiel donné (et à une fréquence de modulation donnée), suivre la forme simplifiée du modèle de Gärtner–Butler, et donc s'écrire comme suit:

$$\left(J_{PH,i}\times E\right)^{1/n} = K_i \times \left(E\text{-}E_{G,i}\right) \qquad (B.5)$$

où $E_{G,i}$ et K_i représentent le gap et une valeur proportionnelle à C (J_{PH} est proportionnel mais pas égal à η) pour le $i^{ème}$ composant semiconducteur. De plus, comme les charges d'espaces s'étendent probablement sur toute l'épaisseur de chaque oxyde, il est fait l'hypothèse que les recombinaisons des paires électron–trou photogénérées, et donc les déphasages, θ_i, ne dépendent pas de l'énergie des photons.

Les valeurs expérimentales de J_{PH} (E) et θ(E) constituant un PES ont été fittées selon le modèle ci–dessus (avec n = 2, car des transitions directes n'ont été que rarement observées pour des matériaux désordonnés) en utilisant un logiciel développé au laboratoire dans l'environnement Matlab® (R2011b release). Pour la procédure d'optimisation, ce logiciel fait appel à la fonction *fminsearch*, qui tire elle–même parti de la méthode du simplex de Lagarias *et al.* [27] pour trouver le minimum d'une fonction scalaire de plusieurs variables non contraintes, en partant de valeurs initiales estimées ou quelconques de ces dernières.

Dans ce travail, pour un vecteur donné de *m* ($E_{G,i}$, K_i, θ_i) triplets, *m* représentant le nombre supposé de phases semiconductrices contribuant au photocourant, la fonction scalaire à minimiser par la fonction *fminsearch* a été définie comme le produit des racines carrées de deux quantités, D^2_{Re} et D^2_{Im}, où D^2_{Re} (resp. D^2_{Im}) est la somme des carrés à chaque énergie de la différence entre la partie réelle (resp. imaginaire) des données expérimentales et celle des valeurs calculées avec l'équation (B.3).

Dans le logiciel en question, la valeur de *m* est fixée par l'utilisateur. Mais l'utilisateur libre de décider, pour chacune des 3 *m* variables, si cette variable restera fixée à une valeur qu'il a fournie, ou si elle sera fittée. Pour chacune des 3 *m* variables, l'utilisateur est en charge de fournir une valeur initiale, ou de laisser le logiciel la fixer aléatoirement. Enfin, il faut noter que plusieurs appels successifs de la fonction *fminsearch* sont généralement nécessaires pour atteindre le minimum de la fonction scalaire avec un jeu stable de paramètres finaux. Lors de ces appels successifs, les paramètres de sortie d'un appel sont utilisés comme paramètres d'entrée pour l'appel suivant.

Les fits ont été le plus souvent conduits en autorisant à varier tous les paramètres des *m* triplets, et en partant toujours de valeurs initiales aléatoires. Plusieurs runs ont été faits pour chaque spectre, pour garantir la stabilité des paramètres finaux. Pour chaque fit présenté, la valeur obtenue pour m sera indiquée, tout comme les 3 coefficients de corrélation linéaires (Linear Correlation Coefficient, LCC), C–M, C–Re, C–Im, qui traduisent la corrélation entre les données expérimentales et les données calculées pour les courbes: $|J_{PH}| = f(E)$, $Re(J_{PH}) = f(E)$ et $Im(J_{PH}) = f(E)$ respectivement.

Fits des PES des échantillons oxydés en vapeur d'eau pendant 30 heures

Tous les PES mesurés, quel que le soit potentiel appliqué (Figure 4.17(a)), ont été fittés. L'exemple en Figure B.18 montre les spectres expérimentaux et fittés à –600 mV. Tous les PES, quel que soit le potentiel appliqué, ont pu être fittés avec $m = 13$, et les valeurs de gaps obtenues à chaque potentiel sont très proches les unes des autres comme le montre la Figure B.19. Quel que soit le potentiel appliqué, le fit fournit les 12 mêmes valeurs de gap à 2.2 eV, 2.3 eV, 2.4 eV, 2.7 eV, 2.8(5) eV, 3.0 eV, 3.1(5) eV, 3.3 eV, 3.5 eV, 3.8 eV, 4.3 eV, et 4.7 eV (bien qu'il y ait quelques légers décalages à –600 mV, mais c'est le potentiel correspondant au minimum de photocourant sur les photovoltammogrammes). On peut donc considérer que le jeu de valeurs de gaps obtenu est digne de confiance.

Les valeurs de ces gaps suggèrent la présence de Fe_2O_3 ou $NiFe_2O_4$ (E_G = 2.2 – 2.4 eV [28–30]), Cr_2O_3 (E_G = 3.0 – 3.5 eV [31–35]), et $NiCr_2O_4$ (E_G = 4.3 eV [29–30]). Les gaps à 2.7 eV et 2.8(5) eV peuvent correspondre à une solution solide oxyde de type corundum riche en Cr, et le gap à 3.8 eV pourrait correspondre à Cr_2O_3 ou à une solution $NiFe_2O_4$–$NiCr_2O_4$ riche en Cr ; le gap à 4.7 eV n'a pas pu être attribué.

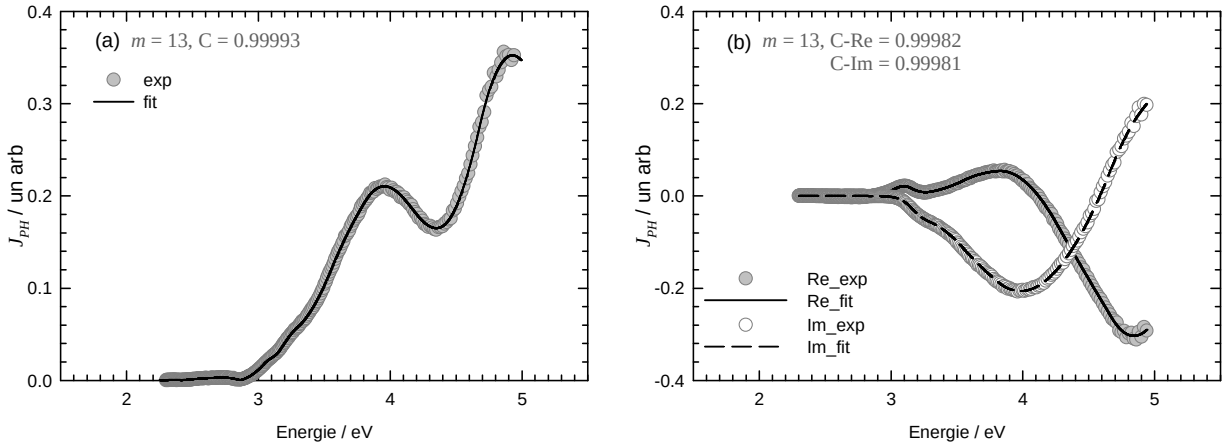

Figure B.18 (a) PES à –600 mV de l'alliage 690 oxydé en vapeur d'eau pendant 30 h et (b) ses parties réelle et imaginaire. "exp" et "fit" désignent les valeurs expérimentales et fittées. "Re" et "Im" désignent les parties réelle et imaginaire de J_{PH}.

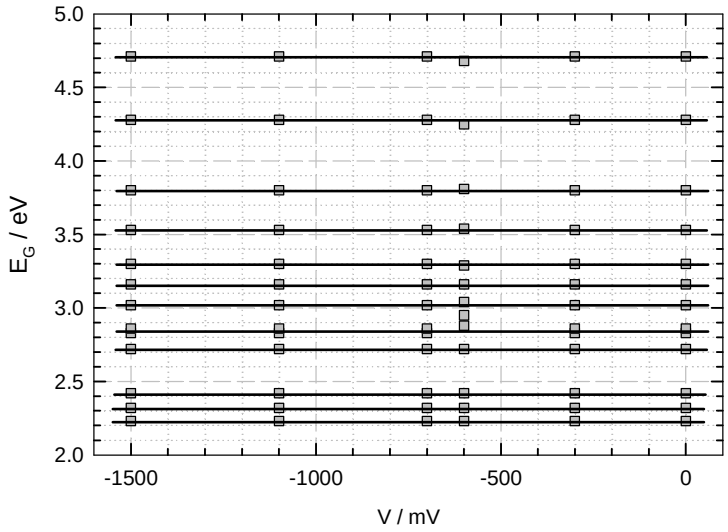

Figure B.19 Récapitulatif des gaps (E_G) obtenus en fittant les PES de la Figure B.17(a)

De tous les résultats macroscopiques ci–dessus, deux points majeurs ressortent: (1) le modèle décrivant les PES model et les procédures d'ajustement à ce modèle sont appliquables à tous les échantillons, et fournissent des fits et des paramètres de fits convaincants, notamment les valeurs de gap (2) le nombre de composants semiconducteurs nécessaire pour obtenir des fits convaincants est élevé.

Ce dernier point pouvant peut–être être attribué à la présence de différentes solutions solides $Fe_{2-x}Cr_xO_3$ sur diverses zones de la surface, des caractérisations mésoscopiques ont été entreprises.

B.5.3 Caractérisations photoélectrochimiques mésoscopiques

L'échantillon oxydé à l'air pendant for 21 heures, qui montrait une surface hétérogène (Figure B.21(a)), a été choisi pour ces caractérisations PEC mésoscopiques. Des PES mésoscopiques obtenus sur des zones foncées et claires de la surface sont présentés en Figure B.20(a). Ces PES montrent clairement des allures différentes sur les zones foncées et claires, et aussi que les zones claires fournissent des photocourants plus élevés. En divisant les valeurs à 3.53 eV par celles à 2.54 eV, on voit que le rapport ainsi défini est 2 fois plus grand sur la zone foncée, ce qui pourrait signifier que Cr_2O_3 (resp. $NiFe_2O_4$) est davantage présent sur le grain foncé (resp. le grain clair).

Les PES ont pu être fittés dans le domaine [2.1 – 3.75 eV], les fits correspondent aux lignes continues en Figure B.20(a). Les valeurs obtenues pour *m* sont 4 and 5 respectivement pour les zones foncées et claires. Les gaps obtenus (Tableau B.8) sont différents d'une zone à l'autre, mais certaines valeurs sont voisines entre zones. Le gap autour de 2.7 eV est un peu plus élevé sur la zone claire, signant une teneur plus en Cr dans $Fe_{2-x}Cr_xO_3$. Pour aller plus loin, pour chaque PES, deux pseudo–spectres ont été calculés à partir des paramètres de fits, i.e. les spectres que l'on aurait obtenus si seuls les composants de gaps en–dessous (resp. au–dessus) de 3.0 eV avaient été présents dans la couche. Ces pseudo–spectres sont présentés en Figure B.20(b). Ils confirment sans ambiguité les suggestions faites plus haut, à savoir que les oxydes formés sur les zones claires comportent davantage de composants à faible gap que les zones foncées, et moins de composants à haut gap.

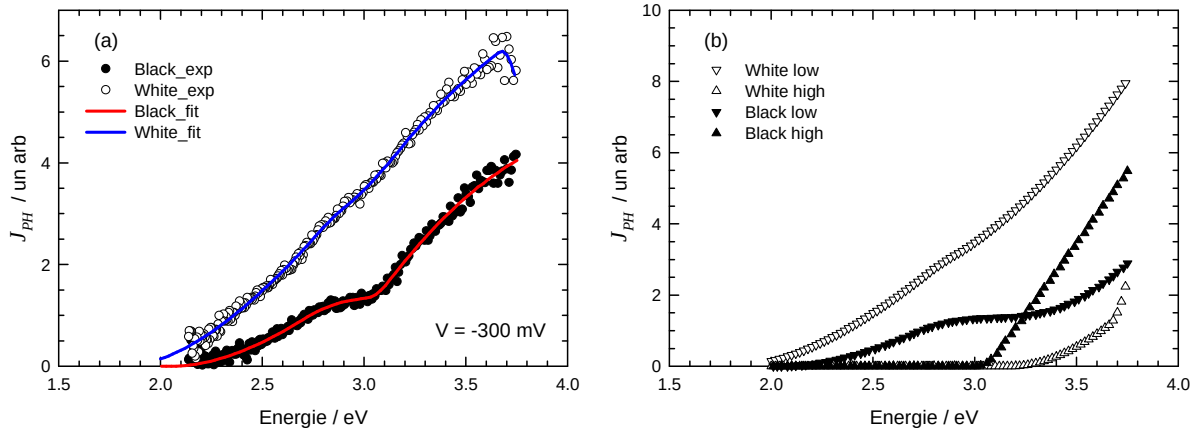

Figure B.20 (a) PES mésoscopiques obtenus sur des zones foncées (cercles noirs : données expérimentales, ligne rouge : spectre fitté) et claires (cercles blancs : données expérimentales, ligne bleue : spectre fitté) de l'alliage 690 oxydé à l'air pendant 21 h, (b) Pseudo–PES calculés à partir des résultats de fits des PES en (a)

Tableau B.8 Récapitulatif des énergies de gap, E_G, obtenus par les fits des PES mésoscopiquesde l'alliage 690 oxydé à l'air pendant 21 h (valeurs en eV). Les PES fittés ont été mesurés à –300 mV.

PEC macroscopique		1.79	2.17	2.25	2.71	3.02	3.16	3.44
PEC mésoscopique	Zone foncée		2.05		2.71	3.01	3.11	
	Zone claire	1.81			2.79	2.90	3.18	3.66

Le tableau B.8 récapitule les valeurs de gaps obtenues aux échelles macroscopique et mésoscopique. Comme les photocourants macroscopiques combinent les photocourants issus de tous les points de la surface de l'échantillon, la liste des gaps "macroscopiques" devraient inclure les gaps mesurés à l'échelle méso. Le tableau B.8 montre raisonnablement que tel est est le cas.

Enfin, les résultats ci–dessus montrent que les produits d'oxydation de l'alliage 690 dépendent de l'orientation de la surface exposée à l'atmosphère.

B.5.4 Caractérisations photoélectrochimiques microscopiques

Les raies à 2.54 eV et 3.53 eV d'un laser argon ont été utilisées pour enregistrer des images photoélectrochimiques. La raie d'énergie la plus faible permet de générer du photocourant dans $NiFe_2O_4$, Fe_2O_3 et $Fe_{2-x}Cr_xO_3$ (riche en fer) tandis que la raie d'énergie plus élevée peut générer du photocourant dans ces mêmes oxydes mais aussi dans d'autres de gap plus élevé tel que Cr_2O_3. Cependant, ces raies ne permettent pas d'″activer″ $NiCr_2O_4$ dont le gap est au–delà de 4.0 eV.

La Figure B.21 présente des images optiques et photoélectrochimiques typiques de celles obtenues avec les échantillons de la section B.5. Les deux images photoélectrochimiques des Figures 4.20(b) and (c) montrent des photocourants plus faibles aux joints de grains et sur la zone foncée. D'après l'image PEC à 2.54 eV, les oxydes de faible gap sont davantage présents sur les zones claires que sur les foncées et aux joints de grains. De plus, la diminution constatée du contraste de l'image à 3.54 eV, attendue au vu des résultats mésoscopiques, implique que la formation de Cr_2O_3 est favorisée aux joints de grains et que la fraction de Cr_2O_3 sur les zones claires est plus faible que sur les foncées.

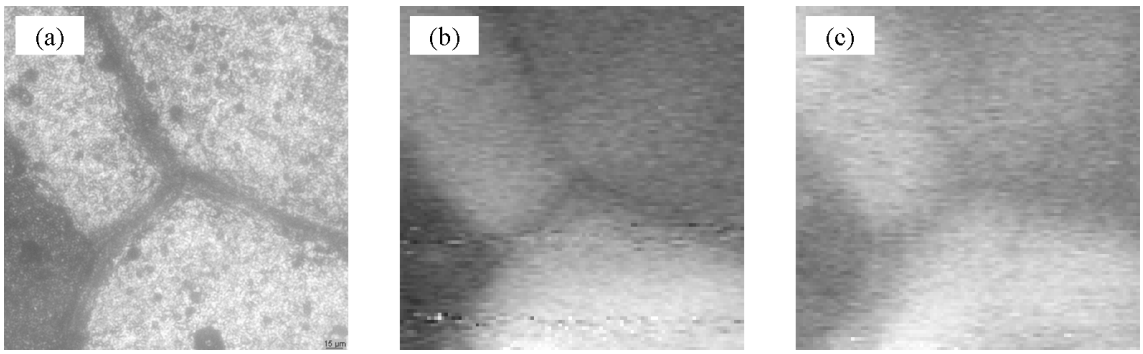

Figure B.21 Images de l'alliage 690 oxydé à l'air pendant 21 h; (a) image optique, (b) et (c) images PEC mesurées à –300 mV: (b) hν = 2.54 eV, et (c) hν = 3.54 eV

B.5.5 Etude de l'échantillon oxydé 2 h en oxygène

Les PES de la couche thermique formée sur l'alliage 690 après 2 h ont été difficiles à modéliser. Si la plupart des PES des couches d'oxydation de l'alliage 690 pouvait à première vue être raisonnablement fittée en considérant 6 à 8 composants dans la couche, il est rapidement apparu impossible, dans le cas des échantillons oxydés en oxygène pendant 2 h, d'obtenir un fit stable et convaincant sans augmenter le nombre de composants à 12 or 13, comme on va le voir dans la suite.

Le succès obtenu en augmentant *m* dans ce cas particulier nous a aussi conduits à réexaminer les cas des autres échantillons, et a permis d'améliorer encore les fits.

Cependant, la présence d'un nombre aussi grand de composants dans la couche d'oxydes pouvait paraître surprenante et introduire un doute sur la validité du modèle développé pour rendre compte des PES. La suite du manuscrit examine cette question importante.

B.5.5.1 Caractérisations photoélectrochimiques macroscopiques

Les PES macroscopiques et leurs transformées linéaires sont présentés en Figure B.22. A nouveau, et clairement, l'allure des spectres dépend du potentiel appliqué, et révèle la présence de plus d'un composant dans la couche. L'examen des transformées suggère qu'il y aurait au moins 4 composants, de gap difficile à évaluer cependant.

La Figure B.23 illustre la haute qualité des ajustements réalisés avec notre modèle ; onze phases semiconductrices (m = 11) sont détectées à –600 mV, tandis que onze (m = 11) and douze (m = 12) phases semiconductrices sont détectées à –300 mV et 0 mV respectivement. Pour chacun des PES, le fit a été répété de nombreuses fois avec des paramètres initiaux aléatoires, les meilleurs fits (distance minimale à la courbe expérimentale) fournissant un jeu stable de paramètres finaux. La Figure B.24 montre que les gaps évalués dépendent peu du potentiel appliqué.

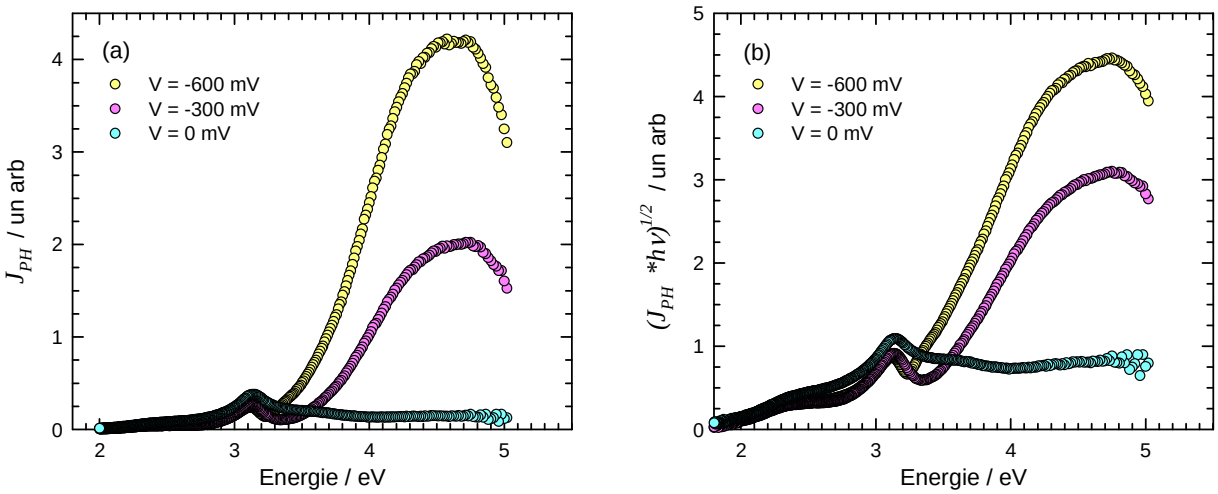

Figure B.22 (a) PES macroscopiques et (b) transformées linéaires correspondantes pour l'alliage 690 oxydé en oxygène pendant 2 h

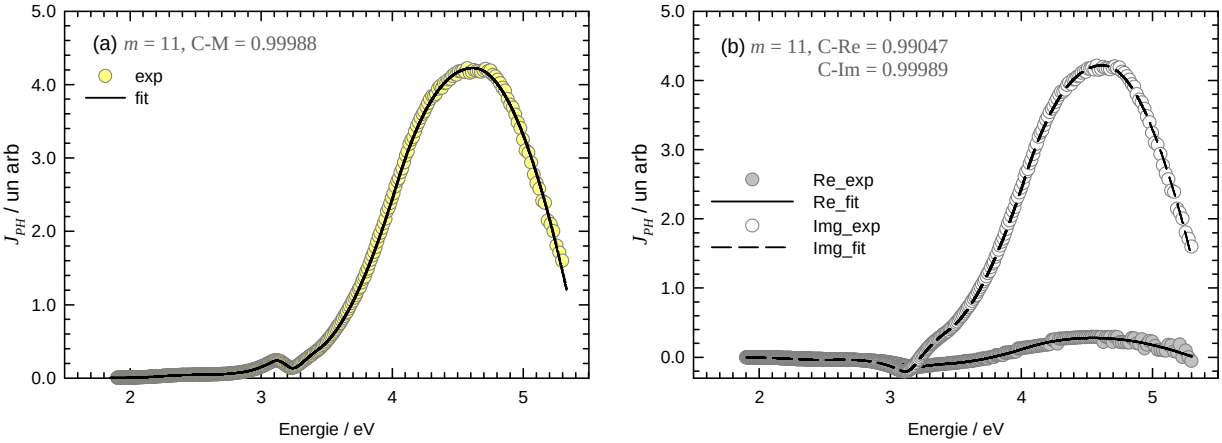

Figure B.23 (a) PES à –600 mV de l'alliage 690 oxydé en oxygène pendant 2 h, (b) parties réelle et imaginaire du photocourant. "exp" et "fit" désignent les valeurs expérimentales et fittées. "Re" et "Im" désignent les parties réelle et imaginaire de J_{PH}.

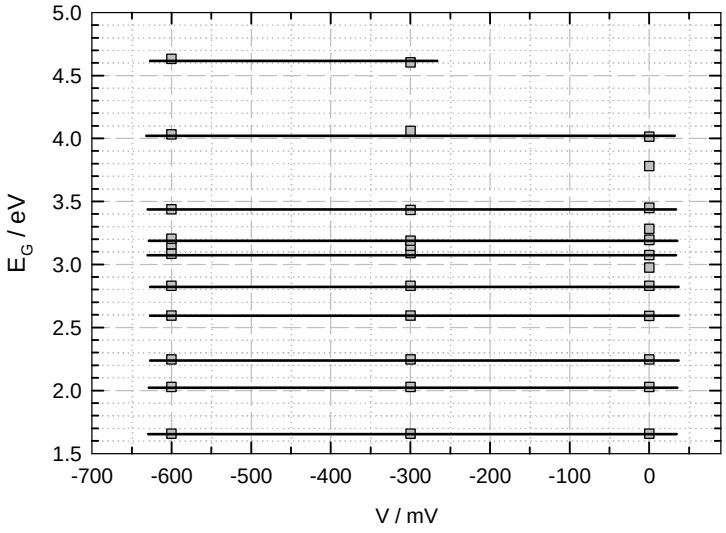

Figure B.24 Gaps obtenus par le fit des PES en Figure B.22(a)

Des résultats ci–dessus, nous concluons que 12 composants semiconducteurs sont réellement présents dans la couche d'oxydation (10 seulement sont détectés quel que soit le potentiel).

B.5.5.2 Imagerie Raman

Par bonheur, la complexité de nos échantillons oxydés sur un temps court en oxygène avait été jugée intéressante par les équipes Raman du CMTC –SIMaP (Dr A.Crisci) et du LEPMI (Dr M. Mermoux). Des images Raman d'une zone choisie de notre échantillon ont été réalisées avec une résolution spatiale de 2 µm en x et en y (la sonde Raman était la raie 514 nm d'un laser focalisée en un spot de diamètre 1µm sur l'échantillon) ; plus de 50000 spectres ont ainsi été enregistrés, chacun correspondant à un point de la zone analysée.

Ce jeu de spectres a d'abord été soumis à une analyse en composantes principales (Principal Components Analysis, PCA), à l'aide d'un logiciel fourni par la société Renishaw, le fabricant de l'installation Raman utilisée. Cette analyse PCA a montré le jeu complet de spectres comprenait 12 composantes principales, dont les signatures sont données en Figure B.25 en même temps que les images de leur « intensité » relative sur la zone analysée.

Ensuite deux analyses multivariées ont été réalisées, d'abord avec 5 (Figure B.26), puis 10 (Figure B.27) des 12 composantes principales détectées. Il s'est avéré que la première analyse a montré que 98% des 50000 spectres pouvaient effectivement être obtenus combinaison linéaire des 5 spectres "purs". Et la seconde analyse a montré que 10 composantes étaient nécessaires pour rendre compte de 99.5% des spectres.

Il est donc plus que certain que la couche thermique étudiée est bien constituée de plus de 10 oxydes, 5 d'entre eux pouvant être considérés comme les composants majoritaires. Et, à notre avis, ces résultats fournissent une corrélation croisée de ceux obtenus en fittant les PES avec notre nouveau modèle (nécessité de 12 SCs pour rendre compte des PES).

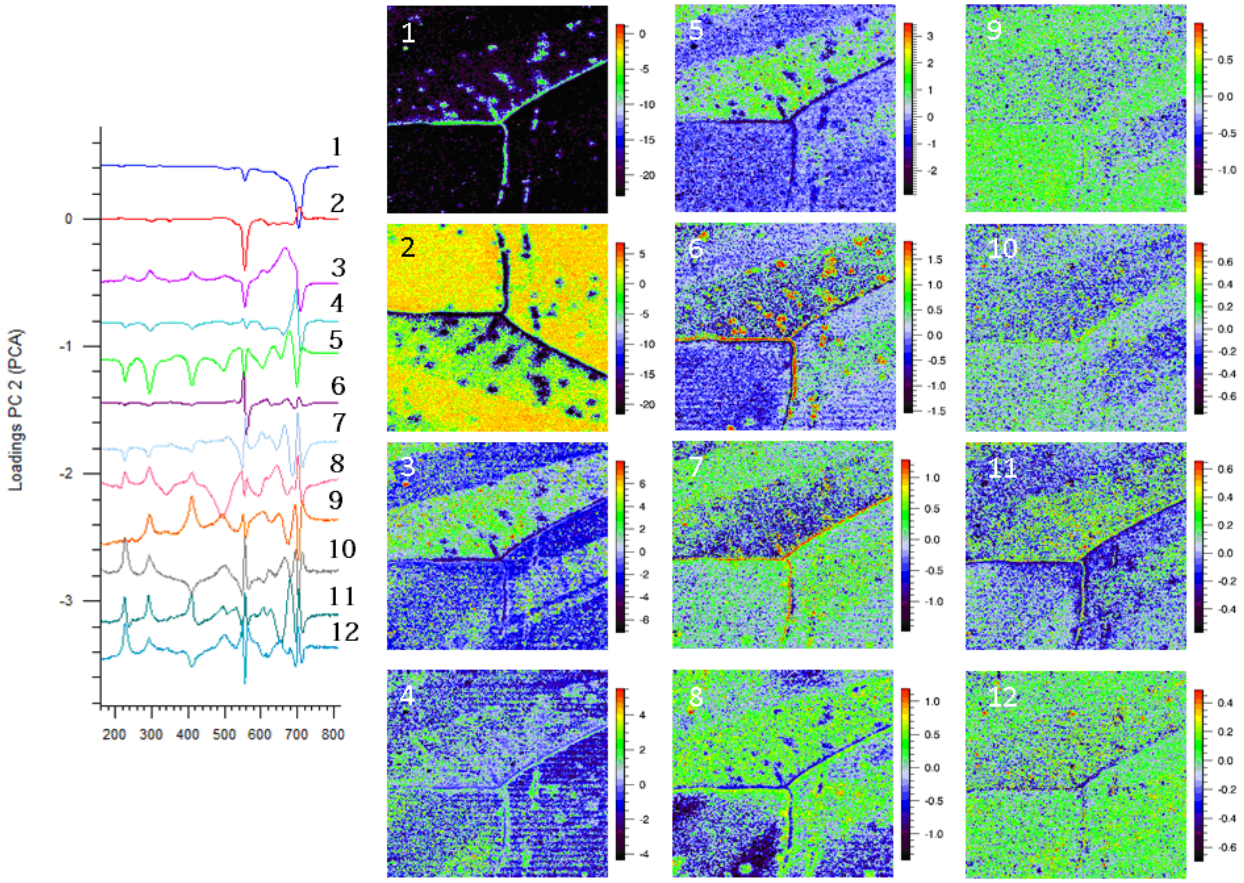

Figure B.25 Résultats de l'analyse en composantes principales des spectres de l'image Raman (Alliage 690 oxydé en oxygène pendant 2h)

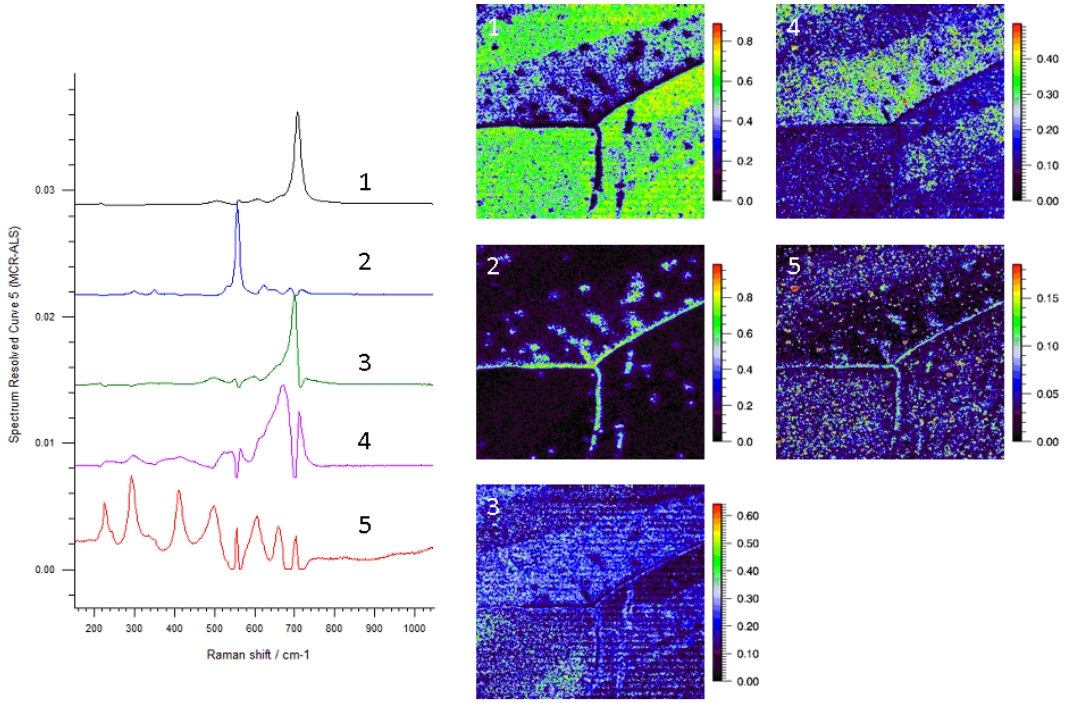

Figure B.26 Images des résultats des analyses multivariées réalisée avec 5 des 12 composantes principales obtenues par PCA

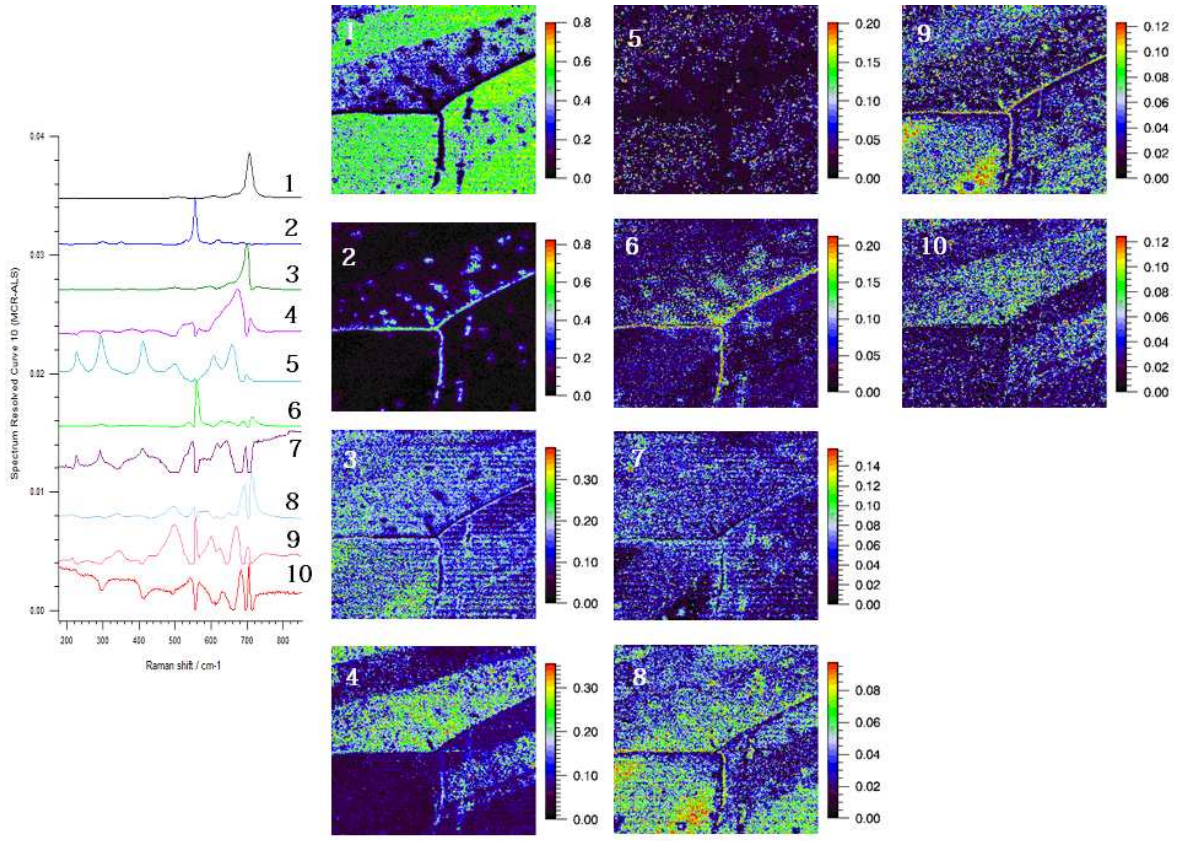

Figure B.27 Images des résultats des analyses multivariées réalisées avec 10 des 12 composantes principales obtenues par PCA

B.5.6 Conclusions sur les caractérisations PEC de l'oxydation de l'alliage base nickel

La photoélectrochimie multi−échelles a montré de manière éclatante son intérêt dans la caractérisation des propriétés semconductrices de l'oxyde thermique formé sur un alliage 690 (base Nickel) and aussi dans l'identification des composantes de la couche, la mésoscopie et la microscopie PEC pointant l'influence sur l'oxydation d'orientations différentes de la surface.

La qualité des informations tirées de l'analyse des PES a été grandement améliorée par l'utilisation du nouveau modèle développé dans notre groupe, même pour des couches très complexes. Et, sur l'exemple particulier de la couche formée en oxygène à temps court, ce modèle a pu être validé par l'analyse d'images Raman traitées de façon novatrice par nos collègues Ramanistes.

B.6 Conclusions générales

Caractérisation photoélectrochimique de solutions solides hématite–chromine

Les gaps de la chromine ont été confirmés à 3.0 eV et/ou [3.3–3.8] eV. La chromine a été observée à nouveau tantôt n– ou p–, tantôt isolante, selon les conditions d'oxydation (durées, atmosphères). A haute température, pour les alliages chromino–formeurs, la chromine est initialement n– ou p, puis devient plus isolante avec l'augmentation de la durée d'oxydation. La présence de vapeur d'eau et/ou d'hydrogène dans l'atmosphère d'oxydation tend à promouvoir la chromine de type n. A haute (resp. base) pression partielle d'oxygène, la chromine tend à être p (resp. n).

Même si des pastilles de solution solide d'oxyde pure n'ont pu être obtenues, l'influence de x sur le gap de $Fe_{2-x}Cr_xO_3$ a pu être observée et grossièrement corrélée aux valeurs attendues au vu de modèles thermodynamiques.

Progrès dans les caractérisations photoélectrochimiques

D'une part, la faisabilité et l'intérêt des caractérisations photoélectrochimiques à l'échelle mésoscopique a été démonstrée pour la première fois sur l'exemple de l'oxydation d'aciers inox duplex. Les caractérisations mésoscopiques ont permis de mesurer des PES locaux sur des micro–zones (30 µm de diamètre), permettant de distinguer les oxydes formés sur des grains individuels de ferrite et d'austénite, en particulier pour ce qui concerne le ratio x dans $Fe_{2-x}Cr_xO_3$. A partir d'aujourd'hui, les outils photoélectrochimiques, au moins dans notre laboratoire, peuvent être utilisés dans 3 modes : (1) à l'échelle macroscopique, pour avoir une vue moyennée des propriétés de l'échantillon, (2) à l'échelle microscopique, pour examiner la distribution latérale des photocourants (et donc des hétérogénéités) avec une résolution de l'ordre du 1 µm, et (3) à l'échelle mésoscopique, pour obtenir des informations complètes sur des zones spécifiques d'échantillons hétérogènes.

D'autre part, notre nouvelle approche de l'analyse des PES s'est montrée efficace et précieuse dans l'analyse de PES, même dans le cas de couches très complexes, permettant d'évaluer le nombre de composants semiconducteurs dans la couche et les gaps de ceux–ci.

REFERENCES

[1] S. Henry, J. Mougin, Y. Wouters, J.–P. Petit, and A. Galerie, Characterization of chromia scales grown on pure chromium in different oxidizing atmospheres, *Microscopy of Oxidation* (2000) 231–234.

[2] T. Norby, The influence of hydrogen defects on transport properties of oxides, *Advances in Ceramics* **23** (1987) 107.

[3] N. Bonanos, Oxide–based protonic conductors: point defects and transport properties, *Solid State Ionics* **145** (2001) 265–274.

[4] P. Kofstad, Defects and transport properties of metal oxides, *Oxidation of Metals* **44** (1/2) (1995) 3–27.

[5] Y. Wouters, A. Galerie, J–P. Petit, Photoelectrochemical characterisation of chromia scales thermally grown on various metal substrates, *Material Science Forum* **595–598** (2008) 1181–1188.

[6] P. Kofstad, *High temperature corrosion*, London and New York: Elsevier applied science, 1988.

[7] A. Srisual, S. Coindeau, A. Galerie, J.–P. Petit, and Y. Wouters, Identification by photoelectrochemistry of oxide phases grown during the initial stages of thermal oxidation of AISI 441 ferritic stainless steel, *Corrosion Science* **51** (2009) 562–568.

[8] F. Di Quarto, S. Piazza, and C. Sunseri, A photocurrent spectroscopic investigation of passive films on chromium, *Corrosion Science* **31** (1990) 721–726.

[9] F. Di Quarto, S. Piazza, and C. Sunseri, Photoelectrochemistry in corrosion studies: Achievements and perspectives, *Materials Science Forum* **192–194** (1995) 633–648.

[10] J. Portier, G. Campet, C. W. Kwon, J. Etourneau, M. A. Subramanian, Relationships between optical band gap and thermodynamic properties of binary oxides, *International Journal of Inorganic Materials* **3** (2001) 1091–1094.

[11] W. W. Gärtner, Depletion–layer photoeffects in semiconductors, *Physical Review* **116** (1) (1959) 84–87.

[12] M. A. Butler, Photoelectrolysis and physical properties of the semiconducting electrode WO_2, *Journal of Applied Physics* **48** (5) (1977) 1914–1920.

[13] D.J. Gardiner, C. J. Littleton, K. M. Thomas, and K.N. Strafford, Distribution and characterization of high temperature air corrosion products on iron–chromium alloys by Raman microscopy, *Oxidation of* **27** (1987) 57–72.

[14] K. F. McCarty and D. R. Boehme, A Raman study of the systems $Fe_{3-x}Cr_xO_4$ and $Fe_{2-x}Cr_xO_3$, *Journal of Solid State Chemistry* **79** (1989) 19–27.

[15] N. Karimi, F. Riffard, F. Rabaste, S. Perrier, R. Cueff, C. Issartel, H. Buscail, Characterization of the oxides formed at 1000 °C on the AISI 304 stainless steel by X–ray diffraction and infrared spectroscopy, *Appl. Surf. Sci.* **254** (2008) 2292–2299.

[16] A. Galerie, S. Henry, Y. Wouters, M. Mermoux, J.–P. Petit, L. Antoni, Mechanisms of chromia scale failure during the course of 15–18Cr ferritic stainless steel oxidation in water vapour, *Mater. High Temp.* **22 (1/2)** (2005) 105–112.

[17] J. Mougin, *Tenue mécanique de couche d'oxyde thermique générées sur le chrome et sur quelques aciers inoxydables ferritiques*, PhD Thesis, Institut National Polytechnique de Grenoble, France, 2001 (in French).

[18] ASM International Handbook Committee, *Metals Handbook Ninth Edition Volume 13, Corrosion*, Park (Ohio): ASM International, 1987.

[19] F. di Quarto, C. Sunseri, S. Piazza, and M. C. Romano, Semiempirical correlation between optical band gap values of oxides and the difference of electronegativity of the elements. Its importance for a quantitative use of photocurrent spectroscopy in corrosion, *J. Phys. Chem. B* **101** (1997) 2519–2525.

[20] Y. Wouters, A. Galerie, J.–P. Petit, Photoelectrochemical study of oxides thermally grown on titanium in oxygen or water vapor atmospheres, *J. Electrochem. Soc.* **154** (10) (2007) C587–C592.

[21] A K Vijh, Correlation between bond energies and forbidden gaps of inorganic binary compounds, *J. Phys. Chem. Solids* **30** (1969) 1999–2005.

[22] A. Srisrual, J.–P. Petit, Y. Wouters, and A. Galerie, Multiscale photoelectrochemical studies on oxidized duplex stainless steels, *Oxid. Met.* **79** (2013) 337–347.

[23] J.–P. Petit, R. Boichot, A. Loucif, A. Srisrual, and Y. Wouters, Photoelectrochemistry of oxidation layers: a novel approach to analyze photocurrent energy spectra, *Oxid. Met.* **79** (2013) 349–359.

[24] S.R. Morrison, *Electrochemistry at semiconductor and oxidized metal electrodes*, Plenum Press, NY, 1980.

[25] U. Stimming, Photoelectrochemical studies of passive films, *Electrochemica Acta* **31 (4)** (1986) 415–429.

[26] J.–P. Petit, R. Boichot, A. Loucif, A. Srisrual, Y. Wouters, Photoelectrochemistry of oxidation layers: A novel approach to analyze photocurrent energy spectra, *Oxid. Met.* **79** (2013) 349–359.

[27] J.C. Lagarias, J.A. Reeds, M.H. Wright and P. E. Wright, Convergence properties of the Nelde—Mead Simplex method in low dimension, *SIAM J. Optimiz.* **9 (1)** (1998) 112–147.

[28] F. Bergmann, M. Handschuh, W. Lorenz, Charge transfer dynamics of electrochemical dark and photoprocesses on semiconductors part II: Fermi energy characteristics and photoadmittance functions, *Chem. Phys.* **215 (1)** (1997) 157–166.

[29] L. P. Bonfrisco and M. Frary, Effects of crystallographic orientation on the early stages of oxidation in nickel and chromium, *J. of Materials Science* **45 (6)** (2010) 1663–1671.

[30] A. R. J. Kucernak, R. Peat, and D. E. Williams, Dissolution and reaction of sulfide inclusions in stainless steel imaged using scanning laser photoelectrochemical microscopy, *J. Electrochem. Soc.* **139 (8)** (1992) 2337–2340.

[31] F. Di Quarto, S. Piazza, and C. Sunseri, A photocurrent spectroscopic investigation of passive films on chromium, *Corr. Sci.* **31** (1990) 721–726.

[32] F. Di Quarto, S. Piazza, and C. Sunseri, Photoelectrochemistry in corrosion studies: Achievements and perspectives, *Materials Science Forum* **192–194** (1995) 633–648.

[33] J. Portier, G. Campet, C. W. Kwon, J. Etourneau, M. A. Subramanian, Relationships between optical band gap and thermodynamic properties of binary oxides, *International Journal of Inorganic Materials* **3** (2001) 1091–1094.

[34] Y. Wouters, A. Galerie, J–P. Petit, Photoelectrochemical characterisation of chromia scales thermally grown on various metal substrates, *Material Science Forum* **595–598** (2008) 1181–1188.

[35] C.–S. Chang, H. Gomi, H. Sakata, Electric and optical properties of Cr_2O_3 films prapared by chemical vapour deposition, *Phys. Stat. Sol.* (a) **155** (1996) 417–425.

Caractérisation photoélectrochimique d'oxydes thermiques développés sur métaux et alliages modèles

La Corrosion Haute Température (HTC), en environnements divers et sévères, d'alliages métalliques toujours plus élaborés en termes de composition et micro–structure, est un sujet industriel et scientifique très complexe. La PhotoElectroChimie (PEC) est une technique de choix pour caractériser les propriétés physico–chimiques et électroniques des couches d'oxydation très hétérogènes formées en HTC. Sur des exemples d'alliages modèles mais représentatifs de la réalité industrielle (aciers duplex, base–Nickel 690), ce travail présente le développement et la validation d'un dispositif expérimental permettant d'appliquer pour la première fois tout l'arsenal des techniques PEC à l'échelle mésoscopique (typiquement 30 µm), ainsi que la validation d'une modélisation originale développée au SIMaP des spectres de photocourants en énergie, qui permet de les décrire et ajuster finement et d'en extraire notamment avec précision les gaps des oxydes semiconducteurs présents dans la couche thermique.

Mots–Clés: Photoélectrochimique, les aciers inoxydables austéno–ferritiques, alliages bas nickel, vapeur d'eau, orientation de surface, analyse à multi–échelles

Photoelectrochemical characterization of thermal oxide developed on metal and model alloys

High Temperature Corrosion (HTC), in various and severe atmospheres, of continually more elaborated (composition, micro–structure) metallic alloys, is a rather complex industrial and scientific topic. PhotoElectroChemistry (PEC) acquired a special place in the characterization of physico–chemical and electronic properties of the highly heterogeneous oxidation layers formed in HTC. Through studies of model but industrially representative samples (duplex stainless steel, Ni–base alloy 690), this work presents the development and validation of an experimental set–up allowing for the first time to use the whole set of PEC techniques at the mesoscopic level (typically 30 µm), as well as the validation of an original model of photocurrent energy spectra, developed at SIMaP, allowing to well describe, and accurately fit the latter spectra, and thus yielding, notably, precise bandgap values for the semiconducting components of the thermal scale.

Keywords: Photoelectrochemistry, duplex stainless steels, nickel–based alloys, water vapor, surface orientation, multiscale analysis

Laboratoire Science et Ingénierie des Matériaux et Procédés (SIMaP) – Université de Grenoble
1130 rue de la Piscine - BP 75 - F - 38402 St Martin d'Hères Cedex
Tél : +33 (0) 4 76 82 65 17
http://simap.grenoble-inp.fr/accueil/